TECHNISCHE UNIVERSITÄT DARMSTADT

Surface Science

Plasma-enhanced chemical vapor deposition of cobalt-based catalysts for the oxygen evolution reaction

Vom Fachbereich Material- und Geowissenschaften
der Technischen Universität Darmstadt

Zur Erlangung des akademischen Grades Doktor-Ingenieur (Dr.-Ing)

genehmigte Dissertation von
M.Sc. Natascha Weidler aus Mannheim

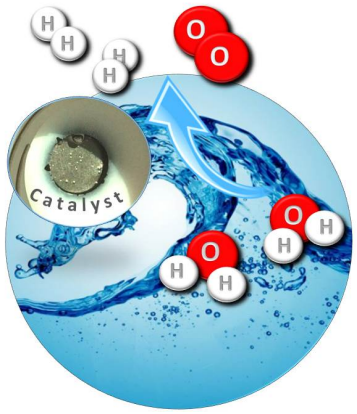

1. Report: Prof. Dr. Wolfram Jaegermann/ PD Dr. Bernhard Kaiser
2. Report: Prof. Dr. Ulrike Kramm
Tag der Einreichung: 03.03.2017
Tag der mündlichen Prüfung 21.04.2017
Darmstadt 2017, D17

Plasma-enhanced chemical vapor deposition of cobalt-based catalysts for the electrochemical oxygen evolution reaction

Department of Materials and Earth Sciences
of the Technical University Darmstadt

Approved dissertation of Natascha Weidler (born in Mannheim)

1. Report: Prof. Dr. Wolfram Jaegermann/ PD Dr. Bernhard Kaiser
2. Report: Prof. Dr. Ulrike Kramm

Submission date: 03.03.2017
Examination date: 21.04.2017

Darmstadt 2017, D17

This thesis is dedicated to my husband Heiko and my father Andreas.

Für den Optimisten ist das Leben kein Problem,
sondern bereits die Lösung.
(Marcel Pagnol)

Thesis Statement pursuant

I herewith formally declare that I have written the submitted thesis independently. I did not use any outside support except for the quoted literature and other sources mentioned in the paper. I clearly marked and separately listed all of the literature and all of the other sources which I employed when producing this academic work, either literally or in content. This thesis has not been handed in or published before in the same or similar form. In the submitted thesis the written copies and the electronic version are identical in content.

Darmstadt,

Natascha Weidler

Abstract

In this thesis a plasma-enhanced chemical vapor deposition system has been installed to synthesize transition metal oxide/hydroxide films as catalysts for the oxygen evolution reaction (OER). First, the influence of various deposition parameters like the substrate temperature, the operation mode (thermal vs. plasma) and the type of reactive gas (oxygen vs. air) on the electrochemical activity has been investigated in detail for single metal oxide/hydroxide films. It turned out, that especially the choice of reactive gas has a great impact on the resulting oxidation state and surface composition. While $CoO_x(OH)_y$ films were deposited when air was used as a reactive gas, the use of oxygen as a reactive gas lead to the deposition of CoO_x. By measuring XPS from before and after the electrochemical characterization, a correlation between the change of oxidation state and the resulting electrochemical activity has been identified. Finally, Co-based bimetallic catalysts, $CoMO_x$ and $CoMO_x(OH)_y$ (M=Ni, Fe, Cu), were deposited and the effect of the admixture of the second metal on the electronic structure and activity was studied.

In dieser Arbeit wurde eine Anlage zur plasma-gestützten Gasphasenabscheidung von Übergangsmetalloxiden/ -hydroxiden als Katalysatoren für die Sauerstoffentwicklung konstruiert. Als erstes wurde der Einfluss verschiedener Abscheideparameter wie der Substrattemperatur, dem Betriebsmodus (thermisch vs. Plasma) und der Wahl des Reaktivgases (Sauerstoff vs. Luft) auf die elektrochemische Aktivität von reinen Metalloxid/-hydroxid Schichten untersucht. Es stellte sich heraus, dass vor allem die Wahl des Reaktivgases einen großen Einfluss auf die resultierende Oxidationsstufe und die Oberflächenzusammensetzung hat. Während mit Luft $CoO_x(OH)_y$ Schichten abgeschieden wurden, führte die Verwendung von Sauerstoff zur Abscheidung von CoO_x Schichten. Durch die XPS Untersuchung der Proben vor und nach der elektrochemischen Charakterisierung konnte eine Korrelation zwischen der Änderung des Oxidationszustandes und der resultierenden Aktivität identifiziert werden. Zum Schluss wurden Co-basierte bimetallische Katalysatoren, $CoMO_x$ and $CoMO_x(OH)_y$ (M=Ni, Fe, Cu), abgeschieden und der Effekt des Zweitmetalls auf die elektronische Struktur und Aktivität studiert.

Contents

Acronyms

BE	Binding energy
BMWI	Bundesministerium für Wissenschaft und Energie
BMBF	Bundesministerium für Bildung und Forschung
CV	Cyclic voltammetry
CVD	Chemical vapor deposition
DSA	Dimensionally stable anodes
DTA	Differential thermal analysis
EC	Electrochemical characterization
EIS	Electrochemical impedance spectroscopy
FWHM	Full width at half maximum
GIXRD	Gracing incidient x-ray photoelectron spectroscopy
GC	Glassy cabon
HBE	High binding energy feature
HER	Hydrogen evolution reaction
IMFP	Inelastic mean free path
LBE	Low binding energy feature
SEM	Scanning electron microscopy
SHE	Standard hydrogen electrode
TGA	Thermogravimetric analysis
OER	Oxygen evolution reaction
UHV	Ultra-high vacuum
UPS	Ultraviolet photoelectron spectroscopy

VB	Valence band
VBM	Valence band maximum
XPS	X-ray photoelectron spectroscopy
XRD	X-ray diffraction

1. Introduction

Only few years ago, energy was predominantly supplied by coal-fired plants, natural gas and nuclear power plants. The energy was generated where it was consumed. Due to the increasing importance of the climate change and the nuclear accident in Fukushima (March 2011), the federal government passed the Renewable Energy Sources Act (German: Erneuerbare Energien Gesetz (EEG)) in 2011.
The goals of the energy transition were to abandon nuclear energy and to reduce the amount of greenhouse-gases with regard to the climate change but also to become independent from the import of fossil fuels. [1] A first progress report to the energy transition was published in 2014 from the federal ministry for economic affairs and energy (Bundesministerium für Wirtschaft und Energie). The report shows, that the final energy consumption from renewable energies increase for different energy sectors (electricity, heat and fuel). [1] Figure 1.1 plots the share of electricity, heat and fuel consumption from renewable energies from the year 1990 to 2013. It comes clear, that renewable energies gain importance in all sectors. [1]

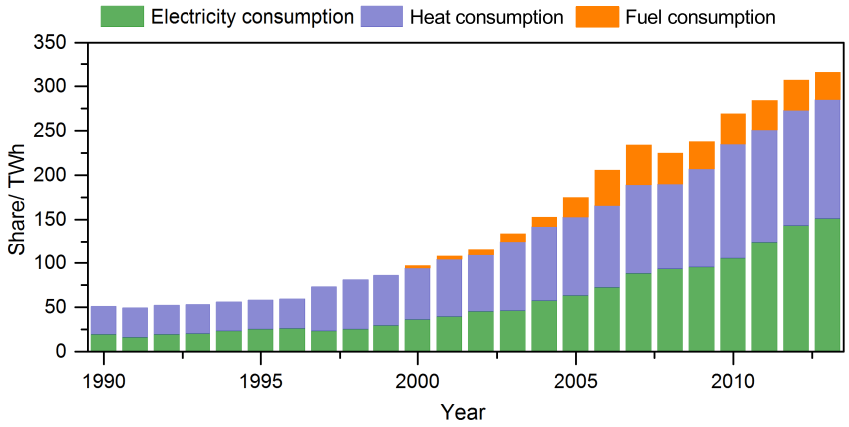

Figure 1.1. Development of the renewable energy consumption divided by energy sectors. [1]

In 2015, renewable energies contributed about 30 % to the gross electricity generation of Germany. [1] For comparison, in 2000 the contribution of renewable energies was only 6.6 %. Figure 1.2 shows the share of various energy sources in the gross power generation of Germany as well as the share of different technologies (hydropower, wind power, photovoltaics and biomass conversion) in the renewable energy produced.
In contrast to conventional primary energy, which is continuously available, wind and solar power generation is highly intermittent and characterized by rapid changes. Nevertheless, in order to maintain the high security of supply and to stabilize the grid, a balance between demand and supply must be secured at any time. This balance can be achieved through a grid expansion, a more flexible energy production, an intelligent load and demand management and by the development of appropriate storage technologies. [2]

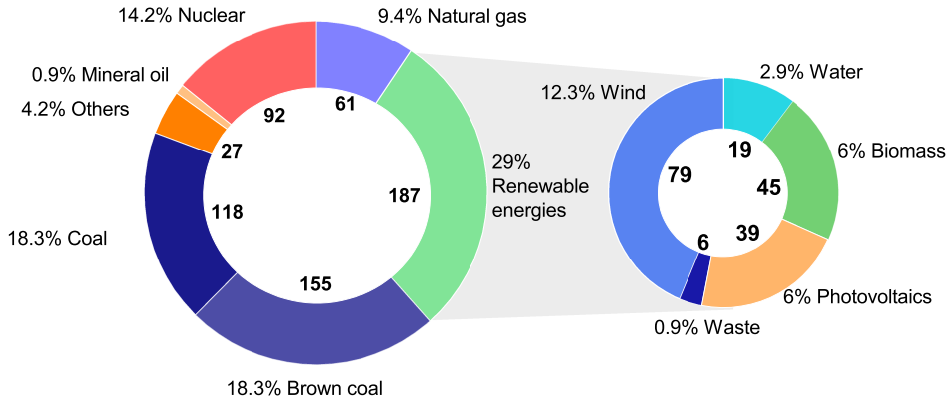

Figure 1.2. Share of various energy sources in the gross electricity generation of germany in the year 2015 in TWh. [1]

Since electricity itself cannot be stored directly in high quantities so far, it has to be converted to other forms of energy e.g chemical energy, heat energy or mechanical energy, which can be converted back into its electrical form in times of demand. The world wide storage capacity of about 111 GW is mainly ensured by pumped hydroelectric storage systems. [3] But the expansion of this technology is geographically limited and therefore alternative technologies have to be developed. Figure 1.3 compares the power and time regimes of different storage technologies. Short-term storage systems like supercapacitors and batteries have limited capacity but provide peak performances within seconds to minutes. In contrast, long-term storage systems based on hydrogen provide GW capacities and supply peak performances within hours to days. Especially since hydrogen has the highest energy density by weight (33.3 kWh/kg), the hydrogen production by water electrolysis is often announced as the crucial key technology for a long-term storage system of excess energy.

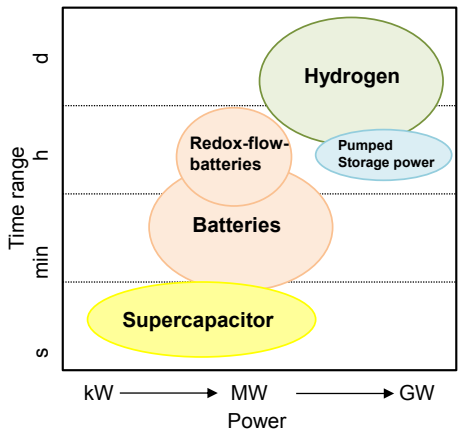

Figure 1.3. Power and time regimes of different storage technologies.

Technical electrolysers operate at current densities between 0.2 - 0.45 A/cm^2, potentials between 1.8 - 2.4 V, operating temperatures and pressures between 50 - 80 °C and 1 - 150 bar. [3]

The atmospheric alkaline water electrolysis represents the most established technology in industry for the electrochemical synthesis of hydrogen. Production rates of 10 - 500 m^3/h are realized with an energy yield of about 60 - 88 %. Up to now, the company Lurgi GmbH installed the biggest commercial stack consisting of 556 cells, which produces hydrogen with a flow of 760 m^3/h. Nevertheless, compared to the technical maturity level of lead batteries and pump storage systems, still high efforts must be directed into the further development and optimization of the water electrolysis process.

In addition to the process optimization, the electrodes design plays a crucial role since the water splitting reaction is kinetically hindered. One of the major obstacles of the electrolysis of water is the overvoltage loss for the oxygen evolution reaction (OER). In terms of overpotential, the noble metal oxides IrO_2 and RuO_2 as well as their bimetallic compounds still represent the best dark water oxidation catalysts but they are rare and expensive. [4,5] Cheap, abundant and highly active catalysts are required to reduce potential energy losses and to increase the process efficiency.

As part of the funding initiative "MatRessource" of the BMBF (Bundesministerium für Bildung und Forschung), the project SusHy "Sustainable Hydrogen-Edelmetallfreie Katalysatoren für die Wasserstoffproduktion aus erneuerbaren Energien" was founded in corporation with Evonik Industries AG, the Forschungszentrum Jülich, Leibniz-Institut für Katalyse, the Ruhr Universität Bochum and the Technical University Darmstadt. [6] The aim of this project is on the one hand to develop non-noble catalysts for both, the hydrogen evolution reaction (HER) and the oxygen evolution reaction (OER) and on the other hand to integrate these in an operating photo-electrochemical device that enable the clean production of hydrogen using sunlight. [6] With respect to the specialized know-how of the project partners, the responsibilities were divided into the development of the solar device (Forschungszentrum Jülich, TU Darmstadt), the investigation of HER/OER catalysts (Leibniz-Institut für Katalyse, Technical University Darmstadt, Ruhr University Bochum) and the establishment of the final photo-electrochemical device for water splitting (Evonik Industries AG).

As part of the SusHy project, the overall objective of this thesis is to investigate cheap and abundant transition metal oxide catalysts as alternatives for the OER. Hereby, the choice of transition metals for the deposition of mono-metallic and bimetallic oxide/hydroxide catalysts include Co, Ni and Fe, whereby Co is set as the predominant metal. The competence of cobalt in form of oxide/hydroxide films and $[Co(H_2O)_6]^{3+}/[Co(H_2O)_6]^{2+}$ complexes as catalysts for the water oxidation is reported many times in literature. [7] In general, the activity trends found for the transition metal oxides differ for different groups. While Delahay et al. reported an increase in overpotential at 1 A/cm^2 in the order of Co>Cu>Ni for the OER in alkaline media, an experimental activity trend in the order of Ni>Co>Fe was found by Lyons et al at 10 mA/cm^2. [8,9] It is commonly known, that an increase in activity of single metal oxides can be achieved by the admixture of a second metal. [5,10–12]

There are several synthesis techniques reported for transition metal oxides including electrodeposition, hydrothermal methods, organic synthesis, sputtering and chemical vapor deposition (CVD). [5,13–17] While the project partners focus on the catalyst synthesis by hydrothermal methods, the focus of this thesis relays on the installation of a PECVD process to deposit thin film catalysts for several reasons:

1. The electrochemical activity of thin film catalysts ($\delta < 10$ nm) is not significantly influenced by the materials conductivity since the charge carriers must move only a short distance before reaching the electrode. Furthermore, the investigated activity should be independent of charge carrier concentrations and interfacial contact properties since thin films do not support large depletion zones. Therefore, the investigation of thin film catalysts as model systems are useful to gain a fundamental understanding of the catalytic behavior in dependence on the preparation conditions, the catalysts composition, structural arrangement and the electronic structure. [5]

2. Thin film techniques like CVD/PECVD or sputtering provide a binder-free deposition of the active material directly onto the substrate. In contrast, the electrode preparation from powdery catalysts do mostly require the additional use of a binder and the layer thickness is difficult to adjust. Furthermore, the presence of grain boundaries can influence the charge carrier transport, which limits the overall electrochemical activity.

3. The PECVD method offers the synthesis of cobalt based oxide catalysts at low-temperatures. Especially with respect to the parallel work done in our group on solar cells, a process should be developed, which offers the possibility to deposit catalysts directly onto the temperature sensitive solar devices.

4. In general, thin film deposition techniques provide the possibility to deposit catalysts onto three-dimensional porous electrodes in a conformal way.

In fact, the establishment of a PECVD process to deposit thin film cobalt based oxide catalysts for the OER is innovative since this was not realized before. Although there is much literature reported on the PECVD deposition and structural characterization of thin CoO_x films, [18, 19] there is not one report about the PECVD deposition of $CoO_x/CoO_x(OH)_y$ films as catalysts for the OER, to the authors knowledge.
Therefore, the influence of preparation parameters like operation mode (plasma vs. thermal), substrate temperature, precursor temperature, deposition time and the type of reactive gas (oxygen vs. air) on the electronic structure and the resulting electrochemical activity of mono- and bimetallic catalysts is studied intensively. X-ray photoelectron spectroscopy is used as a main method to investigate the oxidation state, the composition and structure. Since the layer thickness of the x-ray amorphous catalyst films is at maximum 20 nm, Raman spectroscopy studies did not give any valuable information.
In order to optimize the catalyst's structure and composition systematically, a fundamental mechanistic understanding is needed. Although the OER was investigated intensively in the past, the complex mechanism, which involves four sequential electron transfer steps, is still unclear. It is known from literature, that the activity strongly correlates with the ability of the surface to stabilize OER intermediates like hydroxide-, hydroxo-, oxyhydroxide and oxo-species (OH*, OOH*, O(OH)* and O*). [5, 20–22] The formation of these species mostly involves a change of the oxidation state of the transition metal site, which can be detected in XPS. In fact, not only the oxidation state of the transition metal oxides can change during OER but also the surface

structure. [11] Therefore, much effort has especially been directed into studying the change of oxidation state as well as the electrochemical induced structural transformation of the surface by measuring XPS from the catalysts initial state and after the electrochemical test. With this, an attempt is made to systematically study the effect of the electronic structure on the electrochemical activity and to gain deeper insight into the OER mechanism.

Part I

Theoretical background

The first part of this thesis introduces the underlying theoretical fundamentals.
Chapter 2 presents a general description of the electrolysis of water as well as of the electrochemical concepts which are used. Starting from the thermodynamic considerations, the appearance of different types of overpotentials like charge transfer, mass transport and reaction overpotential are discussed.
Chapter 3 gives an overview of the state of research with regard to the preparation of transition metal oxides as catalysts for the OER, the development of a mechanistic understanding of the OER and the electrochemical reaction behavior of transition metal oxides. Especially the redox properties of transition metals play a central role for discussing the catalytic activity of the catalysts.

2. Electrolysis of water

With the increasing interest in renewable energies, the electrolysis of water attracted attention due to its application as possible energy storage system. The electrolysis of water is the electrochemical reaction of splitting water into hydrogen and oxygen by applying a direct current. In general, electrochemistry deals with chemical reactions occurring at the interface of an electronic conductor and an ionic conductor (electrolyte). An electrochemical reaction always involves an electron transfer, whereby one component looses electrons in an oxidation reaction and the other compound gains electrons by the reduction reaction. With this, every electron transfer involves simultaneously oxidation and reduction, whereby the oxidation state of the reactants change. The overall reaction type is called a redox reaction. Figure 2.1 shows a schematic illustration of a simplified electrolysis cell.

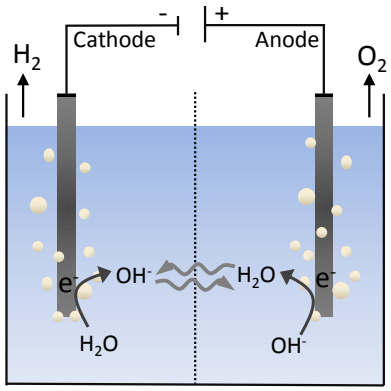

Figure 2.1. Schematic illustration of an alkaline water ectrolysis cell.

In addition to the thermodynamic potential of 1.23 V, excess energy is needed to drive the electrolysis of water in order to overcome the electrolyte resistance (Ohmic drop) and the kinetic limitations in form of overpotentials. The required cell potential difference E can then be written as Equation 2.1.

$$E = E^0_{Anode} - E^0_{Cathode} + \Sigma\eta + iR_{Cell} \tag{2.1}$$

The following sections deal with these basic electrochemical phenomena and discuss their consequences with regard to the interpretation of the results.

2.1 Standard half-cell potentials

Typically an electrochemical cell is assembled of two half-cells which are connected by an external circuit. Since the individual potential of one half cell is not directly measurable, but only the difference of two half cells, the standard hydrogen electrode (SHE) was adopted as the universally reference half cell. The potential of the SHE is defined arbitrary as zero operating under standard conditions (p= 1 bar, 25 °C and a_{ox}=a_{red}=1). Measuring the potential of an unknown half cell against the SHE at zero current gives its standard electrode potential (difference) E^0, which is

listed in the electrochemical series. As a convention, the half cell potentials are listed for the reduction reaction.

2.2 Cell potential and free energy

The maximum electrical work that a galvanic cell can perform is

$$-w_{max} = q * E_0 \tag{2.2}$$

The electromotive force E_0 is the reversible cell potential determined at equilibrium when zero current flows and q represents the electric charge. The change in free energy ΔG equals the maximum useful work nFE_0 of a process if the pressure and temperature are kept constant (Equation 2.3). The Faraday constant F is 96 485 C/mol and n is the number of transferred electrons in moles in the process.

$$\Delta G = -nFE_0 \tag{2.3}$$

Under operating conditions (non-equlibrium), the potential difference is denoted as terminal cell voltage. In contrast to E_0, which describes the thermodynamic voltage a cell can deliver under equilibrium conditions, the terminal voltage E always differs due to overpotential losses. In this context, $E<E_0$ means that the current flow is produced in a galvanic cell and $E>E_0$ means that an external electrical power is used to run the chemical reaction in an electrolyzes cell.

2.3 Calculation of the cell potential: Nernst equation

To calculate electrode potentials differing from the standard conditions, the Nernst equation is used (Equation 2.4).

$$E = E^o + \frac{RT}{nF} \ln\frac{a_{Ox}}{a_{Red}} \tag{2.4}$$

It describes the dependence of the electrode potential E on the temperature T and concentration, which is given as activity a or in case of gases, as pressure, given at unit fugacity f. The activities of the reducing agent a_{Red} and of the oxidizing agent a_{Ox} are defined by $a_x=\gamma_x c_x$, where γ_x is the activity coefficient of species x. At a temperature of 25 °C, the Nernst equation is simplified by subsuming the universal gas constant R, the Faraday constant F and by replacing the natural logarithm by the base-10 logarithm (Equation 2.5).

$$E = E^o + \frac{0.059}{z_e} \log\frac{a_{Ox}}{a_{Red}} \tag{2.5}$$

Considering the electrolysis of water in neutral or acidic solution at a temperature of 25 °C, the Nernst equation can be set up for the hydrogen evolution reaction ($4H^+ + 4\ e^- \rightarrow 2H_2$) as given in Equation 2.6. Since the partial pressure of the produced hydrogen equals the ambient pressure of about 1 bar and the standard half cell potential $E^0_{H^+/H_2}$ is 0 V, the half cell potential E_{H^+/H_2} depend on the pH by 0 V-0.059*pH.

$$E_{H^+/H_2} = E^o_{H^+/H_2} + \frac{0.059}{2} \log\frac{[a_{H_2}]^2}{[p_{H^+}]} \tag{2.6}$$

The same considerations apply to the oxygen evolution reaction ($O_2 + 4e^- + 4H^+ \rightarrow 2H_2O$), the half cell potential E_{H_2O/O_2} depends on the pH by 1.23 V- 0.059*pH. In general, the electrolysis of water is mostly performed either in an acidic or in an alkaline electrolyte solution since pure water itself has a high electrical resistance (>18 MΩcm). Table 2.1 compares the oxidation and reduction reactions of the water electrolysis in acidic and alkaline electrolyte solutions.

Table 2.1. Oxidation and reduction reactions of the water electrolysis in acidic and alkaline electrolyte solution.

	Neutral/acidic solution	Alkaline solution
Cathode	$4H^+ + 4\ e^- \rightarrow 2H_2$	$4H_2O + 4\ e^- \rightarrow 2H_2 + 4OH^-$
Anode	$2H_2O \rightarrow O_2 + 4e^- + 4H^+$	$4OH^- \rightarrow O_2 + 4e^- + 2H_2O$

Also the deviation of the temperature and pressure of standard conditions affect the half cell potential. Based on the relation E_0 = -ΔG/nF (Equation 2.2), the temperature dependence results to Equation 2.7. The dependence of the potential on the pressure is given in Equation 2.8. [3]

$$\Delta E(T) = E_0 - \frac{\Delta S_{p,T}}{nF}(T - T_0) \tag{2.7}$$

$$\Delta E(p) = E_0 + \frac{RT}{zF} \ln K_p \tag{2.8}$$

While an increase in temperature has a positive effect and the potential slightly decreases, the increase of pressure affects the potential negatively.

2.4 Deviations of the thermodynamic potential: Overpotential

The thermodynamic potential of the water electrolysis is 1.23 V at standard conditions. In addition to the thermodynamic expected potential, excess energy is required in form of overpotentials to drive the reaction. For each electrode, the overpotential η is defined as the difference between the experimentally determined electrode potential ϕ_{exp} for a given current density and its equilibrium potential ϕ_0 (Equation 2.9).

$$\eta = \phi_{exp} - \phi_0 \tag{2.9}$$

The total overpotential arises as the sum of different overpotential contributions like: (i) charge transfer η_{CT} , (ii) mass transport η_{MT} and (iii) reaction overpotential η_R. Considering the nature of an electrode reaction, the charge transfer overpotential η_{CT} is defined by the finite rate of the charge transfer across the electrode/electrolyte phase boundary. More specifically, n_{CT} arises from the kinetic inhibition of the charge transfer between the ion and the electrode. In this thesis we will use the standard description of charge transfer processes of electrochemistry assuming an activated electron transfer across the double layer potential drop at the solid/electrolyte interface. A description of the double layer was first given in the 1850s by Helmholtz. The Helmholtz model describes the double layer as a plate capacitor. Figure 2.2 (left) presents a schematic illustration of the double layer considering the Helmholtz model in case of water electrolysis. By applying a voltage, the anode charges positively. This results in an dipole orientation of water

molecules towards the positively charged surface (inner Helmholtz layer) and in an attraction of the negatively charged hydroxide anions (outer Helmholtz layer). The hydroxide anions have to overcome the potential barrier of the Helmholtz double layer to adsorb on the electrode surface so that the charge transfer can take place. Figure 2.2 (right) shows a simplified electrical potential profile which is formed across the double layer. Especially at low currents the electrode potential is largely determined by the charge transfer.

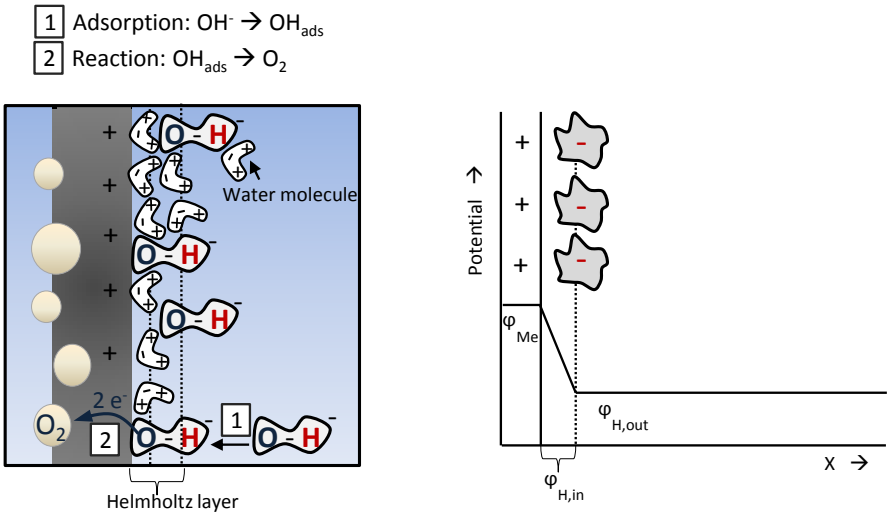

Figure 2.2. Schematic illustration of the Helmholtz layer (left) and the associated potential profile (right).

In the case of high currents, the diffusion overpotential can determine the electrode potential due to a high turnover in connection with a slow mass transport of the ions from the electrolyte to the electrode surface or the removal of the solid, e.g. oxygen release in case of the water electrolysis, from the electrode.
The overall electrode reaction is generally composed of various subsequently occurring reaction steps, whereby at least one of these is a charge transfer reaction. In contrast to the rate of the charge transfer reaction, which is influenced by the potential difference across the double layer, the rate of a chemical reaction depends on the concentrations but it does not directly depend on the electrode potentials. [23] The reaction overpotential is specifically related to a chemical reaction, which can occur before or after the charge transfer reaction.

2.5 Kinetic description of a charge transfer reaction

2.5.1 Butler-Volmer equation: Charge-transfer control

Using a metal electrode and an electrolyte with a high ioni concentration, the change of the electrical potential is limited to the Helmholtz layer. Starting from equilibrium conditions ($\Delta G = 0$), the kinetic of a simple charge transfer redox reaction $Ox + e^- \rightleftharpoons Red$ can be described by the Butler-Volmer equation. [24]

$$J = J_o \left[\exp\left(\frac{\alpha F}{RT}\eta\right) - \exp\left(-\frac{(1-\alpha)F}{RT}\eta\right)\right] \tag{2.10}$$

The equation is based on the theory of the activated complex which predicts the charge transfer by the formation of a transition state with an activation energy $\Delta G^{\#}$. The current density J represents a superimposition of the oxidation current density J^+ and the reduction current density J^- and gives the dependence of the total current density on the overpotential (Equation 2.10). Figure 2.3 illustrates the function of the total current density J as well as the cathodic and anodic current densities J^- and J^+. The current density increases exponentially with a rising overpotential and the slope depends on the exchange current density J_0 as well as on the charge transfer factor α.

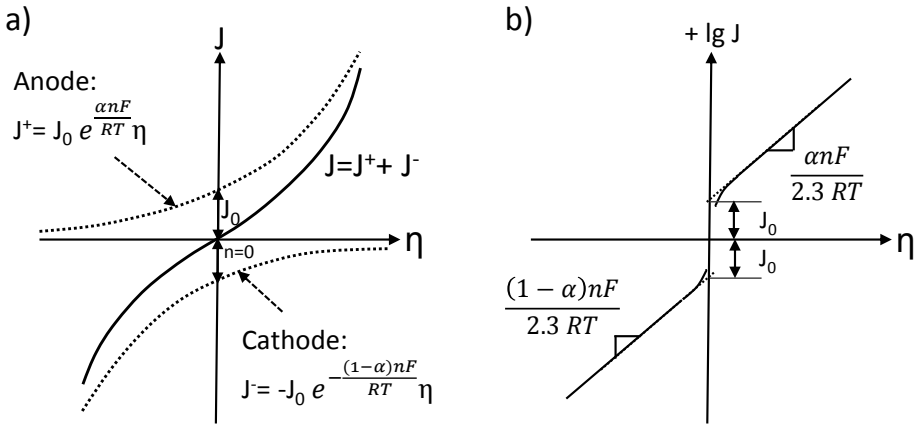

Figure 2.3. a) Illustration of the Butler Volmer dependence of the current density *J* on the overpotential η and b) the Tafel-plot.

Based on the theory of an activated complex, the charge transfer factor describes the influence of the potential difference at the electrode/electrolyte interface on the activation energy of the charge transfer reaction. In case of $\alpha = 0.5$, the curves of the anodic and cathodic current densities are symmetric to each other, $\alpha > 0.5$ means that the slope of the anodic current density is steeper than the slope of the cathodic curve and $\alpha < 0.5$ describes the opposite case. [24] The charge transfer factor can be experimentally determined, typical values for α are around 0.5. [25] In contrast to α, the exchange current density J_0 influences both, the anodic and cathodic curve, equally. It depends on the concentrations of the educts and on the activation energy of the charge transfer without applied potential. Since the activation energy of the reaction is decreased by a catalyst, J_0 is also determined by the electro-catalytic activity of the electrode. J_0 is determined by plotting the logarithmic current density (anodic or cathodic) versus the overpotential.
If $\eta >> \frac{RT}{nF}$ is valid, the respective opposite reaction can be neglected and for the anodic and cathodic current density, the so called Tafel equations result as given in Equation 2.11 and 2.12. The exchange current density J_0 is defined as the y-intercept of the Tafel-plots and α can be determined from the slopes.

$$\lg J^+ = \lg J_0 + \frac{\alpha n F}{2,3RT}\eta \tag{2.11}$$

$$\lg|J^-| = \lg J_0 + \frac{(1-\alpha)nF}{2,3RT}|\eta| \tag{2.12}$$

The Butler-Volmer relation, discussed in Equation 2.10, is valid if the concentration of the active

species c^s in front of the electrode equal to the concentration in the inner solution c_0. This is the case when the mass transport is fast relative to the charge transfer.

2.5.2 Mass-transport control

As described in Chapter 2.4, beside the charge transfer overpotential η_{CT}, the mass transport overpotential η_{MT} has to be considered for a diffusion controlled reaction, in which the ionic transport becomes the rate determining step. The mass transfer of the ions takes place as migration, diffusion and convection. While migration means the movement of the ion is caused by the electric field, diffusion is induced by a concentration gradient and convection by the fluids bulk motion resulting from a density gradient or mechanical stirring.
If a certain potential is applied (potentiostatic mode), the concentration will decrease from the value of c_0 to c^s. The concentration profile in the depletion zone near the electrode extends over the layer of thickness δ_N (Nernst's diffusion layer). The depletion zone expands with increasing current density in the inner solution and can be decreased by convection. [24] Considering a non-stirred diffusion controlled reaction, the current density can be derived from Fick's law of diffusion (Equation 2.13).

$$J = nFD\frac{c_0 - c^s}{\delta_N} \tag{2.13}$$

In case of a time-constant diffusion layer, the current density approaches the so called diffusion-limited current density with decreasing surface concentration of c^s ($c^s \to 0$). The diffusion limited current density J_{lim} increases linearly with the electrolytes concentration and with decreasing δ_N. In the region of limiting current, the overall overpotential is mainly described by the diffusion overpotential η_{diff} (Equation 2.14).

$$n_{Diff} = \frac{RT}{zF}\ln\frac{c^s}{c_0} \tag{2.14}$$

2.5.3 Pre-/downstream-equilibrium reaction control

The overpotential arising from a pre-/downstream-equilibrium reaction or an involved adsorption/desorption step is summarized as reaction overpotential, which is therefore related to the kinetic hindrance of an elementary reaction step and its activation barriers. The mechanism of the hydrogen evolution reaction for example involves the transfer of two electrons and can take place either as a combination of the Volmer-step (Equation 2.15) with the Tafel-step (Equation 2.16) or with the Heyrovsky-step (Equation 2.17). The Volmer-step describes the adsorption of the proton whereby one electron is transferred. Both, the Tafel-step and the Heyrovsky-step describe the formation of hydrogen but whereas the Tafel-step does not involve a charge transfer step and energetically no profit is observed for higher overpotentials, the Heyrovsky-step does involve the transfer of an electron. Therefore, the Volmer-Heyrovsky mechanism dominates at high overpotentials.

$$Volmer - step : H^+ + e^- \rightleftharpoons H_{ads} \tag{2.15}$$

$$\mathrm{Tafel-step}: \mathrm{H_{ads}} + \mathrm{H_{ads}} \rightleftharpoons \mathrm{H_2} \tag{2.16}$$

$$\mathrm{Heyrovsky-step}: \mathrm{H_{ads}} + \mathrm{H^+} + e^- \rightleftharpoons \mathrm{H_2} \tag{2.17}$$

It can be summarized, that only the overall rate determining charge transfer step of the reaction can be described by the Butler-Volmer model. The oxygen evolution reaction is more complex involving the transfer of four electrons and the formation of several intermediates as e.g. $OH^- \rightarrow OH^* \rightarrow O_2^{2-} \rightarrow O_2^- \rightarrow O_2$. Despite the intense research on the OER, the mechanism of the oxygen evolution reaction on metal oxide surfaces is still not clear and the sequence of elementary steps are only hypothesized in literature over the recent years. The development of the mechanistic understanding of the OER on transition metal oxide electrodes will be discussed in detail in the following Chapter.

3. State of research: Transition metal oxides as catalyst for the OER

3.1 General overview

Due to the high price of RuO_2 and the limited stability in alkaline media, non noble metal oxides of Co, Ni or Mn gained great interest. [26–28] Beside transition metal oxides with rutile-type, perovskite-type and spinel type structures, amorphous oxides and hydroxides are investigated to find new active OER catalysts. Various preparation methods, including the anodic and cathodic deposition from metal salts, passivation of metal electrode, reactive sputtering and chemical vapor deposition are reported in literature. [29–32] Most of the transition metal oxide catalyst‘s are able to operate in strong alkaline media showing a higher stability than the noble metal oxides. [26] In the development of active catalyst materials, various approaches have been pursued to modify the properties. Nanosizing of the material itself and the incorporation of a second metal turned out as promising strategies to tune the electro-catalytic and electronic properties.
Table 3.1 presents a literature overview of Co- and Ni-based oxide catalysts, which were tested in potassium hydroxide as well as of noble metal oxides in comparison. Overpotentials of pure cobalt oxides are reported in the range of 290 - 500 mV at 10 mA/cm^2. The highest electrochemical activity was found for nanoparticulate systems. Esswein et al. for example deposited Co_3O_4 nanoparticles of different sizes in a hydrothermal process on Ni-foam and found an enhancement of the electrochemical activity with decreasing size of the nanoparticles. [33] The smallest Co_3O_4 NPs had a size of 5.9 nm and required an overpotential of 328 mV to reach a current density of 10 mA/cm^2. Chou et al. observed an even higher activity for 10 nm sized particles, only an overpotential of 291 mV was needed for a current density of 10 mA/cm^2. [34]
Another strategy to enhance the catalysts activity represents the incorporation of a second metal. There are reports indicating that mixed oxides have higher activities than the single-component oxides. [5,35,36] An increase in the catalytic activity by incorporating a second metal was reported by Crory et al. for example. [36] They synthesized CoO_x, NiO_x $CoNiO_x$, $NiFeO_x$ and $CoFeO_x$ by electrodeposition and tested their OER activity in a benchmark process. [36] The overpotential at 10 mA/cm^2 decreases in the order of NiO_x (0.42 V) > CoO_x (0.39 V) > $CoNiO_x$ (0.38 V) > $CoFeO_x$ (0.37 V) > $NiFeO_x$ (0.35 V). [36] In agreement with these findings, Trotochaud et al. reported a decrease of the overpotential of ultra-thin spun cast spinel CoO_x from 0.38 V to 0.34 V for $Co_{0.75}Ni_{0.25}O_x$ and to 0.32 V for $Co_{0.5}Ni_{0.5}O_x$ at 1 mA/cm^2. Nevertheless, it has to be mentioned that the catalytic enhancement is only valid when judged relatively to the pure CoO_x since NiO_x itself was found to be more active than the bimetallic $CoNiO_x$. It required only an overpotential of 0.30 V at 1 mA/cm^2. [5] The incorporation of Fe traces from the electrolyte solutions in rock-salt NiO_x, however led to an increase in activity. It was found, that $Ni_{0.9}Fe_{0.1}O_x$ provided the lowest overpotential (336 mV at 10 mV/cm^2) and a 10-fold higher activity than IrO_2. Previous studies by Corrigan et al. have shown already the positive effect of Fe impurities in KOH electrolyte solution on the OER activity of electrodeposited $Ni(OH)_2$ electrodes. [28]
Also the incorporation of Cu is reported to have a positive effect on the activity of NiO_x and CoO_x. Grewe et al. for example studied the OER activity of various mesoporous composite

materials in 0.1 M KOH and they identified Co_3O_4-$CuCo_2O_4$ as the most active catalyst with an overpotential of 0.498 V at 10 mA/cm^2. They observed a decrease in overpotential in the order of Co_3O_4-$CuCo_2O_4$ > -$NiCo_2O_4$ > -$CoFe_2O_4$ ≈ -$CoMn_2O_4$ at a current density of 10 mA/cm^2. Serov et al. observed an even lower overpotential of 0.42 V at 10 mA/cm^2 for $CuCo_2O_4$. [37] The performance of different catalysts is typically compared based on the geometric electrode area although this is not straight forward since the current density is strongly influenced by the surface topography and the active surface area of the catalyst. Table 3.1 presents a literature overview of Co- and Ni-based oxide catalysts, which were tested in potassium hydroxide as well as of noble metal oxides in comparison.

Table 3.1. Preparataion conditions, electrochemical test conditions and the overpotential at 10 mA/cm^2 of various OER catalysts. NC=Nanocrystals, NP= Nanoparticles, GC= Glassy carbon, CP= Carbon paper, overpotentials marked with a star were read out from the figures in literature.

Material	**Synthesis route**	**electrode/electrolyte**	**η (10 mA/cm^2)**	**ref.**
RuO_2	hydrothermal	GC/1 M KOH	420	[38]
IrO_2	electrodeposition	GC/1 M NaOH	320	[36]
IrO_2	electrodeposition	Au/Ti 1 M KOH	530	[5]
Co_3O_4 NP-5.9 nm	hydrothermal	Ni/ 1 M KOH	328	[33]
Co_3O_4 NP-21.1 nm	hydrothermal	Ni/ 1 M KOH	363	[33]
Co_3O_4 NP-46.9 nm	hydrothermal	Ni/ 1 M KOH	382	[33]
CoO-NP-10nm	organic synthesis	Ni/1 M KOH	291	[34]
Co_3O_4	hydrothermal	GC/1 M KOH	510	[38]
Co_3O_4 NC	hydrothermal	GC/ 1 M KOH	330	[39]
Co_3O_4	nanocasting	GC/ 1 M KOH	427	[40]
CoO_x	electrodeposition	GC/1 M NaOH	390	[36]
CoO_x	electrodeposited	Au/Ti/ 1M KOH	485*	[5]
CoPi	electrodeposition	FTO/1 M NaOH	420	[36]
$NiCo_2O_4$	solvothermal	CP/1 M KOH	360	[41]
$Ni_{0.5}Co_{0.5}O_x$	electrodeposited	Au/Ti/ 1 M KOH	375*	[5]
$Co_xCu_yO_4$	nanocasting	GC/ 1 M KOH	391	[40]
Co_2CuO_4	pore forming	1 M KOH	420*	[37]
$NiFeO_x$	electrodeposition	GC/1 M NaOH	350	[36]
$Ni_{0.9}Fe_{0.1}O_x$	electrodeposition	Au/Ti 1 M KOH	336	[5]

It may be noticed, that in Table 3.1 no reference is given to a CVD or PECVD prepared CoO_x film as catalyst for the OER. Although thin film deposition techniques are widely used to prepare

battery materials and semiconductors, they are not commonly used to prepare catalyst materials for the OER.
There are many results published on the CVD and PECVD as a process to produce different CoO_x films, but the electrochemical OER activity of these materials has not been intensively studied yet. Combining PECVD as a preparation method for cobalt oxides/hydroxides and their application as catalysts combined with XPS investigation presents a new approach, that is promising for the incorporation of catalysts into porous structures.

3.2 Development of a mechanistic understanding of the OER

In terms of catalysis, the reaction overpotential is considered as a kinetic phenomenon, which is related to the kinetic driving force of elementary reaction steps needed to overcome existing activation barriers. [22] The overpotential and the catalytic rate of the overall reaction process are controlled by the slowest elementary step with the highest activation barrier, the rate determining step. Most early mechanistic work relayed on the investigation of Tafel slopes from current-potential-time analysis to obtain information on the rate determining step of the reaction process. [22]
The OER is a complex, four electron transfer process, which involves the formation of different intermediates. The mechanism is discussed over the recent years in literature by different hypotheses but even nowadays it is not fully understood. Since the mechanism strongly depends on the electrode material and its electrochemical redox behavior, a generalization is anyhow not possible. Since noble metal oxides like RuO_2 and IrO_2 are proven as highly active catalysts with overpotentials below 300 mV at a current density of 10 mA/cm^2, plenty of work have been conducted to understand the mechanism and to find out how the electronic structure determines the activity. [42] An early hypothesis for the mechanism of the OER on RuO_2 electrodes in acidic environments is given by Equation 3.1 to 3.4. [22, 43, 44] The symbol * presents the active site of a catalyst.

$$* + H_2O \rightarrow \quad *OH + H^+ + e^- \tag{3.1}$$

$$*OH \rightarrow \; *O + H^+ + e^- \tag{3.2}$$

$$*OH + *OH \rightarrow \; *O + * + H_2O \tag{3.3}$$

$$*O + * - O \rightarrow \; O_2 + 2* \tag{3.4}$$

The equation sequence (3.1)-(3.2)-(3.4) and the equation sequence (3.1)-(3.3)-(3.4) describe two parallel reaction pathways. These reaction pathways were suggested for Ru(110) oxide single crystal electrodes as well as for compact RuO_2 electrodes. [22, 44] Castelli et al. reported for a RuO_2 single crystal with a face of (110) an experimental Tafel slope of 59 mV/dec at low overpotentials and of 120 mV/dec at high overpotentials in 0.5 M H_2SO_4. They identified the rearrangement of the intermediate surface complex *OH as the rate determining step (denoted as RA) at low overpotentials (0- 0.3 V) and supported the reaction sequence (3.1)-(3.2)-(RA)-(3.4). [45] Furthermore, they related the Tafel slope of 120 mV at high overpotentials (0.3- 0.4 V) to a change of the OER mechanism and suggested the hydroxide formation (Equation 3.1) as the rate determining step, whereby the reaction sequence became (3.1)-(3.2)-(3.4). [45] Since RuO_2

and its mixed oxide compounds are the primary ingredient in many commercial dimensionally stable anodes (DSA), polycrystalline RuO_2 coated Ti electrodes were studied intensively as a model system. [22, 46] A high effort was made to find a correlation between the preparation parameters (e.g the synthesis route itself, the annealing temperature), the resulting properties (like BET surface, morphology) and the resulting electrochemical activity (for example the Tafel slopes). As already mentioned, due to the high price of RuO_2 and the limited stability in alkaline media, non noble metal oxides and hydroxides of Co, Ni or Mn became of great interest. Mehandru et al. proposed as a first step in the reaction sequence of the OER in alkaline media the discharge of the hydroxide ions by binding to the electrodes surface (Equation 3.5). [47] The discharge of the hydroxide ion can be either described as the formation of a bound hydroxide radical or as its ligation to the surface. [22] The hydroxide discharge was thought to be followed either by a deprotonation (Equation 3.6) and a subsequent discharge step (Equation 3.7 to 3.8) or by the breaking of the M-OH bond related to the formation of a peroxide species, which finally decomposes into O_2 (Equation 3.9). [22, 47]

$$* + OH^- \rightarrow \ *OH + e^- \tag{3.5}$$

$$*OH + OH^- \rightarrow \ *O^- + H_2O \tag{3.6}$$

$$*O^- \rightarrow \ *O + e^- \tag{3.7}$$

$$2 \ *O \rightarrow \ O_2 + 2* \tag{3.8}$$

$$*OH + OH^- \rightarrow * + H_2O_2 + e^- \tag{3.9}$$

Experimentally determined Tafel slopes vary in dependence of several influences like the preparation conditions, the choice of substrate, the test conditions (pH, electrolyte) and should be compared with caution. But to get an idea about the order of magnitude Tafel slopes of some in literature reported Co-based catalysts are summarized in Table 3.2.

Table 3.2. Preparation conditions, electrochemical test condition and Tafel slopes of cobalt oxide catalysts for the OER.

Material	**Synthesis route**	**electrode/electrolyte**	**Tafel slope [mV/dec]**	**ref.**
CoO_x	Photochemical MOD	FTO/ 0.1 KOH	42	[48]
Co_3O_4 nanocrystals	hydrothermal	GC/0.1 M KOH	67	[39]
Co_3O_4 nanoparticles	noncovalent functionalization	ITO/0.1 phosphate buffer	104	[49]
CoO_x	electrodeposited	Au/Ti/ 1M KOH	42	[5]
$Ni_{0.25}Co_{0.75}O_x$	electrodeposited	Au/Ti/ 1 M KOH	36	[5]
CoO_x	thermal decomposition	Ni/ 30 % KOH	46	[50]

Based on the early concept introduced in 1955 by Ruetschi and Delahay, which hypothesizes that the OER activity can be correlated to a single microscopic parameter like the chemisorption energy of oxygen, the correlation between the activity and thermochemical quantities was further progressed by the groups of Parsons, Bockris and Trasatti. [8, 51–53]

Bockris and Otagawa for example provided an experimentally proof, that the OER activity is strongly influenced by the binding energy of the surface bonded intermediates. [52,54] This relation can be illustrated in so called vulcano plots, where the activity is plotted versus the binding energy. [55]
Since it is difficult to determine binding energies experimentally, DFT calculations represent a useful tool to calculate them. [8] Rossmeisl et al. developed a method to determine the thermochemistry of the OER as a function of the potential using DFT calculations. [20, 22] They studied the thermochemical aspect of the overpotential considering Au(111) and Pt(111) electrodes by combining the calculated Gibbs free adsorption energy of the adsorbed species as a function of the electrode potential with a pH- and potential- controlled thermodynamic model. [20] The elementary steps used in their calculations are given in Equation 3.10 to 3.13 for the OER in acidic solution.

$$* + 2\ H_2O \rightarrow\ *OH + H_2O + H^+ + e^- \tag{3.10}$$

$$*OH + H_2O + H^+ + e^- \rightarrow\ *O + H_2O + 2H^+ + 2e^- \tag{3.11}$$

$$*O + H_2O + 2H^+ + 2e^- \rightarrow\ *OOH + 3H^+ + 3e^- \tag{3.12}$$

$$*OOH + 3H^+ + 3e^- \rightarrow\ * + O_2 + 4H^+ + 4e^- \tag{3.13}$$

Although the results only discuss the case of an acidic environment, Rossmeisl et al. point out that the analysis could be easily extended to describe the OER in alkaline solution because the intermediates are proposed to be the same. Figure 3.1 gives a schematic illustration of the proposed OER mechanisms in alkaline and acidic media. [20] The discussion of the energy barriers for the different elementary steps is restricted by the barriers coming from the free energy differences of the intermediates. Additional barriers arising from the electron and proton transfer reaction as well as from solvent reconstruction are not considered. [20] Figure 3.2 presents a simplified illustration of the by Rossmeisl et al. calculated energetics of a thermodynamically ideal catalyst in comparison to a metal electrode as a real catalyst. [20, 21]

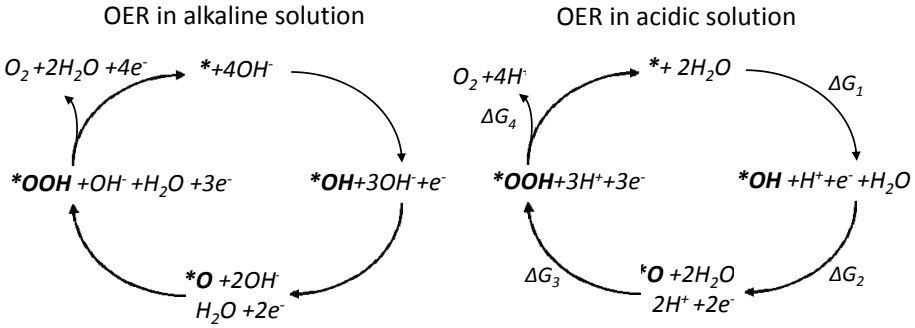

Figure 3.1. Comparison of the OER mechanisms in alkaline (left) and acidic solution (right) proposed by Rossmeisl et al. [20] The different intermediates are highlighted in bold.

The ideal catalysts (marked navy blue) exhibit equal Gibbs reaction energies for each elementary step, what implies equal chemisorption energies. If each elementary step requires 1.23 V, in the sum all thermochemical barriers disappear at a potential of 1.23 V. The real catalysts

shows a different behavior, the Gibbs free energy of the elementary steps decrease in the order $\Delta G_3 > \Delta G_1 = \Delta G_2 > \Delta G_4$. While at a potential of 2.55 V all reaction steps are downhill in case of Pt, the Gibbs free energy of the superoxy-type -OOH formation (ΔG_3) is still positive at a potential of 1.23 V representing the rate determining step. [20, 22] The calculated off set potential of a clean Pt surface is with 2.5 V much higher than the experimentally determined values for Pt electrodes.

A minimum coverage of oxygen has to be considered since the change of oxygen coverage during the OER affects the free energies of the intermediates. On a clean Pt surface for example, the oxygen coverage will start to build up above a potential of 0.78 V since the dissociation of water into $*$O and $*$OH is found to be downhill above this potential. [20]

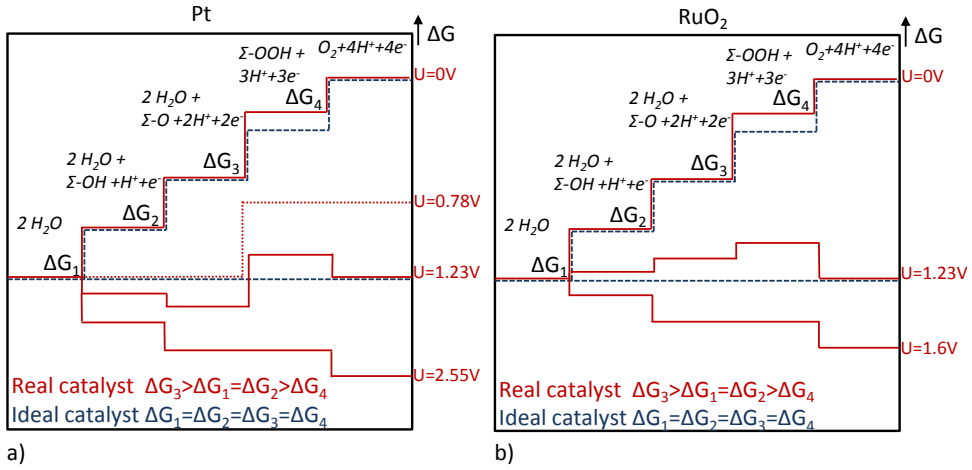

Figure 3.2. Plot of the Gibbs free energy versus the reaction coordinate on the basis of the description by Rossmeisl et al. for a) a Pt electrode and b) a rutile type RuO_2 electrode. [20]

Therefore, a further detailed investigation included the formation of a minimum oxygen coverage. The oxygen coverage of the Pt(111) surface had to be increased from 1/6 to 2/3 in order to facilitate the formation of $*$OOH. Only when the surface is sufficiently covered with oxygen, the dissociatively adsorption of a water molecule on an adsorbed oxygen atom to form an superoxy-type -OOH becomes more favorable than the adsorption on a free metal site. [20] As a conclusion they found, that a certain surface oxidation is necessary to split water. The calculated off set potential of 1.7 V for Pt agreed well with experimental data. By extending these studies to other metals, Rossmeisl et al. approved the simple linear relation between the stability of the different intermediates. Furthermore, their results indicated an universal relationship between the catalytic activity and the oxygen binding energy. [20] The overpotential can be reduced by tuning the chemisorption energies of the intermediates. But a minimum overpotential will always be present due to the calculated linear scaling relation, which implies that the individual chemisorption energies are linked to each other. [20, 22]

In 2007, Rossmeisl et al. investigated the trends in the electro-catalytic properties of three (110) rutile-like oxide surfaces (RuO_2, IrO_2 and TiO_2) using DFT calculation. [21] Since experimentally RuO_2 and IrO_2 represent better OER catalysts than pure metal surfaces, it is of high interest to apply the model in a similar way as described for Pt and Au [20] to the metal oxides. [21] And indeed, a linear relation between the binding energies of the different intermediates $*$O, $*$OH and

$*OOH$ was also found for rutile- type oxides. [21]
Figure 3.2 b) plots the calculated Gibbs free energies of all intermediates at different potentials for the ideal catalyst compared to RuO_2 as a real catalyst. For the RuO_2 electrode, all reaction steps are downhill at a potential of only 1.6 V. As it was discussed for the metal electrode, at the equlibrium potential of 1.23 V the -OOH formation is identified as the rate determining step. [21] Additional, Rossmeisl et al. presented volcano plots, which gives the theoretical activity as a function of the oxygen binding energy. The vulcano plot depicts that in case of a strong oxygen bond (small positive to negative ΔE_O) the -OOH formation becomes limiting. If oxygen bonds to weak to the surface (large ΔE_O) the oxygen formation becomes limiting. Concluding from this, RuO_2 (large ΔE_O) binds oxygen $*O$ to weakly and by contrast, IrO_2 binds oxygen too strongly. The calculations are in agreement with experimental data and show a higher activity for RuO_2 than for IrO_2 and TiO_2. [21] In 2011, Man et al. presented an extended data set based of calculated binding energies including rutile, perovskite, spinel, rock salt and bixbyite oxides using the previously developed method in acidic and alkaline solution. [20, 21, 55] Koper et al. observed a constant experimental scaling factor between $*OH$ and $*OOH$ of 3.2 eV for oxide surfaces whereby Man et al. found that the free energy difference between these intermediates is almost constant independent of the binding strength to the oxide surface indicating an universal scaling relation. [55] These findings are consistent with previous results of Rossmeisl et al. for metal electrodes. [20] Man et al. explained the constant binding energy difference $\Delta E_{*OOH} - \Delta E_{*OH}$ by the fact that both intermediates prefer the same kind of active site. [55] They predicted the optimal binding energy difference $\Delta E_{*OOH} - \Delta E_{*OH}$ to be 2.46 eV for an ideal catalyst and concluded that so far none of the considered oxides provided an optimum binding of both intermediates. Only few catalysts operate in the range of the minimum overpotential (0.4-0.2 V) arising from the difference between $\Delta E_{*OOH} - \Delta E_{*OH}$ of the real catalyst and the ideal catalyst.
As a consequence of these studies, the future challenge in catalyst design will be to find a catalyst with an improved relative stability between $*OOH$ and $*OH$ as well as an optimal positioned $*O$ binding energy. The most promising transition metal oxides resulting from the calculated vulcano plots are Co_3O_4 and NiO and perovskites like $SrCoO_3$, $LaNiO_3$. [55] A comparison of experimentally determined electrochemical activities of theses materials show discrepancies. For example, Co_3O_4 was predicted to be higher active than RuO_2, but most experimental studies observed a more activity for RuO_2. One reason for the discrepancy between the calculated and experimental activity values results from the difficulties to prepare the material in a perfect crystal structure. The theoretical values for NiO were calculated for a perfect single crystal but in reality NiO is mostly a complicated composition of NiO and NiO_x, where Ni is present in higher oxidation states. The experimentally determined activity values for Co_3O_4 depend strongly on the preparation conditions and therefore a comparison with theory is difficult. In general, a real catalyst mostly exhibits a range of different surface sites, where each site can have its own coordination and chemisorption properties. [22] The overpotential is then a convolution of individual overpotentials of different surface sites. Although these theoretical investigations base on several assumptions, they give an important insight into the reaction process and help to interpret and understand experimentally observed phase transformations and activity-structure correlations.

In future, methods like in-situ ambient pressure XPS, which makes the determination of the binding energy of the intermediates possible, will play a key role in the further development of a mechanistic understanding. Since these methods are not simply available, we tried to deduce information about the mechanisms by characterizing the as deposited sample and the sample after the electrochemical test, further notified as *after EC*, with different methods like XRD, Raman, EPS and XPS. The following Chapter focuses on the electrochemical behavior of transition metal oxides and discusses the correlation of the activity with experimentally observed phase transformations and their relation to mechanistic proposals.

3.3 Electrochemical redox reactions of Co, Ni and Fe

In 1978 Gottesfeld and Srinivasan commended; "the science of the OER is a science of the oxides and their properties". [56] This statement aims at the complex redox properties of metal oxide catalysts in an electrolyte. In general, the redox reaction depends on several factors coming from the nature of the oxide and from the manner of its preparation including composition, structure and available oxidation states. The oxidation state, the composition and structure in turn depends on the applied potential and the pH of the electrolyte under operating conditions. The thermodynamically stable equilibrium phases of a material in an aqueous solution are mapped in Pourbaix diagrams with respect to the applied potential and pH. The activity cannot be correlated only with the structure and properties of the initial as-deposited material since a potential induced phase transformation of the material has to be considered.
The Pourbaix diagram of cobalt was already introduced in 1966 by Pourbaix et al. in the *Atlas of Electrochemical Equilibria in Aqueous Solutions*. [57] Under alkaline operation conditions (pH 13-14) $Co(OH)_2$ was suggested as the stable phase in a potential range between -0.8 - 0 V vs. NHE and Co_3O_4/ $Co(OH)_2$ between 0 - 0.6 V vs. NHE. Above a potential of 0.6 V vs. NHE, CoO_2 was proposed as the predominantly stable phase. [58] Baldjich et al. calculated Pourbaix diagrams from the formation free energies and suggested CoO(OH) to be present as a stable phase above a potential of 1.23 vs. RHE in addition to CoO_2 under alkaline conditions (pH = 12- 13). [59] The calculations are in agreement with experimental findings. [59,60] Yeo et al. for example proved the partial transformation of CoO_x to CoO(OH) by Raman spectroscopy in 0.1 M KOH. [60] They suggested the electrochemical formed CoO(OH) as the catalytically active species with regard to the redox couple Co(III)/Co(IV).
Doyle et al. investigated the potential induced surface oxidation process by recording cyclic voltammograms for polycrystalline Co, Fe and Ni electrodes in 1 M KOH with scan rates between 150- 300 mV/s. [61] Figure 3.3 shows for example the cyclic voltammograms of a polycrystalline Co electrode recorded with a scan rate of 300 mV/s. [61] The cyclic voltammogram shows five oxidation peaks, which can be attributed to the potential depended formation of different passive layers like $Co(OH)_2$, CoO, Co_3O_4, CoO(OH) and CoO_2 as given in Equation 3.14 to 3.19. [61] While the origin of peak I, peak II, VI and peak V could be assigned to a specific reaction, the origin of peak III is not as well defined. It is discussed as an overlay of the formation of Co_3O_4, CoO(OH) and Co_2O_3 in literature. [61, 62] Foelske et al. investigated the potential dependent formation of different passive layers of a polycrystalline cobalt electrode using XPS. [63] In contrast

to the peak assignment of Doyle et al., they only detected $Co(OH)_2$ below the potential region corresponding to peak III in Figure 3.3 and no CoO. [61, 63]

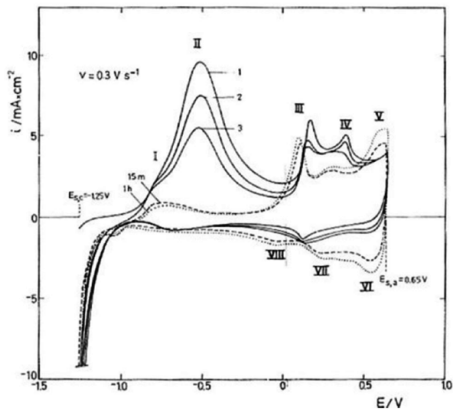

Figure 3.3. Cyclic voltammograms of a polycrystalline Co electrode recorded in 1 M KOH with a scan rate of 300 mV/s and Hg/HgO as a reference electrode (Figure taken from [61]).

At a more anodic potential corresponding to peak III, the XPS results indicate the presence of Co_3O_4 as the dominant species but also CoO(OH) was found. [63] A similar potential induced redox reaction is observed for other transition metal oxides like NiO_x and FeO_x. [61, 64, 65]

$$\text{Peak I} \quad : Co + OH^- \rightarrow Co - OH_{ads} + e^- \tag{3.14}$$

$$\text{Peak II} \quad : Co + 2OH^- \rightarrow Co - (OH)_2 + 2e^- \tag{3.15}$$

$$: Co + 2OH^- \rightarrow Co - O + 2H_2O + 2e^- \tag{3.16}$$

$$\text{Peak IV} : 3Co - O + H_2O \rightarrow Co_3O_4 + 2H^+ + 2e^- \tag{3.17}$$

$$: 3Co - (OH)_2 + 2OH^- \rightarrow Co_3O_4 + 4H_2O + 2e^- \tag{3.18}$$

$$\text{Peak V} : CoO(OH) + OH^- \rightarrow CoO_2 + H_2O + e^- \tag{3.19}$$

Especially the redox behavior of Ni electrodes was intensively studied since $Ni(OH)_2$ is an important cathode material in metal hydride batteries. [61, 65] The typical cyclic voltammogram of a polycrystalline Ni electrode recorded in 1 M NaOH has three oxidation peaks attributed to the formation of NiO, $Ni(OH)_2$ and NiO(OH). [9, 61, 66] Bode et al. found, that $Ni(OH)_2$ can exist as two phases: anhydrous β-$Ni(OH)_2$ and hydrous α-$Ni(OH)_2$. [67] While β-$Ni(OH)_2$ oxidizes to the corresponding β-NiO(OH), the oxidation of hydrous α-$Ni(OH)_2$ leads to the formation of γ-NiO(OH). [61, 67] A transition of α-$Ni(OH)_2$ to β-$Ni(OH)_2$ can result from a dehydration in alkaline solution. Furthermore, at elevated potentials β-NiO(OH) can transform to γ-NiO(OH). [61, 67] The findings of Bode et al. are a significant advancement in the understanding of the redox behavior of Ni and indicate the complexity of potential dependent redox reactions. Studying the redox behavior of a polycrystalline NiO_x film as catalyst for the OER, Trotochaud et al. made an attempt to study the effect of the potential induced phase transformation on the catalytic activity. [5] They identified the formation of a layered nickel hydroxide/(oxy)hydroxide film at resting OER potentials by recording cyclic voltammetry and by measuring XPS from the initial and the electrochemical conditioned films. Furthermore, they found that cobalt suppresses

the in-situ formation of the active nickel hydroxide/(oxy)hydroxide film, which results in a decreased electrochemical activity relative to the pure NiO_x. Based on their findings, they suggested the electrochemical formed $Ni(OH)_2$/NiO(OH) phase to be the catalytically active phase. [5]
With respect to the potential dependent formation of different passivation layers and the complex redox reactions of transition metal oxides, it is difficult to identify the actually catalytic active phase. The understanding of the hydroxide and (oxy)hydroxide catalysts appears to be the crucial key to gain a further fundamental understanding of the OER, since these are often discussed as the active phase. [11, 38, 68, 69] Therefore, over the past few years great efforts have been devoted to the preparation and characterization of transition metal hydroxides and (oxy)hydroxides as catalysts for the OER. [11, 38, 70–72]
Zhan et al. for example synthesized $Co(OH)_2$ in a hydrothermal procedure as a bifunctional catalyst for the HER and OER. [38] They observed a higher performance of $Co(OH)_2$ (η=0.43 V at 10 mA/cm^2) than both cobalt oxides CoO (η=0.45 V at 10 mA/cm^2) and Co_3O_4 (η=0.51 V at 10 mA/cm^2). [38]
Also $Ni(OH)_2$ is reported to be more active than NiO_x. [71,72] Stern et al. for example investigated the OER activity of nanoparticular α-$Ni(OH)_2$ in comparison to NiO_x in 1 M KOH. [71] While $Ni(OH)_2$ films required an overpotential of only 0.299 V to reach a current density of 10 mA/cm^2, NiO_x films needed an overpotential of 0.331 V to reach a current density of 10 mA/cm^2. [71]. They identified the partial oxidation of $Ni(OH)_2$ to NiO(OH) during OER employing GIXRD and Raman spectroscopy. Geo et al. reported an overpotential of 0.331 V at a current density of 10 mA/cm^2 for nanostructured α-$Ni(OH)_2$. [72] Lim et al. investigated the OER activity of several layered (oxy)hydroxides like $CoO_x(OH)_y$, $NiO_x(OH)_y$, $FeO_x(OH)_y$ and $MnO_x(OH)_y$, which were prepared by precipitation. [73]. $CoO_x(OH)_y$ and $NiO_x(OH)_y$ were the most active catalysts requiring overpotentials of about 0.44 V and 0.45 V at 10 mA/cm^2 and Tafel slopes of 55 mV/dec and 144 mV/dec. [73]
From the discussion above it becomes clear, that the redox reaction and the resulting OER activity of transition metal oxides, hydroxides and (oxy)hydroxides in electrolyte solution is very complex and an uniform description can not be given so far.

Part II

Experimentals

The second part of this thesis describes the experimental methodology. First, Chapter 4 explains the chemical vapor deposition process in detail. This includes a description of the basic principles, the CVD setup and the different operation modes (CVD vs. plasma enhanced CVD) as well as the experimental protocol. Following this, Chapter 5 covers the surface characterization using x-ray photoelectron spectroscopy (XPS) as a main method to determine the surface composition, the layer thickness and the oxidation state. Chapter 6 deals with the details of the electrochemical characterization (EC) using a photoelectrochemical cell to investigate the OER activity and stability of the catalysts. To get further insights into the structural composition and arrangement, some catalyst films were additionally analyzed with HREM and GIXRD. Figure 3.4 illustrates the sequence of the experimental protocol including the preparation and characterization.

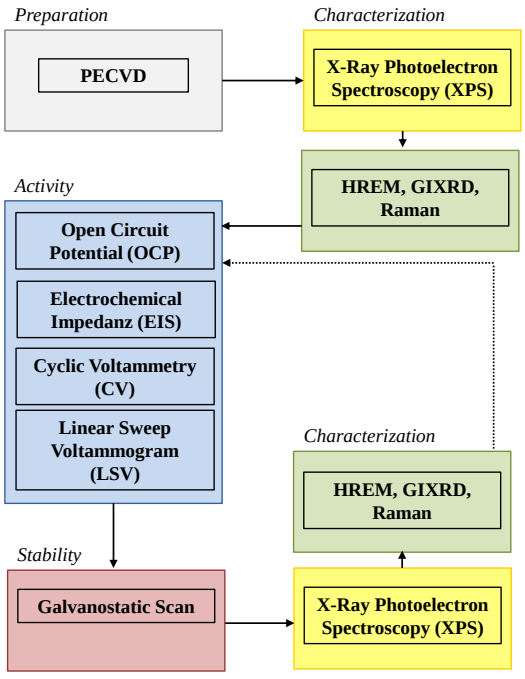

Figure 3.4. Overview of the experimental protocol.

4. Plasma enhanced chemical vapor deposition

In this work, a plasma enhanced chemical vapor process (PECVD) was developed to deposit pure transition metal oxides as well as binary transition metal oxides. On the one hand there are costly and inflexible ultra high vacuum preparation systems, which have a wide parameter window with respect to pressure and gas flows. Turbo pump systems enable the deposition in a pressure regime between $p > 10^{-3}$- $p < 10^{-10}$ mbar. In contrast there are the classical chemical syntheses, which are indeed cheaper and more flexible but usually are limited to pressures $p > 10^{-3}$ mbar due to the use of glass materials. The here constructed PECVD system combines the necessary elements of UHV techniques with the autonomy and flexibility of the classical chemical synthesis.
First, the basic principles of the CVD and PECVD process are explained in Chapter 4.1 to 4.3. Afterwards, the experimental setup as well as the deposition procedure is described in detail in Chapter 4.4.

4.1 Chemical vapor deposition

The chemical vapor deposition describes the process, in which a solid phase material is formed by the reaction and/or decomposition of volatile gaseous chemical components (precursors) on a substrate surface. In dependence on the type of reaction one can discriminate between different processes like thermal CVD, plasma-enhanced CVD or laser-enhanced CVD. If a metal-organic precursor like cobalt acetylacetonate ($Co(acac)_3$) is used, the process is further specified as metal-organic chemical vapor deposition (MOCVD). Other subtypes of CVD are for example the metal organic vapor epitaxy (MOVPE) or the hot filament CVD (HFCVD). In general, the CVD process can be performed at atmospheric pressure (APCVD) or at low pressure (LPCVD). The LPCVD process has the advantages of increased gas phase diffusion and lower gas flows whereby the uniformity and homogeneity of the deposited layer increases. Furthermore, the LPCVD offers the possibility to introduce a plasma excitation. One big disadvantage of the LPCVD are the lower deposition rates compared to APCVD. Independent on the individual CVD technique, a series of quasi steady-state processes are involved in the deposition process.
Figure 4.1 illustrates a general but simplified sequence of the reaction mechanism. [74] The main gas flow passes over the surface of the substrate. It is known from fluid mechanics that a stagnant boundary layer forms adjacent to the surface, where the gas stream velocity, concentration of the reactants and temperature are not equal to the parameters set for the main gas stream. The sequential process of CVD starts with the diffusion of the gaseous reactants to the surface across the boundary layer (1). Within the vapor/substrate phase boundary, the reactants can adsorb and diffuse (2) before either the surface reaction or a nucleation occur (3). Also a possible desorption of the reactive species have to be considered. Finally, the reaction products desorb and diffuse away from the surface (4). [74] The deposition rate is typically controlled by the mass transport in the vapor phase or by the surface kinetics.

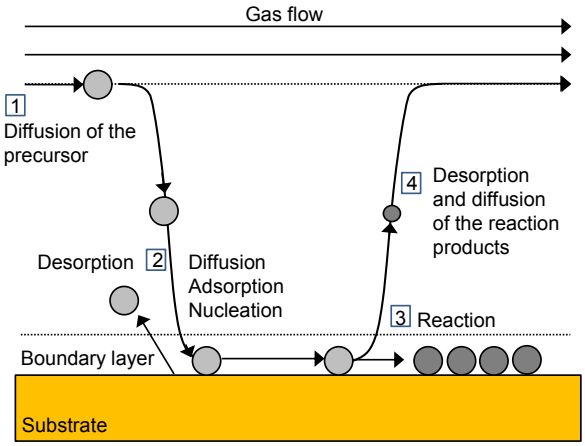

Figure 4.1. Schematic description of the different processes, which can occur during the chemical vapor deposition.

In case of mass transport control the diffusion of the reactants across the boundary layer is the rate-determining step and the surface reaction proceeds fast. This is typically observed at high temperatures and high pressures. Indeed, high deposition rates can be realized but the deposited films have a low conformity and tend to form particles. Furthermore mass transport controlled processes are sensitive to the reactor design, since this influences the main gas flow
In the surface kinetics control regime, the diffusion in the vapor phase is fast and the surface reaction is rate determining. The conditions for a surface kinetics control can be derived from the Arrhenius plots, which show the logarithm of the deposition rate versus the reciprocal temperature (Figure 4.2).

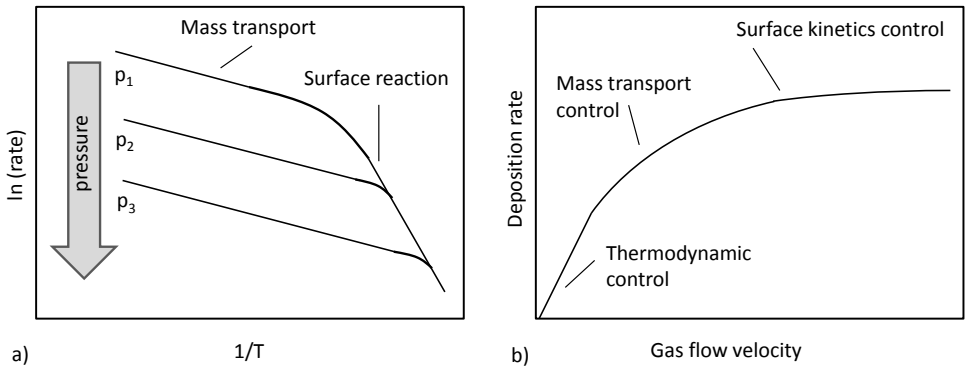

Figure 4.2. a) Schematic Arrhenius plot for an endothermic reaction at different process pressures ($p_1 < p_2 < p_3$). b) Plot of the deposition rate versus the gas flow velocity. [75]

Figure 4.2 shows, that a surface kinetics control is typically achieved a) by operating at low pressures and low temperatures or b) by increasing the gas flow velocity. A decrease of the total pressure results in a higher diffusion rate and the boundary layer can be overcome more easily. The surface reaction control offers the deposition of uniform and homogeneous films with an optimum step coverage. A disadvantage of the process is the strong temperature dependence.

4.2 Inductively coupled plasma

In contrast to thermal CVD, the PECVD process has the advantage that there is no temperature constraint. The coupling of a plasma opens up new reaction pathways, which have a lower activation energy. Hence, the reaction can proceed at a lower substrate temperature compared to the thermal CVD.
In general, a plasma is defined as a quasi-neutral gas of charged particles containing atoms/molecules as well as electrons and positive ions. [74] The plasma can be coupled by a direct current (DC) or by a radio frequency (RF). In case of a DC discharge, the current is driven through a low-pressure gas between two conductive electrodes. The RF discharge has the advantage, that the electrodes do not have to be conductive. In principle, in a RF discharge electrons are accelerated in an oscillating field with amplitudes in a frequency range between 0.1 - 40 MHz. The discharge can be driven capacitively and inductively.
The great advantage of an inductively coupled plasma is that the electric current is supplied by an electromagnetic induction from an externally installed copper coil, which is not contaminated during the deposition process. Figure 4.3 a) shows a schematic illustration of an inductive RF device with a planar coil used as an inductor. Inductive coils are commonly driven at 13.56 MHz combined with a 50 Ohm RF supply and a capacitive matching network. A power between 0.1 - 100 kW is typically required. Figure 4.3 b) shows the magnetic field lines in the presence of a plasma. Faraday's law of induction says that an alternating magnetic field induces an azimuthal electric field with a certain current density. The plasma current is the opposite of the coil current. [76]

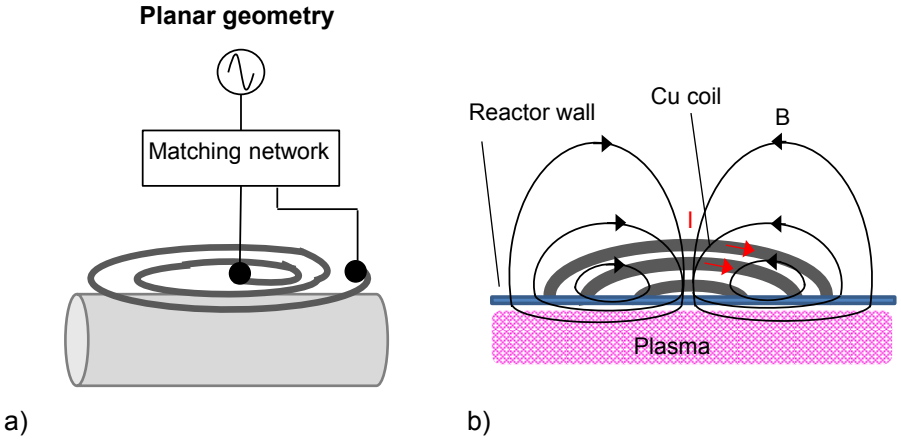

Figure 4.3. a) Schematic illustration of an inductive RF discharge device using a planar coil. b) Schematic RF magnetic field lines of the planar inductive coil.

Independent of the type of discharge, any plasma consists of electrons, ions and neutral atoms/molecules. The electron density regime of 10^{11} - 10^{12} cm^3 for inductively coupled plasmas is typically a factor of 10 times higher compared to capacitive coupled plasmas. In comparison, the concentration of ions and electrons in the atmosphere is negligibly small. The magnetic field decreases exponentially with distance to the reactor wall. The plasma electrons temperatures range between 6 - 100 eV.

4.3 Plasma chemistry

In general, energy can be transferred more rapidly to the plasma electrons than to the heavy ions. If the elastic collision processes of the plasma electrons become less probable, which is the case at low pressures, the electrons can gain sufficient kinetic energy to excite, ionize or dissociate heavier particles by inelastic collisions. Gas phase collision processes are commonly expressed by the cross section. [77] The complex interaction of charged and neutral particles determines the formation of various reactive species and therefore the type of surface modification.
In case of the oxygen for example, which is a simple diatomic gas, a discharge can lead to the formation of O, O_3, O^+, O_2^+, O_4^+, O_3^-, O_2^- and O^-. The concentration of the species depend on the energy and their cross sections. While the formation of O^- and O has a maximum cross section of $1*10^{-18}$ cm^2 at 6.5 eV (Equation 4.1), the ion pair O^+ and O^- has a maximum cross section of $3*10^{-18}$ cm^2 at 24.3 eV (Equation 4.2). [77]

$$O_2 + e^- \rightarrow O^- + O \tag{4.1}$$

$$O_2 + e^- \rightarrow O^- + O^+ + e^- \tag{4.2}$$

With respect to the amount of involved reactive species, the decomposition of the precursor within the plasma is complex and not clearly to define. Unfortunately, a mass spectrometer was not available to analyze the gaseous decomposition products. But independent of the exact reaction mechanism, the simplified reaction can be expressed as given in Equation 4.3 since the deposition product itself is known from the subsequent XPS characterization.

$$O_{2,Plasma} + Co(acac)_3 \rightarrow Co_3O_4 + CO_2 + H_2O \tag{4.3}$$

4.4 Experimental setup

The final experimental setup (Figure 4.4) represents the result of an optimization process, which will be explained in Chapter 8.1 within the results part.
The PECVD system is mainly composed of three parts: a vacuum unit, the reaction chamber and a gas inlet system. The vacuum unit consists of a pressure gauge (Lesker, 275i Series), a rotary pump (Pfeiffer Vacuum, ONF 25 M) and the vacuum sealed manipulator inlet, which are connected to a stainless steel KF 50 cross supplied by Vacom. The system can be evacuated to a pressure of 10 mtorr. It is known, that only UHV conditions guarantee the purity of the surface without contamination by residual gases but with respect to the later application of the catalyst films, carbon contaminations have to be considered anyway. It would not be feasible to install the deposited electrodes in an electrolyzer under inert gas atmosphere.
A glass tee piece purchased by Quarzglas represents the vertical oriented cold-wall reaction chamber with the load lock being positioned on the lateral KF 50 flange. Based on the positive experience gathered with the existing PECVD system for depositing $LiCoO_2$, the decision has been made to use an inductive plasma. Hence, the reaction chamber has to be equipped with a RF-generator (R301, Seren), a matching box (AT3, Seren) and a copper coil. The Cu coil is installed outside of the reaction chamber to avoid its deposition. This requires the reaction

chamber to be made of glass. The home-built substrate holder is attached to the end of the manipulator. The substrate is heated by a halogen lamp (24 V/150 W) regulated by an Eurotherm control (Eurotherm, 2416). The thermo-element is positioned at the substrate holder directly next to the substrate. The substrate itself is fixed using omicron clamps on the bottom of the holder.

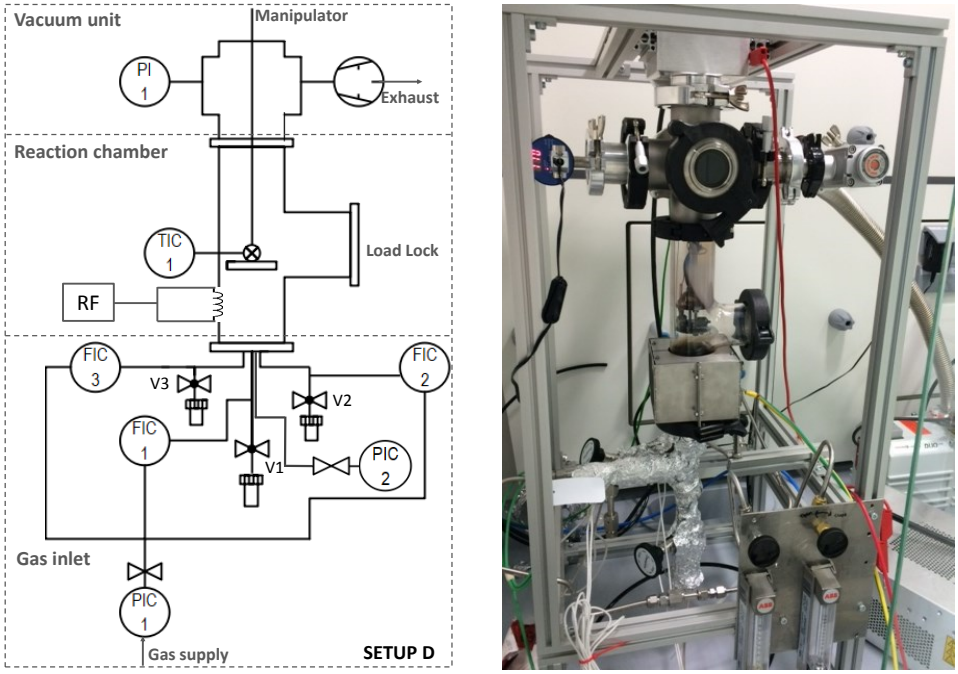

Figure 4.4. Optimized PECVD setup, denoted as setup D. The instrumentation symbols PI, TIC and FIC denote the pressure (P) indicator (I), temperature and flow indicator (I) and controller (C).

The precursor inlet system is mainly built of Swagelok fittings. The three precursor crucibles are isolated from the reaction chamber by 1/4" manual valves (Swagelok, SS4BGVCR). While the precursor line of Co was designed with an inner diameter of 1/2", the precursor lines of the second metals are designed with an inner diameter of 1/4". All precursor lines are heated by heating wires (Horst GmbH, 020103 HS 2.0, 250 W). The reactive gas is introduced in the reaction chamber by a separate supply line, which is installed in a minimum distance to the precursor line on the flange. At the beginning of the experiments, a shower-head gas inlet system was also investigated. In contrast to the standard gas inlet system (Figure 4.5 a) the shower-head (Figure 4.5 b) ensures a premixing of the gases by introducing a turbulent flow. Unfortunately, the acetylacetonate precursors condensed in the shower-head. Since the standard gas inlet system also provided a homogeneous PECVD film deposition with respect to the substrate dimension of only 1x1 cm, no further efforts have been devoted to the development of a heatable shower-head gas inlet. All gas supplies are equipped with a flow meter and a pressure regulator. Whereas simple float-type flow-meters (ABB) are used to set the gas flows of the reactive gas and the carrier gas of the Co line, MKS flow controls (MFCs, MKS Instruments) are used to define the carrier gas flows of the second metals. Since all gases are introduced at the bottom of the reaction chamber, the gas flows meet frontal the substrate.

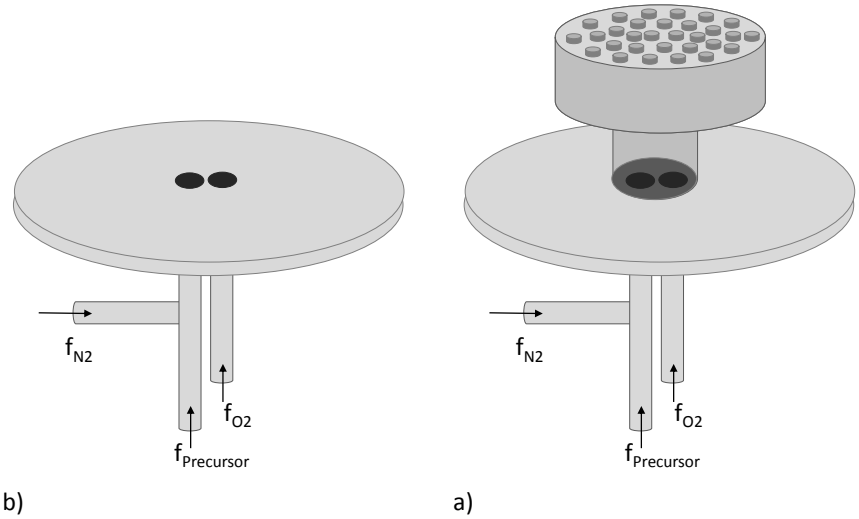

Figure 4.5. Schematic illustration of a) the precursor standard gas inlet and b) the shower-head gas inlet system.

First experiments were performed using argon as a carrier gas, later nitrogen was used. The resulting XPS spectra did not show any differences depending on the carrier gas. Since an installed nitrogen supply was provided in the lab, the use of nitrogen as a carrier gas was more practical. Before the deposition can be carried out, different preparation steps have to be made (Figure 4.6).

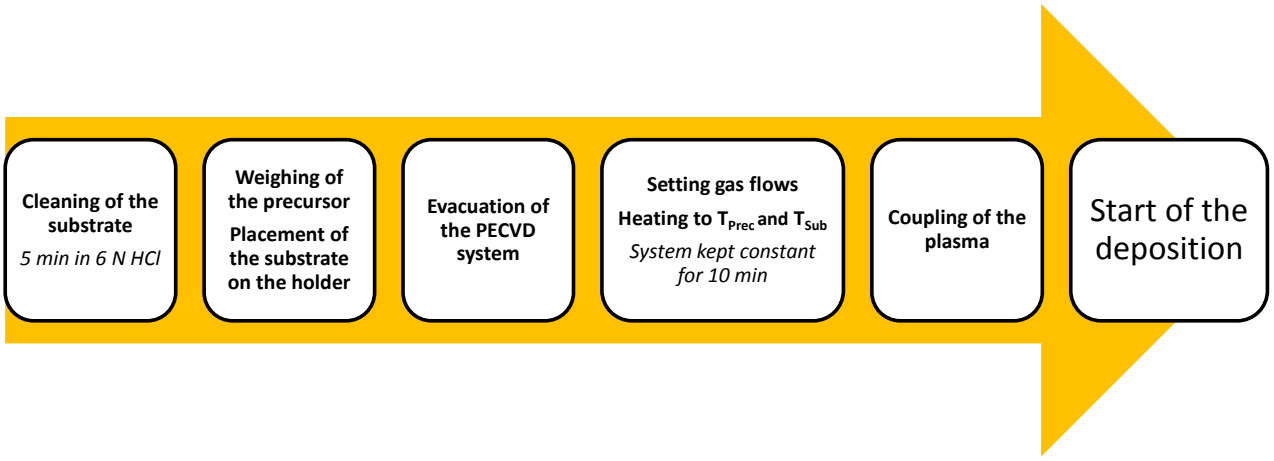

Figure 4.6. Schematic description of the different preparation steps carried out before the deposition.

These include the cleaning of the substrate, the weighing of the precursor and placement of the substrate as well as the evacuation of the PECVD system, the setting of the gas flows, the preheating of the crucibles and the substrate holder. Finally the inductive plasma was coupled. The deposition time started when the precursor valves were opened. After the deposition, the valves were closed again and the PECVD system had to cool down before the coated substrate could be transferred out.

4.5 List of Materials

$Co(acac)_3$	Sigma Aldrich GmbH, 494534 Cobalt (III) acetylacetonate 99.99 % trace metal basis
$Ni(acac)_2$	Sigma Aldrich GmbH, 283657 Nickel(II) acetylacetonate 95 % trace metal basis
$Fe(acac)_3$	Sigma Aldrich GmbH, 517003 Iron(III) acetylacetonate 99.99 % trace metal basis
$Cu(acac)_2$	Sigma Aldrich GmbH, C87851 Copper(II) acetylacetonate 97 % trace metal basis
Ti-foil	Alfa Aesar, 10385, 0.25 mm titanium foil 99.95 % trace metal basis
Ni-foam	Goodfellow (purchased and provided by Evonik)
6 N HCl	Roth, 0281.1 6 N hydrochloric acid

5. Photoelectron Spectroscopy (XPS)

The spectroscopy based on the emission of electrons was developed mainly by Siegbahn and introduced as Electron Spectroscopy for Chemical Analysis (ESCA). [78] Nowadays, Photoelectron Spectroscopy (PES) is established as a general term. In dependence on the used photon source one can discriminate between two experimental cases, X-ray Photoelectron Spectroscopy (XPS) and Ultraviolet Photoelectron Spectroscopy (UPS). In case of UPS the energy of the incoming photons is in the ultraviolet regime between 5 eV to 100 eV and therefore UPS is limited to the energy levels of the valence electrons. XPS operates with photons in the x-ray regime between 100 eV to >1000 eV, which makes the analysis of core level electrons possible. Valence electrons can also be detected with XPS but the fine structure can only be studied in detail with UPS. XPS is used as a main method in this thesis for two reasons. First, with respect to the layer thickness regime of 1 nm to 10 nm and the amorphous nature of PECVD deposited films, a surface sensitive method like XPS is needed. Characterization methods like XRD, EDX, Raman did not provide valuable information of the PECVD films prepared in this thesis. Second, a change in the electronic structure and the composition of the surface can be identified by measuring XPS before and after the electrochemical test.
Since one major challenge is still to understand and elucidate the reaction mechanism of water splitting on oxide surfaces, the combination of XPS as a surface sensitive characterization method with the electrochemical investigation of the catalyst presents a powerful approach to get a better mechanistic and fundamental understanding by correlating the change in electronic structure with the electrochemical performance.

5.1 Basic principles

The phenomenon of photoemission was detected first by Hertz in 1887 and could be explained as the photoelectric effect in 1905 by Einstein [79, 80]. The photoelectric effect states that electrons can be liberated from the solid by electromagnetic radiation with sufficient energy. Considering that electrons in a solid can only occupy discrete energy levels, the binding energy is a function of the atomic number Z as well as of the first quantum number n of the respective orbital. The binding energy E_{bin} can be calculated from the detected kinetic energy E_{kin} of the emitted electron and represents the energy of the initially occupied orbital. Therefore elements can be distinguished and analyzed [81].
The principle of the photoelectric effect is illustrated in Figure 5.1. It becomes clear, that photoionization can only occur if the excitation energy of the photon $h\nu$ is greater than the binding energy E_{bin} of the electron and the work function of the sample ϕ_{Sample}. Equation 5.1 gives a mathematical expression for the kinetic energy.

$$E_{kin} = h\nu - E_{bin} - \phi_{sample} \tag{5.1}$$

To ensure an accurate measurement of the kinetic energy of the photoelectrons by the spectrometer with respect to its own Fermi level, the sample has to be electrically connected to the spectrometer.

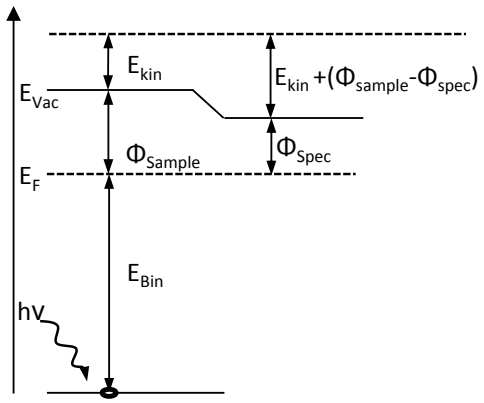

Figure 5.1. Schematic illustration of the photoelectric effect.

The electrical contact equalizes the Fermi level of the sample and the spectrometer and therefore the binding energy is independent from the work function of the analyzed sample. [82] Experimentally, the work function of the spectrometer has to be determined by measuring the Fermi level of a clean metallic surface to calibrate the resulting binding energies with this value. In conclusion, the binding energy can then be calculated as given in Equation -5.2.

$$E_{bin} = h\nu - E_{kin} - \phi_{spec} \tag{5.2}$$

Chemical shift

To distinguish between two different chemical compounds of an element, especially the binding energy difference of their core level lines is of interest. This energy difference is called chemical shift and is mostly influenced by the chemical environment of an atom. With regard to the Koopmans'theorem, which assumes that the orbitals of the ionized atom are identical to the orbitals in the neutral atom (*frozen orbital approximation*), one can attribute the chemical shift directly to a change in the initial state. This means in a first approximation that with increasing positive charge on an atom, the binding energy increases. Therefore, metal oxides have typically a higher binding energy than the pure element. The chemical shift cannot always be attributed to a change in the initial state only. The final state can also have an impact in the binding energy. In case of cobalt for example, the binding energy of the electron in Co^{2+} (780.5 eV) is higher than the binding energy of the electron in Co^{3+} (779.6 eV).

Final state effects

After the process of photoemission the system is lacking one electron with regard to the initial state, a final state is generated. According to the frozen electron approximation, which excludes relaxation energies, the binding energy is given as the difference between the initial state and the final state. But in reality, the final state energy will be decreased due to the relaxation of the outer electrons. The relaxation of the remaining electrons towards the hole lowers the total

energy of the ion and additional features in the spectrum can be observed (final state effects). Equation 5.3 presents a simplified modification, which includes a relaxation term.

$$E_{bin} = E_f - E_i - E_{relax} \tag{5.3}$$

The spin orbit splitting for example, which results from the coupling of the spin of the unpaired electron in the ion with the angular momentum l of the orbital gives two possible final states with $j = l \pm s$.
Since the s-orbital has an orbital angular momentum of $l = 0$, no spin-orbit splitting is observed. The orbital angular momentum of the p-orbital is $l = 1$, therefore the total angular momentum can attain a value of either $j = \frac{3}{2}$ or $j = \frac{1}{2}$ and the photoemission line is splitted into a doublet. The intensity ratio of the resulting photoemission lines $p_{3/2}$ and $p_{1/2}$ correspond to the ratio of the number of degenerated coupling $2j + 1$. Table 5.1 summarizes the parameters of spin-orbit-splitting.

Table 5.1. Parameters of spin-orbit splitting.

Orbital	l	**s**	$j = l \pm s$	**Intensity ratio**
s	0	$\frac{1}{2}$	$\frac{1}{2}$	-
p	1	$\frac{1}{2}$	$\frac{1}{2}$, $\frac{3}{2}$	1: 2
d	2	$\frac{1}{2}$	$\frac{3}{2}$, $\frac{5}{2}$	2: 3
f	3	$\frac{1}{2}$	$\frac{5}{2}$, $\frac{7}{2}$	3: 4

Shake-up and shake-off satellites are another spectral feature, which arise when a core level electron is emitted. The emitting photoelectron can interact with a valence electron by exciting it into an energetically higher unoccupied state. As a consequence the energy of the emitted photoelectron reduces and a shake-up satellite appears below the kinetic energy of the core level line. Also a valence electron can be ejected by the excitation of the photoelectron and a shake-off satellite emerges.

Auger lines

Auger electrons are emitted in the relaxation process of the excited ionized atom. For example the emittance of an electron of the K level creates a hole, which is filled up from an electron of the L_1 level. The transition energy is imparted to an electron of the $L_{2,3}$ level, which is emitted as an KLL Auger electron.

5.2 Determination of the layer thickness

A photoemission spectrum shows several photoemission lines, which are attributed to element specific orbitals X. The intensity of an emission line I depends on the photon flux density $J(h\nu)$, the atomic density in atoms N, the cross section $\sigma(h\nu, \theta, X)$ at the orbital X and the angle of photoemission θ, the mean free path $\lambda(E_k)$ of the electrons and the transmission factor $T(E_k, E_p)$

of the analyzer. E_k represents the kinetic energy of the emitted electrons and E_p is the energy of the electrons crossing the analyzer. [83, 84]

$$I(E_k, X) = J(h\nu) * N * \sigma(h\nu, \theta, X) * \lambda(E_k) * T(E_k, E_p) \tag{5.4}$$

The photon flux density is assumed to be constant over the analyzed range and can be calculated from the spectrometer arrangement excluding scattering effects. The transmission factor T(E_k,E_p) can be approximated by $T(E_k) \propto E_k^{-0.5}$ when the experiments are performed with a constant pass energy E_p. For a qualitative analysis, the mean free path of the photoelectrons was estimated as $\lambda \propto E_k^{0.7414}$. The exponent presents an empirically determined average value. [85]
For the quantitative determination of the layer thickness, the absolute values of the inelastic mean free paths (IMFP) have to be determined. In this work the mean free paths of different materials were calculated using the program NIST-IMFPWIN. Table 5.2 presents the calculated IMFPs λ of several photoemission lines of CoO, Co_3O_4, NiO, Fe_2O_3 as well as the parameters for quantification (the material density ρ, the number of valence electrons VE, the kinetic energy E_k).

Table 5.2. Material parameters and calculated IMPF values of several PES lines at a certain kinetik energy E_k in a defined material

Material	ρ [g/cm^2]	**VE**	**PES line**	E_{kin} [eV]	λ [Å]
CoO	6.45	15	Co 2p	705.1	14.0
Co_3O_4	6.07	51	Co 2p	706.0	14.41
TiO_2	4.23	20	Ti 2p	1028.0	18.0
SiO_2	2.65	20	Si 2p	1384.3	23.0
NiO	6.72	16	Ni 2p	632.0	13.02
Fe_2O_3	5.24	34	Fe 2p	775.0	15.9

A common approach is to assume an exponential attenuation of the substrate signal I_S caused by the overlayer O. [86] The layer thickness can then be calculated as given in Equation 5.5.

$$d = \lambda_O * \ln\left(1 + \frac{I_O/\sigma_O}{I_S/\sigma_S}\right) \tag{5.5}$$

Equations 5.6 give an mathematical expression for the photon intensities of the overlayer O and the substrate S. Since the photon flux density J as well as the layer thickness d are unknown, the equations have to be solved numerically.

$$I_O = J * \sigma_O * \left(1 - exp\left(\frac{-t_O}{\lambda_O(E_O)}\right)\right); \quad I_S = J * \sigma_S * exp\left(\frac{-t_O}{\lambda_O(E_S)}\right) \tag{5.6}$$

The angular dependent electron escape depth is described by λ as given in Equation 5.7.

$$\lambda_O = \cos\theta * \lambda \tag{5.7}$$

Indeed, this method provides the possibility to determine easily the layer thickness d of thin films in the range between 0.1 nm- 10 nm, but it must be noted that this method only fully applies to homogeneous layers with defined stoichiometry since the mean free path of a certain structure was used for the calculation. With regard to the amount of carbon contamination, which is between 15 - 25 % within the layers, the real mean free path will be slightly different to the calculated ones. Also, the presence of holes within the layer, which distort the determination of the layer thickness cannot be ruled out although the investigation of the morphology with SEM indicates a homogeneous film deposition. To conclude, this method does not provide absolute thickness values due to the undefined composition of the here investigated systems, but it can be used to make a rough estimation and to compare differently deposited catalysts relative to each other.

5.3 Determination of the oxidation states and their ratio in mixed valence CoO_x

To understand the catalytic interaction between the catalyst and the electrolyte, one has to find out in which oxidation state the catalyst operates with the highest performance, if there are changes in the oxidation state under operating conditions and in which way the electronic structure can be positively influenced by adding a second metal. The oxidation states of cobalt can be distinguished by a chemical shift in the main line and by its satellites. While the Co(II) oxidation state is identified by a satellite structure at a distance of 6 eV from the main line, the satellite structure of Co(III) is located at a binding energy distance of 10 - 11 eV. [87–89] Figure 5.2 compares the Co $2p_{3/2}$ lines of $LiCoO_2$, CoO and the curve line fitted $Co(II)(III)O_x$ spectrum.

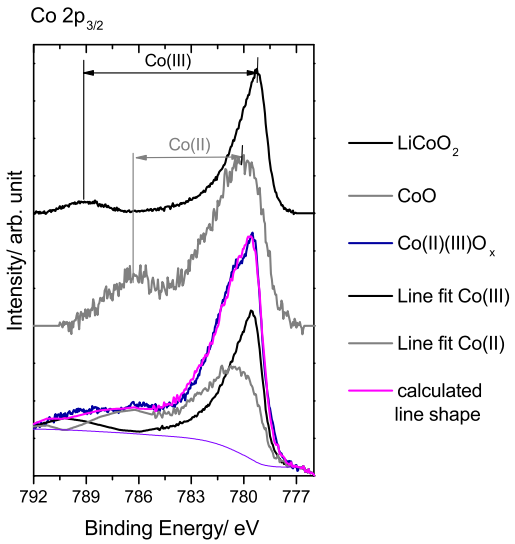

Figure 5.2. Co $2p_{3/2}$ core level spectra of $LiCoO_2$ (black), CoO (grey) and the curve line fitted Co 2p spectrum of a mixed valences $Co(II)(III)O_x$ (magenta).

The relative contributions of Co(II) and Co(III) in an undefined cobalt oxide can be determined in CasaXPS by the deconvolution of the complex spectrum using a defined reference spectrum for each oxidation state. Whereby the Co 2p core level spectrum of CoO defines the reference Co 2p line representing the Co(II) oxidation state, the Co 2p spectrum of $LiCoO_2$ represents the reference Co 2p line of the Co(III) oxidation state. The Co(II)/Co(III) ratio can be finally estimated from the area ratio of the fits.

5.4 Reference spectra of Co_3O_4 and $Co(OH)_2$

Although reference spectra of different cobalt oxides are reported many times in literature, the Co $2p_{3/2}$, O 1s and valence band spectra of Co_3O_4/Si, which was sputter deposited in our group by Thomas Späth, are shown here exemplary as a reference (Figure 5.3). The surface is free from carbon contaminations, since the sputter deposited sample was transferred to the XPS spectrometer under UHV conditions. In case of Co_3O_4, Co is present in both oxidation states, Co(II) and Co(III). Therefore, the Co $2p_{3/2}$ spectrum exhibits in agreement with literature reports the Co(III) satellite at a distance of 10 eV and the Co(II) satellite at a distance of 6 eV as well as the double peak feature of the main line. [87, 89, 90] The O 1s peak of lattice oxygen is typically positioned at around 529.5- 529.9 eV. The valence band spectrum shows the for Co(III) characteristic intense Co 3d feature at a binding energy of 1.28 eV.

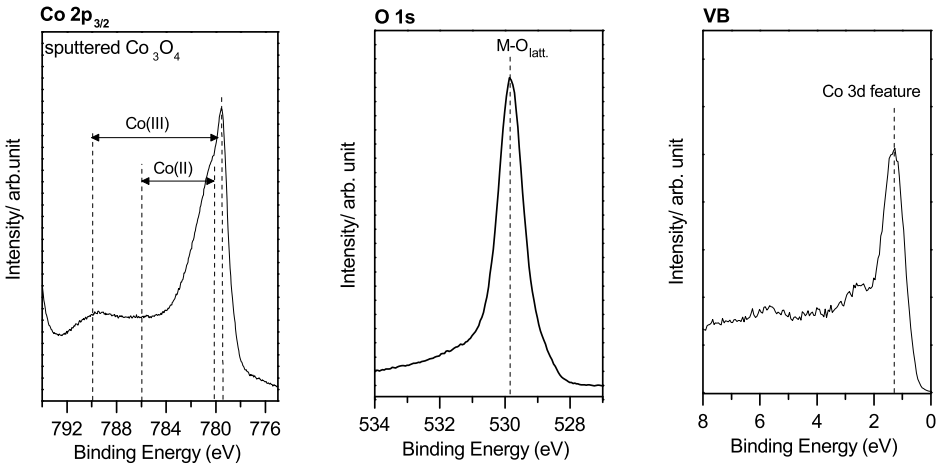

Figure 5.3. Co 2p, O 1s and valence band spectra of sputter deposited Co_3O_4 recorded by Thomas Späth.

For comparison, the reference spectra of $Co(OH)_2$, which only exhibits the Co(II) oxidation state, are shown in Figure 5.4. $Co(OH)_2$ was purchased as powder and characterized by Natalia Schulz. The Co $2p_{3/2}$ peak is located at a binding energy of 780.9 eV with a satellite at a distance of 5.5 eV. The O 1s peak is positioned at a binding energy of 531.3 eV and represents hydroxide moieties. The valence band does not show the Co 3d feature of Co(III) at a binding energy of 1.3 eV, but a valence band feature with maximum intensity at a binding energy of 2.6 eV.
Even the XPS spectra of CoO and $Co(OH)_2$ can be distinguished. The here shown XPS reference spectra of CoO are adapted from literature, since it is expensive and it has already been studied in detail. [90]

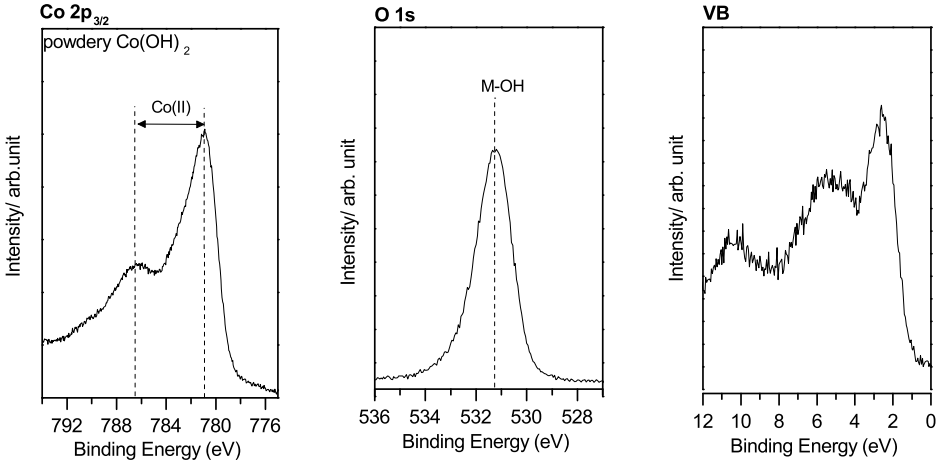

Figure 5.4. Co 2p, O 1s and valence band spectra of powdery $Co(OH)_2$ recorded by Natalia Schulz.

The binding energy of the Co $2p_{3/2}$ of CoO is shifted by 1 eV to a lower binding energy of 780.0 eV and the satellite structure appears at an increased binding energy distance of 6 eV. Furthermore, the O 1s spectrum of CoO exhibits only the O 1s peak attributed to lattice oxygen. McIntyre et al. reported a binding energy of 780.0 eV for the Co $2p_{3/2}$ peak of CoO and an associated binding energy difference of 6- 6.5 eV for the satellite structure of CoO. [87, 91]

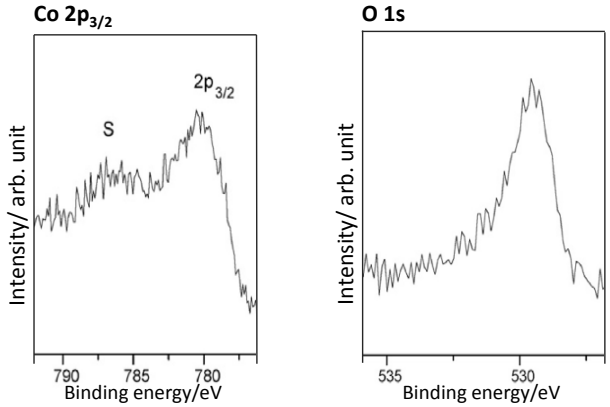

Figure 5.5. Co $2p_{3/2}$ and O 1s spectra of a UHV cleaved CoO(100) sample adapted from literature [90].

The comparison of the reference spectra shows, that each cobalt oxide has its unique line shape and satellite structure and as a consequence the oxidation state and structure can be distinguished by the difference of these.

Since a main task of this thesis represents the XPS characterization of electrochemically characterized cobalt oxides, an attempt was made to deposit cobalt reference materials electrochemically by potentiostatic conditioning starting from a cobalt foil for comparison. For this purpose, the experiments were performed in the electrochemical cell, which is directly connected to the UHV system. This setup allows to transfer the sample under inert gas atmosphere from the electrochemical cell to the XPS system. The potential induced phase transformation of cobalt was already discussed in Chapter 3.3. Analog to the investigations of Doyle et al., cyclic voltammogramms were recorded in 1 M KOH for a polycrystalline cobalt foil with scan rates of 100 mV/s and 300 mV/s. Figure 5.6 a shows the cyclic voltammogram recorded with a scan rate of 100 mV/s. The redox peaks are

not as pronounced as found by Doyle et al. and the redox peak of the Co(III)/Co(IV) transition is superimposed by the oxygen oxidation reaction. Nevertheless, a 15 minutes potentiostatic conditioning was performed before and after the first redox transition at potentials of 0.112 V and 0.250 V vs. Hg/HgO and after the second redox transition at a potential of 0.6 V vs. Hg/HgO. XPS spectra were recorded right after each conditioning step. The Co $2p_{3/2}$ and O 1s spectra are shown in Figure 5.6 b) and c). The O 1s spectra identify the coexistence of oxides and hydroxides at all potentials. Literature suggested $Co(OH)_2$ as the stable phase at potentials below 0.2 V vs. Hg/HgO. [61]

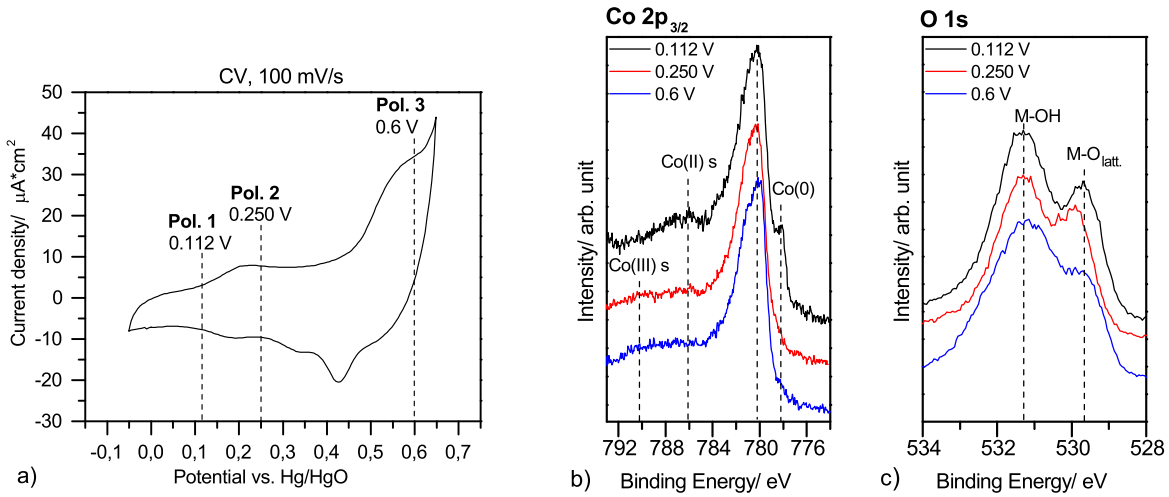

Figure 5.6. Co $2p_{3/2}$ and O 1s detail spectra of potentiostatically conditioned Co-foil. The conditioning was performed at 0.112 V, 0.25 V and 0.6 V vs. Hg/HgO in 1 M KOH for 15 min.

The Co $2p_{3/2}$ spectrum recorded after the potentiostatic conditioning at a potential of 0.112 V identifies Co(II) as the predominant oxidation state, but also metallic Co(O) is still detectable at a binding energy of 778.3 eV. In agreement with literature, the O 1s spectrum confirms the presence of CoO by the O 1s feature at a binding energy of 529.7 V and of $Co(OH)_2$ by the high binding energy O 1s feature at 531.3 eV. The Co $2p_{3/2}$ spectra recorded after the potentiostatic conditioning at a potential of 0.25 V and 0.6 V look similar, the Co 2p line agrees with the one reported for Co_3O_4 as structure of spinel. Nevertheless, the superposition of the Co 2p line of CoO(OH) and Co_3O_4 cannot be ruled out. Due to the complex electrochemical redox behavior of transition metals and their oxides, the resulting XPS spectra are not as clear to interpret.

5.5 Calculating the atomic concentration of hydroxide moieties

The accurate determination of the surface composition is essential for identifying the types and amounts of functional groups. With respect to the investigation of the water splitting mechanism, the identification of hydroxide intermediates after the electrochemical characterization presents a central role of this thesis. Typically the O 1s spectrum of a metal oxide exhibits two peaks: a low binding energy feature (LBE) and a high binding energy feature (HBE). There is general agreement in literature that the LBE feature, which is typically positioned between 529.5 eV to 530 eV, is attributed to metal bonded lattice oxygen. The HBE feature is not as definite to

assign since the BE positions of oxygen defects, hydroxide species and carbon bonded oxygen are close together. To discuss the formation of hydroxide species, especially the contribution of carbon-bonded oxygen to the total area of the HBE feature has to be considered. Therefore, the atomic concentration of carbon bonded oxygen was determined from the C 1s spectrum to constrain the area of the O 1s fit representing the C-O species. Figure 5.7 shows as an example the C 1s spectrum and the construction of the C-O fit (red) in the O 1s spectrum.

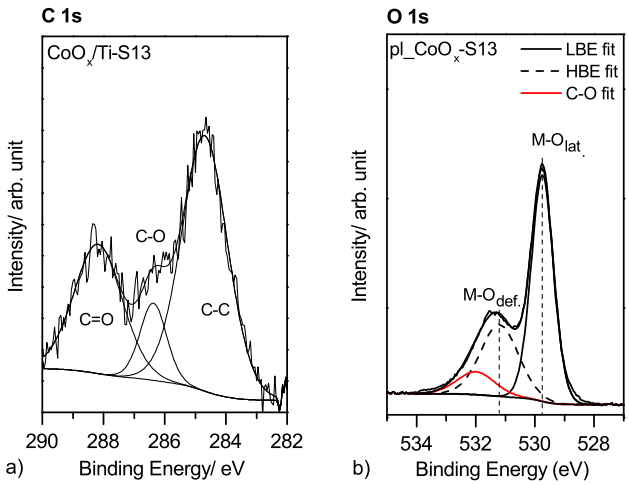

Figure 5.7. XPS detail spectra of the C 1s and O 1s regions of pl_CoO_x.

The C 1s spectrum exhibits ether-type carbon species (C-O) at 286.2 eV and carbonyl species (C=O) at 288 eV. The FWHM of the O 1s fit of the C-O contributions are constrained between 1.6 eV to 1.8 eV. Table 5.3 summarizes the calculated areas of the C-O, the LBE and the HBE fits.

Table 5.3. Calculated areas of the C-O, the LBE and the HBE fits. All areas are corrected for the atomic sensitvity factor (RSF), the transmission factor (TM) and the mean free path (MFP).

Sample	**A(C 1s$_{C-O}$)** *[RSF*T*MFP]*	**A(O 1s$_{C-O}$)** *[RSF*T*MFP]*	**O 1s$_{LBE}$** *[RSF*T*MFP]*	**O 1s$_{HBE}$** *[RSF*T*MFP]*	**LBE:HBE** *[%]*
S13	133.7	338.9	781.4	420.7	65:35

In addition to the carbon contribution, TiO_2 had to be considered if the substrate signal was detectable. Analog to the construction of the C-O fit, a O 1s line fit representing TiO_2 was constrained with the area representing the atomic concentration of Ti. The O 1s fit of Ti-O was constrained to the binding energy position of 530.1 eV and to the full width half maximum (FWHM) of 1.22 eV, since these parameters were obtained from the O 1s spectrum of the pure Ti/TiO_2 substrate.

5.6 Instrumentation

The experimental setup of the PES experiment including the X-ray-source, the analyzer and the detector, is illustrated in Figure 5.8. The XPS system was purchased from SPECS Surface Nano Analysis GmbH. A monochromatic Al-Kα (XR 50 M, Focus 500) tube was used as X-ray source. The hemispherical analyzer Phoibos 150 was operated in Constant Analyzer Energy (CAE) mode. By applying a voltage, the emitted photoelectrons are retarded to a certain pass energy before entering the analyzer. A full spectrum is then recorded by varying the retarding potential keeping the pass energy constant.
The CAE mode has the advantage of a constant spectral resolution. The emitted electrons were detected by a nine channeltron detector.

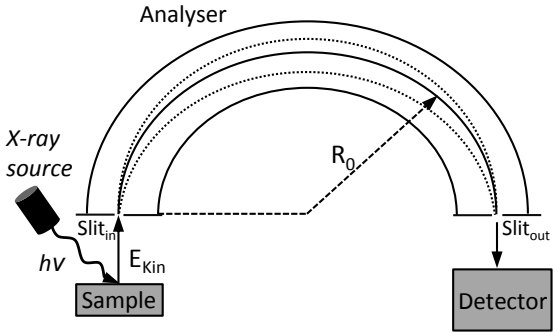

Figure 5.8. Schematic illustration of the PES experiment.

The XPS spectrometer was calibrated by correcting the relative binding energy difference of the measured 3d core level emission lines and the Fermi edges of sputter-cleaned Ag, Au and Cu to their literature values.

6. Electrochemical characterization

The decomposition of water by an electrical discharge into "combustible air" and "live-giving air" was already discovered by Troostwijk and Deinman in 1789. The phenomenon could be further described by Nicholson and Carlisle as the electrolysis of water into hydrogen and oxygen. [92] In general the electrolysis of water means to drive a thermodynamic uphill reaction using a direct electric current as described in Chapter 2). To make this process efficient, catalysts are needed to reduce overpotentials. The field of electrochemistry is complex and one major problem is the missing comparability of the results. A material can show different catalytic behavior in dependence of the applied test protocol. Another reason what makes the comparison to literature data difficult is the different possibilities to declare the determined potentials. Data can be given versus the standard hydrogen electrode, the reversible hydrogen electrode or against the reference electrode. To guarantee the comparability of the results within the project SusHy, an electrochemical test procedure was defined and the reference electrodes were stated. The test protocol included the measurement of the open circuit potential (OCP) for ten minutes, the electrochemical impedance spectroscopy (EIS) (20 Hz-20 kHz), a cyclic voltammogram (CV) and a galvanostatic scan (GS). Table 6.1 summarizes the electrochemical test procedure.

Table 6.1. Electrochemical test protocol specified in the consortium of the project SusHy.

Step N°	Experimental	Determined value
1	10 min at OCP	Open circuit potential
2	EIS (20 kHz-20 Hz)	Electrolyte resistance
3	Pol at 1.23 V	Polarize to start value of step 4
4	CV, 10 mV/s, 1 scan, 1.23 V to 1.8 V	Overpotential η at current density I
5	Pol. at 1.23 V	Polarize to start value of step 6
6	LSV, 1mV/s, 1.23 V to 1.8 V	Onset potential
7	GS at 10 mA/cm^2, 15 min	Degradation slope

In this thesis, all potentials are given versus RHE and are corrected for the electrolyte resistance. Since this test procedure is time consuming a modified test protocol was applied to be able to screen the activity of a greater amount of catalysts. The modified protocol leaves out step 6 because the linear scan does not give a necessary additional information about the activity, for a first assessment of the catalytic activity the determined cyclic voltammograms are used. In some cases a cyclic voltammogram was recorded after the degradation test (Step 7) in addition to the specified test protocol to investigate possible changes induced by degradation.
The electrochemical tests were performed in the ex-situ experimental setup (Chapter 6.1). There was also the possibility to perform the electrochemical characterization in an electrochemical cell, which is directly attached to the UHV system. The advantage of the integrated cell is, that the

sample can be transferred under inert gas atmosphere to the XPS. But due to the required long evacuation times, the experiments are highly time consuming. All in all, only two catalysts were characterized using the integrated electrochemical cell in order to exclude a possible influence of the contact with air on the electronic structure and composition of the characterized catalysts. But since the results did not differ from the ones performed with the ex-situ setup, there is no need to discuss these separately in this thesis. With regard to the catalysts application, an ex-situ characterization anyhow makes more sense, since the transport of the prepared electrodes to the electrolyzer without being in contact to air is not practicable and therefore the carbon contamination also have to be considered in a real system.

6.1 Electrochemical cell

The electrochemical characterization was performed using the potentiostat ZENNIUM supplied by Zahner-Electrik GmbH Co.KG. The Zennium workstation can operate in galvanostatic and potentiostatic mode and is equipped with a frequency response analyzer with a frequency range up to 4 MHz at $\pm$ 2.5 A respectively 10 V. The electrochemical cell (kit PECC-2, Zahner) is equipped with a gas in-/outlet, a channel for the reference electrode, a Pt wire as counter electrode and a working electrode holder. Figure 6.1 shows the schematic drawing of the electrochemical cells front side and the working electrode assembly on the backside.
The working electrode is mounted between the insulating PTFE holder and the conducting metal plate, which are fixed by 6 screws. The volume of the electrolyte chamber is 7.2 cm^3 and the active area of the working electrode (0.5 cm^2) is defined by the 8 mm diameter of the O-ring, which seals its connection to the PTFE plate. All measurements shown in this thesis were conducted in a three electrode setup using either 0.1 M KOH or 1 M KOH as an electrolyte.

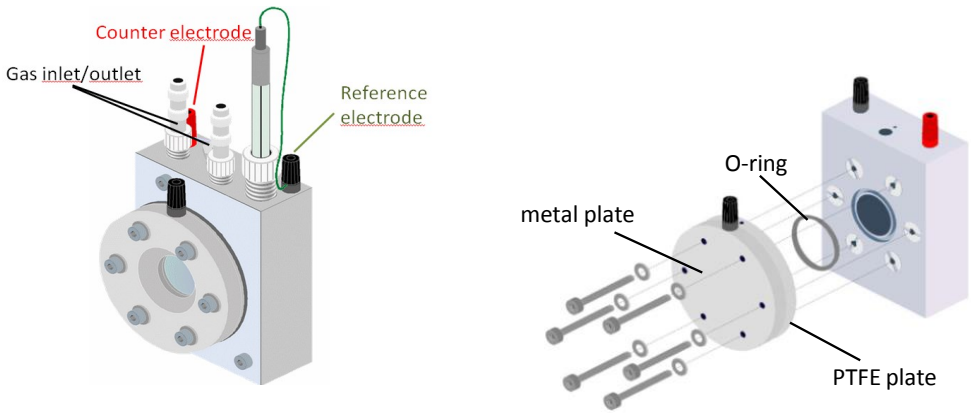

Figure 6.1. Technical drawing of the electrochemical test cells (PECC-2) front side and the working electrode assembly. The technikal drawing is taken from the Zahner manual.

As reference electrodes a 3 M Ag/AgCl electrode (0.205 V vs. SHE) was used for the electrochemical characterization in 0.1 M KOH and a 1 M Hg/HgO electrode was used in 1 M KOH. The potentials of the reference electrodes were verified before each measurement against a RHE electrode. The XPS measurements of the electrochemical tested samples were performed right after dismounting the sample.

6.2 Potentiostat and operation mode

Operating in a three electrode mode makes the exact determination of the investigated half cell reaction, the oxygen evolution reaction, possible. The potential has to be measured relative to the reference electrode, which is placed at a distance of 1.1 cm to the working electrode. Figure 6.2 gives a schematic illustration of the circuit diagram of a three electrode setup. The working electrode W represents the electrode to be examined and the counter electrode C is used to close the current circuit.

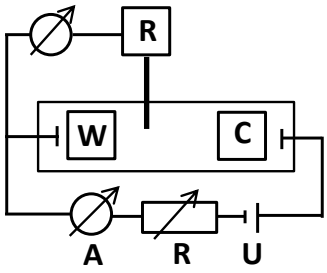

Figure 6.2. Circuit diagram of the three electrode setup including the reference electrode (R), the working electrode (W) and the counter electrode (C).

Since the current flows between W and C, the total surface area of C must be higher than the area of W so that the hydrogen evolution reaction does not become the limiting reaction. The current flow through the reference electrode is kept ideally to zero to guarantee a constant potential. The potential difference U_{is} is measured between R and W and will be adjusted to be equal to the user specified potential U_{set} by applying a matching current. The experimentally determined potentials were given versus the standard hydrogen electrode. For a better comparability, all potentials were converted into the potential versus reversible hydrogen electrode (RHE) using Equation 6.1.

$$E = E_{Exp,NHE} + 0.059 * pH \tag{6.1}$$

6.3 Determination of the electrolyte resistance

To correct the electrochemical data to the electrolyte resistance, electrochemical impedance spectra (EIS) were recorded in a frequency range between 20 kHz to 20 Hz at OCP. The electrochemical impedance is measured by applying an AC (alternating current) potential to an electrochemical cell to determine the AC current response. In general, an electrochemical cell does not behave like a linear system, in which the output signal is simply the superposition of the systems responses to each input signal. But in case of small excitations, the pseudo linear response of an electrochemical cell can be described analog to the impedance of linear systems. The excitation signal is described as a sinusoidal function (Equation 6.2) where E_t is the potential at time t, E_0 the amplitude of the signal and ω the frequency.

$$E_t = E_0 * \sin(\omega t) \tag{6.2}$$

The response signal which is shifted in phase ϕ results as

$$I_t = I_0 * \sin(\omega t + \phi) \tag{6.3}$$

The impedance of a non-linear system is described as a complex number $Z(\omega)$, which composes of a real part and an imaginary part. (Equation 6.4)

$$Z(\omega) = Z_0(\cos\phi + i\sin\phi) \tag{6.4}$$

$Z(\omega)$ is represented graphically in a Nyquist Plot by plotting the real part on the X-axis and the imaginary part on the Y-axis. Figure 6.3 a) shows the simple equivalent circuit corresponding to the Nyquist plot illustrated in Figure 6.3 b). Whereas the electrode in the equivalent circuit is described by a parallel circuit of a capacitor C and a non-ohmic resistance R, the ohmic electrolyte resistance R_E is connected in series. At frequencies larger than 1 kHz, the contribution of C and R become negligible and the AC current flowing through the cell is determined by R_E. In the Nyquist plot of diluted acids and alkalies, R_E is derived from the high frequency intersection of the curve with the X-axis.

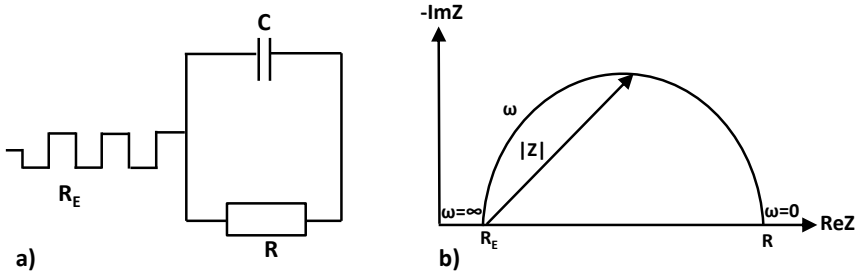

Figure 6.3. a) Simple equivalent circuit of an electrode in a device considering the electrolyte resistance R_E, the charge transfer resistance R and the double layer capacity C. b) Nyquist plot with impedance vector.

The specific conductivity σ_m and the molar conductivity Λ_0 can be calculated from the measured serial resistance by Equation 6.5. The geometric factor Γ of the Zahner cells geometry is 0.756 cm^{-1} for an active area of 0.5 cm^2.

$$\sigma_m = \Gamma * \frac{1}{R_E}; \quad \Lambda_0 = \frac{\sigma_m}{c} \tag{6.5}$$

Values for the specific and the molar conductivities of various electrolytes are reported in literature. [24, 93] While 1 M KOH for example has a molar conductivity of 184 S*cm^2/mol, 0.1 M KOH has a molar conductivity of 213 S*cm^2/mol. [93]

6.4 Determination of the catalytic activity and stability

In order to compare the activity of the various catalysts with each other, the overpotentials at a current densities of 2 mA/cm^2, 5 mA/cm^2 and 10 mA/cm^2 were extracted from the cyclic voltammogram and used as a descriptor for the activity. Additionally, Tafel slopes of promising catalysts were determined by recording linear sweep voltammograms with a scan rate of 1 mV/s. To evaluate the stability of the catalysts, either a potentiostatic scan (PS) or galvanostatic scan (GS) was performed. While the galvanostatic scans were always performed at a current density of 10 mA/cm^2, the operating potential of the potentiostatic scan was determined from the respective CV. The potential at 10 mA/cm^2 was chosen as the operating potential. The GS and the PS

determined for each system was then fitted linearly, the slope defines the degree of degradation in mA/cm^2s or V/s. Since the stability test was carried out for a maximum of 30 min, one can only speak here from the investigation of a short-time stability.

6.5 Materials

0.1 M KOH	Carl Roth GmbH + Co. KG, Standard solution 0.1 M± 0.2 %
1 M KOH	Carl Roth GmbH + Co. KG, Standard solution 1 M± 0.1 %
0.5 M H_2SO_4	Carl Roth GmbH + Co. KG, Standard solution 0.5 M± 0.2 %

Part III

Results and discussion

The result section deals first with the establishment of a demand profile for the OER catalysts in Chapter 7. Commercially available IrO_2 and RuO_2 electrodes were defined as a standard reference since these are known to be the most active OER catalysts. [94] Second, the preparation and characterization of single metal oxide catalysts is discussed. In this context, the optimization of the PECVD deposition process as well as the influence of various deposition parameters like the substrate temperature, the operation mode (thermal vs. plasma) and the type of reactive gas (oxygen vs. air) on the electronic structure, composition and the resulting electrochemical activity of the catalysts is described.
A milestone of this thesis presents the results on the change of oxidation state during OER. By measuring XPS before and after the electrochemical characterization, a correlation between the oxidation state and the activity was found. Chapter 9 compares the detailed XPS studies of thermally deposited th_CoO_x, plasma deposited pl_CoO_x and pl_$CoO_x(OH)_y$ and points out the positive influence of a hydroxylated surface on the resulting electrochemical activity. The promoting effect of hydroxide moieties could also be detected for $NiO_x(OH)_y$.
Beside the deposition of single metal oxide catalysts, an attempt was made to prepare bimetallic $CoMO_x$ and $CoMO_x(OH)_y$ (M= Fe, Ni, Cu) catalyst films by PECVD (Chapter 10). The effect of the second metal on the electronic structure and the activity was studied by measuring XPS from the initial deposited catalyst films and after the electrochemical characterization.
Finally, Chapter 11 presents a summary and conclusion of the results part.

7. IrO_2 and RuO_2 as standard catalysts: Generation of a demand profile

The standard reference catalysts IrO_2 and RuO_2 deposited onto titanium were purchased by Metakem with a load of 15 g/m^2. According to the testimony of Metakem, the electrodes are prepared in a special ink procedure with TiO_2 as a binder. The XPS survey scans proof the purity of the electrodes. It was exclusively oxygen, titanium, carbon and the respective noble metal iridium and ruthenium detectable (Figure 7.1).

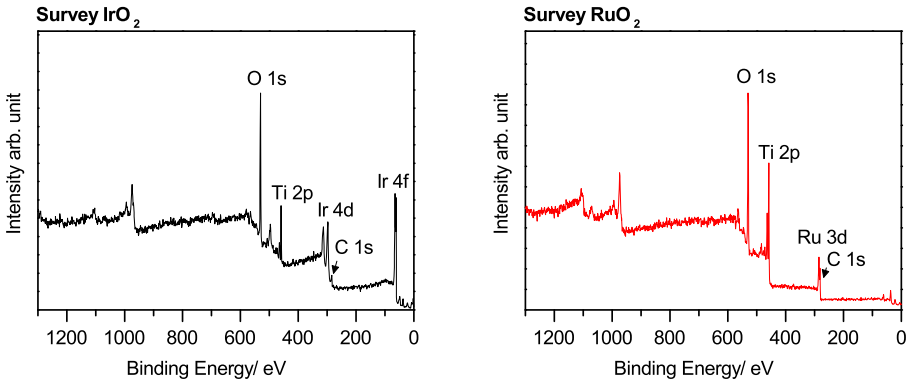

Figure 7.1. XPS survey scans of the standard reference samples IrO_2/Ti and RuO_2/Ti films purchased by Metakem.

The reference catalysts were electrochemically characterized in 0.1 M KOH and in 0.5 M H_2SO_4. The Nyquist plots resulting from the electrochemical impedance measurements are shown in Figure 7.2. An electrolyte resistance of 5.23 Ohm and 5.36 Ohm is determined from the Nyquist plots for H_2SO_4 using IrO_2/Ti and RuO_2/Ti as a working electrode. The conductivity of 0.1 M KOH is lower compared to 0.5 M H_2SO_4, an electrolyte resistance of 29.2 Ohm is found using IrO_2/Ti and 29.75 Ohm using RuO_2/Ti as working electrode.

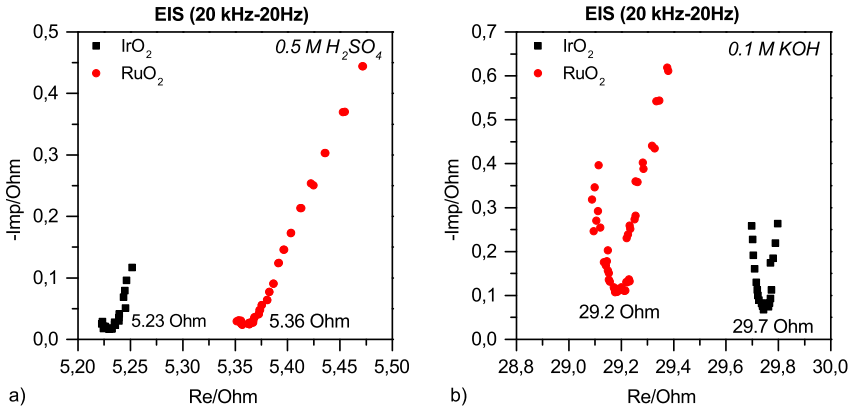

Figure 7.2. Nyquist plots recorded for IrO_2/Ti and RuO_2 in a) 0.5 M H_2SO_4 and b) 0.1 M KOH.

From the Nyquist plots one can assume that there are also other resistance contributions like e.g. electronic resistances. But due to the complexity of the undefined catalyst systems which are investigated, EIS was only used to determine the IR drop. The measured values

for the electrolyte resistances are in good agreement with the ones reported by Ziegler et al. They reported an IR drop of 5.6 Ohm for 0.5 M H_2SO_4 using a platinum foil as a working electrode. [95]. Typically, the specific and molar conductivities that can be calculated from the series resistance (Chapter 6.3) are listed in literature as standard. Table 7.1 lists the with EIS measured series resistances using IrO_2 as a working electrode for 0.5 M H_2SO_4 and 0.1 M KOH as well as the calculated specific and molar conductivities. In literature, a molar conductivity of 213 S/cm^2*mol is reported for 0.1 M KOH and of 44 S/cm^2*mol for H_2SO_4. [93,96] The comparison of the measured values with literature shows a good agreement in view of the complex cell geometry.

Table 7.1. Series electrolyte resistance R_E measured by EIS as well as the calculated specific and molar conductivities σ_m and Λ reported for 0.5 M H_2SO_4 and 0.1 M KOH. The distance between the working electrode and the reference electrode is about 1 cm.

Electrolyte	$\mathbf{R_E}$ *[Ohm]*	σ_m *[S/cm]*	Λ *[S/cm^2 *mol]*	Λ_{Lit} *[S/cm^2 *mol]*
0.5 M H_2SO_4	5.2± 0.2 Ohm	0.145	29	44
0.1 M KOH	29.2± 0.5 Ohm	0.026	260	213

Figure 7.3 shows the cyclic voltammograms of IrO_2/Ti and RuO_2/Ti recorded in 0.5 M H_2SO_4 and 0.1 M KOH with a scan rate of 10 mV/s. IrO_2 requires an overpotential of only 0.23 V to archive a current density of 10 mA/cm^2 in 0.5 M H_2SO_4, while RuO_2 needs an overpotential of 0.28 V. The difference in activity is not as pronounced in alkaline conditions. Both catalysts need about 0.31 V at 10 mA/cm^2. In fact, the results show that the commercially available electrodes exhibit a good activity.

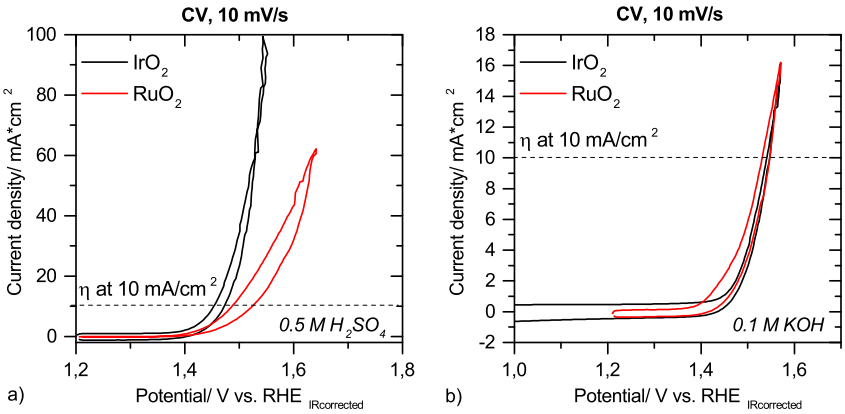

Figure 7.3. Cyclic voltammograms of IrO_2/Ti and RuO_2/Ti recorded in a) 0.5 M H_2SO_4 and b) 0.1 M KOH.

Papazisi et al. found a comparable activity for unsupported IrO_2/GC prepared by the Adams fusion method. [97] An overpotential of 0.259 V can be extracted from the linear sweep voltammogram at a current density of 10 mA/cm^2 recorded in 0.5 M H_2SO_4. [97] Higher overpotentials of 0.48 V and 0.45 V were found in 0.1 M KOH for defined IrO_2 and RuO_2 nanoparticles of 6 nm size by Lee et al. [94] Figure 7.4 shows the galvanostatic scans of IrO_2 and RuO_2, which were

performed at 40 A/g in 0.5 M H_2SO_4 and 0.1 M KOH. In addition, IrO_2 was galvanostatically conditioned at 10 A/g in 0.5 M H_2SO_4. As already seen from the cyclic voltammograms, the performance of both, IrO_2 and RuO_2 is better in 0.5 M H_2SO_4 than in 0.1 M KOH. Higher potentials are required to generate 40 A/g in 0.1 M KOH. The degradation slopes, however, are all in the same order of magnitude (10^{-5} V/s) at 40 A/g. Although the differences in stability are not very pronounced, IrO_2 seems to be slightly more stable in 0.5 M H_2SO_4, while RuO_2 showed a better stability in 0.1 M KOH. An even lower degradation slope of $8.4*10^{-6}$ V/s is found at a current of 10 A/g, which corresponds to the area specific current density of 15 mA/cm^2. A comparison with literature data is difficult since the test conditions vary often considerably. Nevertheless it should be mentioned, that Maljusch et al. investigated the degradation behavior of a model IrO_2 catalysts in 0.1 M KOH at a current density of 10 mA/cm^2. They observed a degradation slope of 2.151± 0.039 mV/h ($5.972*10^{-7} \pm 1.08*10^{-8}$ V/s) from the galvanostatic scans performed at 10 mA/cm^2. [98]

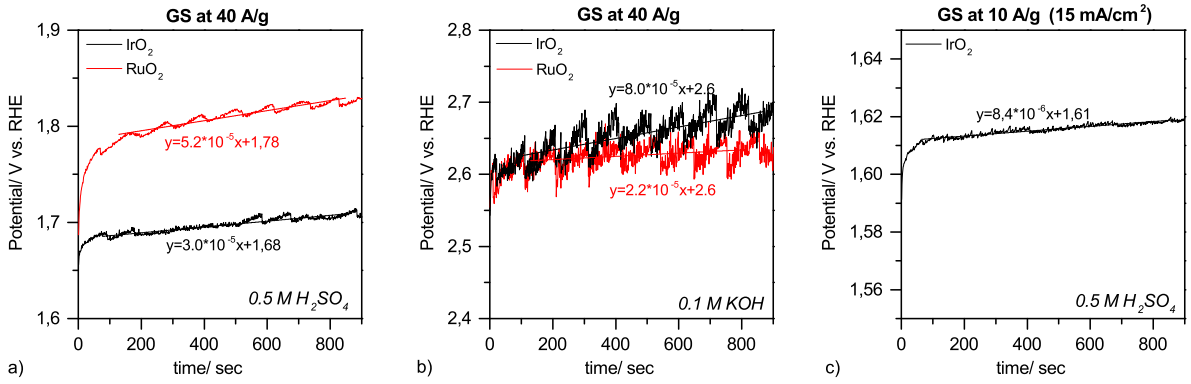

Figure 7.4. Galvanoststic scans of IrO_2 and RuO_2 recorded at 40 A/g in a) 0.5 M H_2SO_4 and b) 0.1 M KOH. c) Galvanoststic scan of IrO_2 recorded at 10 A/g in 0.5 M H_2SO_4.

Typical SEM micrographs of IrO_2/Ti at two magnifications are shown in Figure 7.5. The micrographs reveal a porous and amorphous structure, there were no particle agglomerates detectable. The porosity of the electrode's surface has to be taken into account when comparing the electrochemical activities.

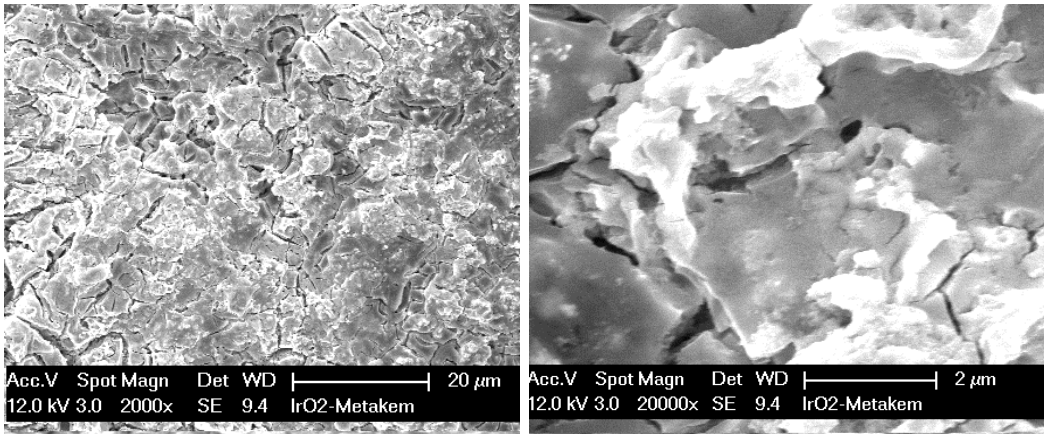

Figure 7.5. SEM images of the IrO_2/Ti electrode recorded after the electrochemical characterization.

Porous electrodes have the advantage of a high active surface area over thin films. For sure, IrO_2 and RuO_2 are highly active OER catalysts but 1 kg of Ir is with a price of 20390.99 €/kg about 886 times more expensive than a 1 kg of cobalt, which costs 23.97 €/kg. Ru costs 1294.56 €/kg and is about 54 times more expensive than 1 kg of Co. [99] Therefore there is an economical interest to find active and stable non-noble catalysts, which make the process of water electrolysis more beneficial.

8. Preparation and characterization of the single metal oxide catalysts

In this Chapter, the preparation of the pure metal oxides CoO_x, NiO_x, FeO_x, as well as of $CoO_x(OH)_y$ and $NiO_x(OH)_y$ is discussed. Since the development and construction of the CVD system was part of the research, the instrument-based details are discussed in combination with the optimization of the setup in Chapter 8.1. This Chapter particularly focuses on the initial challenges concerning the reproducibility of the catalysts and the different implemented solutions. Chapter 8.2 shows the thermogravimetric investigation of the precursor materials $Co(acac)_3$, $Fe(acac)_3$, $Ni(acac)_2$ and $Cu(acac)_2$. The variation of various deposition parameters like the choice of the reactive gas, the substrate temperature, the deposition time and their influence on the structure, the electronic state, the morphology and the layer thickness of the catalysts are then discussed in Chapter 8.3 and Chapter 8.4. Especially the choice of the operation mode and the reactive gas were found to have a high impact on the structure and therefore on the oxidation state. Finally, the electrochemical activity of the as deposited catalysts is investigated in Chapter 8.5 and the influence of the deposition parameters on the activity is established.

8.1 Installation and optimization of the PECVD setup

8.1.1 First step of optimization: Change of the precursor opening valve

Figure 8.1 shows the first draft of the home build CVD system.

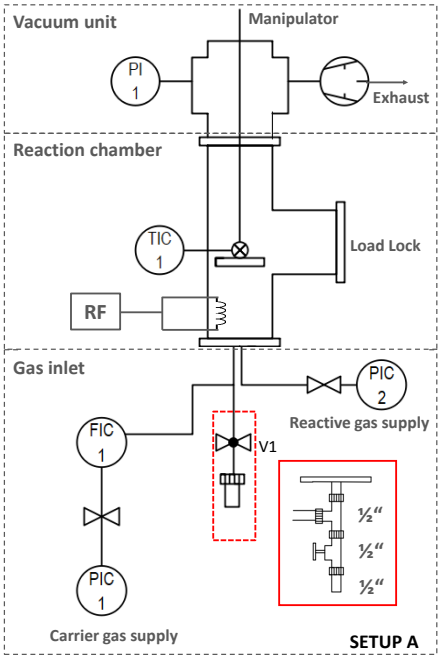

Figure 8.1. Schematic illustration of the CVD system, setup A.

A full description of the optimized PECVD setup was already given in the experimental part (Chapter 4.4). In contrast to the optimized setup, the gas inlet system, which is built of vacuum

fittings, has only one precursor inlet line. Due to the experience made in our group, that the line clocks easily when a solid precursor is used in the CVD process, the inlet system was designed with an inner diameter of 1/2". In the following discussion, the described setup is denoted as setup A.

First of all, the number of depositions, which can be performed with one precursor filling, was investigated. The precursor filling of 0.215 g was reduced to 0.1 g after depositing four samples thermally with a deposition time of 5 min (S3), 5 min (S4), 10 min (S5) and 10 min (S6) onto titanium using a precursor temperature of 190 °C. As a conclusion, the precursor filling of 0.2 g is sufficient for a total deposition time of 40 min. Second, the reproducibility of the deposited layer thicknesses was investigated for the plasma enhanced mode. For this purpose, the deposition of sample S13, S14 and S17 was carried out multiple times. Figure 8.2 shows, that the resulting atomic concentrations of Ti vary strongly in dependence on the number of deposition for one parameter set. In case of sample S14 for example, a titanium signal of 0 % for the first attempt, of 31.6 % for the second and of 11.3 % for the third attempt is observed.

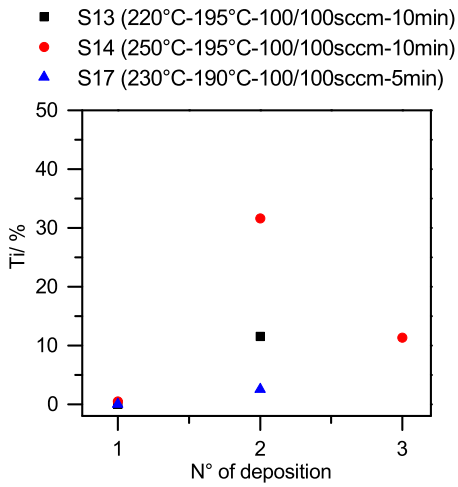

Figure 8.2. Atomic concentration of the substrate Ti 2p signal plotted versus the number of accomplished depositions of sample S13, S14 and S17 using setup A. The deposition conditions are given in the legend in the following sequence: T_{Sub}-T_{Prec}-f_{Ar}/f_{O_2}-t_{Dep}.

The lack in reproducibility was attributed to a missing limitation of the evaporating precursor flow by the 1/2 " valve. If the valve opening is small enough, the precursor flow introduced to the chamber is only limited by the valve opening itself and it is not dominated by the vapor pressure within the crucible. Another problem which was identified is, that the precursor powder was sucked into the reaction chamber when the vacuum pump was switched on even if the valve of the pump was carefully opened. As a consequence, the 1/2 " valve was exchanged in a 1/4" valve.

Figure 8.3 shows the successful PECVD deposition of CoO_x onto silicon using setup B for two different inlet-to-substrate distances d, 12.4 cm and 10 cm. While in Figure 8.3 a the atomic concentration of Si is plotted versus the deposition time, Figure 8.3 b presents the calculated layer thickness of CoO_x. Using an inlet-to-substrate distance of 12.4 cm, pl_CoO_x can be deposited onto Si in a controllable manner, the layer thickness increases with deposition time. The layer thickness does not increase with the deposition time when an inlet-to-substrate distance of 10 cm is set.

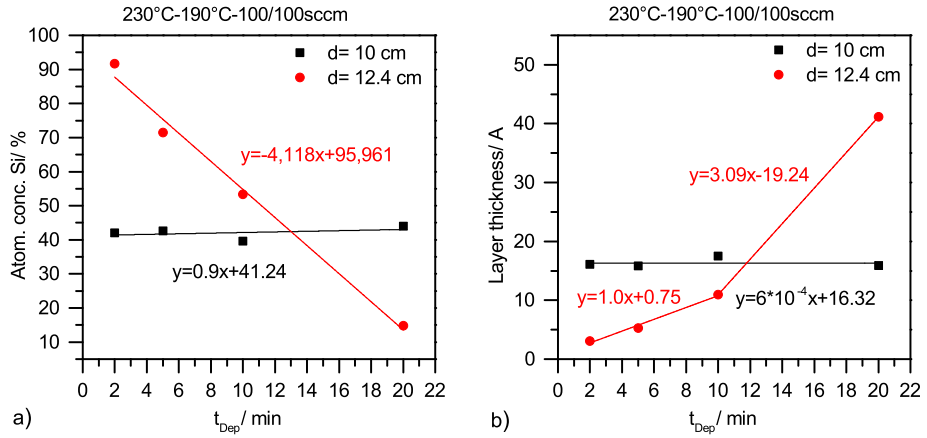

Figure 8.3. a) Atomic concentration of Si plotted versus the deposition time for inlet-to-substrate distance of 10 cm and 12.4 cm. b) Plot of the calculated layer thickness of CoO_x/Si versus deposition time prepared using setup B. The preparation parameters are given in the titles in the following sequence: T_{Sub}-T_{Prec}-f_{Ar}/f_{O_2}.

The determined deposition rate is approximately constant with a value of $6*10^{-4}$ Å /min. This phenomenon can be related to a plasma induced desorption, with the adsorption rate being equal to the desorption rate of CoO_x. The closer the substrate is positioned at the plasma, the more collisions it will be exposed to. By enlarging the inlet-to-substrate distance to 12.4 cm, a deposition rate of 1 Å/min is realized in the coverage regime between 0 - 10 Å, in which the evaporated CoO_x is deposited onto the Si/SiO_2 surface. Above a coverage of 10 Å, the layer growth proceeds with a rate of 3.1 Å/min since the adsorption of evaporated CoO_x onto the deposited CoO_x surface is preferred. Figure 8.4 compares the SEM images of CoO_x/Si using a deposition time of 20 min and an inlet-to-substrate distance of 10 cm and 12.4 cm.

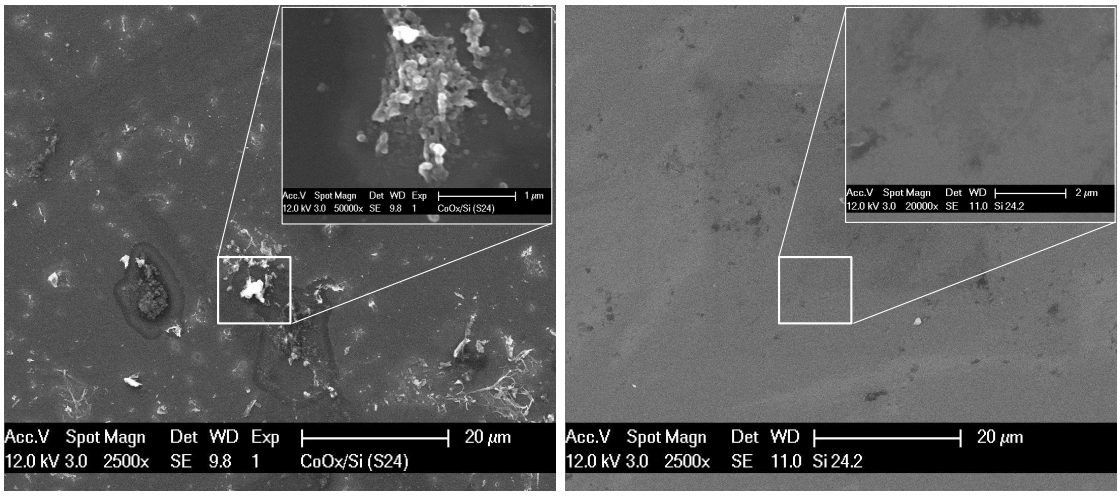

Figure 8.4. SEM pictures of 20 min PECVD deposited CoO_x/Si using setup B with an inlet-to-substrate distance of 10 cm (*left*) and of 12.4 cm (*right*).

The reason for choosing Si as a substrate was, that the morphological differences can be better investigated since the surface of Si is smooth and it shows a better elemental contrast to Co compared to Ti. The SEM image of CoO_x/Si deposited using a inlet-to substrate distance of 10 cm is characterized by a broad distribution of agglomerates consisting of particles with a size

between 88 to 130 nm. However, when depositing CoO_x/Si with the same parameter set at a distance of 12.4 cm a homogeneous layer with no agglomerates is observed. It can be summarized that the installed PECVD setup B provides the possibility to deposit reproducible thin CoO_x films, when using an inlet-to-substrate distance of 12.4 cm and the 1/4" valve.

8.1.2 Upgrade to three precursor sources

With respect to the later goal of depositing binary and ternary catalyst systems, two more precursor sources had to be installed. Analog to the 1/4" precursor line of setup B (V1), two additional inlet lines were set up as simple evaporation sources without a carrier gas supply. Figure 8.5 shows a schematic illustration of the modified gas inlet system, which is denoted as setup C.

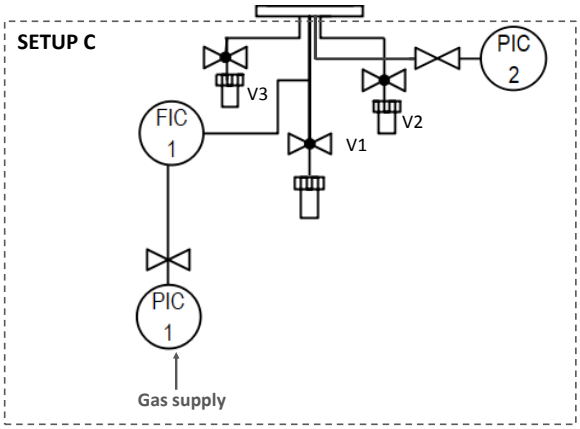

Figure 8.5. Modification of the gas inlet system, installation of two additional precursor sources equipped with 1/4" valves V2 and V3.

First experiments for the deposition of bimetallic $CoNiO_x$ films were carried in setup C using $Co(acac)_3$ and $Ni(acac)_2$ as precursors, precursor temperatures of 180 °C, an argon and oxygen flow of 200 sccm and Ti-foil as a substrate. Unfortunately it turned out, that the amount of nickel in $CoNiO_x$ could not be controlled only by the evaporation temperature. Figure 8.6 a plots the resulting different atomic concentrations of cobalt and nickel in $CoNiO_x$ with increasing deposition time. Although the evaporation temperatures of cobalt and nickel, as well as the argon and oxygen flows were kept constant, the stoichiometric composition differs. Figure 8.6 b compares the resulting nickel content in dependence on the Ni precursor temperature for a deposition time of 20 min (samples CoNi4 and CoNi5) and of 15 min (samples CoNi8 and CoNi9). One would expect that with increasing precursor temperature, the nickel content increases. This was not observed. Indeed, the highest Ni content was realized with a precursor temperature of 170 °C but pure NiO_x could not be successfully deposited by evaporation using a precursor temperature between 170- 180 °C. Nevertheless, all samples were electrochemically tested and the results are discussed within Chapter 10.3. In order to have an improved control over the secondary metal sources, the respective supply lines were equipped retrospectively with carrier gas supplies. The schematic illustration of the final PECVD system (Setup D) was already shown in Figure 4.4 in the experimental section Chapter 4.4.

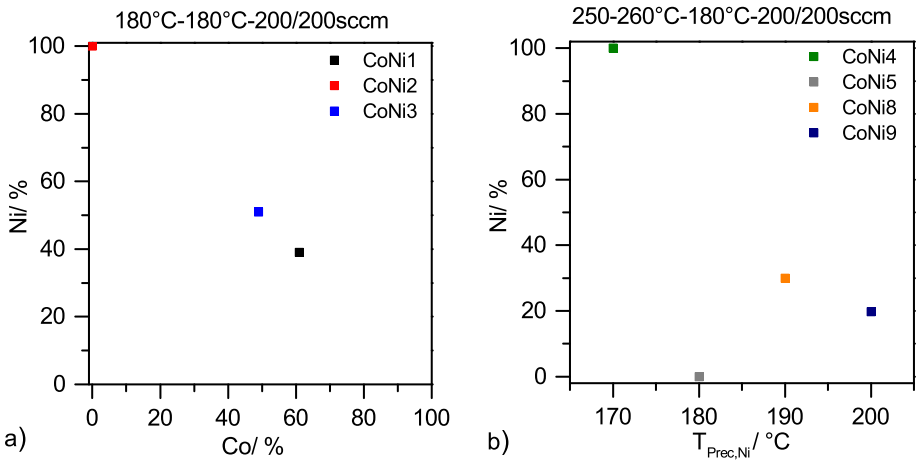

Figure 8.6. a) Comparison of pl_CoNiO$_x$ films deposited at T_{Sub}=230°C and t_{Dep}=7 min (CoNi1), T_{Sub}=260°C and t_{Dep}=10 (CoNi2), T_{Sub}=260°C and t_{Dep}=20 min (CoNi3) using setup C. The remaining parameters are given in the title in the following sequence: $T_{Prec,Co}$-$T_{Prec,Ni}$-f_{Ar}/f_{O_2}. b) Deposition of pl_CoNiO$_x$ films varying $T_{Prec,Ni}$ at t_{Dep}=20 min (CoNi4 and CoNi5) and t_{Dep}=15 min (CoNi8 and CoNi9). The title lists the following deposition parameters: T_{Sub}-$T_{Prec,Co}$-f_{Ar}/f_{O_2}

Finally it should be noted, that it turned out to be difficult to ensure a certain degree of comparability while establishing the PECVD system, since the setup had to be modified several times. In addition, the deposition control itself was not satisfying. Many experiments failed due to clogging of the precursor inlet pipes and plasma breakdowns. Especially the coupling of an inductive plasma operating with a planar coil in the pressure regime between $1*10^{-3}$- $1*10^{-2}$ mbar was difficult to realize. Many times, the plasma was breaking down due to various technical issues, which are not further discussed here.

8.2 Thermogravimetric and XPS investigation of the precursor materials

Metal acetylacetonates are commonly used as precursors in chemical vapor deposition processes since they are stable in air and readily soluble in organic solvents. Metal acetylacetonates are complexes where the metal is coordinated by two oxygen atoms to form a chelate ring. The chemical structure of the acetlyacetonate ligand is illustrated in Figure 8.7.

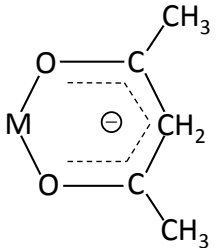

Figure 8.7. Chemical structure of the acetylacetonate ligand.

The chemical composition and purity of all precursor powders were verified with XPS. Figure 8.8 compares the survey scans of $Cu(acac)_2$, $Ni(acac)_2$, $Co(acac)_3$ and $Fe(acac)_3$. The survey

scans confirm, that the precursor powders are of high purity. Beside the XPS signals originating from the indium foil, which was used as a substrate, only the specific transition metal, carbon and oxygen were detectable. All spectra were calibrated to the C 1s peak of C-C/C-H species located at a binding energy of 284.8 eV and the O 1s spectra were calibrated to the O 1s peak of In-O at 530 eV. With regard to the chemical structure of the acetylacetonate ligand, one would expect three C 1s peaks according to C-H/C-C, C-O, C=O and three O 1s peaks representing C=O,C-O and M-O in XPS. Depending on the chemical environment, literature reports a certain binding energy range for each carbon functionality. Widely agreed, the C-C bond is reported at a binding energy of 284.8 eV and the C-H bond at a binding energy of 285.7 eV. [100] Ether type oxygen (C-O) is reported to have a binding energy between 286.5 eV to 286.8 eV in polymers, at 287.6 eV in $Pt(acac)_2$-loaded PAA nanofibers and at 286.4 eV in cobalt hydroxy carbonate. Carbonyl oxygen (C=O) is typically located at higher binding energies of 287.7- 287.9 eV in polymers, 288.6 eV in $Pt(acac)_2$-loaded nanofibers and at 288.0 eV in cobalt hydroxy carbonate. [100–102] Han et al. reported the C 1s spectrum of $Co(acac)_3$. They observed three C 1s peaks located at a binding energy of 284.8 eV, 286.5 eV and 288.8, which are assigned to C-C, C-O and C=O moieties. [103]

The deconvolution of the C 1s spectra of $Co(acac)_3$ (black) and $Cu(acac)_2$ (blue) is shown in Figure 8.8. Both C 1s spectra exhibit two predominant peaks, a major peak at 284.8 eV due to C-H/C-C bonds and a less intense peak, which is located at a binding energy of 287.0 eV in case of $Co(acac)_3$ and at a binding energy of 287.7 eV in case of $Cu(acac)_3$. The less intense C 1s peak represents a superposition of two peaks attributed to C-O and C=O species. The O 1s spectra of $Co(acac)_3$ (black) and $Cu(acac)_2$ (blue) confirm the presence of C-O moieties by the O 1s peak at a binding energy of 532.4 eV, which is close to the binding energy of 532.7 eV reported for C-O species in $Co(acac)_3$ by Han et al. The O 1s peak representing C=O species is not as predominant in the spectrum of $Co(acac)_3$ as for $Cu(acac)_2$. The O 1s line of $Cu(acac)_2$ identifies C=O by an additional feature at 531.4 eV.

Although Ni and Fe are also coordinated by acetylacetonate ligands, the C 1s spectra of $Ni(acac)_2$ (red) and $Fe(acac)_3$ (magenta) differ from the one of $Co(acac)_3$ and $Cu(acac)_2$. The C 1s lines comprise of three peaks with similar intensity located at 284.8 eV, 286.6 eV and 288.9 eV in case of $Ni(acac)_2$ and at 284.8 eV, 286.9 eV and 288.9 eV in case of $Fe(acac)_3$. These C 1s features are mainly attributed to the presence of C-C/C-H, C-O and C=O moieties but also the presence of carboxylate moieties have to be considered. The associated O 1s lines identify the presence of carboxylate moieties by the peak at a binding energy of 534 eV. The more pronounced C=O peak in the C 1s spectra as well as the increased amount of carboxylate moieties indicate, that the $Ni(acac)_2$ and $Fe(acac)_3$ precursors are partly decomposed. The appearance of the C=O feature may be attributed to a decreased delocalisation of the electrons in the chelate system due to the decomposition into carboxylate. It has to be mentioned, that the precursor powders were not stored under inert atmosphere. They have been exposed to air for at least three months before the XPS characterization was carried out, since this represents the time period in which the powder was typically depleted. It can be concluded, that although the $Co(acac)_3$ and $Cu(acac)_2$ are less air sensitive than $Ni(acac)_2$ and $Fe(acac)_3$, none of the precursors is fully decomposed and all of them can still be used. An advantage of the metal chelats is that they are often more volatile than

the inorganic derivate (e.g. metal chlorides) of the same metal but not as toxic as organometallic compounds in which the metal center is coordinated by carbon atoms. [104]

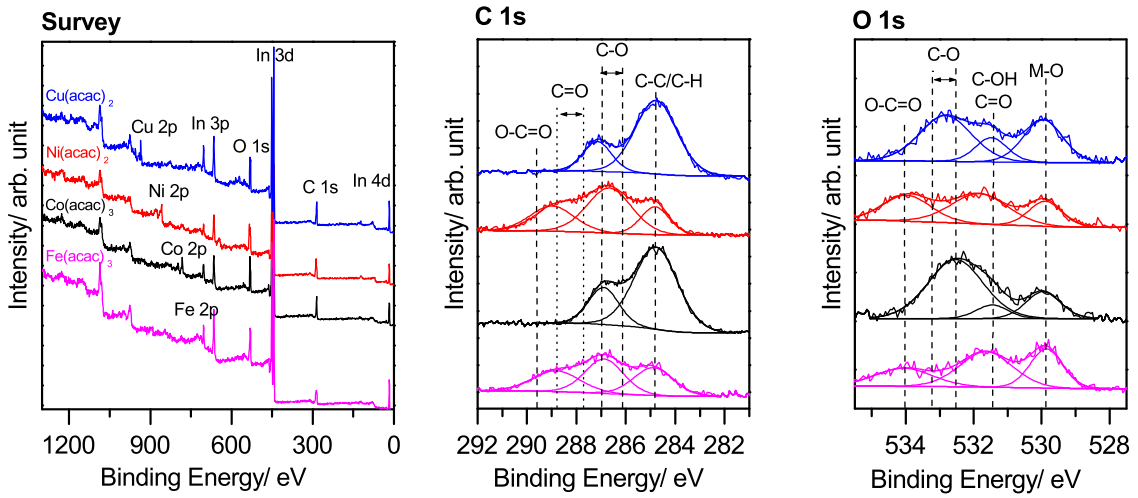

Figure 8.8. XPS characterization of $Cu(acac)_2$ (*blue*), $Ni(acac)_2$ (*red*), $Co(acac)_3$ (*black*) and $Fe(acac)_3$ (*magenta*) including a survey scan and detail spectra of the C 1s and O 1s region. All spectra are calibrated to the C 1s peak at 284.8 eV.

The evaporation temperature of the precursor material is one of the main parameters, which determines the success of the deposition. In ideal case, the precursor is evaporated without decomposing.mTherefore, the evaporation process of the precursors was studied using thermogravimetric analysis (TGA) in combination with differential thermal analysis (DTA).
While TG detects the mass loss as a function of temperature, the DT registers material changes like crystallization and melting by measuring the temperature difference with respect to the reference sample. The weight loss curves give information on the thermal stability of the precursor and the starting temperature of the evaporation process can be determined. From TGA theory, a linear mass loss is expected for a simple one step evaporation whereby no residuals should remain. [105] Figure 8.9 presents the thermograms, recorded in a non-isothermal mode, of all characterized precursor materials: $Co(acac)_3$, $Ni(acac)_2$, $Fe(acac)_3$ and $Cu(acac)_2$. $Co(acac)_3$, $Ni(acac)_2$, and $Fe(acac)_3$ are found to evaporate in a multi step process leaving residual masses of 21 %, 25.5 % and 18 %. The different evaporation steps are observed most clearly in the TG-DTA curve of $Ni(acac)_2$ (Figure 8.9 b), where each mass loss is followed by an isothermal plateau and confirmed by an endothermal peak in the DTA. Siddiqi et al. reported in agreement with our findings a three step evaporation for $Ni(acac)_3$ leaving a residual mass of 23.4 %. [105] The first mass loss in the TG of $Ni(acac)_2$ of 14.39 % correspond to the molar mass of two water molecules, what identifies the formation of hydrates due to the air sensitivity. It was reported earlier, that anhydrous $Ni(acac)_2$ tends to form hydrates. Hereby each $Ni(acac)_2$ forms an octahedral complex with two water molecules. [106] Only the thermogram of $Cu(acac)_2$ shows a linear mass loss with a small residual mass of 6.7 %. In general, the presence of a residual mass and a non linear curve indicate that the evaporation process is accompanied by decomposition reactions. It can be concluded, that the precursors are not thermally stable in the complete temperature range from 25 °C to 700 °C. Also the in literature reported TGA investigations of $Co(acac)_3$, $Fe(acac)_3$ and

$Cu(acac)_2$ indicate that the precursors thermally decompose during evaporation. [105, 107] Since the precursor should ideally be evaporated without decomposition, an evaporation temperature was chosen from the regime where the sublimation just started, as marked in the figures.

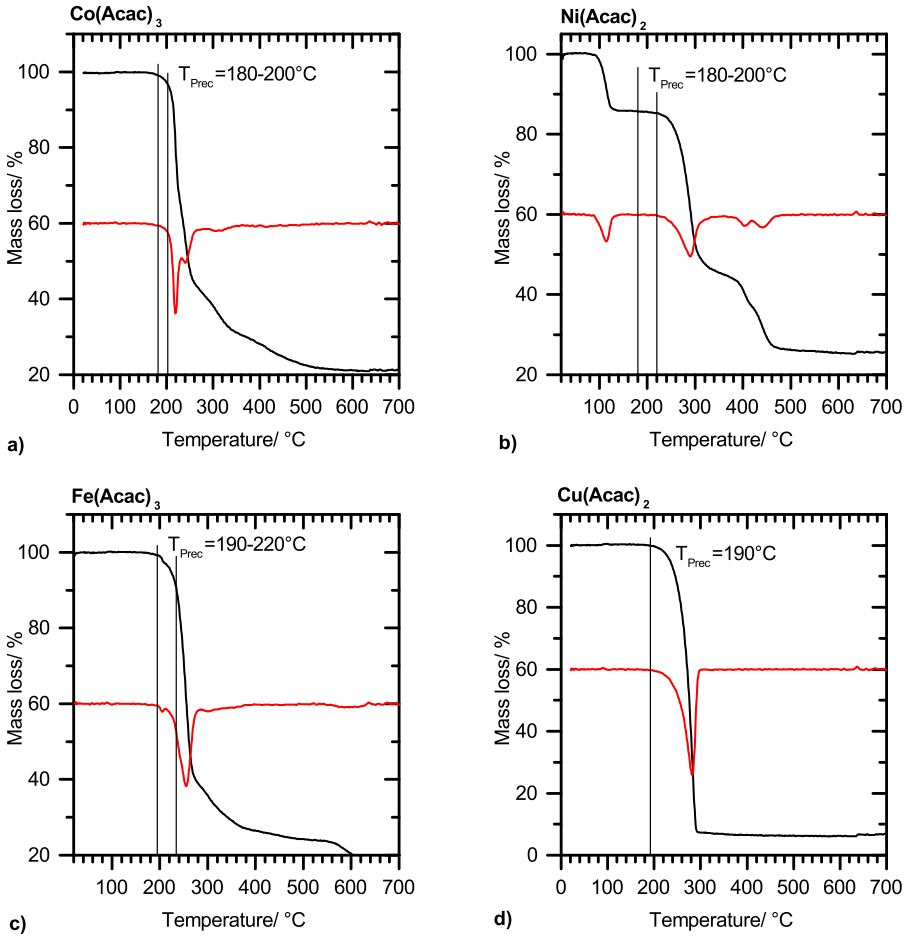

Figure 8.9. TG (*black*) and DT (*red*) curves of a) $Co(acac)_3$, b) $Ni(acac)_2$, c) $Fe(acac)_3$ and d) $Cu(acac)_2$. The DT curve is plotted as arbitrary units in the diagrams.

8.3 Deposition of CoO_x and $CoO_x(OH)_y$ films

Although it is known from literature, that binary catalysts like $CoNiO_x$ and $NiFeO_x$ are more active than the pure metal oxides, we first start to investigate the electrochemical properties and the electronic structure of the pure cobalt catalysts in detail. This is important due to the complexity of the mixed metal oxides XPS spectra for assigning the spectral features. Even more important is the expectation that it provides the basis to understand the influence of a second metal like Ni and Fe on the electrochemical behavior of a CoO_x and $CoO_x(OH)_y$ catalyst.

8.3.1 Decomposition of $Co(Acac)_3$ and the resulting chemical composition

8.3.1.1 Thermal operation mode

Although the final goal is to develop a low temperature PECVD process, the thermal deposition of CoO_x/Ti was investigated first since the process is commonly known and well studied. Table 8.1

summarizes the various deposition parameters of the thermal CVD deposited CoO_x/Ti samples. As a starting point, the first deposition (CoO_x/Ti-S3) was performed choosing a precursor temperature of 190 °C, a deposition time of 5 min and an argon/air ratio of 0.5.

Table 8.1. Preparation parameters of the first experimental set of thermal deposited CoO_x/Ti using setup B.

Sample	T_{Sub} *[°C]*	T_{Prec} *[°C]*	t_{Dep} *[min]*	f_{Ar} *[sccm]*	f_{O_2} *[sccm]*	f_{Air} *[sccm]*	p_{proc} *[mtorr]*	**d** *[cm]*
S3	250	190	5	50	0	100	753	3,1
S4	350	190	5	50	0	100	-	3.1
S5	350	190	10	50	0	100	950	3.1
S6	350	190	10	50	100	0	1000	3.1
S7	350	190	10	100	100	0	1300	4.3
S8	380	195	10	100	100	0	1100	2
S9	430	195	10	100	100	0	860	2
S10	430	195	10	150	150	0	1000	2

As a first variation the substrate temperature was increased from 250 °C (CoO_x/Ti-S3) to 350 °C (CoO_x/Ti-S4) and the deposition time was set to 10 min in case of sample CoO_x/Ti-S5. Figure 8.10 a visualizes the resulting percentage shares of Co, O, C and Ti in the as deposited samples CoO_x/Ti-S3- S5. Neither increasing the substrate temperature, nor the extension of the deposition time led to an increase in the layer thickness of CoO_x. The lowered titanium concentration could be attributed to increased carbon contamination within the deposited layers arising from the incomplete decomposition of the precursor material due to an insufficient low substrate temperature. To realize a complete decomposition of the precursor, oxygen was introduced as a reactive gas with an argon/oxygen ratio of 0.5 to deposit sample CoO_x/Ti-S6. The carbon content of CoO_x/Ti-S6 was reduced to 20.7 % by using oxygen as a reactive gas. In comparison, the CoO_x/Ti-S5 film, which was deposited using air as a reactive gas showed a carbon content of 71.4 %. To enable an inductive plasma discharge in the here presented PECVD setup, a minimum argon/oxygen ratio of 1 was found to be required. Therefore, the argon/oxygen ratio of 1 was investigated depositing sample CoO_x/Ti-S7. The increase of the argon/oxygen ratio resulted in an increase of the carbon content by 40.5 % compared to CoO_x/Ti-S6. Finally, the presence of carbon contaminations could be reduced by increasing the substrate temperature from 350 °C (CoO_x/Ti-S7) to 430 °C (CoO_x/Ti-S10), whereby in case of CoO_x/Ti-S10 a cobalt concentration of 23.4% was realized.

The C 1s detail spectra of CoO_x/Ti-S4 and -S10, given in Figure 8.10 b, show both a main signal at a binding energy of 284.8 eV, which is typically assigned to C-C bonded carbon. [102] Besides the C-C bounded carbon, C-O and C=O bonds are identified at 286.2 eV and 287.8 eV for CoO_x/Ti-S4 and at 286.12 eV and 287.5 eV for CoO_x/Ti-S10. In case of CoO_x/Ti-S3 and CoO_x/Ti-S4, which were deposited using air as a reactive gas, a slight carbide formation was detected by the appearance of an additional peak at a binding energy of 281.9 eV. But beside of this, the C 1s spectra of the air deposited films agreed with the onces deposited with oxygen.

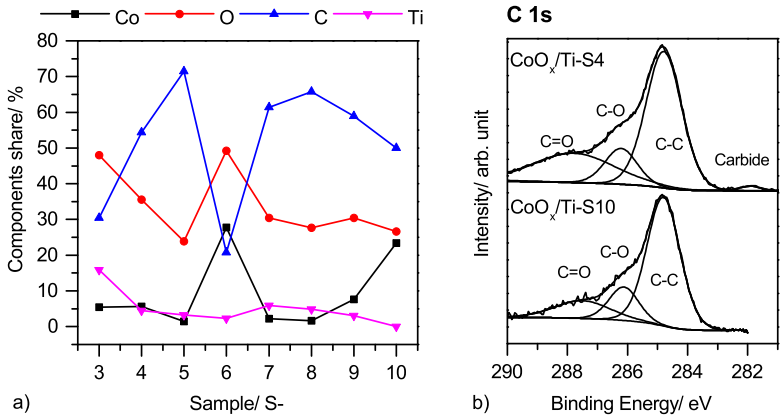

Figure 8.10. a) Comparison of the percentages of various components (C, O, Co, Ti) of thermally deposited CoO_x in dependence on the preparation conditions. b) C 1s detail spectra of thermally deposited CoO_x-S4 and CoO_x-S10.

It has to be mentioned that since the samples are not in-situ transferred into the XPS system, adventitious carbon will anyhow always be present. In summary these data show that clean and defined CoO_x layers can hardly be deposited in the temperature regime between 250-450 C ˚with the given equipment.

8.3.1.2 Plasma enhanced operation mode

Operating in plasma enhanced mode allows the use of lower substrate temperatures. While a substrate temperature of 430 ˚C was needed to thermally deposit a Co content of 22.4 %, 34.3 % were realized with a substrate temperature of only 180 ˚C operating in plasma enhanced mode. With regard to the catalysts future application, the PECVD deposition process seems to be suitable to deposit the catalyst directly onto a solar device at substrate temperatures between 150-200 ˚C. Table 8.2 summarizes the preparation parameters of the first experimental set of PECVD using setup B. The resulting atomic concentrations of Co, O, C and Ti are plotted for selected samples in Figure 8.11 a.

Table 8.2. Preparation parameters of selected CoO_x/Ti samples of the first plasma-enhanced deposition experiments using setup B and oxygen as reactive gas.

Sample	T_{Sub} *[˚C]*	T_{Prec} *[˚C]*	t_{Dep} *[min]*	f_{Ar} *[sccm]*	f_{O_2} *[sccm]*	p_{proc} *[mtorr]*	**d** *[cm]*
S11	180	195	10	100	10	803	11.2
S12	200	195	10	100	100	890	10
S13	220	195	10	100	100	1200	10
S14	250	195	10	100	100	781	10
S14-2	250	195	10	100	100	1230	10
S15-2	300	195	10	100	100	1140	10
S13-2	220	195	10	100	100	1000	10
S37	230	180	10	200	100	1240	13.5
S38	230	180	40	200	100	1230	13.5

The plasma induced decomposition of the acetylacetonate ligands using oxygen as a reactive gas differs from the thermal decomposition. At first, the carbon content is overall lowered. It varies between 10-25 % for plasma deposited CoO_x/Ti when an argon/oxygen ratio of 1 was used and between 35-45 % using an argon/oxygen ratio of 2. But the C 1s spectra of CoO_x/Ti-S11 and CoO_x/Ti-S37 (Figure 8.11 b) show an increased intensity of the C 1s peak representing carbonyl type oxygen (C=O). While the C-C/C=O ratio in case of thermally decomposed CoO_x was between 2 and 6.4, the ratio of plasma decomposed CoO_x varied between 1.3 to 2.9 using an argon/oxygen ratio of 1. An even lower C-C/C=O ratio of 0.6 was found for the plasma induced decomposition using an argon/oxygen ratio of 2. The different C-C/C=O ratios in the deposited CoO_x films indicate variations in the decomposition mechanism.
Beside the presence of ether (C-O) and ketone (C=O) type carbon, carboxylate moieties (O-C=O) can be identified at a BE of 289.8 eV. The C 1s spectrum of CoO_x/Ti-S37 shows even minor chloride contamination arising from the etching procedure. [108] Dittmar et al. discussed the microwave plasma enhanced decomposition of $Co(acac)_3$ during the deposition of CoO_x supported on titanium. [18] By investigating the nature of the residual carbon using IR spectroscopy, they also identified C=O species as a decomposition product. Moreover they found, that the carbon content, including C=O and C-O species, decreases with increasing time of plasma treatment applying a microwave power of 120 W, an oxygen flow of 20 sccm and a final pressure of 100 Pa. [18]

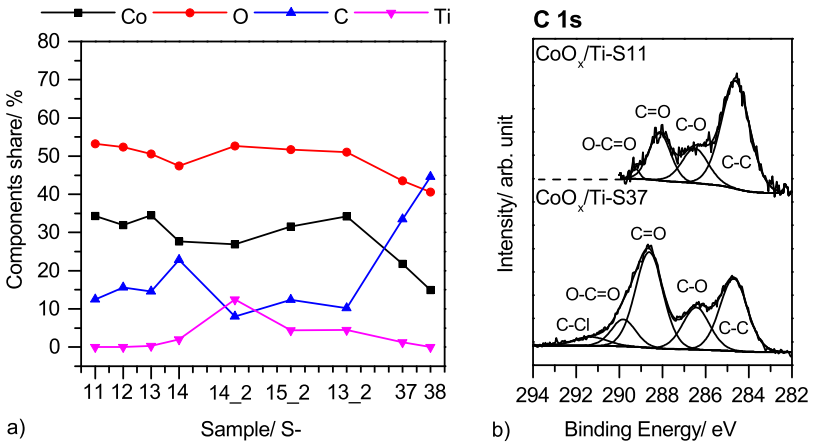

Figure 8.11. a) Comparison of the atomic concentrations of C, O, Co, Ti of plasma deposited CoO_x/Ti films in dependence on the deposition parameters using setup D. b) C 1s detail spectra of PECVD deposited CoO_x/Ti-S11 and -S37.

While CoO_x is deposited when oxygen is used as a reactive gas, the use of air as a reactive gas results in the deposition of $CoO_x(OH)_y$ films. Table 8.3 lists the various deposition parameters of the PECVD deposited $CoO_x(OH)_y$ films using air as a reactive gas. From the previous experiments, a precursor temperature of 180 °C was found to be sufficient.
Figure 8.12 shows the resulting composition of the plasma deposited $CoO_x(OH)_y$ films as well as the according C 1s spectra of samples $CoO_x(OH)_y$-S56 and -S57 for comparison. The use of air as a reactive gas results in a higher atomic concentration of carbon within the films. This indicates a less effective oxidation of the acetylacetonate ligands compared to the case when oxygen is used as reactive gas. Interestingly, the C 1s spectra of the $CoO_x(OH)_y$ films show an increased presence

of carbonyl groups and the C-C/C=O ratio varies in the range between 0.6 to 1.6, which is similar to the one reported for PECVD deposited CoO_x films using an argon/oxygen ratio of 2.

Table 8.3. Preparation parameters of selected samples of the first plasma-enhanced deposition experiments using setup B and air as reactive gas. Except of sample S56, which was deposited onto Ni, Ti-foil was used as a substrate.

Sample	T_{Sub}	T_{Prec}	t_{Dep}	f_{Ar}	f_{Air}	p_{proc}	d
	[°C]	*[°C]*	*[min]*	*[sccm]*	*[sccm]*	*[mtorr]*	*[cm]*
S33	230	180	2	200	200	-	13.5
S36-1	250	180	5	200	200	1380	13.5
S56	260	180	20	200	200	2300	13.5
S57	260	180	40	200	200	1230	13.5

Also the atomic concentration of oxygen in $CoO_x(OH)_y$ films is comparable to the one reported for PECVD deposited CoO_x using an argon/oxygen ratio of 2. It varies between 38- 47 %. In contrast, the PECVD deposited CoO_x using an argon/oxygen ratio of 1 shows an increased oxygen content of 48-53 %. It can be summarized, that the operating mode (thermal vs. plasma) as well as the choice of the reactive gas has an high impact on the resulting composition of the deposited material.

The following results presented in Chapter 8.3.3 will show, that not only the overall composition is influenced by the operation mode and the choice of reactive gas but also the resulting electronic structure. Hereafter the indices th_ and pl_ denote the operation mode applied for the deposition.

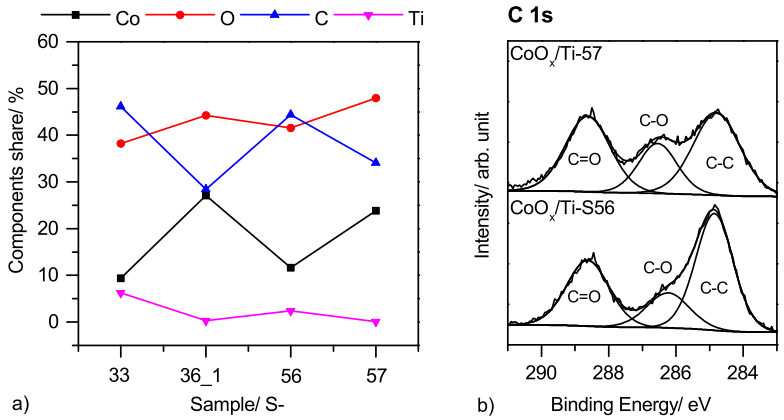

Figure 8.12. a) Comparison of the percentages of C, O, Co and Ti of plasma deposited $CoO_x(OH)_y$ films in dependence on the deposition parameters using setup D. b) C 1s detail spectra of $CoO_x(OH)_y$ films S57 and S56.

8.3.2 Determination of the deposition rate

As described in the experimental section, XPS was used as a main method to determine the layer thickness. As part of the optimization of the PECVD setup, the deposition rate of pl_CoO_x on silicon was already discussed in Chapter 8.1. Figure 8.13 a shows the layer thickness of pl_CoO_x/Ti and pl_$CoO_x(OH)_y$/Ti for different substrate temperatures. In case of pl_CoO_x, the increase of the substrate temperature results in a decrease of the growth rate from 1.7 Å/min (blue) to 1.0 Å/min

(black). The deposition of pl_$CoO_x(OH)_y$ shows an increased growth rate of 4.15 Å/min. The deposition rate of th_CoO_x is with 1.18 Å/min in the same range as the growth rate of pl_CoO_x deposited using a substrate temperature of 300 °C (Figure 8.13 b).
With respect to the different amount of carbon contaminations in dependence on the preparation method, the layer thickness can not be determined accurately with XPS since the substrate signal is not only suppressed by the pure metal oxide film but also by the carbon contaminations within the film. The most accurately calculation of the layer thickness can be done for pl_CoO_x using an Ar/O_2 ratio of 1 for two reasons. On the one hand a specific structure type can be identified in XPS as it will be discussed later. This makes the choice of an appropriate mean free path possible. On the other hand the carbon content varies only between 10-20 % with respect to the overall composition including Co, C, Ti and O. Figure 8.13 c and d show the atomic concentrations of Co, Ti, and C as a function of time for pl_CoO_x and pl_$CoO_x(OH)_y$. Especially in case of pl_$CoO_x(OH)_y$ the atomic concentration of carbon within the film increases drastically with increasing deposition time. The high degree of carbon impurities makes the accurate calculation of the layer thickness in case of pl_$CoO_x(OH)_y$ impossible.

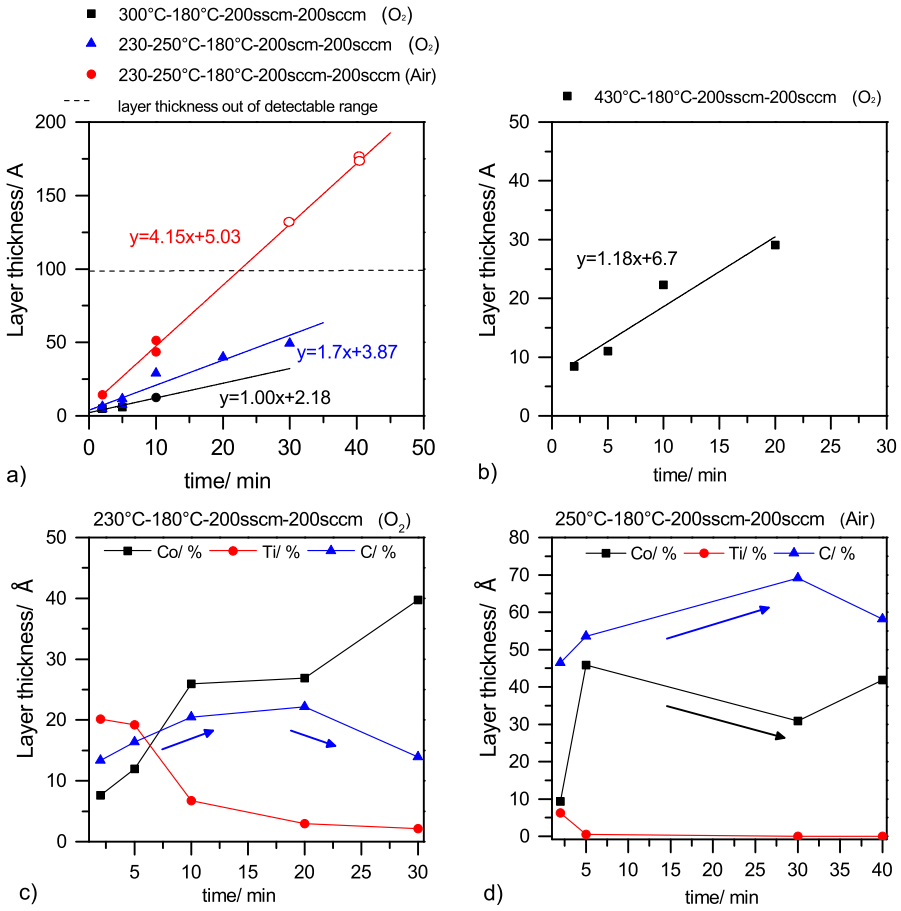

Figure 8.13. a) Plot of the layer thickness as a function of time for pl_CoO_x/Ti and b) th_CoO_x. The preparation parameters are given in the legend as the following T_{Sub}-T_{Prec}-f_{N_2}-$f_{O_2/Air}$. c) Plot of the atomic concentration of Co, Ti, C versus time of pl_CoO_x and d) of pl_$CoO_x(OH)_y$.

Since the nm-thick layers are very thin in relation to the µm roughness of the titanium substrate, the use of a profilometer did not yield any meaningful results. Indeed the layer thickness

determination with XPS does not provide absolute values, but it can be used to make a rough estimation and to compare differently deposited catalysts relative to each other.

8.3.3 XPS investigation of the electronic structure of films with $\delta > 10$ nm

The investigation of the electronic structure of the catalyst's surface is indispensable if one want to find out how to optimize the catalysts electrochemical properties. The active site is on the one hand strongly defined by the oxidation state itself and on the other hand by the morphology and structure. XPS was used as a main method to determine the oxidation state and to identify the active site. As described in the methodology (Chapter 5.3), the binding energy difference between the position of the main line to its satellite reveals the oxidation state in case of cobalt. Additional, the line shape contains information about the morphology and structure. In the O 1s line for example a high binding energy feature is discussed to represent non-stoichiometric oxygen, which would indicate a missing crystallinity. [89]
First of all, the electronic structure of catalyst films with a layer thickness of larger than 10 nm are discussed to exclude an eventual influence of the substrate on the differently deposited catalyst layers. Figure 8.14 compares the typical Co $2p_{3/2}$ lines of thermally and plasma deposited CoO_x films using oxygen as a reactive gas with the Co $2p_{3/2}$ line of plasma deposited $CoO_x(OH)_y$ using air as a reactive gas.

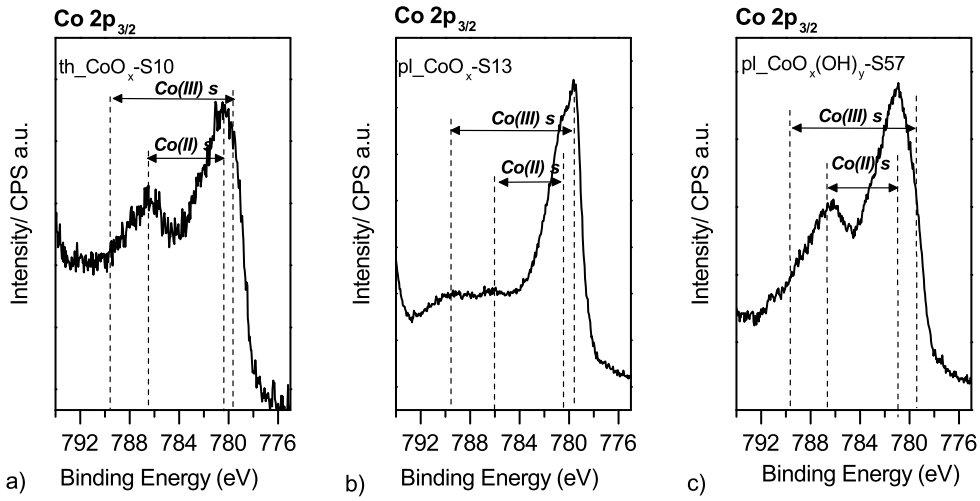

Figure 8.14. Co 2p detail spectra of a) a thermally and b) a plasma deposited CoO_x/Ti film using oxygen as a reactive gas (samples th_CoO_x/Ti-S10 and pl_CoO_x/Ti-S13) and c) a plasma deposited film using air as a reactive gas (sample pl_CoO_x/Ti-S57).

It is commonly known, that a high spin Co(II) compound exhibits an intense satellite band in a distance of 6 eV to the main line whereas a low spin Co(III) material only shows a weak satellite band in a distance of 10 eV. [87–89, 109] On the basis of the satellite bands, the oxidation states can be distinguished. In the Co $2p_{3/2}$ spectrum of th_CoO_x/Ti-S10, the main peak at a BE of 780.0 eV and the presence of a satellite band at 786.5 eV identify the oxidation state Co(II) in CoO. There is no satellite structure in a distance of 10 eV found, which would indicate the presence of Co(III).

In contrast to this, both satellites are clearly visible in the Co $2p_{3/2}$ spectrum of pl_CoO_x/Ti-S13. The double peak feature and the presence of two satellites in the Co $2p_{3/2}$ line shape indicate the formation of a spinel structure of Co_3O_4, in which both oxidation states, Co(II) and Co(III), are present. [87, 89, 90] Similar to the line shape of th_CoO_x, the Co $2p_{3/2}$ spectrum of pl_$CoO_x(OH)_y$/Ti suggests Co(II) as the predominant oxidation state. But in contrast to th_CoO_x/Ti, the Co $2p_{3/2}$ peak appears at a higher BE of 781.0 eV and the Co(II) satellite is located at a distance of only 5.5 eV to the main peak. The binding energy difference of about 1 eV with respect to the binding energy of th_CoO_x/Ti and the decreased binding energy difference of the main peak to the satellite identifies the deposition of $Co(OH)_2$ as main compound in pl_$CoO_x(OH)_y$/Ti. McIntyre et al. reported a binding energy of 780.0 eV for the Co $2p_{3/2}$ peak of CoO and of 781.0 eV for the Co $2p_{3/2}$ peak of $Co(OH)_2$. [87] In agreement with our results, the binding energy difference between the main peak and the satellite structure is reported to be 5.5 eV for $Co(OH)_2$ and between 6- 6.5 eV for CoO. [87, 91] The Co(III) satellite, which is only of weak intensity, indicates the coexistence of either Co_3O_4 or CoO(OH) in pl_$CoO_x(OH)_y$/Ti.
To further clarify the electronic structure and to distinguish between Co(II) and Co(III), the valence bands were recorded. Quiao et al. recorded spectra for Co_3O_4 and CoO and identified a sharp valence band feature at about 1.3 eV as a characteristics for the presence of Co(III). [110] In $LiCoO_2$, this sharp feature is evident arising from Co 3d $(t_{2g})^6$ valence band electrons. Figure 8.15 shows that the Co(III)-feature is observed only in the valence band of oxygen plasma deposited pl_CoO_x/Ti-S13. Since the Co 2p spectra of th_CoO_x/Ti-S10 and of pl_$CoO_x(OH)_y$/Ti-S57 identify Co(II) as the oxidation state, no $3d(t_{2g})^6$ feature is expected in their valence band spectra.

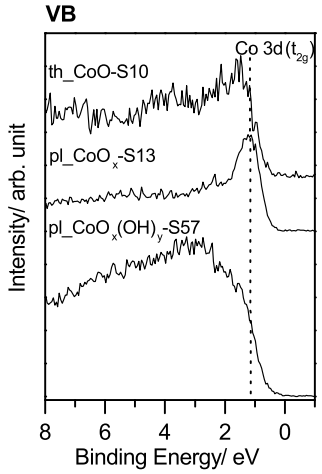

Figure 8.15. Valence band spectra of a thermal deposited film th_CoO_x/Ti-S10, a plasma deposited film using oxygen as a reactive gas pl_CoO_x/Ti-S13 and a plasma deposited film using air as a reactive gas pl_CoO_x/Ti-S57.

The associated O 1s spectra of the differently prepared cobalt oxides are presented in Figure 8.16. All O 1s spectra show the low binding energy signal positioned between of 529.6 to 529.7 eV representing the lattice metal bonded oxygen (M-O), which is in agreement with the binding energy reported in literature for CoO, Co_3O_4 and $Co(OH)_2$. [87, 89]
The high binding energy features differ from each other in dependence on the deposition method. There are some disagreements concerning the origin of the high binding energy feature (HBE) in

the O 1s region of metal oxides. On the one hand the HBE feature of in air exposed pl_CoO_x is attributed to a hydroxylation of the surface since the O 1s peak of bulk $Co(OH)_2$ is located at around 531.2 eV. [89, 90] On the other hand, it is ascribed to oxygen defects due to a missing stoichiometry. [89, 90] Concerning the studies from Petitto et al. who reported XPS spectra of the Co 2p and O 1s regions of UHV-cleaved Co_3O_4 and CoO crystals in comparison with XPS spectra after oxygen annealing, the hypothesis of assigning the HBE feature to oxygen defects makes sense. [90] If the HBE feature could only be related to a hydroxylation, one would not expect the increase of the HBE feature by annealing an UHV-cleaved crystal in pure oxygen atmosphere. Applying HREELS, they could also confirm the absence of hydroxide groups. Supporting their hypothesis, an additional phonon structure could be detected which indicated a lower symmetry of the thin film surface. In case of the here reported CVD/PECVD prepared thin film catalysts, the interpretation of the HBE feature becomes even more complex due to the presence of carbon contaminations. The C 1s spectra of all catalysts exhibit ether- and keton-type oxygen (C-O) and carbonyl oxygen (C=O), which are positioned in the O 1s spectrum in the binding energy range between 532.0 to 533.5 eV. Therefore, the HBE feature represents a superposition of two peak fits, one located at around 532.0 eV due to the carbon contamination and another at a binding energy of 531.6 eV, representing metal hydroxide species. Han et al. reported the O 1s peaks attributed to C=O and C-O in $Co(acac)_3$ at 531.3 eV and 532.7 eV. [103] Using an O 1s line fit representing the C-O species, the amount of hydroxide could be determined as described in the experimental part (Chapter 5.5). In the following discussion, the calculated area of the HBE feature represents only the amount of hydroxide since the C-O contributions are considered by the C-O fit.

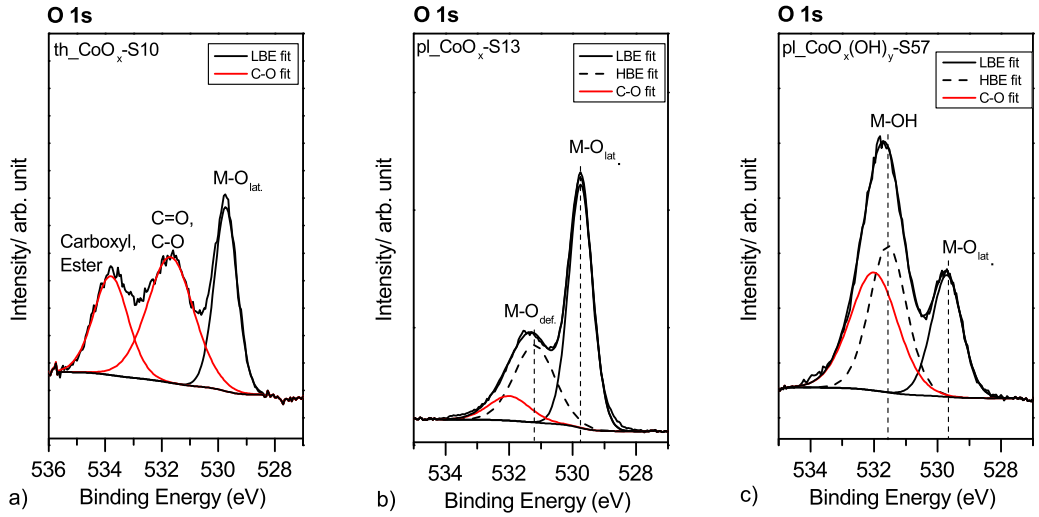

Figure 8.16. O 1s detail spectra of a) a thermally and b) a plasma deposited CoO_x/Ti film using oxygen as a reactive gas (Samples th_CoO_x/Ti-S10 and pl_CoO_x/Ti-S13) and c) a plasma deposited film using air as a reactive gas pl_$CoO_x(OH)_y$/Ti-S57.

The O 1s spectrum of th_CoO_x/Ti shows an additional O 1s feature at 533.8 eV, which is typically assigned to carboxyl and ester moieties as well as to adsorbed water. [90, 101, 103, 111] In comparison to the thermal deposition, the oxidation of the organic ligands was more efficient operating in the plasma-enhanced mode. The O 1s detail spectrum of pl_CoO_x/Ti (Figure 8.16 b) agrees well to the in literature reported O 1s spectrum of Co_3O_4. The spectrum is composed of the

O 1s peak at 529.74 eV, which is characteristic for lattice oxygen and a HBE feature at 531.3 eV which is about 35 % of the O 1s area arising from oxygen defects. In contrast to this, the HBE feature of pl_$CoO_x(OH)_y$/Ti does not mainly arise from oxygen defects. With a percentage share of about 59 % of the total O 1s area, the HBE feature is correlated to the presence of hydroxide groups. Since the Co 2p spectrum identified Co(II) as the main oxidation state, the HBE feature is correlated to the deposition of $Co(OH)_2$. The coexistence of CoO or Co_3O_4 is probable since the LBE feature is about 41 %.
Table 8.4 lists the component's area of the Co $2p_{3/2}$ and the O 1s peak, the calculated percentages of the HBE and the LBE feature as well as the calculated Co/O ratio.

Table 8.4. Calculation of the Co/O ratio using XPS determined component's intensity areas for the samples th_CoO_x/Ti-S10, pl_CoO_x/Ti-S13 and pl_$CoO_x(OH)_y$/Ti-S57. All areas are corrected for the atomic sensitvity factor (RSF), the transmission factor (TM) and the mean free path (MFP).

Sample	**A(Co $2p_{3/2}$)** *[RSF*T*MFP]*	**A(O $1s_{LBE+HBE}$)** *[RSF*T*MFP]*	**O $1s_{LBE}$** *[%]*	**O $1s_{HBE}$** *[%]*	**A(Co 2p)/A(O 1s)**
S10	226.7	274.7	100	0	0.8
S13	867.0	1202.2	65	35	0.72
S57	6893.8	3020.5	41	59	0.93

While the Co/O ratio of 0.8 of th_CoO_x/Ti is decreased compared to the ratio of stoichiometric CoO, the Co/O ratio of 0.72 in case of pl_CoO_x/Ti matches the one of Co_3O_4. In case of $Co(OH)_2$ one would expect a Co/O ratio of 0.5, this is not observed for the in air deposited pl_$CoO_x(OH)_y$/Ti. The calculated ratio of 0.93 can be explained by the coexistence of CoO and $Co(OH)_2$ since the O 1s spectrum exhibits a LBE feature of 41 % (representing CoO) and a HBE feature of 55.8 % (representing $Co(OH)_2$). Larger amounts of Co_3O_4 or CoO(OH) can be ruled out with respect to the Co(II) oxidation state being primarily present. Furthermore, the Co/O ratio is increased as the construction of the C-O fit is not as definite due to the complexity of the C 1s spectrum and uncertainties in the assignment of the carbon species. Nevertheless, the XPS detail spectra give useful information about the oxidation state and the type of oxygen bonds from which conclusions can be made about the formed phases.
In summary, the choice of reactive gas has a great impact on the resulting structure and composition in case of the PECVD deposition. While pure metal oxides are deposited when oxygen is used as a reactive gas, the use of air as a reactive gas resulted in the deposition of a metal oxide/hydroxide mixture. For completeness it should be mentioned, that a partially hydroxylation could also be realized by the PECVD deposition using an argon/oxygen ratio of 2. The similarities in the C 1s spectra and in the overall composition of these films with those deposited using air were already addressed in Chapter 8.3.1. But since these catalysts were electrochemically not as active as those deposited with air, no further efforts have been spend for their investigation and the focus was directed to the use of air as a reactive gas instead.
While the CVD deposition of CoO and Co_3O_4 is well studied, the PECVD deposition of pl_$CoO_x(OH)_y$/Ti with air as a reactive gas has not been reported yet to our knowledge.

[18, 106, 112] In general, there is not much literature reported on the PECVD deposition of cobalt oxides using acetylacetonate precursors but plasma treatments are extensively used to functionalize the surface of polymers and other materials with -NH, -OH or COOH groups using oxygen as a reactive gas. [113–115] In contrast to the effect of the reactive gas in the PECVD process, the XPS investigation of th_CoO_x/Ti films using air as a reactive gas did not significantly differ from the one of th_CoO_x/Ti using oxygen as reactive gas. Therefore, there is no need to discuss the XPS spectra separately. It should be remarked that using air as a reactive gas indeed leads to a slightly decreased amount of carbon contaminations, but the formation of hydroxides cannot be clearly identified. We did not find any literature reports on the thermal deposition of $CoO_x(OH)_y$ using $Co(acac)_3$ as a precursor in the chosen parameter range. Weiss et al. for example reported results on the addition of water to the thermal CVD process of metal oxides using acetylacetonate precursors [106] For instance, Utriainen et al. found, that the acetylacetonate precursors react with water to metal oxides in the ALD process. [116] Marzouk et al. discussed the decrease of carbon content when water was added to the CVD mixture depositing MO_x. [106, 117] Nevertheless, only few systematic studies on the decomposition of acetylacetonate ligands in the presence of water in the reactive gas are available and their results are discussed contradictory. [106] Thus, the deposition of a hydroxylated metal oxide catalyst using the PECVD process is a novel approach for the synthesis of electrocatalysts.

8.3.4 Structural evolution of CoO_x depending on the layer thickness

Differences in the thickness-dependent structural evolution of differently prepared cobalt oxides were observed with XPS. Figure 8.17 a presents the binding energy of the Co $2p_{3/2}$ peak as a function of the layer thickness of th_CoO_x, pl_CoO_x and pl_$CoO_x(OH)_y$ deposited onto Ti-foil. The percentage atomic concentration of Ti can be used as a descriptor for the layer thickness since the increase of the layer thickness results in the amplified attenuation of the Ti 2p signal. The binding energy of the Co $2p_{3/2}$ peak of th_CoO_x/Ti shifts from about 780.4- 780.6 eV down to the bulk value of 780.0 eV reported for CoO. [87, 89]

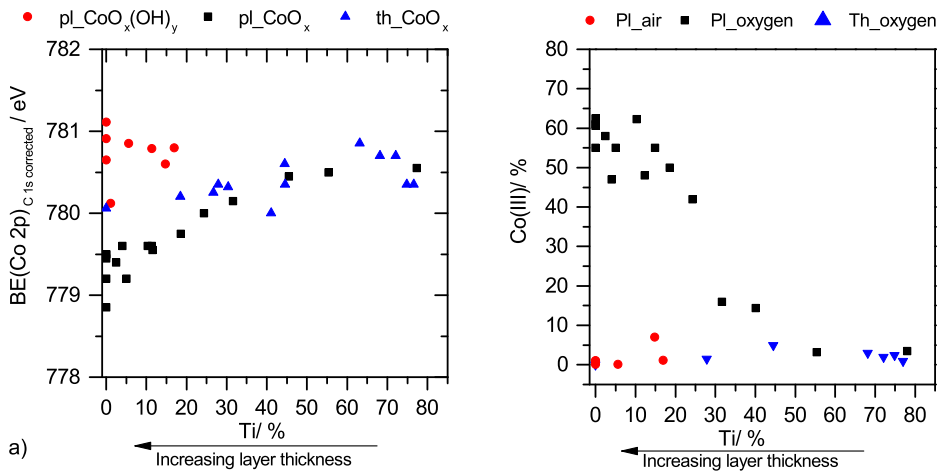

Figure 8.17. a) Binding energies of the Co $2p_{3/2}$ peak and b) calculated Co(III) content in dependence of the atomic concentration of Ti for differently prepared th_CoO_x/Ti, pl_CoO_x/Ti and pl_$CoO_x(OH)_y$/Ti films.

In agreement with the binding energy position of CoO, the Co(III) content varies independent of the layer thickness only between 1-5 % (Figure 8.17 b). In both, th_CoO_x and pl_$CoO_x(OH)_y$, the atomic concentration of Co(II) is constant and no increase in Co(III) is observed in dependence on the layer thickness. But in contrast to th_CoO_x, the binding energy of the Co $2p_{3/2}$ peak of pl_$CoO_x(OH)_y$/Ti is positioned at higher binding energy values (780.0 eV-781.2 eV) in the coverage regime 0-10 % titanium signal. In case of pl_CoO_x/Ti, the binding energy shift of the Co $2p_{3/2}$ from 780.5 eV to about 779.5 eV is not only correlated to the increasing layer thickness but also to the increase in the percentage of Co(III) from 3 % to 65 %. The higher the Co(III) content, the lower the binding energy of the Co $2p_{3/2}$. This indicate the structural evolution from CoO to Co_3O_4 in dependence on the layer thickness in case of pl_CoO_x/Ti. In the layer thickness regime below 1 nm (55 % Ti) mainly CoO is deposited with a Co(III) content below 5 %. Above a layer thickness of 1 nm, the Co(III) content increases and the BE shifts to the typical value of bulk Co_3O_4 (779.6 eV). [89]

Figure 8.18 shows the Co $2p_{3/2}$ and the valence band spectra as a function of the layer thickness exemplary for pl_CoO_x/Ti. One can clearly see, that with increasing layer thickness the Co $2p_{3/2}$ shows an additional main peak at 779.6 eV with a satellite structure at a distance of about 10 eV at 789.7 eV corresponding to the Co(III) oxidation state. In addition, the growing $3d(t_{2g})^6$ feature in the valence bond becomes more distinct attributed to the increased presence of Co(III) within the layer. The same dependence of structural evolution of the layer thickness was observed for pl_CoO_x, which was grown on n-Si substrates.

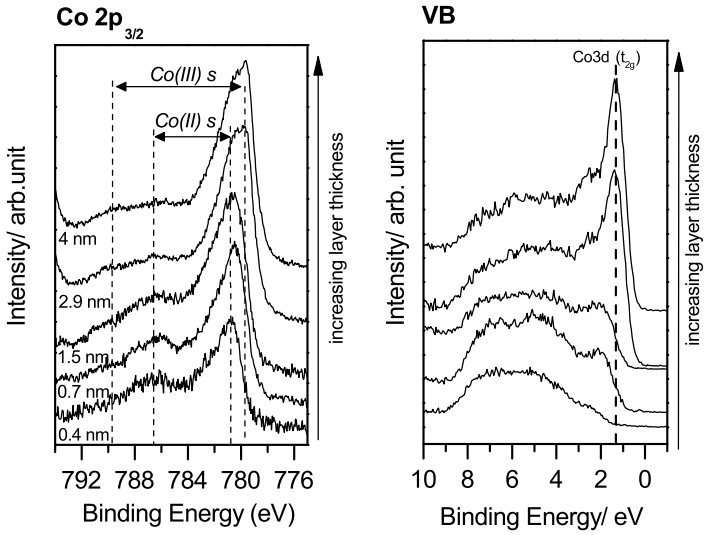

Figure 8.18. Co 2p and valence bond spectra of pl_CoO_x/Ti as a function of layer thickness.

Gragnaniello et al. investigated the thickness dependent structural evolution of cobalt oxide nanolayers on palladium (Pd(100)) by LEED and STM experiments. [118] They found that CoO_x grows in the coverage regime up to 2-3 ML in the structure of rock salt CoO. At a higher coverage above 10 ML, the growth of spinel Co_3O_4 was identified. [118] Klett et al. reported a binding energy shift of the Pt 4f line from a higher energy value of 72.4 eV down to the bulk value of 71.2 eV with increasing layer thickness when Pt was deposited on TiO_2. [119]

8.3.5 Structure and Morphology

Applying GIXRD, the PECVD deposited CoO_x and $CoO_x(OH)_y$ films using oxygen and air as a reactive gas were found to be x-ray amorphous. Figure 8.19 shows the GIXRD patterns of a 1.5 nm thick pl_CoO_x/Ti film and a 17 nm pl_$CoO_x(OH)_y$/Ti film. Diffraction peaks of brucite type β-$Co(OH)_2$ are reported at 2θ to appear at 19.0°, 32.5° and 37.8° for the (001), (100) and (101) planes (JCPDS card No. 30-0443). In case of Co_3O_4 diffraction peaks at 2θ of 31.3°, 36.8° are expected for the (220) and (311) planes (JCPDS card No. 76-1802 and 42-1467). [120,121] Neither the characteristic diffraction peaks identifying Co_3O_4, CoO nor that for $Co(OH)_2$ are found in the GIXRD patterns of pl_CoO_x and pl_$CoO_x(OH)_y$ (Figure 8.19). All of the observed diffraction peaks are attributed to Ti (JCPDS card No. 005-0682) and TiO_2 (JCPDS card No. 088-1175).

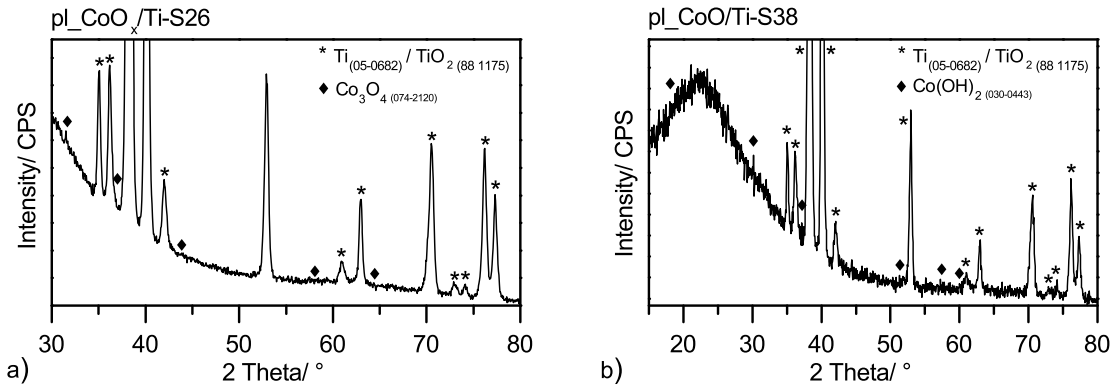

Figure 8.19. GIXRD pattern of a) pl_CoO_x/Ti-S26 (1.5 nm) and b) pl_$CoO_x(OH)_y$/Ti-S38 (17 nm).

In agreement with our results, Dittmar et al. reported that plasma-enhanced CVD deposited cobalt oxides are x-ray amorphous. They also used the $Co(acac)_3$ precursor and TiO_2 as a substrate. [18]

Figure 8.20 shows the SEM images of a 2.4 nm thin pl_CoO_x/Ti film and a 17 nm thin pl_$CoO_x(OH)_y$/Ti film in comparison to the etched titanium substrate.

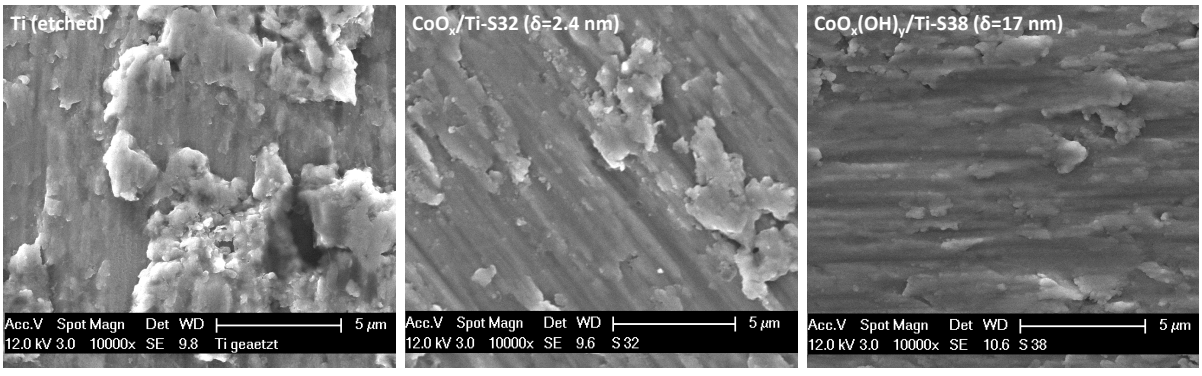

Figure 8.20. SEM images of the cleaned Ti substrate, pl_CoO_x/Ti-S32 (2.4 nm) and pl_$CoO_x(OH)_y$/Ti-S38 (17.0 nm).

Judging the SEM images with a magnification of 10000x, the surface morphology closely follows that of the pure substrate material. Also at higher magnifications no differences could be identified but the surface seems overall to be smoother after the deposition. Later it was

found, that morphological differences could be mainly observed at positions where the film was damaged. Figure 8.21 shows these differences in dependence on the preparation method. The titanium substrate itself shows a roughness in the µm range as we identify using a profilometer. The magnified SEM image of th_CoO_x/Ti shows some sponge-like structures growing out from the surface. Instead, the image of pl_CoO_x/Ti displays a structure consisting of particles in addition to the original scale structure of the substrate. Furthermore, the surface seems to be smoother after deposition. Also in case of pl_$CoO_x(OH)_y$/Ti the surface is less rough compared to the plain substrate.

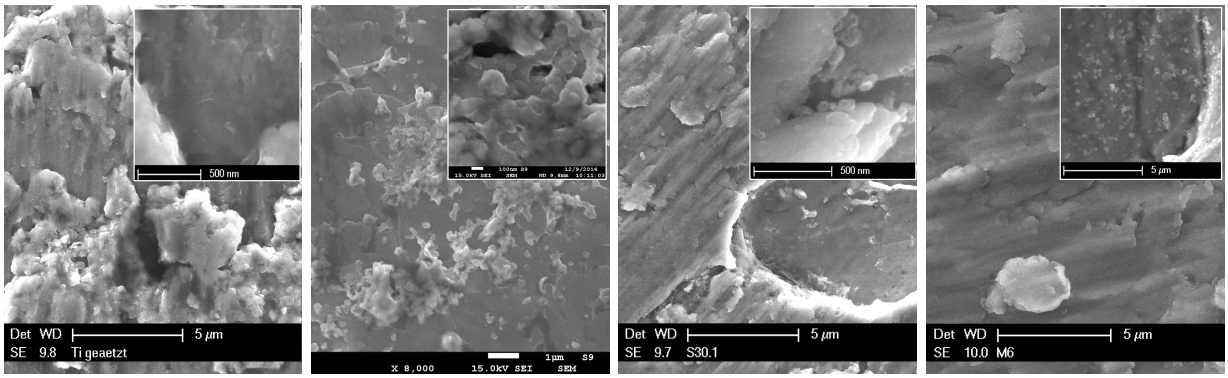

Figure 8.21. SEM images of the cleaned Ti substrate, th_CoO_x/Ti-S9 (2.2 nm), pl_CoO_x/Ti-S30_1 (2.9 nm) and pl_$CoO_x(OH)_y$/Ti-S57 (17 nm).

Due to charging effects, a higher magnification could not be resolved in case of pl_$CoO_x(OH)_y$/Ti but the SEM image taken at a position where the film was damaged show, that the film consists of a number of particles as observed for pl_CoO_x/Ti. Nevertheless, the excerpts shown here are not representative for the entire surface, the majority of the surface looks like the scale structure of titanium. Since the nanometer thick catalyst films are very thin in relation to the µm roughness of the titanium substrate, pl_CoO_x were deposited on smoother silicon substrates for comparison (Figure 8.22).

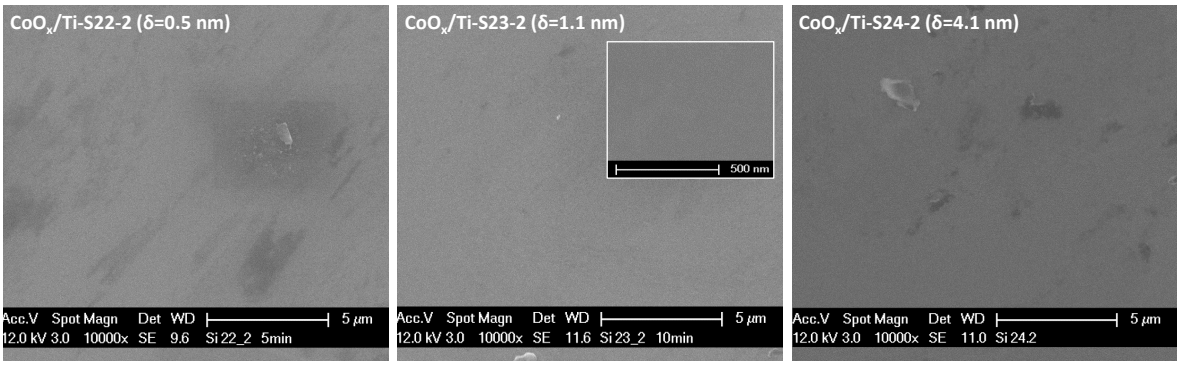

Figure 8.22. SEM images of pl_CoO_x/Si-S22_2 (δ= 0.5 nm), pl_CoO_x/Si-S23_2 (δ= 1.1 nm) and pl_CoO_x/Si-S24-2 (δ= 4.1 nm).

It can be seen, that with increasing deposition time and thickness, the coverage of the silicon substrate improves. In case of the 1.1 nm thin pl_CoO_x sample, the magnification of 10 0000x does not show any special structural features. In case of the 4.1 nm thin pl_CoO_x film, images

with higher magnification could not be resolved due to charging effects arising from the poor conductivity of the silicon substrate. It can be concluded that the x-ray amorphous films cover the surface analog to the substrate structure and the coverage seems uniform.

8.4 Deposition of NiO_x, $NiO_x(OH)_y$ and FeO_x

In the following section, the deposition of pure $NiO_x/NiO_x(OH)_y$ and FeO_x is discussed since Ni and Fe were chosen as the second metal within the bimetallic catalysts $CoMO_x$ and $CoMO_x(OH)_y$ (M= Ni, Fe). It should be remarked, that the deposition of NiO_x/Ti and $NiO_x(OH)_y$/Ti was part of a bachelor thesis and the deposition of FeO_x/Ti was part of a master thesis. [122, 123] Table 8.5 summarizes the deposition parameters.

Table 8.5. Preparation parameters of the PECVD deposition of pl_NiO_x/Ti and pl_$NiO_x(OH)_y$/Ti using setup B, whereby $Ni(acac)_2$ was introduced by the main precursor line (V1). Pl_FeO_x/Ti was deposited using setup C.

Sample	T_{Sub} *[°C]*	T_{Prec} *[°C]*	t_{Dep} *[min]*	f_{N_2} *[sccm]*	f_{O_2} *[sccm]*	f_{Air} *[sccm]*	p_{proc} *[mtorr]*	**d** *[cm]*
Ni3	260	220	10	100	0	200	-	13.5
Ni4	260	220	10	200	100	0	-	13.5
Ni5	260	220	10	200	200	0	-	13.5
Ni6	260	220	10	100	100	0	-	13.5
Ni7	260	220	5	100	100	0	-	13.5
Ni8	260	200	10	100	100	0	-	13.5
Ni9	260	200	10	100	0	100	-	13.5
Fe1	230	210	10	100	100	0	1260	13.5
Fe2	230	205	10	100	100	0	1260	13.5
Fe3	230	200	10	100	100	0	1240	13.5
Fe4	230	195	10	100	100	0	1260	13.5
Fe5	230	200	10	50	50	0	678	13.5

Since the FeO_x films showed only low catalytic activity and degraded fast during the electrochemical test, not much effort has been devoted to the optimization of the deposition. In contrast to FeO_x/Ti, NiO_x/Ti and $NiO_x(OH)_y$/Ti films showed a comparable electrochemical behavior to CoO_x/Ti and $CoO_x(OH)_y$/Ti and therefore, their preparation and characterization is discussed in the following chapters.

8.4.1 Decomposition of $Ni(acac)_3$ and $Fe(Acac)_3$ and the resulting composition

The resulting composition is plotted in Figure 8.23 for differently prepared Ni and Fe catalysts. The plasma induced decomposition of $Ni(acac)_2$ is similar to the one of $Co(acac)_3$ except that the carbon content is slightly increased when oxygen is used as a reactive gas. While the contribution of carbon in pl_CoO_x/Ti varied between 15 % to 20 %, it was between 20 % to 25 % for samples

pl_NiO_x-Ni4 and -Ni7.
As it was also observed for the deposition of pl_$CoO_x(OH)_y$/Ti, the carbon content is increased when air is used as a reactive gas in pl_$NiO_x(OH)_y$/Ti (samples pl_$NiO_x(OH)_y$/Ti-Ni3 and pl_$NiO_x(OH)_y$/Ti-Ni9). Also differences in the C 1s spectra attributed to the choice of the reactive gas were observed depositing pl_NiO_x/Ti and pl_$NiO_x(OH)_y$/Ti. The carbon content in pl_FeO_x/Ti films is comparable with the one observed in pl_NiO_x/Ti films. Due to different oxygen/metal ratio in NiO and Fe_2O_3, pl_FeO_x shows an higher oxygen content than pl_NiO_x.

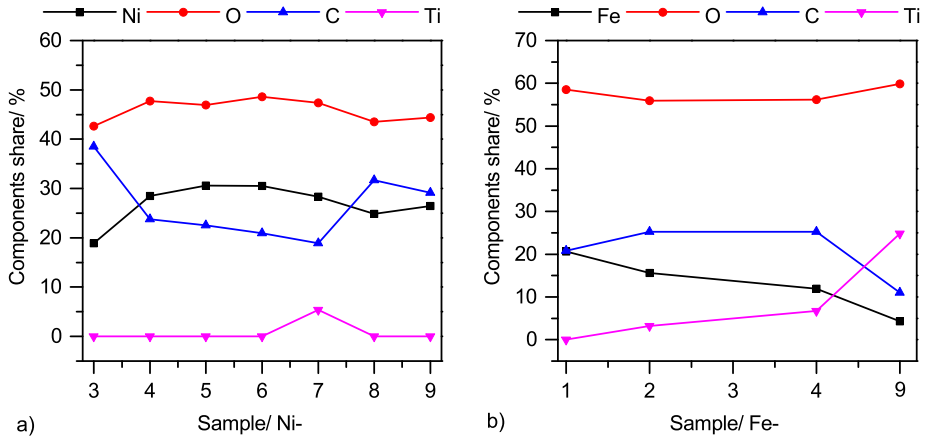

Figure 8.23. Comparison of the atomic concentration of various components (C, O, Ni/Fe, Ti) of a) pl_NiO_x/Ti and pl_$NiO_x(OH)_y$/Ti and b) of pl_FeO_x/Ti in dependence on the preparation conditions.

Since the C 1s spectra of pl_NiO_x and pl_FeO_x agree with the one observed for deposited pl_CoO_x using oxygen as a reactive gas and the C 1s spectra of pl_$NiO_x(OH)_y$ is comparable to the one observed for pl_$CoO_x(OH)_y$ using air as a reactive gas, they are not specifically discussed here.

8.4.2 Determination of the deposition rates

The deposition rates of $Ni(acac)_2$ and $Fe(acac)_3$ were investigated using the PECVD system setup C. While FeO_x/Ti films can be deposited reproducibly and the deposition rate is controllable by the precursor temperature T_{Prec} as well as by the carrier gas flow, the deposition rate of NiO_x/Ti is difficult to adjust.
Figure 8.24 a shows the deposition rates of NiO_x/Ti (black, red) and FeO_x/Ti (blue) using a precursor temperature of 200 °C and 195 °C respectively, a substrate temperature of 230 °C and a carrier gas flow of 100 sccm. The growth rate of FeO_x/Ti is with 1.92 Å/min much larger than the one of NiO_x/Ti, which is 0.43 Å/min. In case of NiO_x/Ti, the film deposited for 2 min, which represents the first deposition after the precursor was freshly filled, shows an increased layer thickness compared to the following depositions. Also a change of the precursor powder was identified: The initially fine powder was baked together after 2 min of deposition using a precursor temperature between 195-200 °C. This observation indicates the precursor‘s dehydration. It was discussed earlier, that $Ni(acac)_2$ is highly air sensitive and hydrates are formed.

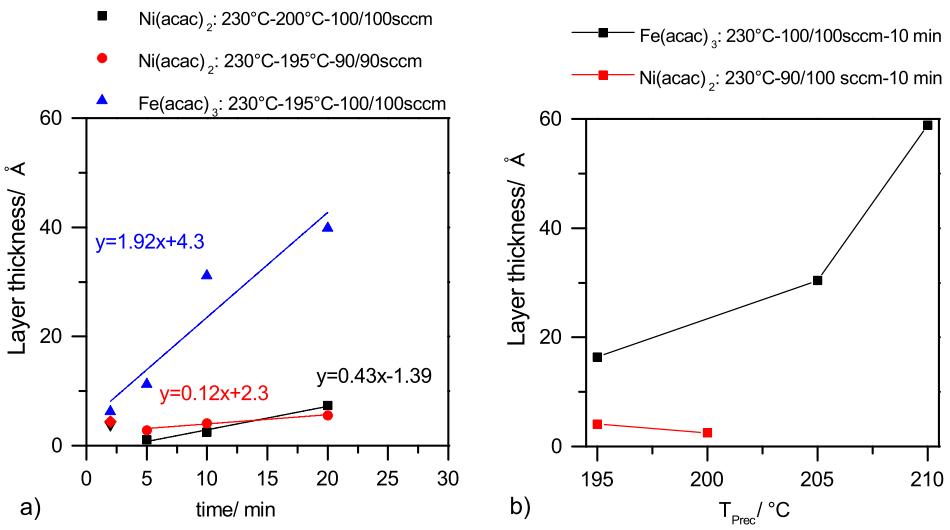

Figure 8.24. a) Deposition of pl_NiO_x/Ti (black and red) and FeO_x/Ti (blue) using different deposition times. The preparation parameters are given in the title in the following sequence: T_{Sub}-T_{Prec}-N_2/O_2 flow. b) Plot of the layer thickness depending on T_{Prec} at a deposition time of 10 min. The preparation parameters are given in the title in the following sequence: T_{Sub}-N_2/O_2 flow-t_{dep}.

As the TG has shown, water evaporates at a temperature of around 100 °C. Due to the dehydration, the octahedral $Ni(acac)_2$*H_2O has to change its coordination to form the anhydrous trimer. This may change the volatility of the precursor powder during the first deposition. Another reason for the observed reduced layer thickness could be the decreased surface area by a change in morphology.

With regard to the further goal to deposit bimetallic oxide catalysts with PECVD, the carrier gas flows of the "second" metals are limited, since a total gas flow of maximum 300 sccm can be set due to the pressure limitation by the use of plasma. To realize higher Ni contents within the layer, higher precursor temperatures have to be used even if the reproducibility is not fully guaranteed due to the dehydration of the precursor powder and the eventually staving of the precursor line. Preliminary experiments performed in setup B show, that NiO_x can be deposited also with a precursor temperature of 220 °C (Chapter 8.4.1). In contrast to NiO_x/Ti, the Fe content can be controlled by increasing the precursor temperature (Figure 8.24 b). Finally, the $Ni(acac)_2$ precursor turned out to be unsuitable since the deposition rate could not be adjusted in the given parameter window. Unfortunately, there was not enough time to investigate an alternative precursor within this thesis.

8.4.3 XPS investigation of the electronic structure of NiO_x and $NiO_x(OH)_y$

As it was observed in case of the preparation of the cobalt catalysts, the deposition using air as a reactive gas results in a mixed nickel oxide/hydroxide catalyst, $NiO_x(OH)_y$, whereas the deposition using oxygen as a reactive gas leads to a nickel oxide NiO_x. The peak position of the Ni 2p line is difficult to assign to only one chemical state. Grosvenor et al. presented a detailed XPS study focusing on the differences in the multiplet splitting of NiO, $Ni(OH)_2$ and NiO(OH) as well as considering the plasmon loss structure. [124, 125] Calculating the center of gravity (CG) from the Gupta and Sen (GS) multiplets, they found that the Ni^{3+} state has a slightly increased

intensity at higher binding energies. The CG values were found at 855.3 eV for $Ni(OH)_2$ and at 855.8 eV for NiO(OH). [124] Other studies have reported binding energies of 854.6 eV for Ni^{2+} in oxides and 856.1 eV for Ni^{2+} and Ni^{3+} in hydroxides and oxyhydroxides. [124]
Differences in the line shape have to be used for the assignment. The Ni 2p line of NiO for example is characterized by a unique multiplet structure, which exhibits an intense peak feature at around 854.6 eV. The Ni 2p line of NiO(OH) can be identified by the asymmetric shape of the main peak, whereas the shape of the $Ni(OH)_2$ main peak is symmetric. Figure 8.25 compares the XPS detail spectra of the Ni $2p_{3/2}$, the O 1s and the valence band region (VB) of a typical NiO_x/Ti sample with the detail spectra of a $NiO_x(OH)_y$/Ti sample.

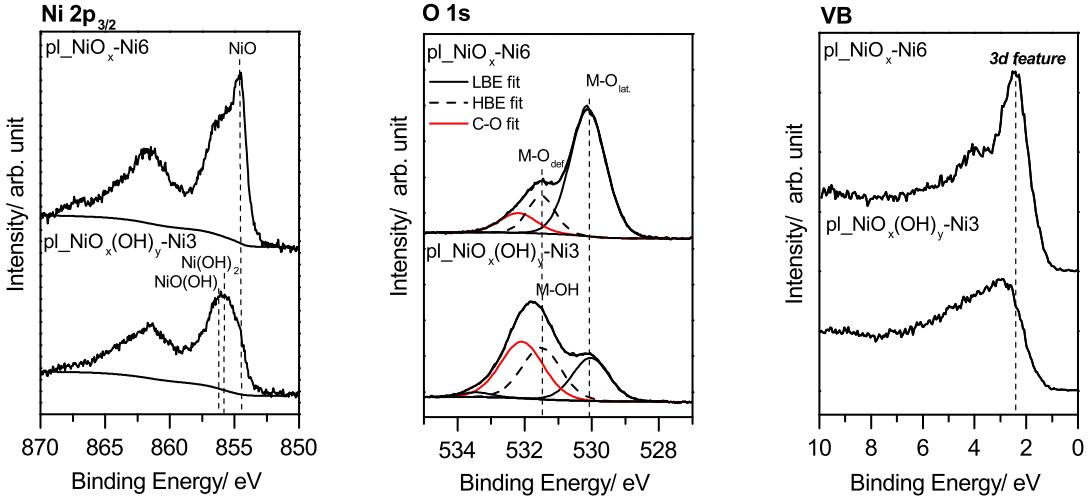

Figure 8.25. XPS details spectra of the Ni $2p_{3/2}$, the O 1s and VB region of a plasma deposited pl_NiO_x/Ti film using oxygen as a reactive gas (sample pl_NiO_x/Ti-Ni6) and of plasma deposited pl_$NiO_x(OH)_y$/Ti film using air as a reactive gas (sample pl_$NiO_x(OH)_y$/Ti-Ni3).

The Ni $2p_{3/2}$ line of NiO_x shows the unique multiplet structure of NiO and exhibits an intense peak feature at 854.5 eV. This multiplet splitting is neither observed for $Ni(OH)_2$ nor for NiO(OH). In literature the Ni $2p_{3/2}$ peak position of NiO is reported in the range of 854 eV-854.7 eV. [124, 126, 127]
The O 1s spectrum of NiO_x is composed of two peaks, a low binding energy feature (LBE) at 530.1 eV which is assigned to the lattice oxygen in NiO_x and a high binding energy feature (HBE) at 531.5 eV. The signal at 532.1 eV is attributed to carbon species, since the C 1s spectra of NiO_x and $NiO_x(OH)_y$ exhibit carbon species like C-O, C-OH and C=O. [103, 128] The lattice oxygen peak in the O 1s of polycrystalline NiO was found at 529.3 eV with a high binding energy feature at 531.1 eV by Biesinger et al. and at 529.4 eV and 531.3 eV by Ratcliff et al. [125, 127]
Similar to the O 1s spectrum of cobalt oxide, the HBE feature is discussed in literature to arise due to oxygen defects, adsorbed oxygen or to the spontaneous hydroxylation of the Ni surface. [125, 129–131] Payne et al. for example suggested the HBE to result from oxygen defects basing on the observation that the HBE feature is also present for oxide films grown in pure oxygen atmosphere. [125, 129] In agreement with the findings of Payne et al., the HBE feature of the as deposited NiO_x is found to have a maximum amount of 30 % of the total O 1s area. Hall et al. reported the formation of an 6- 8 Å thick hydroxide/oxide layer if a clean Ni-surface is exposed

to air. [130] Based on these findings, the HBE feature represents both, non-stoichiometric oxygen as well as hydroxide species. The VB line shape of NiO_x provides the intense characteristic 3d feature at 2.4 eV, which is attributed to localized Ni 3d states in NiO and a less intense O 2p peak feature at 4.3 eV. [127]

The O 1s line of $NiO_x(OH)_y$ shows a HBE feature at a binding energy of 531.4 eV, which is 56 % of the O 1s area and a LBE feature at a binding energy of 530.0 eV, which represents only 44 % of the O 1s area. The HBE feature is clearly assigned to hydroxide species as it occurs either in $Ni(OH)_2$ or in NiO(OH). The LBE feature may be attributed to the presence of NiO(OH) or NiO_x. The valence band provides a first hint that NiO(OH) was deposited because the intense Ni 3d state feature at 2.4 eV, which is characteristic for NiO, is absent. [132] Furthermore, the Ni $2p_{3/2}$ peak does not provide the multiplet structure of NiO. The maximum of the Ni $2p_{3/2}$ peak is located at 856.0 eV, which agrees to the binding energy position of NiO(OH) and $Ni(OH)_2$. Table 8.6 lists the calculated intensity percentages of the LBE and the HBE features as well as the VBM of the as deposited NiO_x and $NiO_x(OH)_y$.

Table 8.6. Binding energies for pl_NiO_x/Ti and pl_$NiO_x(OH)_y$/Ti as well as the with XPS determined components intensity areas of the HBE fit, the LBE fit and the Ni $2p_{3/2}$ and the calculated Ni/O ratio. All areas are corrected for the atomic sensitvity factor (RSF), the transmission factor (TM) and the mean free path (MFP).

Sample	**Ni $2p_{3/2}$** *[eV]*	**A(Ni $2p_{3/2}$)** *[RSF*T*MFP]*	**A(O $1s_{LBE+HBE}$)** *[RSF*T*MFP]*	**O $1s_{LBE}$** *[%]*	**O $1s_{HBE}$** *[%]*	**Ni/O**	**VBM** *[eV]*
Ni6	854.5	4700.0	6555.5	81	19	0.7	1.3
Ni3	856.0	3233.9	4247.9	44	56	0.8	1.4

The construction of difference spectra offers another approach to identify differences in the line shape. Figure 8.26 a shows a difference spectrum, which was calculated by subtracting the Ni $2p_{3/2}$ line of pl_NiO_x/Ti from the Ni $2p_{3/2}$ spectrum of pl_$NiO_x(OH)_y$/Ti. One can clearly see, that the typical NiO peak feature at 854.5 eV appears as a strong negative signal in the difference spectrum confirming the deposition of a $NiO(OH)/Ni(OH)_2$ phase.

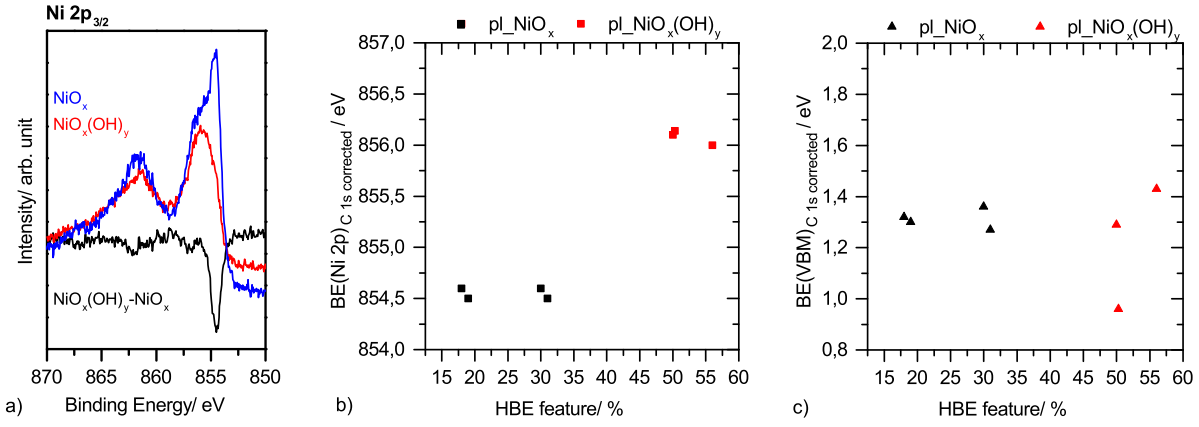

Figure 8.26. a) Difference spectrum of pl_NiO_x/Ti and pl_$NiO_x(OH)_y$/Ti. b) Plot of the Ni $2p_{3/2}$ binding energy versus the amount of the HBE O 1s feature. c) VBM of pl_NiO_x/Ti and pl_$NiO_x(OH)_y$/Ti films.

As an overview, Figure 8.26 b plots the binding energies of the differently prepared NiO_x/Ti and $NiO_x(OH)_y$/Ti films (Table 8.5) in dependence on their percentage of the HBE feature. The Ni $2p_{3/2}$ main peak of all four NiO_x/Ti films is located at around 854.5 eV when oxygen was used as a reactive gas. In agreement with the binding energy reported for NiO(OH), the Ni $2p_{3/2}$ peak of the in air deposited $NiO_x(OH)_y$ films has a binding energy of about 856.0 eV. Compared to the VBM of pl_CoO_x/Ti and pl_$CoO_x(OH)_y$/Ti, which varied between 0.4 and 0.9 eV, the VBM of the pl_NiO_x/Ti and pl_$NiO_x(OH)_y$/Ti films are located at higher binding energy values between 0.9 eV to 1.42 eV (Figure 8.26 c).

8.4.4 XPS investigation of the electronic structure of FeO_x

The PECVD deposited pl_FeO_x/Ti is identified as Fe_2O_3 with XPS. It has been previously reported that the Fe $2p_{3/2}$ line of Fe_2O_3 exhibits an emission line at a binding energy between 710.6 eV and 711.2 eV and a satellite structure at a distance of 8.5 eV, which is attributed to the presence of Fe(III). [133, 134] The O 1s line of Fe_2O_3 shows an emission line representing lattice oxygen at a binding energy of 529.9 eV. [134] As in the case of cobalt, differences in the satellite structure can be used to distinguish between the oxidation states and to identify the catalysts structure. In contrast to the Fe $2p_{3/2}$ line of Fe_2O_3, the Fe $2p_{3/2}$ line of Fe_3O_4 does not show a satellite structure. The Fe $2p_{3/2}$ line of FeO however exhibits a satellite structure at a distance of approximately 6 eV due to the presence of Fe(II). [133, 135, 136] Figure 8.27 shows the XPS detail spectra of the Fe $2p_{3/2}$, O 1s and VB regions of pl_FeO_x. In agreement with the Fe 2p line of Fe_2O_3, the Fe 2p peak is located at a binding energy of 710.9 eV showing a satellite feature at a binding energy of 719.4 eV. The associated O 1s peak for lattice oxygen is positioned at a binding energy of 529.9 eV. The valence band spectrum of Fe_2O_3 exhibits three features at binding energies of 3.0 eV, 5.3 eV and 7.8 eV. The relative energy differences of these features as well as the extended width of the valence band of about 6 eV agree with the reported values for Fe_2O_3. [134] Li et al. attributed the extension of the valence band to the strong hybridization of the Fe 3d and the O 2p states. [134] The presence of FeO can be ruled out since there is no satellite structure observed for Fe(II).

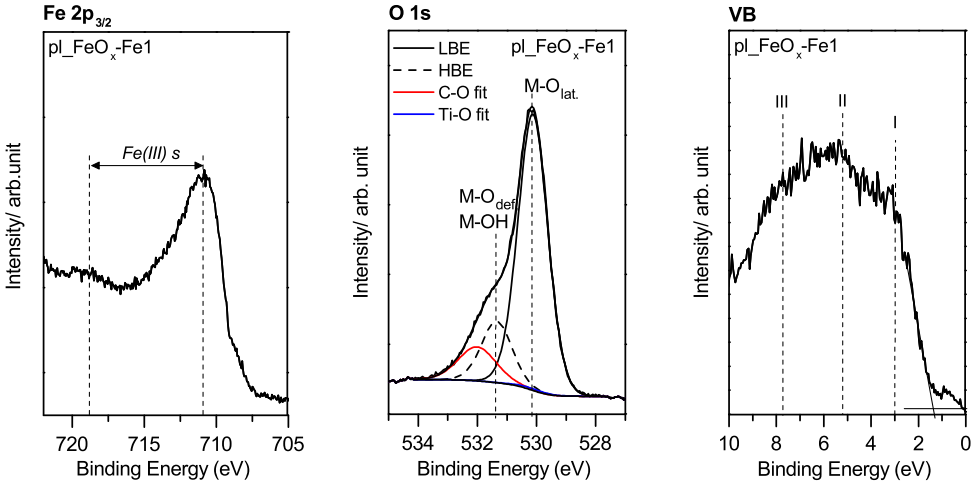

Figure 8.27. XPS detail spectra of the Fe $2p_{3/2}$, the O 1s and the VB regions of pl_FeO_x-Fe1.

8.5 Electrochemical characterization of pure metal oxides

8.5.1 The open circuit potential

The open circuit potential (OCP) is described by the difference of the electrical potential between two electrodes when no current is applied. The test protocol, which was defined by Evonik within the consortium of the SusHy project, provided a ten minutes measurement of the OCP. This time range turned out to be insufficient to detect a stable open circuit potential. Figure 8.28 shows as an example the measurement of the OCP over time for some selected CoO_x and $CoO_x(OH)_y$ electrodes.

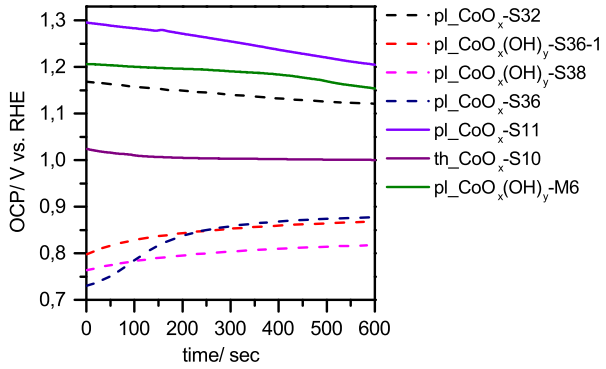

Figure 8.28. Measurement of the open circuit potential over time.

Since the OCP either increases or decreases in the chosen time range, one can not assume the electrode being in equilibrium with the electrolyte and therefore, the measured potential does not agree with the OCP yet. On the one hand, the change of the OCP versus time can be related to adsorption/ desorption processes of ions from the electrolyte to the electrodes surface and on the other hand to corrosion processes of the metal oxide itself or of the carbon impurities within the deposited catalysts. All in all, the here recorded OCP values did not give any valuable information and no correlation with the activity or the degradation behavior could be found.

8.5.2 Electrochemical impedance spectroscopy: Determination of the IR-drop

The measurement of the high-frequency electrochemical impedance spectroscopy allows the determination of the electrolyte resistance (R_E) (Chapter 6.3). Figure 8.29 a shows the Nyquist Plots, which were typically recorded in 1 M KOH and 0.1 M KOH for various single metal oxide catalysts.

In the chosen frequency range, the semi-circle is not pronounced and the electrolyte resistance R_E is derived from the intersection with the X-axis. Typically, the values of R_E vary between 5.6- 6.3 Ohm for 1 M KOH and between 47- 53 Ohm for 0.1 M KOH. Figure 8.29 b shows the R_E of various Co-, Ni- and Fe-catalysts. As expected, the R_E of 1 M KOH is independent of the deposited material and the layer thickness consistent around 6 Ω with a standard error of 0.02. The values of R_E for 0.1 M KOH show a larger scattering with a standard error of 0.19.

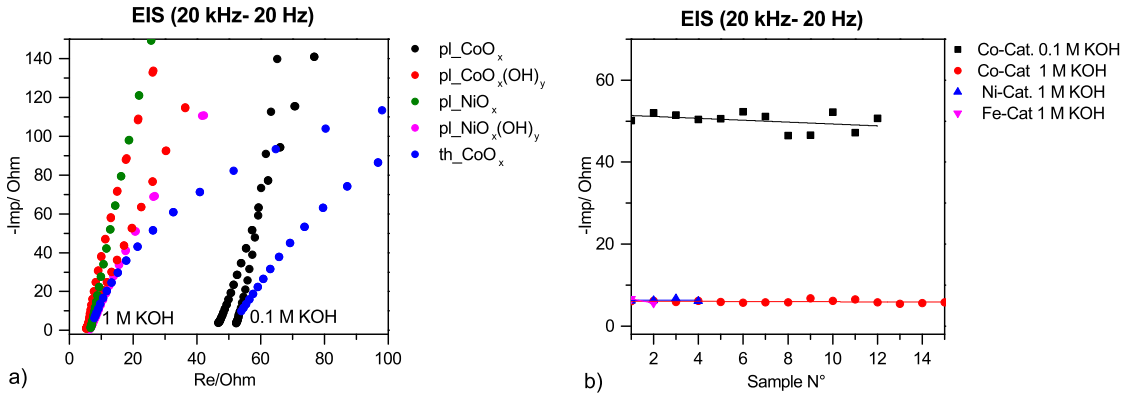

Figure 8.29. a) Nyquist Plots recorded for th_CoO_x/Ti, pl_CoO_x/Ti, pl_$CoO_x(OH)_y$/Ti, pl_NiO_x/Ti, pl_$NiO_x(OH)_y$/Ti in 1 M KOH and 0.1 M KOH. b) R_E plotted for various Co-, Ni-, Fe-catalysts.

Table 8.7 summarizes the measured electrolyte resistances for 0.1 M KOH and 1 M KOH as well as the calculated specific and molar conductivities.

Table 8.7. Seriel electrolyte resistance R_E measured by EIS as well as the calculated specific and molar conductivities σ_m and Λ for various electrolytes.

Electrolyte	$\mathbf{R_E}$ *[Ohm]*	σ_m *[S/cm]*	Λ *[S*cm²/mol]*	Λ_{Lit} *[S*cm²/mol]*
0.1 M KOH	47± 5 Ohm	0.016	160	213 [93]
1.0 M KOH	5.6± 0.5 Ohm	0.135	135	184 [24, 93]

The comparison with the measured values show, that the tabulated molar conductivities are over-estimated, since these are only valid for infinite dilution. In case of a real solution, the electrostatic ionic interaction leads to a drop in the molar conductivity.

8.5.3 Cyclic voltammetry and galvanostatic polarization: Determination of the activity and stability

Cyclic voltammograms (CV) provide information about the electrochemical activity and stability of the catalysts. Primarily the overpotential at a specified current density (2 mA/cm², 5 mA/cm² and 10 mA/cm²) was extracted from the CV as a first descriptor of the activity to compare differently prepared catalysts. Deviating from the specified test protocol, at least two CVs were recorded. Ideally, the CVs are superimposing and the electrochemical activity is constant over cycling. An increase in activity with the number of cycles mainly indicate an electrochemical induced transformation to an active species whereby a decrease of the activity is mostly correlated with a degradation process.

The following subsections discuss the influence of the preparation parameters like deposition time t_{dep}, the substrate temperature T_{Sub}, the choice of the reactive gas and the operation mode (plasma vs. thermal) on the activity of the pl_CoO_x films. Afterwards, the CVs of pure Ni and

Fe catalysts are shortly discussed since these are important for the later interpretation of the electrochemical behavior of the bimetallic catalysts.

8.5.3.1 Influence of the layer thickness

The comparison of OER catalysts is complicated since the measured current does not only depend on the catalytic activity but also on the active surface area and electron/mass properties. Thin film catalysts provide the possibility to circumvent these issues and to study the area specific electrochemical activity of different materials in detail. The layer thickness plays a critical role investigating the electrochemical activity of catalyst films. With increasing layer thickness electron/hole transport conductivity become more influential. To investigate the activity free from such current limitations, we tried to find the lowest possible layer thickness, which represents the best compromise between activity and stability.
Figure 8.30 a shows the CVs of pl_CoO_x/Ti films of various layer thicknesses. The electrochemical activity of pl_CoO_x/Ti enhances with increasing layer thickness from 4.4 Å to 7.4 Å. In case of the 4.4 Å thin layer, the current density drops off within the first CV due to a lack of stability. With respect to the lattice constants of CoO (4.25 Å) and Co_3O_4 (8.05 Å), the increase in activity can be assigned to the increase in active sites up to the coverage of a mono-layer (ML). Indeed the increase of the layer thickness from 7.4 Å to 29 Å had no remarkable positive effect on the activity, but the pl_CoO_x film having a layer thickness above 10 nm shows an improved increase in current density at a similar onset potential. Furthermore, the discrepancy between the first and the second CV diminishes what indicate a better stability. The potentiostatic scans show that the 6.1 Å thin film (S27, blue) degrades completely already within 30 sec of conditioning while the 7.4 Å thin film (S29-1, magenta) only shows a degradation slope of -0.002 mA/cm^{2}s (Figure 8.30 b).

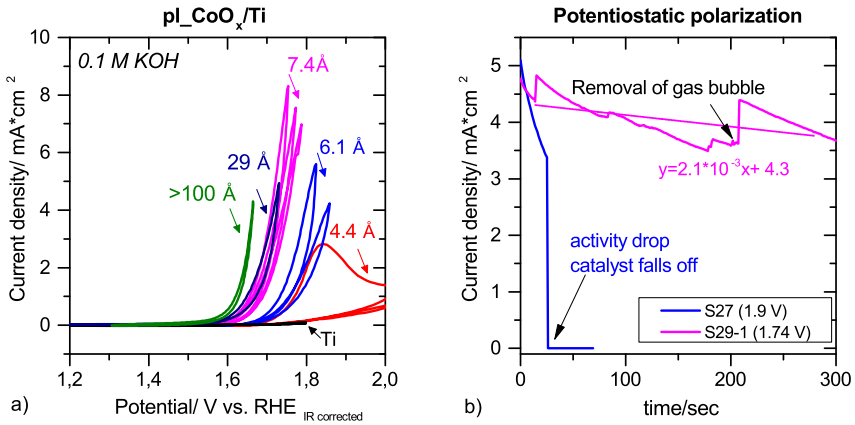

Figure 8.30. Cyclic voltammograms of a) pl_CoO_x/Ti (S25-2-*red*, S27-*blue*, S29-1-*magenta*, S30-1-*navy*, S25-*green*) as well as of the pure Ti substrate *black* and b) potentiostatic scans of the 7.4 Å pl_CoO_x/Ti thin film (magenta) compared to the 6.1 Å thin pl_CoO_x/Ti film (blue).

With consideration to the later technical application of the catalysts, the use of 1 M KOH was established in the project consortium. Figure 8.31 a shows the cyclic voltammograms of pl_CoO_x/Ti of different layer thicknesses recorded in 1 M KOH. Similar to the measurements

performed in 0.1 M KOH, the activity improves with increasing layer thickness but the catalysts are found to be less stable in 1 M KOH. Compared to the cyclic voltammograms recorded in 0.1 M KOH, the discrepancy between the first and the second cyclic voltammogram is more pronounced for the catalyst films tested in 1 M KOH having a layer thickness between 9 Å to 38 Å. Above a layer thickness of 53.5 Å, no further increase in activity is observed. The galvanostatic scans were performed at 10 mA/cm^2 and confirm that the stability improves with increasing layer thickness.

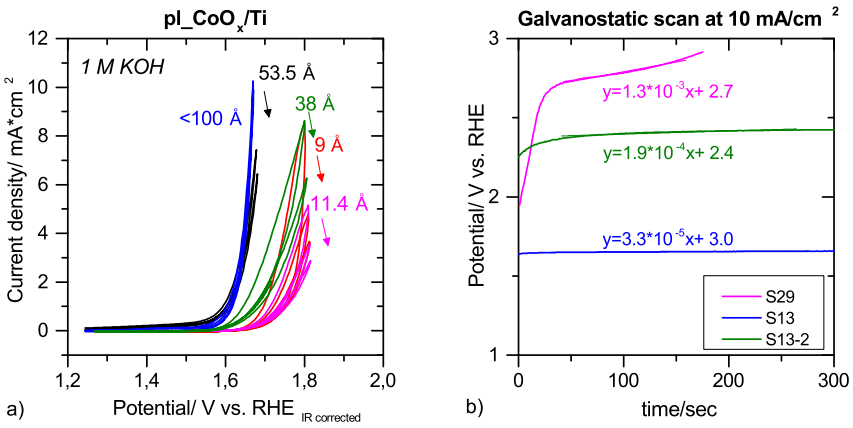

Figure 8.31. a) Cyclic voltammograms of pl_CoO$_x$ (S25-*black*, S16-*red*, S13-*blue*, S29-*magenta*, S13-2-*green*). b) Galvanostatic scans performed at a current density of 10 mA/cm^2 of the 11.4 Å (29-*magenta*), 38 Å (S13-2-*green*) and < 100 Å (S13-*blue*) thin pl_CoO$_x$/Ti samples. All catalysts were tested in 1 M KOH.

The results show, that the minimum layer thickness of 5 nm represents the best compromise between activity and stability. The all in all cell resistance determined with EIS was constant representing only the electrolyte resistance in this layer thickness regime for all samples. This means that no additional resistance attributed to the catalysts layer thickness was present. To perform other spectroscopic methods in addition to XPS, catalyst films were deposited in the layer thickness range between 2.5- 20 nm.

8.5.3.2 Influence of the substrate temperature

Figure 8.32 a presents the cyclic voltammograms of pl_CoO$_x$/Ti samples, which were deposited using different substrate temperatures. The substrate temperature of 250 °C resulted in the deposition of the most stable and active pl_CoO$_x$/Ti sample. The 2.4 nm thin film (red) shows an overpotential of 0.42 V at a current density of 2 mA/cm^2 in 0.1 KOH, which agrees with the overpotential of the pl_CoO$_x$/Ti sample (δ >10 nm) deposited at 230 °C (Figure 8.30 a). None of the pl _CoO$_x$/Ti films, which were deposited using a substrate temperature of 230 °C, were as stable and active below a layer thickness of 3 nm as it was found for the pl_CoO$_x$/Ti film deposited at 250 °C. In conclusion, the change of the substrate temperature does not have an effect on the onset potential but on the stability of the catalyst films in the chosen temperature range. Figure 8.32 b present the CVs recorded in 1 M KOH of pl_CoO$_x$/Ti samples deposited at different substrate temperatures and Figure 8.32 c shows the galvanostatic scans performed at a current density of 10 mA/cm^2. The first effect to be noticed is that the performance of the 3.8 nm thin pl_CoO$_x$/Ti sample deposited at a substrate temperature of 250 °C (blue) is worse in 1 M KOH

than the performance of the 2.4 nm sample tested in 0.1 M KOH. The decrease in current density observed after each CV indicate a lacking stability.

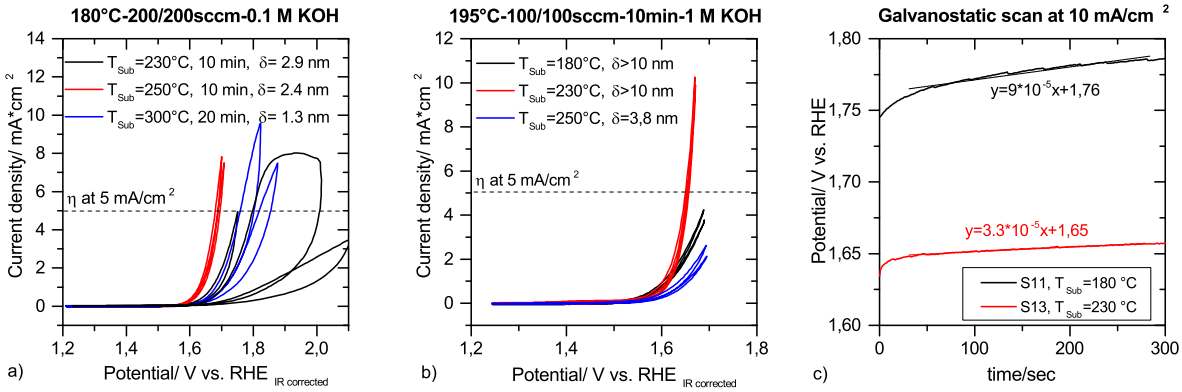

Figure 8.32. a) Cyclic voltammograms of pl_CoO_x/Ti (S30-1-*black*, S32-*red*, S41-*blue*) recorded in 0.1 M KOH and b) cyclic voltammograms of pl_CoO_x/Ti (S11-*black*, S13-*red*, S14-3-*blue*) recorded in 1 M KOH. c) Galvanostatic scans of S11-*black* and S13-*red* performed at 10 mA/cm^2 in 1 M KOH. The deposition parameters are given in the title in the following order: T_{Prec}-O_2/Ar flow-t_{Dep}.

The pl_CoO_x/Ti sample deposited at a substrate temperature of 230 ˚C has a layer thickness of greater than 10 nm and shows the overall best performance and stability with an overpotential of 0.42 V at a current density of 5 mA/cm^2 and a degradation slope of only 3.3*10^{-5} V/s. In contrast, the pl_CoO_x/Ti sample deposited at a substrate temperature of 180 ˚C shows a decreased performance with an overpotential of above 0.47 V at 5 mA/cm^2. As previously discussed, a maximum layer thickness of 5 nm is needed to guarantee a certain stability in 1 M KOH. Nevertheless, one can see that the onset potential is not strongly dependent on the substrate temperature. The galvanostatic scan of pl_CoO_x, deposited at 230 ˚C (S13, red), confirms the superior stability by a degradation slope of only 3.3 10^{-5} V/s. A degradation slope of 9 10^{-5} V/s was observed in case of pl_CoO_x deposited at 180 ˚C (S11, black). Finally, the substrate temperature has been set between 230 ˚C to 250 ˚C for the PECVD deposition of pl_CoO_x catalyst films.

8.5.3.3 Influence of the operation mode: Plasma versus thermal

The aim of this thesis was to develop a low temperature CVD process to deposit amorphous catalyst films. Especially with respect to the future goal to deposit the catalyst films directly onto solar devices, the substrate temperature has to be kept between 150 ˚C to 200 ˚C. A strategy for the realization of a low deposition temperature has been the use of a plasma-assisted oxidation process.

Thermally, the $Co(acac)_3$ precursor decomposes between 350 ˚C and 410 ˚C in nitrogen atmosphere. [19] Backman et al. reported the atomic layer deposition of CoO onto SiO_2 using $Co(acac)_2$ as a precursor. They found a substrate temperature of 450˚C sufficient in order to remove the acetylacetonate ligands by an air treatment. [137] We found that oxidation becomes more efficient with increasing substrate temperature from 350 ˚C to 430 ˚C (Chapter 8.3.1) by the decrease of carbon content from 65 to 51 % in case of thermal CVD for an Ar/O_2 ratio of 1.

Operating in the plasma enhanced mode, the acetylacetonate ligands were removed even at lower

substrate temperatures between 180 to 250 °C. In this temperature range, the carbon content varied between 10 to 30 %. Although the focus of this work is on the development of a PECVD process, it is useful to discuss the thermal deposition for comparison. Figure 8.33 a compares the cyclic voltammograms of the most active th_CoO_x/Ti sample (black) and pl_CoO_x/Ti sample (blue).

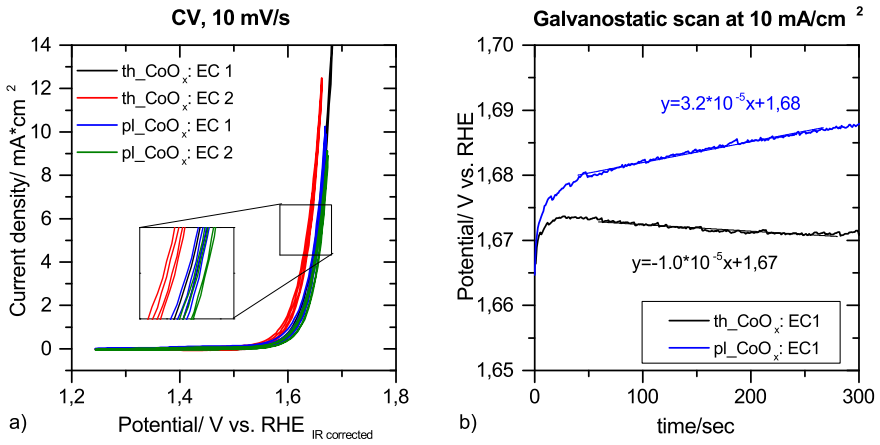

Figure 8.33. a) First (EC1) and second (EC2) cyclic voltammograms of th_CoO_x/Ti (S10:EC1-*black*, S10:EC2-*red*) and of pl_CoO_x/Ti (S13:EC1-*blue*, S13:EC2-*green*). b) Galvanostatic scans of S10-*black* and S13-*blue* performed at 10 mA/cm² in 1 M KOH.

The catalysts show a similar activity with overpotentials of 0.43 V at 5 mA/cm^2. A different behavior of the thermal and plasma deposited catalyst is observed in the galvanostatic scans (Figure 8.33 b): While the activity decreases in case of the plasma deposited catalyst (black), the activity increases in case of the thermal deposited catalyst (blue). The second performed electrochemical characterization (EC2) shows a decreased overpotential in case of the CV of th_CoO_x (red), the CV of pl_CoO_x (green) does not change remarkably. The reason for this behavior and the effect of conditioning on the electronic structure will be discussed in detail in Chapter 9.1.1. Although the overpotential of th_CoO_x is slightly decreased to 0.41 V after conditioning, the PECVD process provides a good possibility to deposit cobalt oxides with similar activity at low temperatures. As the discussion in the next chapter will show, the PECVD deposited $CoO_x(OH)_y$ films using air as a reactive gas show an improved catalytic activity. The thermal CVD process, did not result in the deposition of $CoO_x(OH)_y$ films if air was used as a reactive gas and therefore no activity enhancement was observed.

8.5.3.4 Influence of the choice of the reactive gas

Since the change of the substrate temperature did not have an remarkable impact on the catalytic behavior and the gas flows can only be varied in a small parameter window due to the instability of the induced plasma, the use of air as a reactive gas was investigated as a another strategy to optimize the pure metal oxide catalyst. The influence of the reactive gas on the electronic structure was already discussed in Chapter 8.3.3. It was found, that using air as a reactive gas leads to the deposition of pl_$CoO_x(OH)_y$ films.
Figure 8.34 a presents the cyclic voltammograms of pl_$CoO_x(OH)_y$ films deposited onto titanium

with a deposition time of 30 min (blue, 15 nm), 40 min (black, 19 nm) and onto an Ni-RDE-Tip with a deposition time of 30 min (green, 2.8 nm) in comparison to the pl_CoO_x/Ti (red) and IrO_2 (magenta) films. IrO_2 and pl_$CoO_x(OH)_y$/Ni was tested in the RDE setup of Evonik in 0.1 M KOH.

First of all, the onset potential of all pl_$CoO_x(OH)_y$ films is lowered compared to pl_CoO_x/Ti. Second, the activity increases with the layer thickness: The overpotential reduces from 0.39 V (pl_$CoO_x(OH)_y$-15 nm) to 0.36 V (pl_$CoO_x(OH)_y$-19 nm) at a current density of 5 mA/cm^2. The 19 nm thin pl_$CoO_x(OH)_y$ film shows even a higher activity than the IrO_2 reference sample of Evonik. To compare the catalyst within the project consortium, all project partners had to deposit the best catalyst onto a Ni-RDE-Tip, which was finally tested at the laboratory of Evonik. As expected, the pl_$CoO_x(OH)_y$/Ni film showed a better performance in the RDE test than the analog catalyst film in the Zahner setup, since the produced gas bubbles, which block the active centers on the surface are removed by rotating the electrode. The cyclic voltammograms of the pl_$CoO_x(OH)_y$/Ti films, which were deposited using an Ar/O_2 ratio of 0.5, are shown in Figure 8.34 b. While the overpotential of 0.44 V of the 5.1 nm film (grey) is similar to that of pl_CoO_x (η=0.43 V at 5 mA/cm^2), the activity of the 19 nm film (orange) is improved with an overpotential of only 0.39 V at a current density of 5 mA/cm^2. Nevertheless, using air as a reactive gas resulted in the most active catalyst films.

The stability of the pl_$CoO_x(OH)_y$ films was partly determined from the galvanostatic scans (Figure 8.35 a) and partly from the potentiostatic scans (Figure 8.35 b).

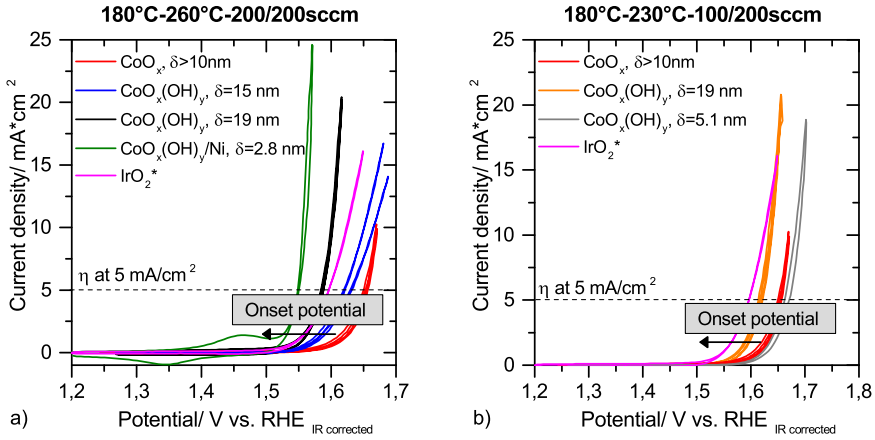

Figure 8.34. a) Cyclic voltammogram of pl_CoO_x/Ti (*S13-red*) compared to the onces of pl_$CoO_x(OH)_y$/Ti (S57-*black*, S79-*blue*) recorded in 1 M KOH using the Zahner setup. The cyclic voltammograms of IrO_2/Ni (Evonik-*magenta*) and $CoO_x(OH)_y$/Ni (S56-*green*) were tested in 0.1 M KOH in a RDE setup* at Evonik. b) Cyclic voltammograms of pl_$CoO_x(OH)_y$/Ti films (S37-*grey*, S38-*orange*) deposited using an N_2/O_2 ratio of 0.5 recorded in 1 M KOH. The deposition parameters of all pl_$CoO_x(OH)_y$ films are given in the title in the following order: T_{Prec}-T_{Sub}-Air/N_2 flow. The deposition parameters of pl_CoO_x-S13 were given in Figure 8.32 b). All CVs were recorded with a scan rate of 10 mV/s.

The galvanostatically conditioned pl_$CoO_x(OH)_y$/Ni film (green, 2.6 nm) and pl_$CoO_x(OH)_y$/Ti (blue, 15 nm) show an improved degradation slope of only 2.0*10^{-5} V/s and 2.6*10^{-5} V/s compared to the one of 3.3*10^{-5} V/s of pl_CoO_x (red, δ >10 nm). The IrO_2 film shows the best stability with a degradation slope of only 1.7*10^{-5} V/s.

Unfortunately sample pl_$CoO_x(OH)_y$/Ti-S57 (black, 19 nm) was conditioned at a too low potential

and can be therefore not directly compared to the potentiostatic scans pl_$CoO_x(OH)_y$/Ti-S38 (orange, 19 nm) and pl_$CoO_x(OH)_y$/Ti-S37 (grey, 5.1 nm). Nevertheless, one can see, that the degradation slopes of the pl_$CoO_x(OH)_y$/Ti films S37 and S38 are with a value of -5.1*10^{-3} and -3.2*10^{-3} mA/cm^2s in the same order of magnitude as the slope of the 0.7 nm thin pl_CoO_x/Ti film (-2.1*10^{-3} mA/cm^2s).

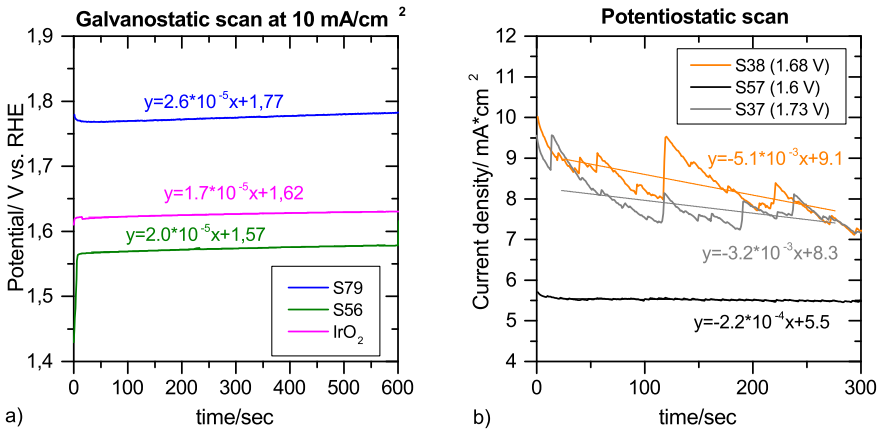

Figure 8.35. a) Galvanostatic scans of pl_$CoO_x(OH)_y$ films (S79-*blue*, S56-*black*, IrO_2-*magenta*) recorded in 1 M KOH at a current density of 10 mA/cm^2. Potentiostatic scans of pl_$CoO_x(OH)_y$ films (S38-*orange*, S57-*black* and S37-*grey*) recorded in 1 M KOH at potentials of 1.68 V, 1.6 V and 1.73 V vs. RHE.

The use of air as a reactive gas did not have a positive effect on the activity in case of the thermally deposited catalysts. Figure 8.36 a compares the cyclic voltammogram of th_CoO_x/Ti-S10 (black,>10 nm), which was deposited using oxygen as a reactive gas, with the cyclic voltammograms of th_CoO_x/Ti films of various layer thicknesses deposited using air as a reactive gas S59 (red, 1.1 nm), S61 (blue, 2.2 nm), S62 (magenta, 2.9 nm).

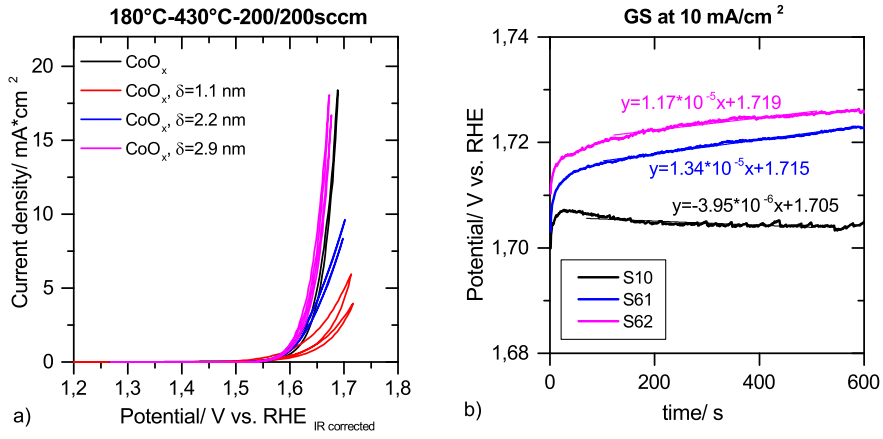

Figure 8.36. a) Cyclic voltammograms of PECVD deposited th_CoO_x/Ti (S10-*black*) using oxygen as a reactive gas in comparison to PECVD deposited th_CoO_x/Ti films (S59-*red*, S61-*blue* and S62-*magenta*) deposited using air as a reactive gas. b) Galvanostatic scans of th_CoO_x (S10-*black*), th_CoO_x (S61-*blue*) and th_CoO_x (S62-*magenta*) recorded in 1 M KOH at a current density of 10 mA/cm^2.

The 2.9 nm thin th_CoO_x/Ti-S62 film deposited with air as a reactive gas shows with an overpotential of 0.41 V at a current density of 5 mA/cm^2 a similar performance as the th_CoO_x/Ti-S10

film (0.42 V at 5 mA/cm^2), which was deposited using oxygen as a reactive gas. In contrast to the in oxygen deposited th_CoO_x films, the galvanostatic conditioning did not have an positive effect on the performance of the in air deposited films, the th_CoO_x samples directly degraded with degradation slopes of 1.34*10$^-$5 (S61) and 1.17*10^{-5} (S62) (Figure 8.36 b).

8.5.3.5 Cyclic voltammetry and galvanostatic polarization of NiO_x and FeO_x

With respect to the later goal to deposit cobalt based bimetallic catalysts, pure NiO_x and FeO_x films have to be deposited for comparison. In case of NiO_x, also the effect of the reactive gas (oxygen versus air) was studied since the pure NiO_x showed a moderate activity. Figure 8.37 a presents the cyclic voltammograms of the most active NiO_x/Ti (Ni3, black), $NiO_x(OH)_y$/Ti (Ni9, red) and FeO_x/Ti (Fe1, blue) samples recorded in 1 M KOH. As observed in case of the PECVD deposited $CoO_x(OH)_y$ films, the use of air as a reactive gas leads to the deposition of $NiO_x(OH)_y$, which is with an overpotential of 0.35 V at a current density of 5 mA/cm^2 more active than NiO_x (0.45 V at 5 mA/cm^2).
The activity of the pure FeO_x/Ti film is much lower compared to the CoO_x//Ti and NiO_x/Ti films, an overpotential of 0.49 V is needed to reach a current density of 5 mA/cm^2. Figure 8.37 b shows the associated galvanostatic scans performed at a current density of 10 mA/cm^2 in 1 M KOH. The NiO_x film degraded the most, it shows a degradation slope of 6.36*10^{-5} V/s. The degradation slope of $NiO_x(OH)_y$/Ti and FeO_x/Ti is with 1.24*10^{-5} V/s and 1.63*10^{-5} V/s comparable with that of $CoO_x(OH)_y$/Ni (2.0*10^{-5} V/s).

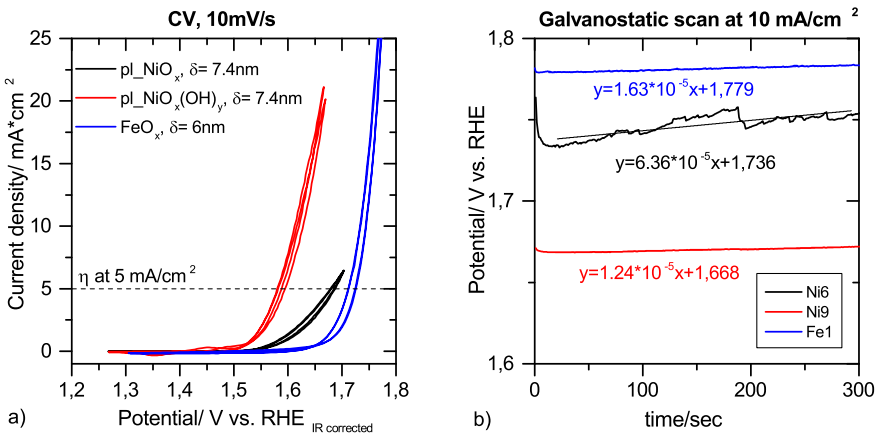

Figure 8.37. a) Cyclic voltammograms of pl_NiO_x/Ti (Ni3-*black*), pl_$NiO_x(OH)_y$/Ti (Ni9-*red*) and pl_FeO_x/Ti (Fe1-*blue*) recored in 1 M KOH with a scan rate of 10 mV/s. b) Galvanostatic scans of pl_NiO_x/Ti (Ni3-*black*), pl_$NiO_x(OH)_y$/Ti (Ni9-*red*) and pl_FeO_x/Ti (Fe1-*blue*) recorded in 1 M KOH at a current density of 10 mA/cm^2.

8.5.4 Linear Sweep measurements: Tafel slopes

Although the electrochemical test protocol included the performance of a Tafel measurement, this has only been done for the optimized active catalyst films due to time constraints. Figure 8.38 compares the Tafel plots of the most active pl_$CoO_x(OH)_y$ (red, S56), th_CoO_x (blue, S62), pl_$NiO_x(OH)_y$ (orange, Ni9) and pl_FeO_x (green, Fe1) film with the IrO_2 reference film of Evonik

(black). The linear sweep scans were recorded with a scan rate of 1 mA/cm^2 in either 1 M KOH or 0.1 M KOH.

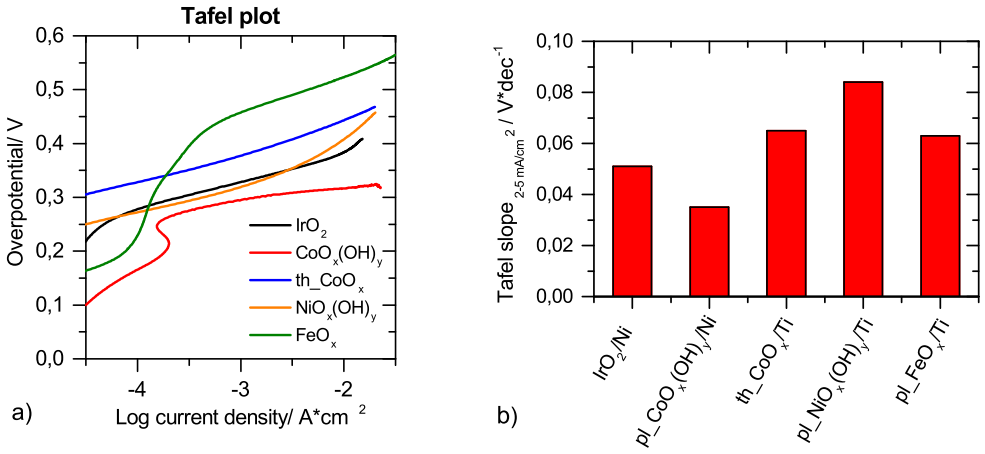

Figure 8.38. a) Tafel measurements of IrO_2 (Evonik-*black*) and pl_$CoO_x(OH)_y$/Ni (S56-*red*) recorded in 0.1 M KOH as well as of th_CoO_x/Ti (S62-*blue*), pl_$NiO_x(OH)_y$/Ti (Ni9-*orange*) and pl_FeO_x/Ti (Fe1-*green*) recorded in 1 M KOH. b) Overview of the determined Tafel slopes fitted in the current density region between 2-5 mA/cm^2.

The Tafel slope is a relevant value of the catalytic activity and was determined by a linear fit in the region between 2-5 mA/cm^2. Consistent with the voltammetry measurements, the $CoO_x(OH)_y$ shows the best activity with a Tafel slope of only 35 mV/dec. Interestingly, the highest Tafel slope (84 mV/dec) is observed for $NiO_x(OH)_y$/Ti, which is even higher than the Tafel slope of FeO_x/Ti (63 mV/dec). The $CoO_x(OH)_y$ film deposited on the Ni-RDE Tip shows even a lower Tafel slope than the IrO_2 reference sample (51 mV/dec), which was characterized by Evonik. In comparison, Trotochaud et al. reported a Tafel slope of 49 mV/dec for solution spin-cast IrO_2 and 42 mV/dec CoO_x, determined from the linear region below 1 mA/cm^2.

8.6 Overview and conclusion

Two types of catalysts were investigated: MO_x and $MO_x(OH)_y$ (M=Co, Ni, Fe). While the thermal CVD and the PECVD process result in the deposition of MO_x films when oxygen is used as a reactive gas, the deposition of $MO_x(OH)_y$ was simply realized by using air as a reactive gas in the PECVD process. The results show, that the choice of the reactive gas has an high impact on the electronic structure and also on the electrochemical activity. Figure 8.39 gives an overview of the overpotential needed at a current density of 10 mA/cm^2 of differently prepared catalysts compared to the IrO_2 reference films purchased by Metakem and Evonik.
One can clearly see the progress in optimizing the catalyst during this theses: Starting with the thermal CVD deposition process, the catalyst films required overpotentials between 0.48 and 0.41 V at a current density of 10 mA/cm^2. By attaching the RF-generator, the PECVD deposition of pl_CoO_x films at substrate temperatures below 250 °C was realized. The use of air as a reactive gas opened the possibility to deposit $CoO_x(OH)_y$ films, which had a decreased onset potential as well as lower overpotentials and Tafel slopes. Most of the pl_$CoO_x(OH)_y$ films showed a higher activity than the IrO_2 films prepared by Evonik. The RDE tested pl_$CoO_x(OH)_y$/Ni had an

activity, which was even close to the one reported for the IrO_2 electrode purchased by Metakem (0.31 V at 10 mA/cm^2).

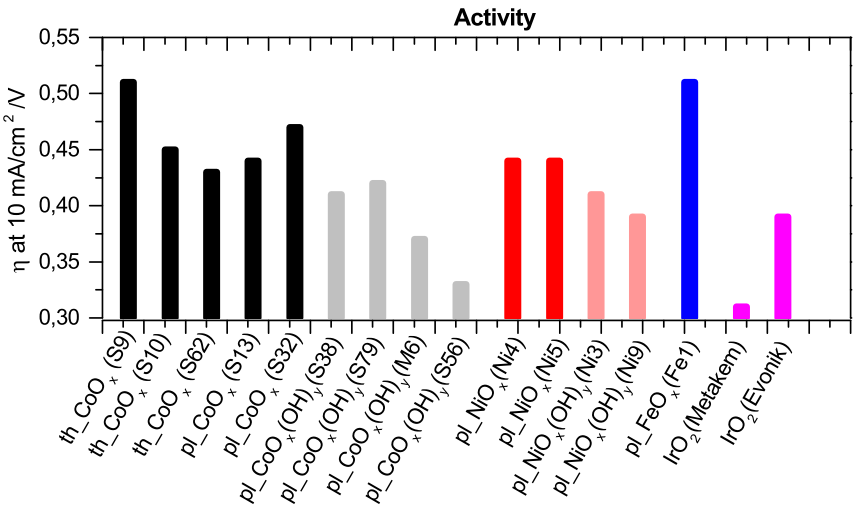

Figure 8.39. IR corrected overpotentials at 10 mA/cm^2 plotted for various catalyst films tested either in 1 M KOH or 0.1 M KOH. All the here shown catalyst films have a layer thickness above the critical layer thickness (see Chapter 8.5.3.1).

Figure 8.40 provides an literature overview of various metal oxides. The PECVD deposited pl_$CoO_x(OH)_y$ film presents one of the best cobalt catalysts. Only the Co_3O_4 nanoparticles, which were impregnated on a highly porous Ni foam, show a comparable electrochemical activity. The pl_$NiO_x(OH)_y$ films are not as active as the spin-cast NiO_x films reported by Trotochaud et al. or Stern et al. But not much effort was devoted to the optimization of the pure pl_$NiO_x(OH)_y$ films, the parameters for the deposition were only deduced from the deposition of pl_$CoO_x(OH)_y$. Nevertheless, the presented pl_$CoO_x(OH)_y$ film is with an overpotential of 0.33 V one of the best transition metal catalysts. Only the nanoparticular $Ni(OH)_2$, reported by Stern et al., has a lower overpotential of 0.299 V at 10 mA/cm^2.
With this, one can conclude, that the as deposited transition metal oxide-hydroxides show a superior catalytic activity from the beginning of the electrochemical test compared to their analog transition metal oxides. With respect to the commonly known redox behavior of transition metal oxide catalysts one must consider a potential-dependent structural change during OER. It is not guaranteed that the as deposited material represents the catalytically active catalyst. In case of th_CoO_x for example, the potential decreased during the galvanostatic conditioning. This indicate an activation process. How far the activation process is correlated to a change in the electronic structure can be identified by measuring XPS after the electrochemical testing. Furthermore, XPS measurements were performed for the MO_x and $MO_x(OH)_y$ films (M=Co, Ni) from before and after the electrochemical treatment to understand the promoting effect of the hydroxide sites on the electrochemical activity.

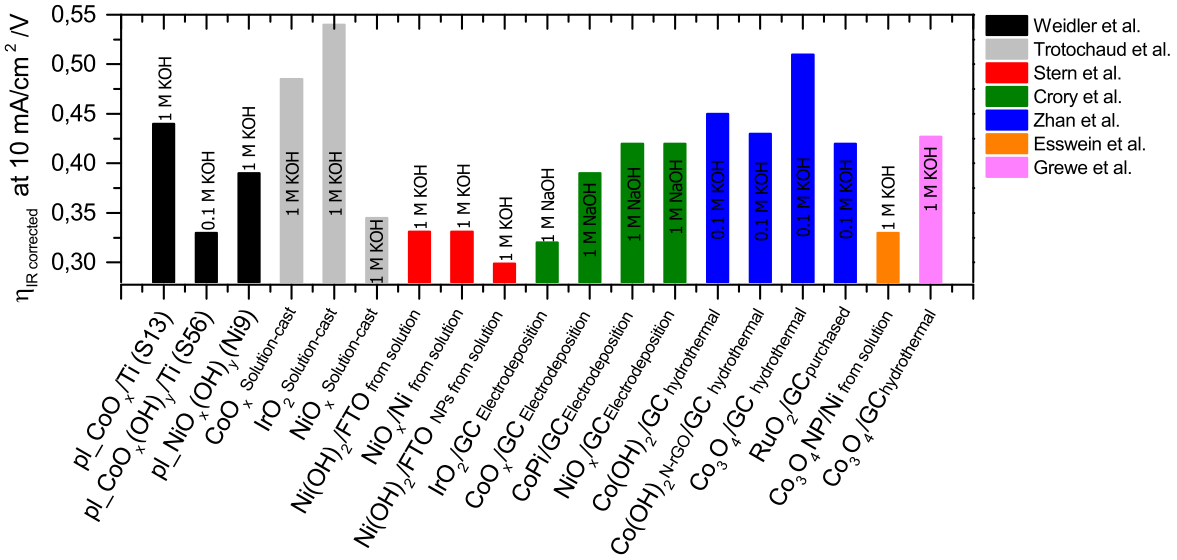

Figure 8.40. IR corrected overpotentials at 10 mA/cm^2 plotted for various catalyst films tested either in 1 M KOH or 0.1 M KOH.

In Chapter 9 I will discuss in detail the effect of the structural evolution of various single metal oxide catalysts during oxygen evolution reaction on the electrochemical activity.

9. Change of the catalyst's oxidation state and its correlation to the activity

Over the past 50 years considerable research have been focused on the investigation of the redox and electrocatalytic properties of transition metal oxides (see Chapter 3.3). The understanding of the fundamental electrochemical processes is a valuable ingredient for the systematic design and optimization of the catalysts. The characterization of the catalysts surface before and after the OER provides information about the nature of the active surface sites.

9.1 CoO_x and $CoO_x(OH)_y$: Co(III) as the active precursor oxidation state

To investigate the change of the oxidation state during the OER and its correlation to the electrochemical activity, a modified test procedure was developed (Figure 9.1). Deviating from the original test protocol, which is described in Chapter 6, no LSV was recorded and the galvanostatic scan was performed immediately after the cyclic voltammetry followed by the surface characterization with XPS. Optionally an additional CV was recorded after the galvanostatic scan. Since the concentration of the electrolyte to be used was increased during the project from 0.1 M to 1 M KOH, some catalysts were tested first in 0.1 M and then in 1 M KOH or others were directly tested in 1.0 M KOH. Nevertheless, all plots are given IR corrected to exclude the influence of the electrolyte concentration. Parts of these results were already published. [138]

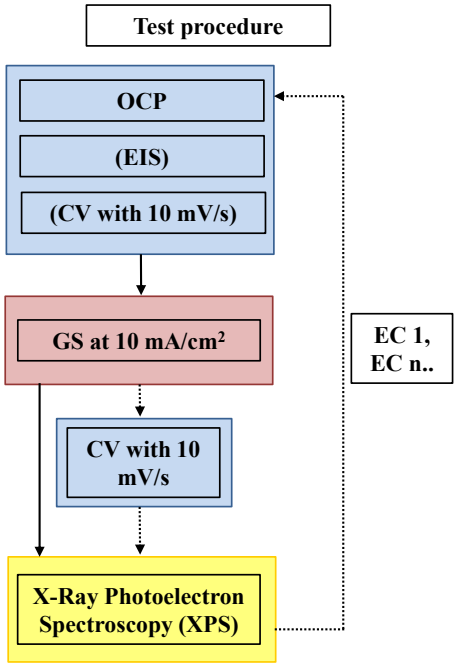

Figure 9.1. Experimental procedure to investigate the change of the oxidation state during the OER.

9.1.1 Thermally deposited th_CoO_x

The electrochemical characterization (EC) of th_CoO_x/Ti, which was already discussed in Chapter 8.5, indicated the activation of the catalyst: the recorded cyclic voltammograms did not superimpose but the second CV showed a higher current density than the first. Figure 9.2 presents the series of cyclic voltammograms recorded for the as deposited th_CoO_x film and after several conditioning steps. First, an electrochemical characterization, including the measurements of the OCP, EIS and CV was performed in 0.1 M KOH with respect to the starting conditions defined in the SuShy consortium (as deposited, red). Thereafter, the electrochemical characterizations (EC 1, EC 2 and EC 3) were carried out after the previously presented test procedure (Figure 9.1) in a technical relevant electrolyte concentration of 1 M KOH. The degradation test of EC 1 was performed in the potentiostatic mode at a potential of 1.8 V vs. RHE (EC 1) for 2 min, since this potential corresponds to the current density of 10 mA/cm^2 in the recorded CV (EC1, blue). The degradation tests of EC 2 and EC 3 however were performed in the galvanostatic mode at a current density of 10 mA/cm^2 for 10 min (EC 2) and 15 min (EC 3).
Figure 9.2 a shows, that the activity increases remarkably after the conditioning: Whereas the as deposited film requires an overpotential of 0.57 V to reach a current density of 5 mA/cm^2, the CV recorded after 2 min of potentiostatic conditioning during EC1 shows already a reduced overpotential of 0.42 V (blue). A further decrease of the overpotential is observed after ten minutes of conditioning within the EC 3 to 0.41 V (green). The CV recorded right after the 15 min galvanostatic conditioning during EC 3 (orange) does not show a further improvement. The catalytic improvement is reflected by the decrease of the onset potential from larger than 1.6 V vs. RHE (as deposited) to 1.53 V vs. RHE after an overall time of 12 min conditioning (EC 1 and EC 2). Figure 9.2 b shows a dramatic increase in current density with time for the potentiostatically performed conditioning during EC 1.

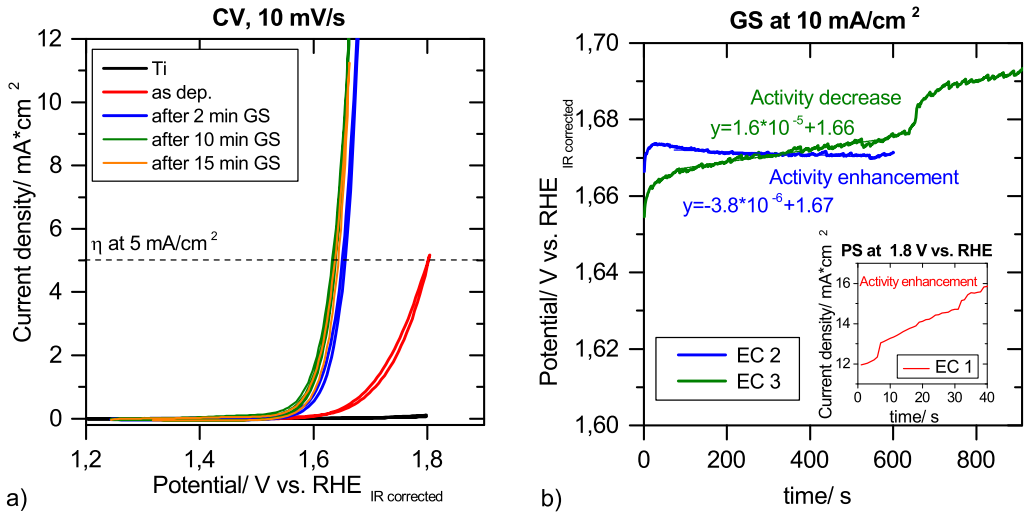

Figure 9.2. CV scans of the as deposited th_CoO_x/Ti-S10 film (red), after 2 min of potentiostatic conditioning (blue), after 10 min of galvanostatic conditioning (green) and after 15 min of galvanostatic conditioning (orange). b) Potentiostatic scans of EC 1 (blue) and galvanostatic scans of EC 2 (magenta) and EC 3 (green).

This can be attributed to the oxidation of the carbon impurities as well as to the formation of

an catalytically more active phase. Also the galvanostatic scan of EC 2 (Figure 9.2 b, magenta) shows an increase in activity with decreasing potential. In contrast to this, the potential increase, which occurred during the galvanostatic scan of EC 3 (Figure 9.2 b, green), indicates to the degradation of the catalyst itself.
The comparison of the XPS results from before and after the EC tests show, that the increase in the activity correlates with the decrease of the carbon content but also with the phase transformation from an amorphous rock salt CoO to the crystalline spinel Co_3O_4. Table 9.1 summarizes the atomic concentrations of Co, O, C and Ti, as well as the overpotential at 5 mA/cm^2 and the degradation slopes of the galvanostatic scans. The sample name th_CoO_xaECn denotes the XPS characterization, which followed the respective electrochemical test (EC1, .., ECn). First, a decrease in carbon content is evident. It reduces from 66.3% in the as deposited th_CoO_x/Ti to 20.7 % in the conditioned th_CoO_xaEC1. A further decrease is observed from 20.7 % in th_CoO_xaEC1 to 3.1 % in th_CoO_xaEC2. In agreement with the GS test of EC 3, the Ti 2p substrate signal appears after conditioning, which indicates the dissolution of the catalyst.

Table 9.1. Atomic concentration of Co, O, C and Ti as well as the overpotential at 5 mA/cm^2 and the slope of the degradation tests reported for the as deposited th_CoO_x/Ti-S10 and after conditioning.

Sample	**Co**	**O**	**C**	**Ti**	**η at 5 mA/cm^2**	**GS slope**
	[%]	*[%]*	*[%]*	*%*	*V*	*mV/s*
th_CoO_x	7.5	26.2	66.3	0	0.57	-
th_CoO_xaEC1	28.4	50.9	20.7	0	0.42	PS
th_CoO_xaEC2	31.9	65.1	3.1	0	0.41	-3.8*10^{-2}
th_CoO_xaEC3	20.4	57.5	17.2	5.0	0.41	1.6*10^{-2}

The atomic concentration of oxygen within the layer increases during conditioning. The oxygen uptake makes sense with regard to the structural change from CoO to Co_3O_4, which is clearly observable in the Co 2p detail spectra. Figure 9.3 shows the XPS detail spectra of the as deposited th_CoO_x/Ti sample and after 2 min (th_CoO_xaEC1), 12 min (th_CoO_xaEC2) and 27 min (th_CoO_xaEC3) of conditioning. The Co 2p line of the as deposited th_CoO_x/Ti shows the characteristic Co(II) satellite at a distance of 6 eV and a Co $2p_{3/2}$ peak at a binding energy of 780.36 eV, which fits well with the binding energy of CoO (See Chapter 8.3.3). The Co 2p line of th_CoO_xaEC1 identifies the oxidation of Co(II) to Co(III) by the decreased intensity of the Co(II)-satellite, the appearance of the Co(III)-satellite at around 789 eV and the binding energy shift of the Co $2p_{3/2}$ peak from 780.4 eV to 779.6 eV. The calculated Co(III) content increases with conditioning time from 0 % in the as deposited th_CoO_x/Ti to 77 % in the conditioned th_CoO_xaEC3 (Table 9.2). The increase in the Co(III) content as well as the line shape changes indicate the formation of a Co_3O_4 spinel under operating conditions. Starting from a thermally deposited Co(II) oxide, a maximum Co(III) content of 77 % was realized in the electrochemically formed Co_3O_4 during the OER.
Spectral differences can also be observed in the associated O 1s spectra. As previously discussed

in Chapter 8.3.3 the O 1s line of a as deposited CoO_x contains of two signals: A LBE signal and a HBE signal. Whereby the LBE signal is assigned to the lattice oxygen, the HBE feature is assigned either to oxygen defects or to hydroxide species. The here reported O 1s spectra all show the LBE signal at 529.6 eV ± 0.3 eV representing the lattice metal bonded oxygen (M-O). The O 1s spectrum of the as deposited th_CoO_x shows two additional peaks located at 531.7 eV and at 533.8 eV. These are mainly attributed to water and CO_x adsorbed species, since also the C 1s spectrum confirms the presence of C-O. With respect to the high degree of carbon contamination, the O 1s spectrum can not be interpreted unambiguously. To discuss the change of the HBE feature with respect to the formation of hydroxides during conditioning, one has to exclude the carbon and titanium contributions to the O 1s spectrum. This has been done by creating O 1s fits, whose intensity areas are constrained by the extracted components area representing C-O or Ti-O species from the respective detail spectra (see Chapter 5.5). Unfortunately, this method could not be successfully applied to the O 1s spectrum of the as deposited th_CoO_x due to the high degree of unspecified contamination.

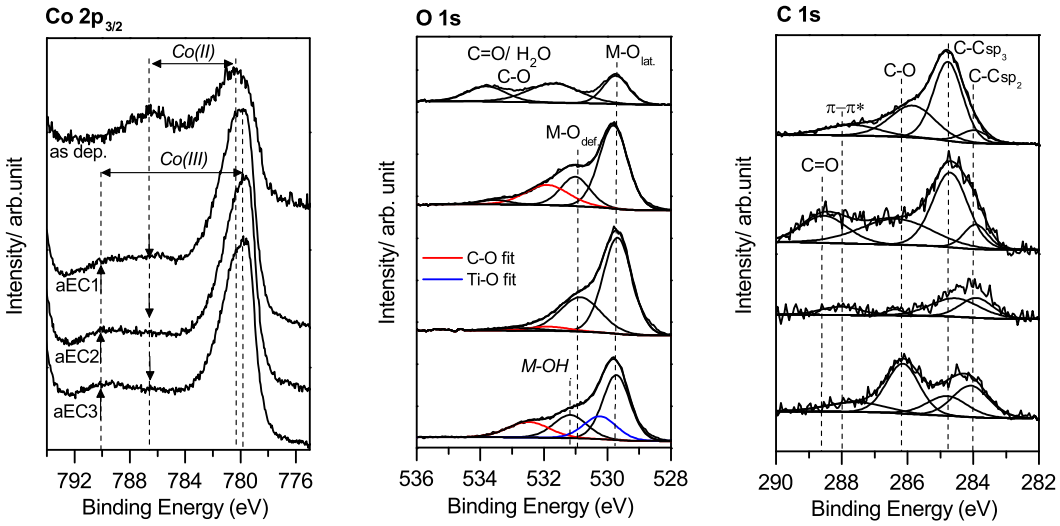

Figure 9.3. XPS Co 2p, O 1s and C 1s details spectra of the as deposited th_CoO_x/Ti-S10 and after 2 min (aEC1), 12 min (aEC2) and after 27 min (EC3) of conditioning.

With regard to the mechanism of water splitting, the formation of different intermediates like hydroxide-, oxyhydroxide- or peroxo-species is expected. The formation of such species would manifest itself in the O 1s spectrum by an increase in the HBE feature. Table 9.2 lists the binding energies of the Co $2p_{3/2}$ peak, the work function, the valence band maximum as well as the calculated Co(III) content and the percentages of the O 1s features for the as deposited th_CoO_x/Ti film and after several conditioning steps performed during the electrochemical characterization EC 1, EC 2 and EC 3. Corresponding to the decrease in carbon content, the O 1s peak at a BE of 533.8 eV vanished after conditioning. The O 1s spectrum of th_CoO_xaEC1 exhibits a HBE feature of only 33.8 %, which can be either attributed to oxygen defects or to hydroxide moieties. With further conditioning, the HBE feature decreases from 33.8 % in case of th_CoO_xaEC1 and th_CoO_xaEC2 to 24.9 % for th_CoO_xaEC3.

Table 9.2. Binding energies of the Co $2p_{3/2}$ peak, the work function, the valence band maximum as well as the calculated Co(III) content and the percentages of the O 1s features reported for th_CoO_x/Ti-S10. All BEs are corrected for the C 1s at 284.8 eV.

Sample	**Co(III)** [%]	**Co $2p_{3/2}$** [eV]	**O $1s_{LBE}$** [%]	**O $1s_{HBE}$** [%]	**VBM** [eV]	**ϕ** [eV]
th_CoO_x-S10	0	780.4	42.6	57.4	0.57	4.7
th_CoO_xaEC1	52.6	779.4	66.2	33.8	0.55	5.4
th_CoO_xaEC2	62.5	779.6	66.2	33.8	0.61	5.4
th_CoO_xaEC3	76.9	779.6	75.1	24.9	0.43	5

Additionally, the HBE feature shifts to 531.2 eV after 27 min of conditioning, which agrees with the BE position of bulk cobalt hydroxide. Anyhow, a clear identification of hydroxide species is not possible in this case and the catalysts surface is identified to be predominantly present in the spinel structure. The electrochemical induced formation of a spinel Co_3O_4 surface is also confirmed by the change of the valence band (Figure 9.4 a). The sharp increase in the intensity of the characteristic Co 3d feature at a binding energy of 1.2 eV $\pm$ 0.1 eV identifies clearly the presence of Co(III) after conditioning. In agreement with literature, the Co(II) feature at 2.3 eV $\pm$ 0.3 eV is not as pronounced. [110] Although the work function is reported for completeness in Table 9.2, no statement can be derived from these values since the work function is influenced by the leftover carbon contaminations and the high surface roughness.

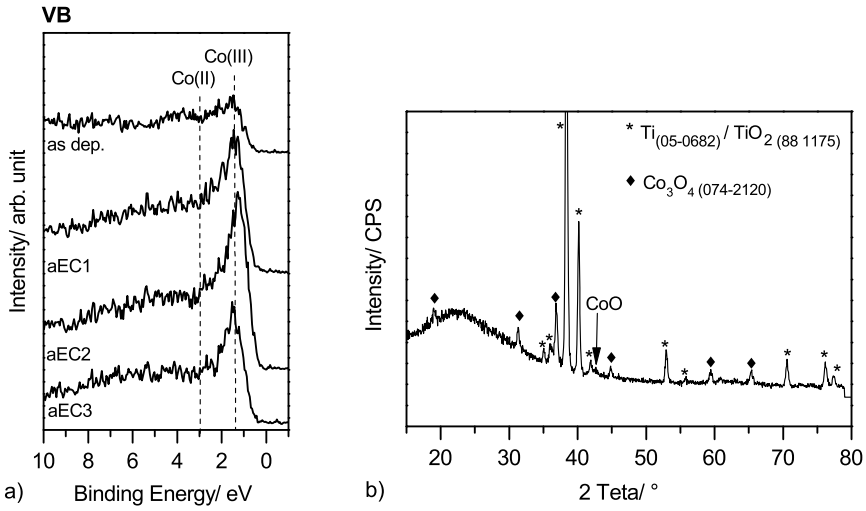

Figure 9.4. a) VB spectra of the as deposited th_CoO_x/Ti-S10 and after 2 min (aEC1), 12 min (aEC2) and 27 min (EC3) of conditioning. b) XRD pattern of 27 min conditioned th_CoO_x/Ti.

In addition to the XPS investigation, the structural change was confirmed by recording a XRD measurement of the electrochemical conditioned sample. The XRD pattern of th_CoO_xaEC3 (Figure 9.4 b) shows the reflexes of Co_3O_4 (JCPDS No. 74-2120) at 31.3°, 37°, 44.8°, 59.3° and 65.3°. [139]

In summary, the XPS results clearly show that the CoO surface transforms to a Co_3O_4 spinel phase under operating conditions. The formation of hyroxides is probable but not definite to interpret from the O 1s spectra. Nevertheless, a clear correlation was found between the activity and the oxidation state: The activity enhances with increasing Co(III) content. With regard to the in literature proposed active OER redox couple Co(III)/Co(IV), the formation of a Co(III) precursor state is indispensable. [140]

9.1.2 Plasma deposited pl_CoO_x

In contrast to thermally deposited th_CoO_x/Ti, the electrochemical conditioning did not have an positive effect on the activity of pl_CoO_x/Ti. Figure 9.5 shows the CV curves of two pl_CoO_x/Ti samples (S11 and S13) recorded in 1 M KOH. While the voltammetry of the thermal deposited Co(II)O_x film changed with the transformation to the active spinel-type oxide catalyst within 27 min, the plasma deposited films achieve the highest activity already within the first CV. Further conditioning has no positive effect on the catalytic activity. This observation makes sense if we identify Co(III) as the active state for the OER. Unlike the th_CoO_x/Ti, in which the Co(III) content increases with conditioning time, the as deposited pl_CoO_x/Ti films show already a Co(III) content of about 60%. In correlation to this fact, the pl_CoO_x/Ti is more active right from the beginning of the OER: a lower onset potential of 1.57 V vs. RHE and a considerably smaller overpotential of 0.43 V at 2 mA/cm^2 can be noted for the CVs of both pl_CoO_x/Ti samples (S11 and S13).
While in case of p_CoO_x/Ti-S11, the overpotential of the CV recorded after the galvanostatic conditioning (blue) increases, no activity loss is observed for the CV of the pl_CoO_x/Ti-S13 film after the GS test. Both, the CV recorded before and the CV recorded after the GS test, show an overpotential of 0.43 V at a current density of 5 mA/cm^2. The potential drop during conditioning is plotted versus the time in Figure 9.5 c for both samples.

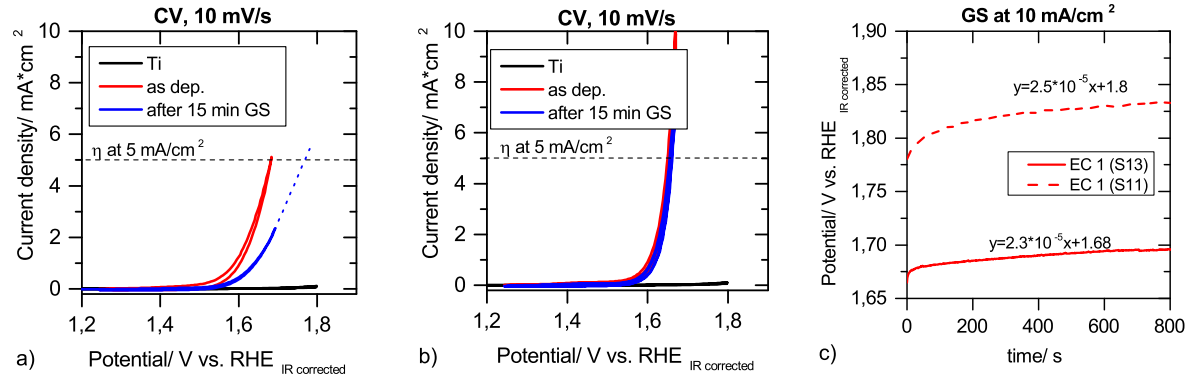

Figure 9.5. a) CV scans of pl_CoO_x/Ti-S11 recorded for the as deposited sample in 1 M KOH (red) and after 15 min conditioning (blue) and b) CV scans of pl_CoO_x/Ti-S13 recorded for the as deposited sample in 1 M KOH (red) and after 15 min conditioning (blue). c) Galvanostatic scan of pl_CoO_x/Ti-S11 (red dashed line) and -S13 (red line).

The potential decay is with 2.5*10^{-5} V/s for pl_CoO_x/Ti-S11 and 2.3*10^{-5} V/s for pl_CoO_x/Ti-S13 in the same range as observed for th_CoO_xaEC3, which was found to be 1.6*10^{-5} V/s. Although the degradation slopes of p_CoO_x/Ti-S11 and -S13 are almost similar, the activity loss is more pronounced in case of p_CoO_x/Ti-S11.

With XPS it was proven, that the Ti 2p signal of pl_CoO_x/Ti-S11 only increases by 3.2 % and therefore the activity drop cannot be attributed to the dissolution of the catalyst. Table 9.3 summarizes the atomic concentration of Co, O, C and Ti of the as deposited pl_CoO_x samples (S11 and S13) and after conditioning pl_CoO_xaEC1. While the oxygen content remains unchanged, a decrease of the cobalt concentration is observed accompanied with the increase of the carbon content by 9.1 %. The increase in carbon indicates the poisoning of the catalyst by carbon contaminations in the electrolyte solution. An increase in carbon within the pl_CoO_x/Ti films was not systematically observed after conditioning. In case of sample pl_CoO_x-S13 for example, no increase in the carbon content was found.

Table 9.3. Atomic concentration of Co, O, C and Ti as well as the overpotential at 5 mA/cm^2 and the slope of the GS for the as deposited pl_CoO_x-S11 and pl_CoO_xaEC1.

Sample	**Co**	**O**	**C**	**Ti**	**η at 5 mA/cm^2**	**GS slope**
	[%]	*[%]*	*[%]*	*%*	*V*	*mV/s*
pl_CoO_x-S11	34.4	53.2	12.5	0	0.45	2.5*10^{-2}
pl_CoO_xaEC1	23.1	52.2	21.6	3.2	0.54	-
pl_CoO_x-S13	34.5	50.6	14.6	0.3	0.45	2.3*10^{-2}
pl_CoO_xaEC1	23.8	59.7	11.7	4.7	0.45	-

Figure 9.6 presents the XPS detail spectra of the Co $2p_{3/2}$, the O 1s and the valence band region for sample pl_CoO_x/Ti-S11 from before and after the galvanostatic conditioning. The Co $2p_{3/2}$ lines of the as deposited pl_CoO_x and pl_CoO_xaEC1 reflect the typical line shape of Co_3O_4 with the double peak feature of the main peak and the satellite structure of the oxidation states Co(II) and Co(III). The O 1s of the as deposited pl_CoO_x line has also hardly changed after conditioning. Both O 1s lines show the LBE signal at a binding energy of 529.7 eV, which represents the lattice oxygen within the oxide and the HBE feature, which is attributed to oxygen defects and hydroxide moieties.

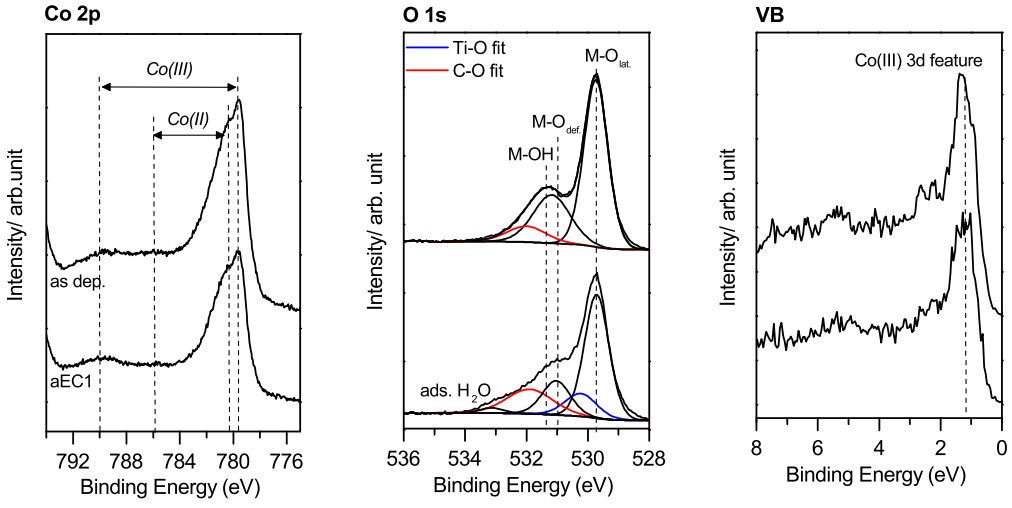

Figure 9.6. XPS Co 2p, O 1s and C 1s details spectra of the as deposited pl_CoO_x/Ti-S11 and after 15 min of conditioning (aEC1).

The O 1s spectrum of the 15 min conditioned sample exhibits an additional feature at a binding energy of 533 eV, which can be assigned to adsorbed water. Since the HBE signal at 531.3 eV slightly decreases during conditioning by 6.8 %, the electrochemical induced formation of additional hydroxide sites on the catalysts surface can be ruled out. Also the valence band spectra of the as deposited and the conditioned film do not show a significant change, both exhibit the characteristic Co(III) 3d feature at 1.3 eV ±0.1. Also the binding energy of the Co $2p_{3/2}$ peak, the work function or the valence band maximum do not show any significant change after conditioning (Table 9.4). It can be summarized that the pl_CoO_x/Ti films seem to operate in a spinel-type active phase under operating conditions similar to thermally deposited th_CoO_x/Ti and that the formation of hydroxides or oxyhydroxides cannot be clearly identified.

Table 9.4. Binding energies of the Co $2p_{3/2}$ peak, the work function, the valence band maximum and the maximum intensity as well as the calculated Co(III) content and the percentages of the O 1s features of pl_CoO_x/Ti-S11. All BEs are corrected for the C 1s at 284.8 eV of adventitious carbon.

Sample	**Co(III)** [%]	**Co $2p_{3/2}$** [eV]	**O $1s_{LBE}$** [%]	**O $1s_{HBE}$** [%]	**VBM** [eV]	**I_{VBM}** [eV]	**ϕ** [eV]
pl_CoO_x-S11	63	779.5	66.6	33.4	0.36	1.3	4.8
pl_CoO_xaEC1	77	779.5	71.8	28.2	0.39	1.2	4.9

The XPS results show that the Co(III) content in the initial state of the pl_CoO_x (60-62 %) correspond to the 12 min conditioned th_CoO_xaEC2 (62 %). Furthermore, the electrochemical activity is comparable. Whereas pl_CoO_x requires an overpotential of 0.45 V at 5 mA/cm^2, th_CoO_xaEC2 needed 0.41 V. This supports our argumentation that the oxidation state of the CoO_x catalyst is correlated to the electrochemical activity.

9.1.3 Plasma deposited pl_$CoO_x(OH)_y$

The oxide surfaces of thermally and plasma deposited CoO_x showed only a low ability to form hydroxides and oxyhydroxides. But since the reaction mechanism of the OER proposes the formation of different intermediates like hydroxides, oxyhydroxides or oxyperoxides before molecular oxygen can be released, one would expect to identify different intermediates on the catalysts surface after the OER. The superior electrochemical activity of air deposited pl_$CoO_x(OH)_y$ was already addressed in Chapter 8.5.

Figure 9.7 a presents the CV of pl_$CoO_x(OH)_y$-S57 recorded in 1 M KOH. It shows the lowest overpotential of 0.35 V at a current density of 5 mA/cm^2 and a steep increase in the current density. At 10 mA/cm^2 only an overpotential of 0.37 V is required. There was no further increase in activity observed during the potentiostatic conditioning at 1.6 V vs. RHE but a current drop of $2.4*10^{-4}$ mA/cm^{2}s (Figure 9.7 b).

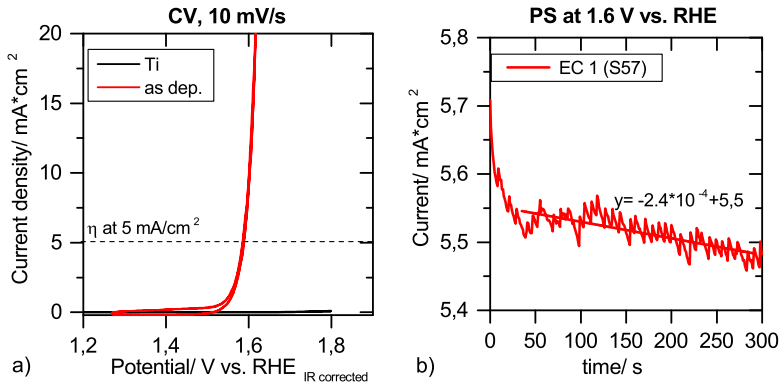

Figure 9.7. a) CV scans of pl_$CoO_x(OH)_y$-S57 (red) and of Ti (black) recorded in 1 M KOH. b) Potentiostatic scan of pl_$CoO_x(OH)_y$-S57 (red) performed at a potential of 1.59 V vs. RHE.

The atomic concentration of Co, O, C and Ti of the as deposited pl_$CoO_x(OH)_y$/Ti-S57 and the conditioned pl_$CoO_x(OH)_y$aEC1 are listed in Table 9.5. While the atomic percentages of Co and O increases by 2.3 % and 9.1 %, the carbon content decreases from 34.1 % to 14 %. The percentage of Ti increases by only 2.7 %. Since the cobalt content even increases within the layer, the appearance of the substrate signal is attributed to the removal of only the carbon impurities and not the catalyst itself.

Table 9.5. Atomic concentration of Co, O, C and Ti as well as the overpotential at 5 mA/cm^2 and the slope of the PS test for the as deposited pl_$CoO_x(OH)_y$ (S57) and pl_$CoO_x(OH)_y$aEC1.

Sample	**Co** *[%]*	**O** *[%]*	**C** *[%]*	**Ti** *%*	**η at 5 mA/cm^2** *V*	**PS slope** *mA/cm^{2}s*
pl_$CoO_x(OH)_y$-S57	23.9	48	34.1	0	0.36	2.36*10^{-4}
pl_$CoO_x(OH)_y$aEC1	26.2	57.1	14	2.7	-	-

Figure 9.8 presents the detail spectra of the Co 2p, O 1s and the valence band region of the as deposited catalyst and after 5 min of conditioning. The Co $2p_{3/2}$ spectra clearly show the oxidation of the Co(II) to Co(III) by the binding energy shift of the Co $2p_{3/2}$ peak from 780.6 eV to 780.1 eV and by the change of the satellite structure. The Co(II) satellite, which is positioned at a distance of 5.5 eV in case of the as deposited pl_$CoO_x(OH)_y$, vanishes after conditioning whereas a new satellite appears at a distance of 10 eV, which confirms the formation of the Co(III) oxidation state. The calculated Co(III) content increases from 0 % in the as deposited sample to 91 % after conditioning (Table 9.6). The O 1s spectrum of the as deposited pl_$CoO_x(OH)_y$/Ti-S57 shows two predominant peaks: The LBE feature at 529.7 eV and the HBE feature at 531.6 eV. These BE values are consistent with the one reported for CoO and $Co(OH)_2$. The valence band confirms Co(II) as initial oxidation state since the characteristic intense Co(III) 3d feature is only observed after conditioning. The O 1s spectrum after conditioning is consistent with the one reported for CoO(OH). The LBE feature representing lattice oxygen is shifted towards a higher BE whereas the HBE feature shifts towards a lower BE value. Furthermore, the LBE/HBE peak ratio of 0.8 is close to the ratio of 1, which is characteristic for CoO(OH).

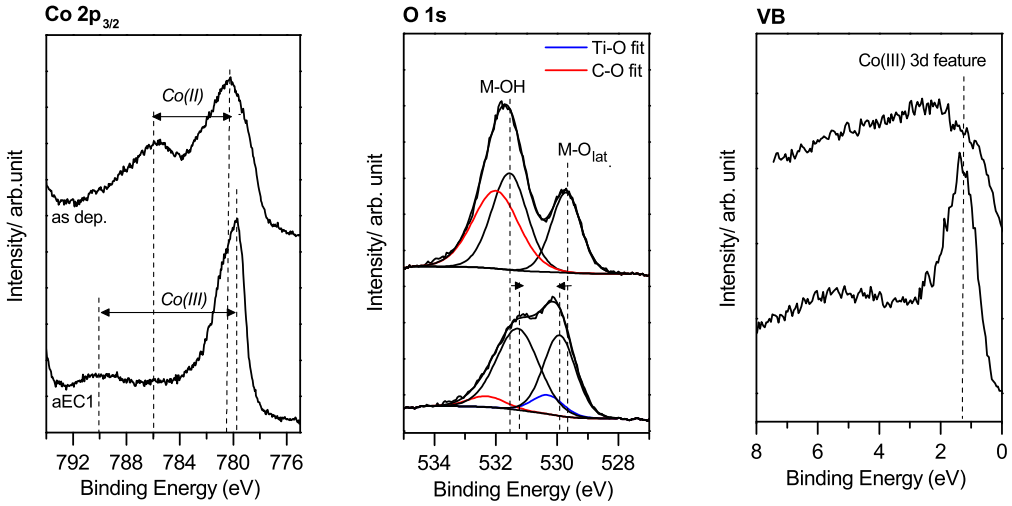

Figure 9.8. XPS Co 2p, O 1s and C 1s details spectra of the as deposited pl_$CoO_x(OH)_y$-S57 and after 5 min of conditioning (aEC1).

Table 9.6 lists the electron binding energies for all peak fits of the O 1s line and their ratio of the as deposited and the conditioned catalyst. Associated with the appearance of the Co(III) satellite in the Co 2p spectrum and the unique intensity ratio of the O 1s features characteristic for CoO(OH), the valence band shows the Co(III) 3d feature at 1.4 eV. Accompanying with the electrochemical induced transformation of Co(II)$O_x(OH)_y$ to Co(III)O(OH) the valence band maximum shifts from 0.3 eV to 0.7 eV and the work function increases from 3.9 eV to 5.6 eV.

Table 9.6. Binding energies of the Co $2p_{3/2}$ peak, the work function, the valence band maximum as well as the calculated Co(III) content and the percentages of the O 1s features of as deposited pl_$CoO_x(OH)_y$/Ti-S57 and after conditioning pl_$CoO_x(OH)_y$aEC1 . All BEs are corrected for the C 1s at 284.8 eV of adventitious carbon.

Sample	**Co(III)** [%]	**Co $2p_{3/2}$** [eV]	**O $1s_{LBE}$** [%]	**O $1s_{HBE}$** [%]	**VBM** [eV]	**ϕ** [eV]
pl_$CoO_x(OH)_y$-S57	0-10 %	780.7	40.8	59.2	0.3	3.9
pl_$CoO_x(OH)_y$aEC1	91	780.1	45.5	55.5	0.7	5.6

In contrast to th_CoO_x/Ti and pl_CoO_x/Ti, which was found to operate in a spinel structure under operating conditions, the XPS results show that the superior electrochemical activity of in air deposited pl_$CoO_x(OH)_y$/Ti is related to a change in oxidation state from Co(II) to Co(III) and to the surface transformation from a not well defined Co(II)$O_x(OH)_y$ film to the active precursor phase Co(III)O(OH).

9.1.4 Discussion

Although the DFT calculations of Rossmeisl and Man et al. consider the oxidation of Co(II) to Co(III) accompanying the formation of a superoxy-type (-OOH) intermediate as the difficult step in the water splitting reaction instead of the formation of an oxyhydroxide (-O(OH)) species, our findings agree with the hypothesis that the formation of the Co(III) oxidation state presents a

critical role and might be the limiting factor. [20] Our results clearly show that with increasing Co(III) content, the catalytic activity is strongly improved and that the ability to transform into the highly active CoO(OH) precursor phase does depend on the surface structure of the as deposited film and with this on the preparation method. Figure 9.9 a shows the correlation between the atomic concentration of Co(III) and the resulting overpotential at a current density of 10 mA/cm^2. The overpotential decreases with increasing Co(III) content. While in case of the spinel-type CoO_x surfaces a Co(III) content of maximum 75 % could be realized after conditioning due to the Co(II)/Co(III) ratio being limited by the spinel structure, the Co(III) oxidation state was stabilized best in form of the CoO(OH) precursor phase with a content of larger than 90 % after conditioning of $CoO_x(OH)_y$.

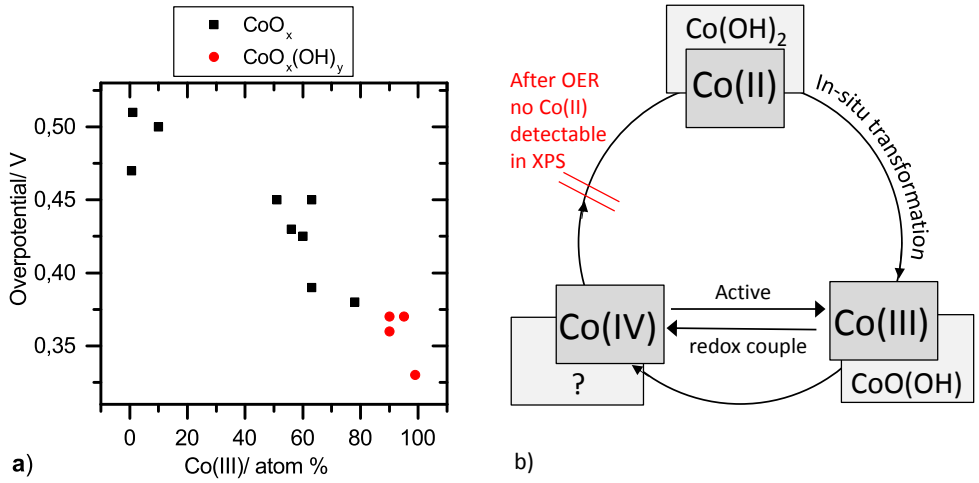

Figure 9.9. a) Atomic concentration of Co(III) plotted versus the overpotential at a current density of 10 mA/cm^2 of various thermally and plasma deposited CoO_x samples (black) and $CoO_x(OH)_y$ samples (red). b) Schematic illustration of the hypothesized OER mechanism of $CoO_x(OH)_y$.

With respect to the proposed active redox couple Co(III)/Co(IV) for the OER, Co(III) presents the necessary active site on the surface. Since the Co(IV) state may only be present under operation conditions, it is not possible to directly observe the Co(IV) species by measuring XPS after the conditioning. Nevertheless, EPR spectroscopy provided the evidence of Co(IV) species for the oxygen evolution reaction studying cobalt oxide/hydroxide precipitate films, also known as Co-Pi catalysts. [7,141] The Co-Pi catalysts are prepared by the potential controlled electrolysis of Co(II) salts in phosphate buffer at pH 7 at a potential of 1.3 V vs. NHE. [7,142] The catalytically active Co-Pi films exhibit EPR signals for both oxidation states: Co(II) and Co(IV). When the deposition voltage was raised into the potential region of the water oxidation, an increase of the Co(IV) population was observed and a decrease of the Co(II) population. [141] Based on these findings, Co is suggested to undergo the oxidation from Co(II)-Co(III)-Co(VI)-Co(II) during OER. Co(II) is regenerated in the last step when oxygen is produced from the Co(IV) oxo species. [7] There are also literature reports identifying the Co(IV) oxidation state by its redox peak at around 1.38 V vs. RHE in the cyclic voltammogram recorded in 0.1 M NaOH at 300 mV/s for a polycrystalline Co electrode. [61] The redox peak of Co(IV) was reported to become more predominant with an appreciable film thickness of CoO(OH), which forms at a potential of around 0.97 V vs. RHE. [61] Surprisingly, almost no Co(II) species were found on the catalysts surface after the conditioning in

our studies. Therefore, contrary to the catalytic mechanism of the Co-Pi catalyst, where Co(II) is regenerated from the Co(IV) centers when oxygen is released, the OER mechanism suggested for the $CoO_x(OH)_y$ only involves the contribution of the Co(III)/Co(IV) redox couple as illustrated in Figure 9.9 b.

9.2 NiO_x and $NiO_x(OH)_y$: Ni(II)/Ni(III) as the active redox couple

9.2.1 Plasma deposited pl_NiO_x

Similar to the results of PECVD deposited pl_CoO_x samples, the galvanostatic conditioning did not have a positive effect on the activity of pl_NiO_x. Figure 9.10 presents the CV of a pl_NiO_x-Ni6 film recorded in 1 M KOH and after 5 min of galvanostatic conditioning. The first CV recorded for the as deposited pl_NiO_x-Ni6 sample (red) agrees with the one recorded after the GS test (blue). In both cases an overpotential of 0.45 V is requires to achieve a current density of 5 mA/cm^2. The positive degradation rate of 5.8*10^{-5} V/s and the appearance of the substrate Ti 2p signal after the conditioning indicate the dissolution of the pl_NiO_x sample during the GS test (Figure 9.10 b).

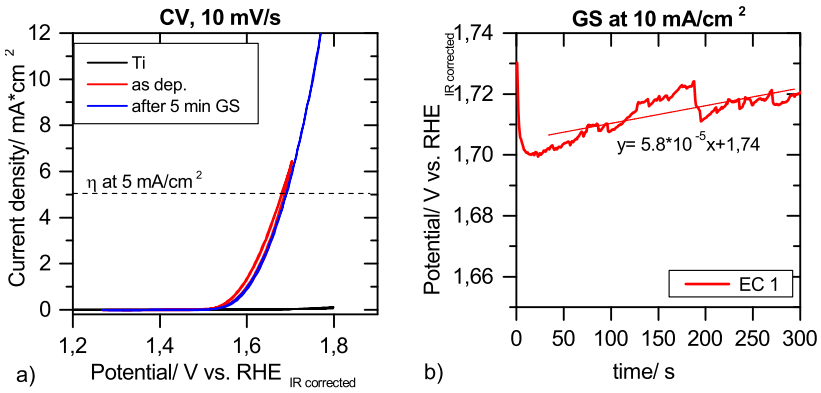

Figure 9.10. a) CV scans of as deposited pl_NiO_x/Ti-Ni6 (red) and after 5 min conditioning (blue) as well as of Ti-foil (black) recorded in 1 M KOH with a scan rate of 10 mV/s. b) Galvanostatic scan of EC 1 (red) performed at 10 mA/cm^2 in 1 M KOH.

Table 9.7 summarizes the atomic concentration of Ni, O, C and Ti from before and after the conditioning of pl_NiO_x/Ti.

Table 9.7. Atomic concentration of Ni, O, C and Ti as well as the overpotential at 5 mA/cm^2 and the slope of the GS for the as deposited pl_NiO_x/Ti-Ni6 film and the 5 min conditioned sample pl_NiO_xaEC1.

Sample	Ni	O	C	Ti	η at 5 mA/cm^2	GS slope
	[%]	*[%]*	*[%]*	*%*	*V*	*V/s*
pl_NiO_x	30.5	48.6	20.9	0	0.45	5.8*10^{-6}
pl_NiO_xaEC1	26.2	52.8	14.5	6.5	0.45	n.r.

Figure 9.11 shows the associated XPS detail spectra of the Ni 2p, the O 1s and the VB region of the as deposited pl_NiO_x/Ti-Ni6 sample and the conditioned one (pl_NiO_x/TiaEC). The electronic structure of the as deposited pl_NiO_x was already discussed in detail in Chapter 8.4.3.

The Ni 2p line of pl_NiO_x/Ti is located at a binding energy of 854.5 eV and shows the unique multiplet splitting of NiO, which is neither present for $Ni(OH)_2$ nor for NiO(OH). [124] The O 1s spectrum of pl_NiO_x/Ti consists of a LBE feature at a binding energy of 530.1 eV, which is assigned to the lattice oxygen and a HBE feature at a binding energy of 531.5 eV, which is attributed to hydroxide moieties and oxygen defects. The O 1s fit (red) at BE of 532.3 eV is attributed to carbon species including C-O and C=O. Since the C 1s spectrum is similar to the one reported for pl_CoO_x/Ti, it is not shown separately. The VB spectrum provides the intense characteristic 3d feature at a binding energy of 2.1 eV and a less intense feature at 4 eV, which are attributed to localized Ni 3d states in NiO. [132]

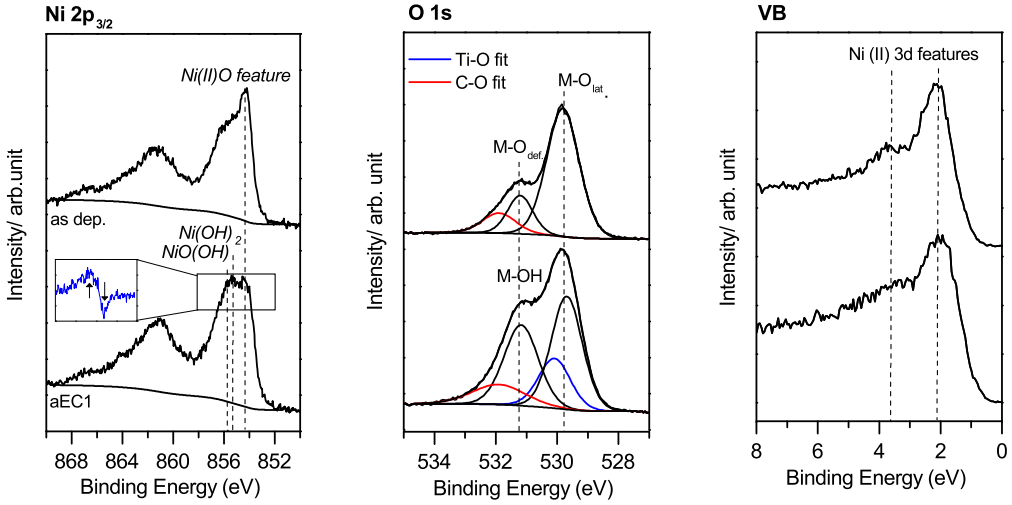

Figure 9.11. XPS Ni 2p, O 1s and VB detail spectra of the as deposited pl_NiO_x-Ni6 sample and after 5 min of conditioning (aEC1). The Ti-O fit (blue) and C-O fit (red) represent the contribution of TiO_2 and C-O species like C=O and C-O to the O 1s spectrum.

After 5 min of galvanostatic conditioning, the Ni $2p_{3/2}$ line does not show anymore the distinct peak feature located at 854.5 eV, which is characteristic for NiO. The resulting asymmetric shape of the Ni $2p_{3/2}$ main peak as well as the increase of the HBE feature from 19 % to 30 % in the O 1s spectrum identify the formation of hydroxide species as either $Ni(OH)_2$ or NiO(OH). Probably, a mixed $Ni(OH)_2$/NiO(OH) is formed. The valence band confirms the partial transformation of NiO_x to NiO(OH) by the decrease in intensity of the Ni 3d feature at 2.1 eV.
To further clarify the differences in the electronic structure, a difference spectrum between the as deposited NiO_x and the galvanostatically conditioned NiO_xaEC is calculated. An excerpt of the difference spectrum is shown enlarged in the Ni $2p_{3/2}$ spectrum in blue. It shows the appearance of a new Ni 2p signal at 856.0 eV identifying the formation of either $Ni(OH)_2$ or NiO(OH) sites. The disappearance of the oxide multiplet splitting feature at 854.5 eV in the difference spectrum confirms the partial transformation of NiO_x to $Ni(OH)_2$/NiO(OH). Table 9.8 lists the binding energies of the Ni $2p_{3/2}$ peak, the work function, the valence band maximum as well as the percentages of the HBE and the LBE features.

Table 9.8. Binding energies of the Ni $2p_{3/2}$ peak, the work function, the valence band maximum as well as the percentages of the O 1s features of pl_NiO_x-Ni6 and of NiO_xaEC1. All BEs are corrected for the C 1s at 284.8 eV of adventitious carbon.

Sample	Ni $2p_{3/2}$ [eV]	O $1s_{LBE}$ [%]	O $1s_{HBE}$ [%]	VBM [eV]	ϕ [eV]
pl_NiO_x	854.5	81	19	1.3	4.3
pl_NiO_xaEC1	856.0	70	30	1.3	5.3

In conclusion, the asymmetric Ni $2p_{3/2}$ line positioned at 856.0 eV as well as the increase of the HBE feature suggest the transformation of NiO_x into $Ni(OH)_2$/NiO(OH) under OER conditions. The potential dependent transformation of NiO_x to a layered (oxy)hydroxide was reported several times in literature. [5, 11, 71]

9.2.2 Plasma deposited pl_$NiO_x(OH)_y$

As discussed in Chapter 8.6, the air deposited pl_$NiO_x(OH)_y$/Ti film shows an superior electrochemical activity than pl_NiO_x/Ti. Figure 9.12 a compares the CVs recorded for the as deposited pl_$NiO_x(OH)_y$-Ni9, after 10 min (EC1) and after 5 min (EC2) of galvanostatic conditioning performed at 10 mA/cm^2 in 1 M KOH. The as deposited pl_$NiO_x(OH)_y$/Ti sample needs an overpotential of only 0.37 V at a current density of 5 mA/cm^2 (red). The overpotential is slightly reduced to 0.35 V in the CV recorded after 10 min of galvanostatic conditioning (blue). The positive effect of conditioning is also reflected by the negative degradation slope of -2.1*10^{-5} V/s found in the GS test (Figure 9.12 b, red). Furthermore, the appearance of the redox wave attributed to the oxidation of $Ni^{2+} \rightarrow Ni^{3+}$ in the cyclic voltammogram after 10 min conditioning indicate a potential dependent change of the oxidation state. This redox wave was not observed in the cyclic voltammogram of the conditioned pl_NiO_x/Ti. The second galvanostatic conditioning step performed during EC 2 did not have a positive effect on the activity, a degradation slope of 1.22*10^{-5} V/s is observed.

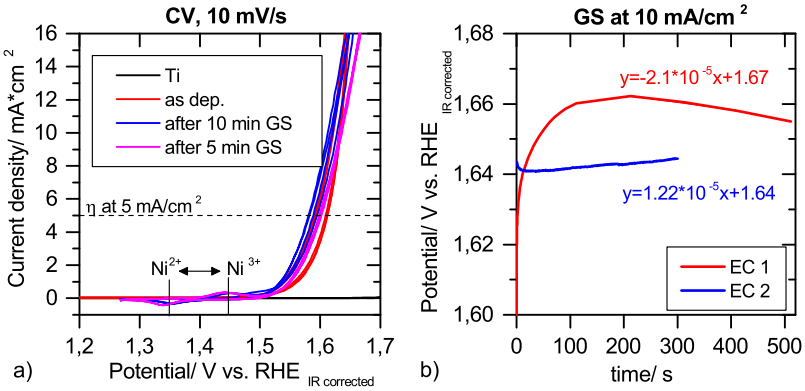

Figure 9.12. a) CV scans of as deposited pl_$NiO_x(OH)_y$/Ti-Ni9 (red), after 10 min (blue) and after 5 min of galvanostatically conditioning (magenta) as well as of Ti (black). b) Galvanostatic scans of EC 1 (red) and EC 2 (blue) performed at 10 mA/cm^2 in 1 M KOH.

In agreement with the results of the GS tests, the Ti 2p substrate signal is absent in the XPS

investigation after the first conditioning (EC 1), but it appears after the second conditioning (EC 2). Table 9.9 summarizes the atomic concentration of Ni, O, C and Ti as well as the overpotential at 5 mA/cm^2 and the slope of the GS scan for the as deposited pl_$NiO_x(OH)_y$-Ni9 sample and after conditioning.

Table 9.9. Atomic concentration of Ni, O, C and Ti as well as the overpotential at 5 mA/cm^2 and the slope of the GS scan for the as deposited pl_$NiO_x(OH)_y$-Ni9 and the conditioned pl_NiO_xaEC1 and pl_NiO_xaEC2.

Sample	**Ni**	**O**	**C**	**Ti**	**η at 5 mA/cm^2**	**PS slope**
	[%]	*[%]*	*[%]*	*%*	*V*	*V/s*
pl_$NiO_x(OH)_y$	27	61	12	0	0.37	-2.1*10^{-5}
pl_$NiO_x(OH)_y$aEC1	32	38	30	0	0.35	1.22*10^{-5}
pl_$NiO_x(OH)_y$aEC2	23	46	25	5	0.37	n.r.

As already discussed in Chapter 8.4.3, the electronic structure of the as deposited pl_$NiO_x(OH)_y$ is not as definite to interpret as the spectrum of a well defined NiO_x. The XPS detail spectra of the Ni $2p_{3/2}$, the O 1s and the VB region of as deposited pl_$NiO_x(OH)_y$/Ti and after conditioning are shown in Figure 9.13.
Since the BE of $Ni(OH)_2$ and NiO(OH) are located close together, the line shape has to be used for identification. The Ni $2p_{3/2}$ line of the as deposited pl_$NiO_x(OH)_y$-Ni9 sample has an asymmetric shape and a maximum peak position of 855.8 eV. Also the intense Ni 3d state feature at 2.4 eV, which is characteristic for NiO, is absent in the valence band. [132] Although this confirms the deposition of a NiO(OH)/$Ni(OH)_2$ phase, the presence of NiO_x in the as deposited films cannot be ruled out completely. The O 1s line of as deposited pl_$NiO_x(OH)_y$ shows the HBE signal at a binding energy of 531.4 eV and the LBE signal at a binding energy of 530 eV.

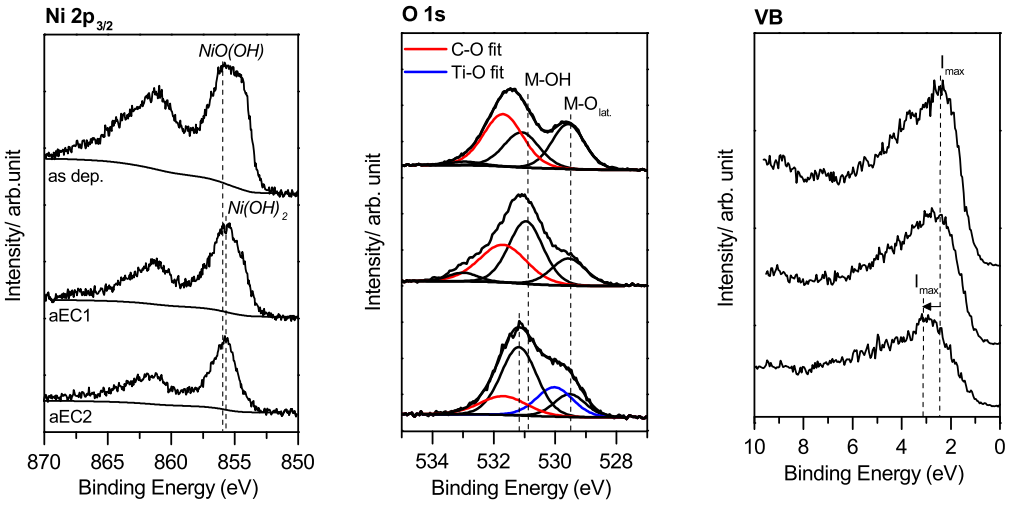

Figure 9.13. XPS detail spectra of the Ni 2p, O 1s and VB region of the as deposited pl_NiO_x/Ti-Ni9 sample, after 10 min (aEC1) and after 15 min (aEC2) of galvanostatic conditioning. The Ti-O fit (blue) and C-O fit (red) in the O 1s spectrum represent the contribution of TiO_2 and C-O species like C=O and C-O to the O 1s line.

The HBE feature is about 50 % of the O 1s area and can be clearly assigned to the presence

of hydroxide species. The LBE feature of 50 % is ascribed to metal bonded oxygen within a regular oxide crystal (O^{2-}). With respect to the asymmetric shape of the Ni $2p_{3/2}$ peak and the difference spectrum, which confirmed that NiO_x can only be present in small amounts, the LBE feature is mainly assigned to NiO(OH). The shape of the Ni $2p_{3/2}$ line changes during the galvanostatic conditioning: The FWHM decreases and the maximum peak position shifts by 0.2 eV to a lower BE. In contrast to the asymmetric shape of the Ni $2p_{3/2}$ peak of the as deposited pl_$NiO_x(OH)_y$, the Ni $2p_{3/2}$ spectrum of 15 min conditioned pl_$NiO_x(OH)_y$aEC2 shows one predominant symmetric peak at a BE of 855.6 eV with a FWHM of about 2.2 eV, which agrees well with the one reported for $Ni(OH)_2$ in literature. The O 1s spectrum confirms the formation of $Ni(OH)_2$ by the increase of the HBE feature from 50 % to 75 % after the second galvanostatically conditioning performed during EC2.
Whereas the Ni 2p spectrum is in good agreement with those reported in literature for pure $Ni(OH)_2$, the presence of the LBE feature of 25 % in the O 1s line is attributed to metal bonded oxygen. The LBE feature can be assigned to a small amount of NiO(OH). The presence of NiO can be ruled out since the multiplet feature at 854.6 eV and the intense Ni 3d feature at 2.1 eV are not observed. [127]
In agreement with the findings of Diplas et al., who reported the valence bands of NiO, $Ni(OH)_2$ and NiO(OH), the Ni 3d features of $Ni(OH)_2$ and NiO(OH) are shifted towards higher binding energies and are broader compared to NiO_x. [132] Table 9.10 lists the calculated area percentages of the LBE and the HBE features as well as the BE of the VBM an the work function of as deposited $NiO_x(OH)_y$ films and after conditioning.

Table 9.10. Binding energies of the Ni $2p_{3/2}$ peak, the work function, the valence band maximum as well as the percentages of the O 1s features of pl_$NiO_x(OH)_y$-Ni9. All BEs are corrected for the C 1s at a BE of 284.5 eV of adventitious carbon.

Sample	**Ni $2p_{3/2}$** [eV]	**O $1s_{LBE}$** [%]	**O $1s_{HBE}$** [%]	**VBM** [eV]	ϕ [eV]
pl_$NiO_x(OH)_y$	855.8	50	50	1.0	3.4
pl_$NiO_x(OH)_y$aEC1	855.6	28	72	0.9	3.8
pl_$NiO_x(OH)_y$aEC2	855.6	25	75	1.1	4.9

In conclusion, the increase of the HBE feature, the BE shift of the Ni $2p_{3/2}$ main peak from 855.8 to 855.6 eV and the decrease in the FWHM identify the presence of $Ni(OH)_2$ after the galvanostatic conditioning.

9.2.3 Discussion

The complex interfacial redox chemistry of transition metal oxides is commonly known and often discussed in literature. The electrochemical induced oxidation of a polycrystalline Ni electrode to a complex NiO/$Ni(OH)_2$ film is known to occur in the potential range between -0.1 V to 0.3 V vs. RHE. The further oxidation to NiO(OH) is observed at potentials between 1.3 V to 1.5 V

vs. RHE in 1 M NaOH. [31, 61] The in-situ transformation of NiO_x to the catalytically active $Ni(OH)_2/NiO(OH)$ phase requires a long and tedious conditioning. [71] Trotochaud et al. reported for example the conversion of a spin-cast NiO_x to $Ni(OH)_2/NiO(OH)$ to occur within 6 hours of galvanostatic conditioning at 10 mA/cm^2. [5] But ultimately, the here presented PECVD prepared NiO_x, which transformed partly to a $NiO_x/NiO(OH)$ within 5 min, also end up as a $Ni(OH)_2/NiO(OH)$ mixture after a sufficient time of galvanostatic conditioning.

In contrast to NiO_x, we found that PECVD deposited $NiO_x(OH)_y$ transforms quickly already within the first CV to the active $Ni(OH)_2/NiO(OH)$ precursor phase and the electrochemical activity is enhanced. The XPS results show, that the enhanced activity is related to the amount of hydroxide moieties on the electrodes surface: the higher the content of hydroxide moieties, the more accelerated is the conversion to the active precursor phase and the lower is the resulting overpotential. Figure 9.14 plots the overpotential as a function of the amount of the HBE feature. Stern et al. studied the electrochemical properties of NiO_x in comparison to nanoparticular $Ni(OH)_2$. They also found, that NiO_x needs a long conditioning time to transform into the active precursor phase while the $Ni(OH)_2$ films showed the highest activity already from the beginning. [71] Our results confirm the hypothesis of Stern et al. that hydroxide functional groups on the electrodes surface may accelerate the formation of the active precursor phase. [71] To our knowledge, this is the first time, that PECVD deposited $NiO_x(OH)_y$ films with different content of hydroxide moieties are systematically investigated. We report a clear correlation between the overpotential and the surface functionality.

With respect to the strong oxidative conditions during the galvanostatic conditioning at 10 mA/cm^2 the question arises why $Ni(OH)_2$ is identified as dominating phase in XPS after conditioning. For sure, the $Ni(OH)_2$ sites undergo an oxidation to Ni(III) at potentials above 1.43 V, which is identified by the redox wave in the CV of $NiO_x(OH)_y$ (Figure 9.12). Assuming a further oxidation of Ni(III) to Ni(IV), the dominating presence of $Ni(OH)_2$ after conditioning suggests the recovering of Ni(II) after the oxygen release by Ni(IV) under operating conditions. Figure 9.14 b gives a schematic illustration of the hypothesized mechanism.

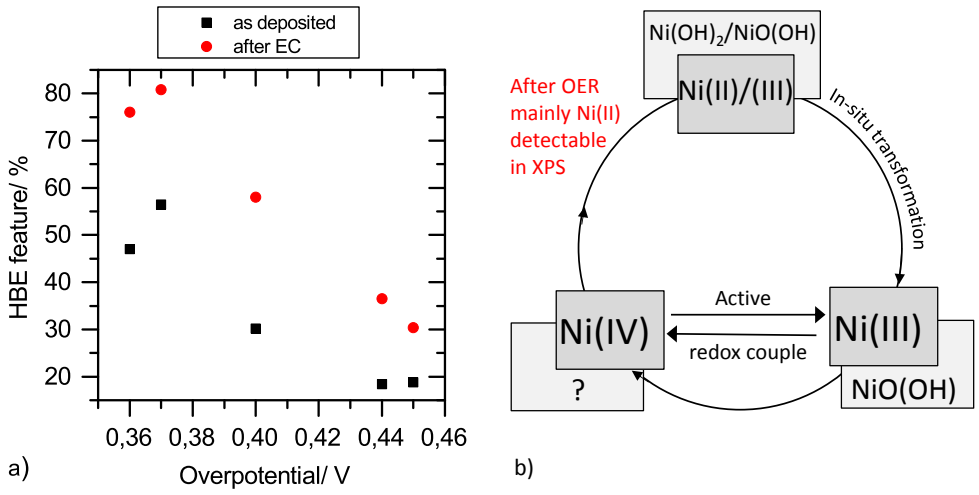

Figure 9.14. a) Plot of the overpotential as a function of the percentage of the HBE feature of $NiO_x(OH)_y$/Ti and NiO_x films. b) Schematic illustration of the hypothesized catalytic OER mechanism of $NiO_x(OH)_y$/Ti.

The formation of a formal Ni(IV) oxidation state during OER is widely discussed in literature. [143, 144] Bediako et al. for example found an average oxidation state of +3.6 by correlating coulometric measurements with X-ray absorption near-edge structure spectra. As a conclusion it seems probable that the Ni(III)/Ni(IV) redox pair represents the actual active state under operating condition. The decomposition of the NiO(OH) phase after switching off the potential can be ruled out since the electrochemical deposited NiO(OH) phase is reported to be stable and is subsequently characterized for example with XRD and XPS. [71, 127, 145–147] From the discussion above and for the cobalt oxides/hydroxides in the previously discussion it comes clear, that the development of an in-situ ambient pressure XPS technique is indispensable to identify the active oxidation state under operating conditions.
Nevertheless we could show, that the as deposited $NiO_x(OH)_y$ was found to be the better starting material, since the electrochemical transformation to the active phase is favored and therefore the activity is enhanced from the start of the OER. The results clearly show that the presence of hydroxide sites on the catalyst surface enhances the possibility to transform to the active phase and promote the catalytic activity.

10. Preparation and characterization of bimetallic metal oxide catalysts

Chapter 10 deals with the preparation and characterization of the bimetallic oxide catalysts $CoMO_x$/Ti and $CoMO_x(OH)_y$/Ti (M=Ni, Fe, Cu). Since the intensively optimized deposition parameters of the pure pl_CoO_x and pl_$CoO_x(OH)_y$ films were taken for the deposition of the bimetallic catalysts, the optimization of the deposition itself is not part of the discussion. The results focus on the investigation of the resulting composition (Chapter 10.1) as well as on the electronic structure (Chapter 10.2) and its influence on the electrochemical activity (Chapter 10.3). Although at the beginning of this project the development of CoNi-, CoFe- and CoNiFe-catalysts were considered, the most effort has been devoted to the development of CoNi-catalysts, since the admixture of Fe turned out to have no positive effect in case of $NiFeO_x$. The PECVD deposition of $NiFeO_x$ was investigated in a Master thesis within this project. [122] Hence, the preparation and characterization of PECVD deposited $NiFeO_x$ will not be discussed, only the electrochemical results are shown for comparison.

10.1 Decomposition of the precursors: Composition and morphology

As a first strategy to deposit pl_$CoNiO_x$ films, the $Ni(acac)_2$ precursor was introduced into the reaction chamber by evaporation without using a carrier gas (setup C). Table 10.1 lists the deposition parameters of the differently prepared $CoNiO_x$/Ti samples. In fact, the optimized preparation parameters of pure pl_CoO_x/pl_$CoO_x(OH)_y$ films were taken for the deposition of the bimetallic catalysts.

Table 10.1. Preparation parameters of the PECVD deposition of pl_$CoNiO_x$/Ti using the experimental setup C and the with XPS determined atomic concentrations of Co and Ni within the catalyst films. The deposition parameters of samples CoNi5,-6,-7 are not listed since the deposition was not successful.

Sample	$\mathbf{T_{Sub}}$ *[°C]*	$\mathbf{T_{Prec}}$ *[°C]*	$\mathbf{T_{Prec}}$ *[°C]*	$\mathbf{f_{Ar}}$ *[sccm]*	$\mathbf{f_{O_2}}$ *[sccm]*	$\mathbf{t_{Dep}}$ *[min]*	$\mathbf{p_{proc}}$ *[mtorr]*	**d** *[cm]*	**Co** *[%]*	**Ni** *[%]*
CoNi1	230	180	180	200	200	7	1410	13.5	62	38
CoNi2	260	180	180	200	200	7	1240	13,5	20	80
CoNi3	260	180	180	200	200	20	1180	13.5	51	49
CoNi4	260	180	170	200	200	20	1240	13.5	21	79
CoNi8	250	180	190	100	100	15	1570	13.5	71	29
CoNi9	250	180	200	200	100	15	1540	13.5	82	18
CoNi10	250	180	200	200	200	15	1440	13.5	53	47

The atomic concentrations of Co and Ni are determined from the intensity ratio of the Ni $2p_{3/2}$/Co $2p_{3/2}$ peaks with XPS. The overall composition including the atomic concentration of Co, Ni O, C and Ti of the $CoNiO_x$/Ti samples is shown in Figure 10.1 a. Except of sample CoNi4, the atomic concentrations of carbon and oxygen vary between 20-25 % and 40-50 %, which is

similar to the carbon and oxygen content in the PECVD deposited pl_CoO_x (15-20 % C, 40-50 % O) and pl_NiO_x (20-30 % C, 40-50 % O) samples. In analogy to the pure metal oxides, the C 1s spectra, which are shown in Figure 10.1 b, exhibit C-O species like C=O, C-O and C-C/C-H.

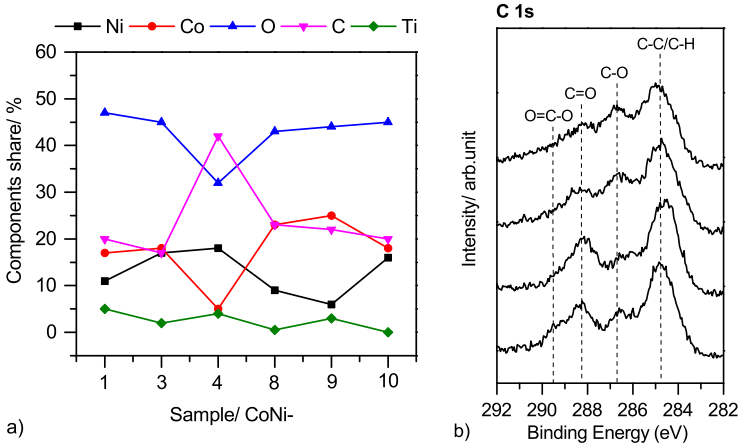

Figure 10.1. a)Atomic concentration of various components (Co, Ni, O, C, O and Ti) within different pl_$CoNiO_x$/Ti films. b) C 1s detail spectra of pl_$CoNiO_x$ samples CoNi-1, -3, -8 and -10.

As expected, the HREM images of PECVD deposited pl_$CoNiO_x$/Ti do not show any special morphological differences. Figure 10.2 compares the image of sample CoNi3 with the clean titanium foil. Similar to the HREM images of pl_CoO_x, the morphology agrees with the one of the plain titanium foils but the surface appears smoother after the deposition.

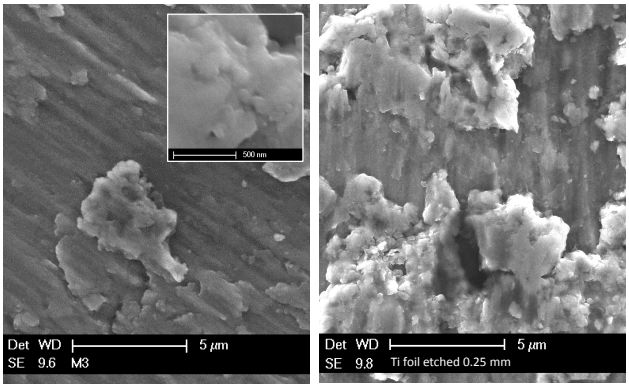

Figure 10.2. HREM images of samples pl_$CoNiO_x$/Ti-CoNi3 and of the clean Ti foil.

Afterwards the precursor inlet of Ni was equipped with a carrier gas supply (setup D), $CoNiO_x(OH)_y$/Ti films with different Ni contents were deposited using air as a reactive gas. Table 10.2 lists the deposition parameters and the percentages of Co and Ni. As for the deposition of the pure metal oxides, the carbon content is slightly increased to 20-30 % within the layer when air is used as a reactive gas. Furthermore, the C 1s spectra show an increased amount of C=O relatively to C-O. Due to the similarities, there is no need to discuss the C 1s spectra and the resulting composition in detail. The Ti substrate signal varied between 1-2 %. Although the carrier gas flow of the Ni precursor line was increased for the deposition of sample CoNi12, the resulting Ni content is lower compared to sample CoNi11. This has to be attributed to a blocking of the precursor supply line by condensed $Ni(acac)_2$ as it was observed several times.

Table 10.2. Preparation parameters of the PECVD deposition of $CoNiO_x(OH)_y$/Ti using the experimental setup D.

Sample	T_{Sub} *[°C]*	T_{Prec} *[°C]*	T_{Prec} *[°C]*	$f_{N_2,Co}$ *[°C]*	$f_{N_2,Ni}$ *[sccm]*	f_{Air} *[sccm]*	t_{Dep} *[min]*	p_{proc} *[mtorr]*	**d** *[cm]*	**Co** *[%]*	**Ni** *[%]*
CoNi11	260	180	220	200	20	200	30	2680	13.5	67	33
CoNi12	260	180	220	200	40	300	30	3010	13,5	89	11
CoNi13	260	180	220	200	60	600	30	3830	13.5	37	63

GIXRD measurement of PECVD deposited pl_$CoNiO_x(OH)_y$ films were not conducted since they did not give any valuable results for pl_CoO_x and pl_$CoO_x(OH)_y$ samples. All as deposited samples were X-ray amorphous.

10.2 Differences in electronic structure compared to the pure metal oxides

10.2.1 PECVD of pl_$CoNiO_x$ and pl_$CoNiO_x(OH)_y$

The electronic structure of the catalysts was examined with XPS. Figure 10.3 shows the Co $2p_{3/2}$, Ni $2p_{3/2}$ and O 1s detail spectra of pl_$CoNiO_x$/Ti films. As discussed for the O 1s spectra of pure metal oxides, the HBE feature at a BE of 531.3-531.5 eV is generally assigned to surface hydroxides, oxygen defects and C-O species. The LBE feature representing lattice oxygen is found at a BE of 529.7 ±0.1 eV in $CoNiO_x$ for all samples (CoNi1- CoNi10).
Interestingly, the Co $2p_{3/2}$ spectra of all PECVD deposited pl_$CoNiO_x$ films show a satellite structure at a distance of 6 eV to the main peak, which identifies Co(II) as the predominant oxidation state. In contrast to this, the Co $2p_{3/2}$ spectrum of pure PECVD deposited pl_CoO_x (S13, red) exhibits the satellite structure of both oxidation states, Co(II) and Co(III), identifying the structure of spinel-type. With a BE position of the main peak of 780.2 eV and the satellite structure at a distance of 6 eV to the main line, the Co $2p_{3/2}$ spectra of $CoNiO_x$ agree with the one reported for th_CoO_x (S10, red), which indicates the deposition of CoO.
Also the Ni $2p_{3/2}$ spectra of the pl_$CoNiO_x$ films differ from the one of pure pl_NiO_x (Ni6, red). The characteristic multiplet structure of NiO at a BE of around 854.4 eV is not as pronounced in the Ni 2p spectra of the pl_$CoNiO_x$ films as for pure pl_NiO_x. In addition, the peak at a BE of 855.8 eV identifies the presence of either NiO(OH) or $Ni(OH)_2$. Sample CoNi1 shows even an asymmetric shape of the Ni 2p line as observed for in air deposited pl_$NiO_x(OH)_y$ (Ni9, red). All in all, the double peak structure of the Ni 2p lines identify a superimposition of different compounds like NiO and NiO(OH) or $Ni(OH)_2$.
Nickel cobaltite has been widely studied with XRD, Mössbauer spectroscopic techniques and also with XPS. [148–151] Contradictory to our findings, the Co 2p spectrum of $NiCo_2O_4$, which was prepared by a low temperature combustion method, shows clearly the dominating presence of the Co(III) oxidation state. [150] Interestingly, the Ni 2p spectrum of $NiCo_2O_4$ does not show the multiplet feature which is characteristic for Ni(II) in NiO. [148] Instead the Ni $2p_{3/2}$ line is composed of a symmetric peak at a BE of 854.5 eV and an associated satellite structure at a BE

of 861.3 eV. [150] Kim et al. compared the XPS spectra of $NiCo_2O_4$ synthesized by a sol-gel route and by thermal decomposition of cobalt and nickel nitrates. [148] They report a BE of 780.1 eV for the Co $2p_{3/2}$ peak and a flat, weak satellite structure, which indicate that only few Co^{2+} cations occupy octahedral sites whereas the majority of the cobalt cations are found in the octahedral sites as Co^{3+}. [148] Nickel cations are reported to mainly occupy the octahedral sites in $NiCo_2O_4$ as Ni^{2+}. The Ni $2p_{3/2}$ is positioned at a BE of 854.9 eV spectrum like in NiO and the intense satellite structure of high spin Ni^{2+} is reported. [148]

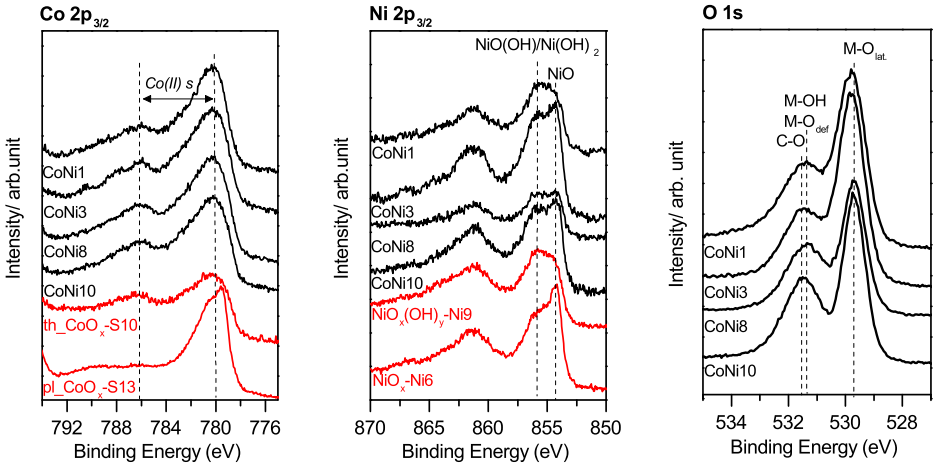

Figure 10.3. XPS Co $2p_{3/2}$, Ni $2p_{3/2}$ and O 1s detail spectra of the as deposited pl_$CoNiO_x$ samples (CoNi1, CoNi3, CoNi8 and CoNi10). For comparison, the Co 2p and Ni 2p detail spectra of pure pl_CoO_x-S13, th_CoO_x-S10, NiO_x-Ni6 and $NiO_x(OH)_y$-Ni9 are shown in addition.

The XPS detail spectra of the Co $2p_{3/2}$, Ni $2p_{3/2}$ and O 1s region of the pl_$CoNiO_x(OH)_y$ samples are presented in Figure 10.4. The intense satellite structure at 786.3 eV shows, that the majority of the Co cations are present as Co(II) in all samples (CoNi11-13). Since air is used as a reactive gas, the Co $2p_{3/2}$ appears at a BE of 780.5-781 eV with a satellite structure at a distance between 5.3-5.7 eV suggesting the presence of $Co(OH)_2$ and CoO.

The electronic structure of Ni differs, while the maximum intensity of the Ni $2p_{3/2}$ peak is in case of CoNi11 at a BE of 854.7 eV as observed for NiO, the Ni $2p_{3/2}$ peak of CoNi13 has its maximum intensity at 856.1 eV indicating the presence of either NiO(OH) or $Ni(OH)_2$. Anyhow, the Ni 2p spectra are not easy to assign and suggest the deposition of a mixture of NiO(OH), $Ni(OH)_2$ and NiO.

The O 1s peak of lattice oxygen is positioned at a BE of 529.9±0.1 eV for all pl_$CoNiO_x(OH)_y$/Ti films (CoNi11-13). The presence of hydroxide moieties is only clearly identified for pl_$CoNiO_x(OH)_y$ films CoNi12 and CoNi13 by the increased HBE feature at a BE of 531.7 eV. The HBE feature is about 62 % of the total O 1s line (excluding C-O and Ti-O contributions) in case of pl_$CoNiO_x(OH)_y$-CoNi13 and about 36 % in case of pl_$CoNiO_x(OH)_y$-CoNi12. The O 1s spectrum of pl_$CoNiO_x(OH)_y$-CoNi11 exhibits a HBE feature of only 23 %. Hence, the majority of Co and Ni has to be present as CoO and NiO in pl_$CoNiO_x(OH)_y$-CoNi11.

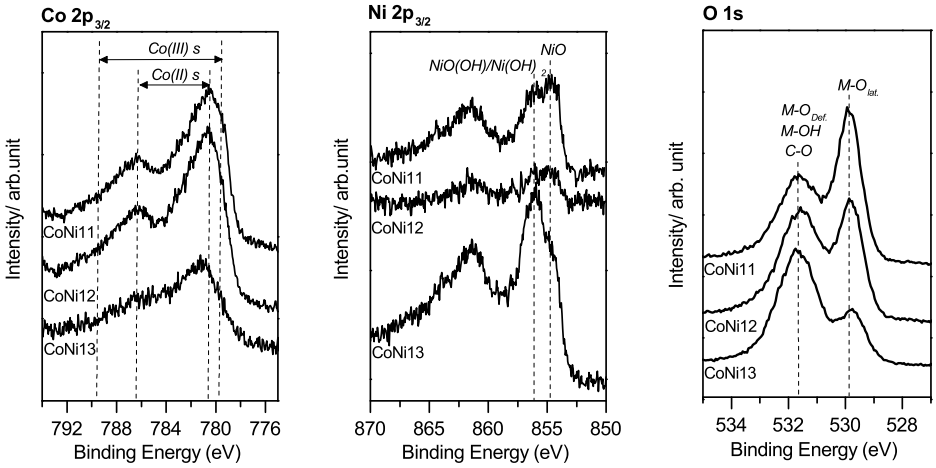

Figure 10.4. XPS Co $2p_{3/2}$, Ni $2p_{3/2}$ and O 1s detail spectra of the as deposited pl_$CoNiO_x(OH)_y$ samples (CoNi11, CoNi12, CoNi13).

Neither the use of air as a reactive gas nor the use of oxygen as a reactive gas results in the deposition of a bimetallic $CoNiO_x$ film. The XPS characterization suggests the deposition of an undefined mixture of $CoO/Co(OH)_2$ and $NiO/NiO(OH)/Ni(OH)_2$. From the previous discussion it becomes clear, that the XPS detail spectra of the PECVD deposited $CoNiO_x$ and $CoNiO_x(OH)_y$ films are highly complex and difficult to interpret.

It was reported earlier, that $NiCo_2O_4$ needs to be deposited in a low temperature process since it is thermally and structurally unstable at temperatures above 400 °C at atmospheric pressure. [150] Verma et al. for example synthesized $NiCo_2O_4$ by the thermal combustion reaction of Co and Ni nitrates at 200 °C for 4 h, which was followed by an 4 h annealing at either 300 °C or 400 °C. Whereas the XRD patterns of samples annealed at 300 °C showed a pure spinel phase, additional reflexes corresponding to NiO or CoO appeared when the samples were annealed at 400 °C. [150] To our knowledge, there are no literature reports about the low-temperature PECVD deposition of $NiCo_2O_4$ but previous researchers successfully deposited off-stoichiometric Ni-Co-O spinels by radio-frequency (RF) cosputtering from CoO and NiO targets and by reactive sputtering from alloyed metal targets. [152–155] McCloy et al. for example deposited $NiCo_2O_x$ films on cleaned Si substrates using RF reactive magnetron sputtering at a substrate temperature of 300 °C using a mixture of 50 % Ar/50 % O_2 gas at a partial pressure of 5 mTorr. [154]

Unfortunately we can not report the successful deposition of bimetallic CoNi- catalyst phases with PECVD. Our XPS results indicate, that the formation of pure metal oxide phases are thermodynamically favored using an inductively coupled N_2/O_2 plasma in the pressure regime between 1000-3000 mtorr and substrate temperatures between 230-260 °C.

10.2.2 PECVD of pl_$CoFeO_x(OH)_y$ and pl_$CoCuO_x(OH)_y$

Based on the electrochemical characterization, which will be discussed in Chapter 10.3, we focused on the deposition of $CoMO_x(OH)_y$ since these were more active. The XPS detail spectra of PECVD deposited pl_$CoFeO_x(OH)_y$/Ti are not shown since no relevant changes were observed in the electronic structure: The Co $2p_{3/2}$ spectra of the pl_$CoFeO_x(OH)_y$/Ti samples agree with those reported for pl_$CoNiO_x(OH)_y$/Ti indicating the deposition of $CoO/Co(OH)_2$. The Fe $2p_{3/2}$

spectrum is similar to the one reported for pl_FeO_x. Table 10.3 lists the preparation parameters of pl_$CoFeO_x(OH)_y$/Ti samples.

Table 10.3. Preparation parameters of PECVD deposited pl_$CoFeO_x(OH)_y$/Ti using the experimental setup D.

Sample	T_{Sub} *[°C]*	$\mathbf{T_{Prec}}$ *[°C]*	$\mathbf{T_{Prec}}$ *[°C]*	$\mathbf{f_{N_2,Co}}$ *[°C]*	$\mathbf{f_{N_2,Fe}}$ *[sccm]*	$\mathbf{f_{Air}}$ *[sccm]*	$\mathbf{t_{Dep}}$ *[min]*	$\mathbf{p_{proc}}$ *[mtorr]*	**d** *[cm]*
CoFe81	260	180	185	200	20	200	30	2730	13.5
CoFe82	260	180	190	200	20	200	30	2590	13.5

During the SusHy project, the incorporation of Cu as a second metal was decided. Table 10.4 summarizes the deposition parameters of pl_$CoCuO_x(OH)_y$/Ti. Since CuO_x itself was not deposited and characterized, the Cu 2p spectrum of sample pl_$CoCuO_x(OH)_y$-CoCu98 is shown as an example in Figure 10.5.

Table 10.4. Preparation parameters of the PECVD deposited pl_$CoCuO_x$/Ti films using either oxygen (CoCu95) or air (CoCu96) as a reactive gas and of thermally deposited th_$CoCuO_x$/Ti (CoCu97). All samples are deposited in the experimental setup D. In case of sample CoCu98 no XPS measurement was conducted.

Sample	T_{Sub} *[°C]*	$\mathbf{T_{Prec,Co}}$ *[°C]*	$\mathbf{T_{Prec,Cu}}$ *[°C]*	$\mathbf{f_{N_2,Co}}$ *[°C]*	$\mathbf{f_{N_2,Cu}}$ *[sccm]*	$\mathbf{f_{O_2}}$ *[sccm]*	$\mathbf{f_{Air}}$ *[sccm]*	$\mathbf{t_{Dep}}$ *[min]*	$\mathbf{p_{proc}}$ *[mtorr]*	**Co** *[%]*	**Cu** *[%]*
CoCu95	260	180	190	200	30	500	0	40	3450	77	23
CoCu96	300	180	190	200	30	0	500	40	2640	45	55
CoCu98	260	180	190	200	30	0	200	30	2750	-	-
CoCu97	460	180	190	200	30	100	0	30	4730	87	13

The primary peak of the Cu $2p_{3/2}$ line is located at a BE of 932.4±0.1 eV, which agrees well with the BE reported for Cu_2O and Cu. [156] Cu_2O and Cu are not distinguishable by a chemical shift of the BE but by a different position of their LMM-2 Auger transition. The peak of the Auger transition at a BE of 570 eV, which is shown in Figure 10.5 b, reveals the deposition of Cu_2O. [157]

The less intense peaks are attributed to the presence of CuO and $Cu(OH)_2$. The Cu $2p_{3/2}$ peak of CuO and $Cu(OH)_2$ are typically located at higher BE of 933.6 eV and of 934.8 eV. [156] In addition, the main peak of CuO is accompanied by a satellite feature at a BE distance of 9 eV. Since Cu_2O has a fully occupied d shell, no O-Cu 3d charge transfer is possible and the satellite is absent. [157] The Co $2p_{3/2}$ spectrum of pl_$CoCuO_x(OH)_y$-CoCu98/ is similar to the one reported for pl_$CoNiO_x(OH)_y$ and pl_$CoFeO_x(OH)_y$.

Contradictory to our findings, Cu cations are present as Cu^{2+} in $CuCo_2O_4$. Liu et al. synthesized $CuCo_2O_4$ by thermal combustion of Cu and Co nitrates and confirmed the structure of spinel with XRD. They identified Cu^{2+} as the predominant species in XPS by the Cu $2p_{3/2}$ peak at a BE 934.4 eV, which is higher in BE compared to Cu^{2+} in CuO. [158, 159] It can be concluded that also in case of PECVD prepared pl_$CoFeO_x$ and pl_$CoCuO_x(OH)_y$ the XPS results suggest

the deposition of a mixture of single metal oxide phases.

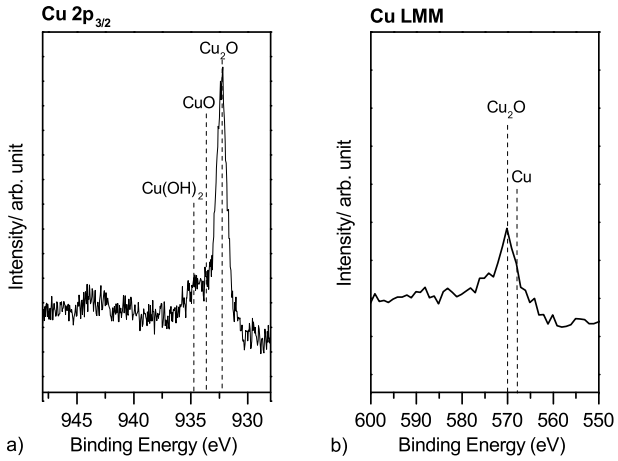

Figure 10.5. a) XPS detail spectrum of the Cu $2p_{3/2}$ region of pl_$CoCuO_x(OH)_y$/Ti-CoCu98. b) The extract of the survey spectrum shows the auger transition LMM-2.

Also the thermal operation mode did not offer an alternative to deposit a homogeneous bimetallic oxide catalyst. The XPS spectra of th_$CoCuO_x(OH)_y$ (CoNi97) matches the one reported for PECVD deposited pl_$CoCuO_x(OH)_y$.
In literature, the actual low temperature deposition reaction is always followed by an 4-6 hour annealing procedure at temperatures between 300-400 °C. [37, 150, 152, 159, 160] Verma et al. for example synthesized $NiCo_2O_4$ at a temperature of 200 °C. After keeping the temperature constant for 4 h, the samples were annealed at 300 °C for 4 h. [150] The solvothermal synthesis of $CuCo_2O_3$, which was performed at 150 °C for 3 h, was followed by a 2 h annealing at 300 °C and $NiCo_2O_y$ was annealed for 24 h at 320 °C. [159, 160] One can assume, that in case of PECVD deposited catalyst films a subsequent annealing would have resulted in a bimetallic catalyst phase but this was not the aim of this work. A solar device cannot be annealed for several hours at temperatures above 200 °C. Hence, a subsequent annealing procedure was not included in the deposition procedure.

10.3 Electrochemical characterization

10.3.1 Open circuit potential and electrochemical impedance spectroscopy

Although the experimentally determined open circuit potential does not give any valuable information, some values of differently prepared $CoMO_x$ and $CoMO_x(OH)_y$ (M=Ni Cu) are plotted in Figure 10.6 a. There is neither a correlation found between the OCP and the resulting overpotential nor between the OCP and the atomic concentration of the second metal. The potential range of the OCP agrees with the one observed for the pure metal oxides and varies between 0.55- 1.2 V. Independent of the catalysts composition, the electrolyte resistance is 6.5 ±1 Ohm in case of 1 KOH and 48.9 ±1.5 Ohm in case of 0.1 M KOH.

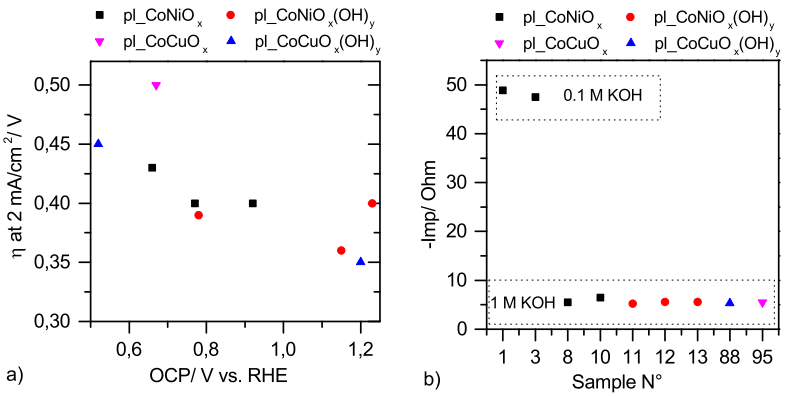

Figure 10.6. a) Plot of the OCP of $CoMO_x$/Ti and $CoMO_x(OH)_y$/Ti (M=Ni Cu) recorded in 1 M KOH as a function of the overpotential at a current density of 2 mA/cm^2. b) R_E plotted for various pl_CoNi- and pl_CoCu- catalysts.

10.3.2 Cyclic voltammetry and galvanostatic polarization: Determination of the activity and stability

Figure 10.7 shows the cyclic voltammograms of pl_$CoNiO_x$ and of pl_$CoNiO_x(OH)_y$ samples in comparison to the most active pl_CoO_x, pl_$CoO_x(OH)_y$, pl_NiO_x and pl_$NiO_x(OH)_y$ samples. First it can be noticed, that none of the bimetallic catalysts is as active as the pure pl_$CoO_x(OH)_y$ and pl_$NiO_x(OH)_y$ samples. Except of sample pl_$Co_{62\%}Ni_{38\%}O_x$-CoNi1 all $CoNiO_x$ films showed an even lower electrochemical activity than the pure metal oxides. The $CoNiO_x(OH)_y$ films, which were deposited with air as a reactive gas, show overall lower overpotentials compared to the $CoNiO_x$ films deposited with oxygen as a reactive gas. To figure out the influence of adding Ni to pl_$CoO_x(OH)_y$ on the activity, pl_$CoNiO_x(OH)_y$ films with different Ni contents were deposited. But no correlation between the Ni content and the activity could be found.

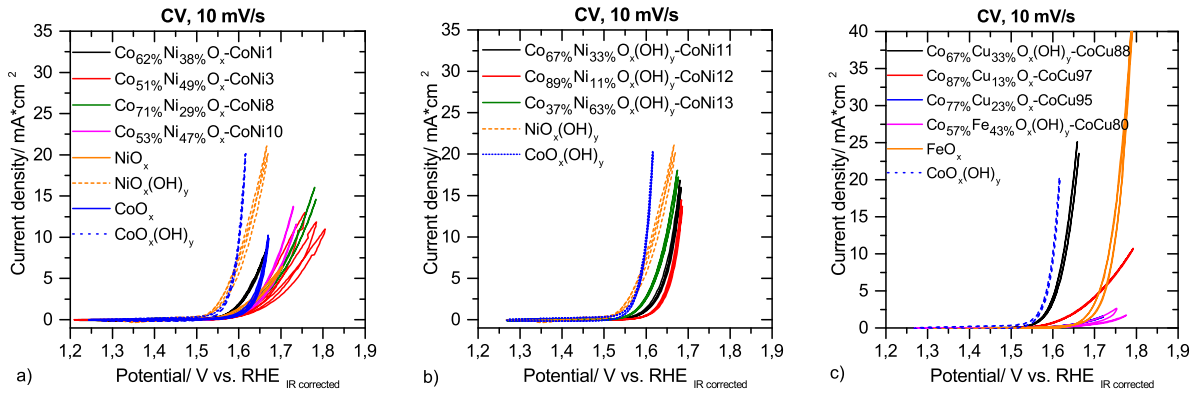

Figure 10.7. Cyclic voltammograms of a) pl_$CoNiO_x$ films (CoNi1-*black*, CoNi3-*red*, CoNi8-*green*, CoNi10-*magenta*), b) pl_$CoNiO_x(OH)_y$ films (CoNi11-*black*, CoNi12-*red*, CoNi13-*green*) and c) pl_$CoCuO_x(OH)_y$ (CoCu88-*black*), th_$CoCuO_x$ (CoCu97-*red*), pl_$CoCuO_x$ (CoCu95-*blue*), pl_$CoFeO_x(OH)_y$ (CoCu80-*magenta*). All cyclic voltammogrames were recorded with a scan rate of 10 mV/s in 1 M KOH, only samples CoNi1 and CoNi3 were tested in 0.1 KOH.

The fact that the onset potentials of all catalysts are in a similar range and that only the increase in the current density differs suggest even more that two separate phases are deposited instead of a real bimetallic CoNi-oxide. Also the addition of Cu or Fe did not improve the catalytic activity of pl_$CoO_x(OH)_y$. Sample pl_$Co_{67\%}Cu_{33\%}O_x(OH)_y$-CoCu88 represents the most active bimetallic catalyst with an overpotential of 0.4 V at a current density of 10 mA/cm^2 and an onset

potential similar to the one of pure pl_$CoO_x(OH)_y$.
Figure 10.8 provides an overview of the overpotentials reported at a current density of 10 mA/cm^2 for different catalysts with a layer thickness of at least 100 Å. In conclusion, the admixture of a second metal did not result in an increased activity of the PECVD deposited catalysts. The cyclic voltammograms of the bimetallic catalysts show a deteriorated increase in current but a similar onset potential compared to the single metal catalysts.

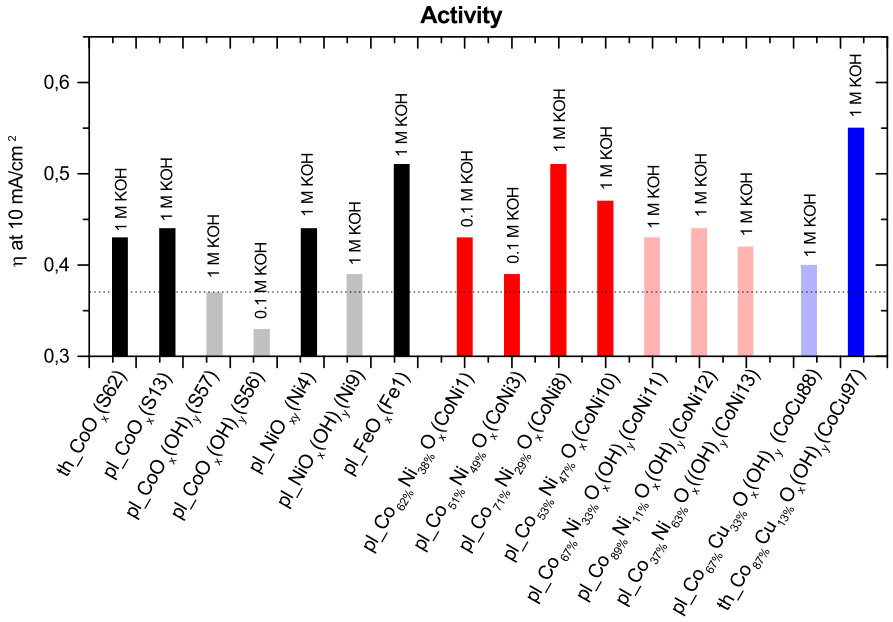

Figure 10.8. IR corrected overpotentials at a current density of 10 mA/cm^2 plotted for various bimetallic catalyst films tested either in 1 M KOH or 0.1 M KOH in comparison to the once of the pure catalyst films.

Figure 10.9 shows the degradation slopes, which were obtained from the 5 min GS test performed at a current density of 10 mA/cm^2 in 1 M KOH.

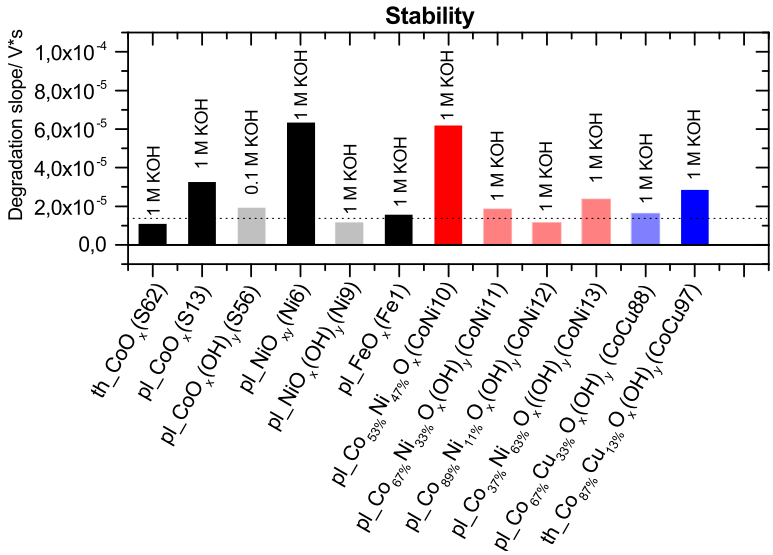

Figure 10.9. Degradation slopes of various bimetallic catalyst films derived from the GS tests.

The degradation slopes are comparable to the ones reported for the single metal oxide catalysts.

Pl_CoNiO$_x$-CoNi10 for example shows with a value of 6.2*10^{-5} V/s a similar degradation slope as pl_NiO$_x$ (6.4*10^{-5} V/s) and the degradation slopes of the samples pl_CoNiO$_x$(OH)$_y$-CoNi11 and -CoNi13 are comparable to the ones reported for pl_CoO$_x$(OH)$_y$ and pl_NiO$_x$(OH)$_y$. The electrochemical results confirm which was already suggested from the XPS results. There was rather a complex mixture of CoO/Co(OH)$_2$ and NiO/NiO(OH)/Ni(OH)$_2$ deposited instead of a real bimetallic $NiCo_2O_4$ catalyst film.

To further clarify the catalysts nature, XPS measurements were conducted after the electrochemical characterization since the comparison of the catalysts composition from before and after the electrochemical test can give a hint if there are separate phases existing which degrade differently. Figure 10.10 compares the catalysts composition from before and after the electrochemical characterization. The different relative loss of Co and Ni can be assigned to the separate degradation of the coexisting pure metal oxide catalysts. In case of samples pl_CoNiO$_x$-CoNi1 and -CoNi10 for example, the relative loss of Co is about 39 % and 37 % whereas the relative loss of Ni is only about 9 % and 19 %. With this, the PECVD deposited Co phase seems to be less stable compared to the Ni phase in pl_CoNiO$_x$ and pl_CoNiO$_x$(OH)$_y$ films. Only in case of sample CoNiO$_x$(OH)$_y$-CoNi13 the relative percentages of Co and Ni increased due to the degradation of carbon impurities indicating a certain stability. The admixture of Cu does not have a negative effect on the stability of the Co phase. The pl_CoCuO$_x$(OH)$_y$-CoCu88 film shows a Cu loss of 100 % whereas the relative Co loss is only about 17 %. The fact, that the degradation slope of pl_CoCuO$_x$(OH)$_y$-CoCu88 agrees with the one reported for pl_CoO$_x$(OH)$_y$ and that no Cu is found after the electrochemical test indicate that the main catalyst loss have to occur already during the CV. Therefore the galvanostatic scan itself represent the stable catalyst phase which emerged after the CV. Otherwise a stronger gradient in the GS test should be observed.

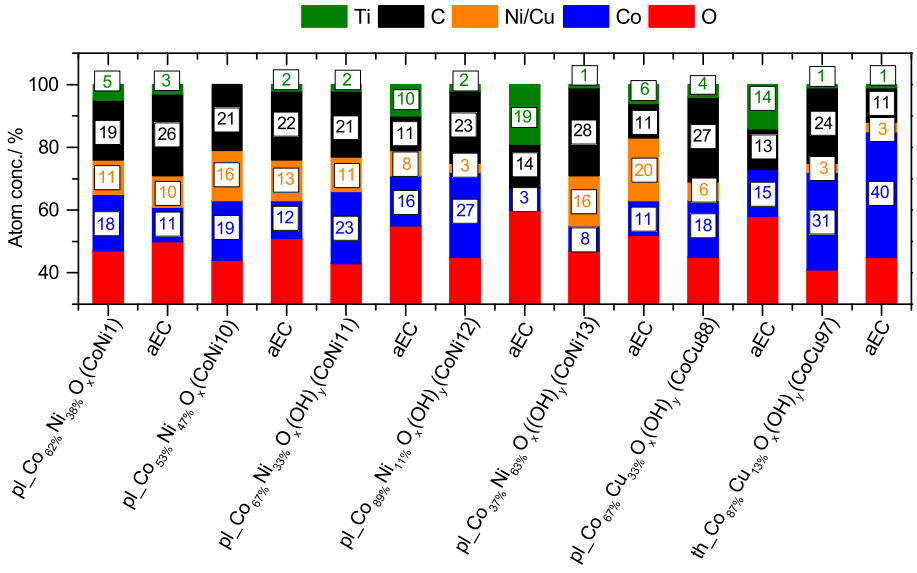

Figure 10.10. Comparison of the catalysts composition (Co, Ni/Cu, O, C, Ti) detemined with XPS from before and after the electrochemical characterization.

This means that in case of sample pl_CoCuO$_x$(OH)$_y$-CoCu88 an only 1.3 nm thin pl_CoO$_x$(OH)$_y$ film operates as a catalyst during the galvanostatic polarization. The results of the electrochemical

test in combination with the XPS characterization show that the deposition of a bimetallic catalyst phase was not successful and, therefore, no activity enhancement is observed.

10.4 Change of the oxidation state of Co and Ni in $CoMO_x$ and $CoMO_x(OH)_y$

The electrochemical induced change of the catalysts surface structure and the accompanied change of the oxidation state has already been discussed in Chapter 9 for differently prepared Co and Ni catalysts. Figure 10.11 compares the XPS spectra of the most active bimetallic CoNi catalyst ($Co_{37\%}Ni_{63\%}O_x(OH)_y$-CoNi13) with the XPS data after a galvanostatic conditioning of 5 min. The Co $2p_{3/2}$ peak matches with the one reported for in air deposited pl_$CoO_x(OH)_y$. It is located at a BE of 780.9 eV and the Co(II) satellite is observed at a distance of 5.1 eV identifying $Co(OH)_2$. The characteristic satellite of CoO is typically positioned at a distance of 6 eV to the main peak. In agreement with published results on pl_$CoO_x(OH)_y$, the $Co(OH)_2$ sites transform to the active CoO(OH) precursor phase during OER. The structural change is confirmed by the shift of the Co $2p_{3/2}$ peak to a lower energy of 780.3 eV and the appearance of the Co(III) satellite at a distance of 10 eV after the electrochemical test. [138] The intensity of the Co(II) satellite is decreased for $Co_{37\%}Ni_{63\%}O_x(OH)_y$aEC.
The Ni $2p_{3/2}$ peak is located at 856.0 eV with a FWHM of 2.8 eV, which agrees with the BE position and the FWHM reported for in air deposited pl_$NiO_x(OH)_y$ (856.0 eV; 2.7 eV).The oxidation states of different Ni species are not as easy to distinguish by their satellite structure as those of Co. Hence, the Ni 2p line shape has to be used for identification as described for the investigation of pl_NiO_x and pl_$NiO_x(OH)_y$. For a further validation of the Ni 2p line shape component fits have to be defined for $Ni(OH)_2$ and NiO(OH). For this purpose, the Ni 2p line of the as deposited $NiO_x(OH)_y$/Ti-Ni9 was used as a NiO(OH) reference line shape, since the LBE:HBE ratio of 53:47 and the asymmetric of the Ni 2p peak are closest to the literature values. The line shape of the electrochemical conditioned $NiO_x(OH)_y$-Ni9 was used to construct the line shape representing $Ni(OH)_2$. Figure 10.11 shows the fitted Ni $2p_{3/2}$ spectrum of $Co_{37\%}Ni_{63\%}O_x(OH)_y$-CoNi13 using the component line shape fits for NiO(OH) (red) and $Ni(OH)_2$ (blue). All in all the component fit provide a good description of the Ni $2p_{3/2}$ spectrum (green) and suggest the coexistence of NiO(OH) and $Ni(OH)_2$. Also the valence band does not show the characteristic Ni 3d feature of NiO (Figure 10.13). The increase of the $Ni(OH)_2$/NiO(OH) component fit ratio from 0.3 for the as deposited film to 1.0 after the conditioning shows the in part conversion of NiO(OH) to $Ni(OH)_2$ during conditioning.
As found for the pure $CoO_x(OH)_y$ and $NiO_x(OH)_y$, the O 1s spectrum exhibits a LBE feature of 38 % relative intensity, which is attributed to lattice oxygen in NiO(OH) and a HBE feature of 62 % relative intensity, which is assigned to M-OH in $Co(OH)_2$, $Ni(OH)_2$ and NiO(OH). The amount of the LBE feature increases from 38 % in the as deposited film to 44 % after the galvanostatic conditioning. This is mainly attributed to the formation of CoO(OH) since Co is mainly found as Co(III) after the electrochemical test. Table 10.5 summarizes the calculated areas of the LBE and the HBE features excluding the contribution of the C-O and Ti-O species.

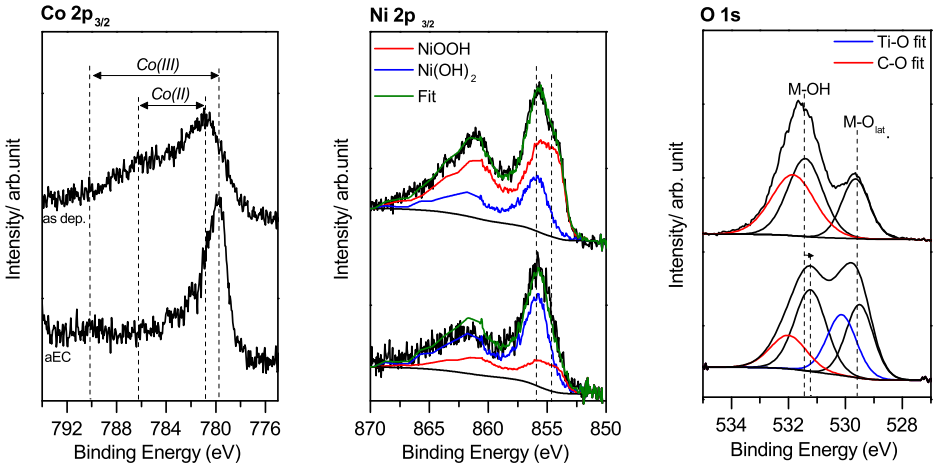

Figure 10.11. XPS details spectra of the Co 2p, Ni 2p and O 1s region of as deposited $Co_{37\%}Ni_{63\%}O_x(OH)_y$/Ti and after the electrochemical test.

While the Co-sites in pl_$CoNiO_x(OH)_y$/Ti seem to behave similar to the Co sites in pure pl_$CoO_x(OH)_y$, differences are observed for the Ni sites. The XPS results of pure pl_$NiO_x(OH)_y$ suggested, that the $Ni(OH)_2$ sites are oxidized to the active NiO(OH) during OER and that $Ni(OH)_2$ recovers after the oxygen release from NiO(OH). The Ni sites in the bimetallic catalyst only show a low ability to recover $Ni(OH)_2$, a $Ni(OH)_2$/NiO(OH) component fit ratio of only 1 was determined after the electrochemical characterization, which identifies the coexistence of NiO(OH) and $Ni(OH)_2$ in a similar ratio after the conditioning. Compared to this, a $Ni(OH)_2$/NiO(OH) ratio of 4 was calculated for the pure $NiO_x(OH)_y$ sample. Recent results published by Trotochaud et al. have already hypothesized a negative influence of Co on the formation of the active layered Ni hydroxide phase, which forms during the galvanostatic conditioning at 10 mA/cm^2. [5] Also the XPS detail spectra of $Co_{67\%}Cu_{33\%}O_x(OH)_y$-CoCu88 show that Co(II) undergoes an oxidation to Co(III) and the LBE/HBE ratio of 58:42 suggest the formation of CoO(OH) (Figure 10.12).

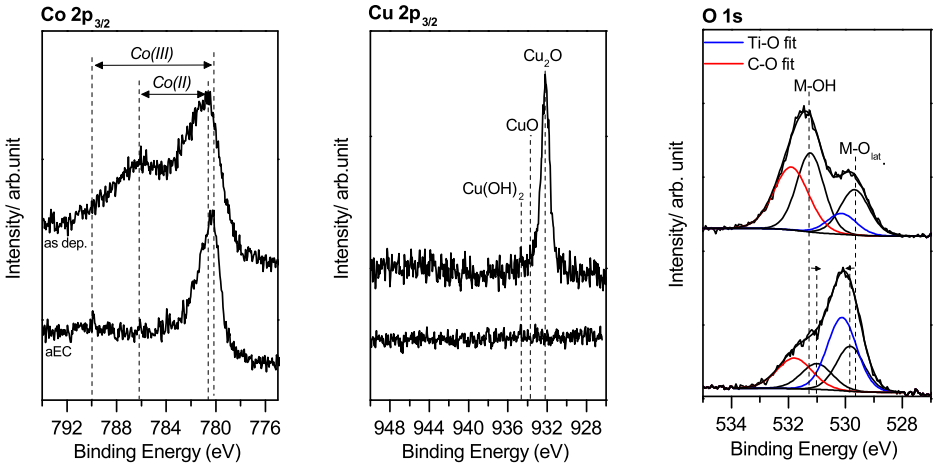

Figure 10.12. XPS details spectra of the Co $2p_{3/2}$, Cu $2p_{3/2}$ and O 1s region of as deposited $Co_{67\%}Cu_{33\%}O_x(OH)_y$/Ti-CoCu88 and after the conditioning of 5 min.

Whereas Co can transform to its active precursor phase, Cu_2O completely dissolves and no Cu is found after the electrochemical characterization in the Cu $2p_{3/2}$ spectrum. Hence, the

electrochemical activity is only attributed to pl_$CoO_x(OH)_y$ and the formation of CoO(OH). Table 10.5 lists the Co(III), the HBE and the LBE contents as well as the BE position of the Co 2p3/2 peak, the VBM and the work function. Both catalysts show an increased work function after the electrochemical test, which matches to the ones reported for the conditioned pure pl_$CoO_x(OH)_y$ and pl_$NiO_x(OH)_y$ samples.

Table 10.5. Binding energies of the Co $2p_{3/2}$ peak, the work function, the valence band maximum as well as the calculated Co(III) content and the percentages of the O 1s features. All binding energies are corrected for the C 1s at 284.5 eV.

Sample	Co(III) [%]	Co $2p_{3/2}$ [eV]	O $1s_{LBE}$ [%]	O $1s_{HBE}$ [%]	VBM [eV]	ϕ [eV]
pl_$Co_{37\%}Ni_{63\%}O_x(OH)_y$	0	780.9	38	62	0.6	4.3
pl_$Co_{37\%}Ni_{63\%}O_x(OH)_y$aEC	75	780.2	44	56	0.6	5.7
pl_$Co_{67\%}Cu_{33\%}O_x(OH)_y$	0	780.3	40	60	0	4.5
pl_$Co_{67\%}Cu_{33\%}O_x(OH)_y$aEC	84	780.2	58	42	0.9	5.8

Figure 10.13 shows the valence band spectra of sample pl_$Co_{37\%}Ni_{63\%}O_x(OH)_y$-CoNi13 and of sample pl_$Co_{67\%}Cu_{33\%}O_x(OH)_y$-CoCu88 from before and after the 5min galvanostatic conditioning in 1 M KOH. The valence band maximum of the as deposited pl_$Co_{37\%}Ni_{63\%}O_x(OH)_y$-CoNi13 does not change after the electrochemical test and is with a value of 0.6 eV in the region of the VBM reported for pl_$CoO_x(OH)_y$.

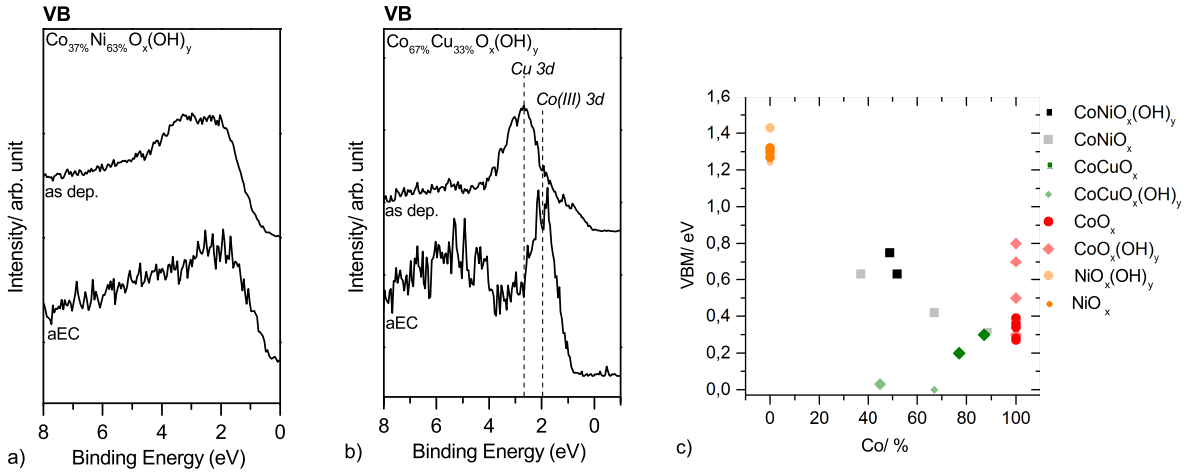

Figure 10.13. Valence band spectra of a) pl_$Co_{37\%}Ni_{63\%}O_x(OH)_y$-CoNi13 and b) pl_$Co_{67\%}Cu_{33\%}O_x(OH)_y$-CoCu88 from before and after the electrochemical characterization in 1 M KOH. c) VBM of various catalysts in dependence on the Co content.

Figure 10.13 c shows the VBM in dependence on the percentage of Co. The pure pl_$CoO_x(OH)_y$ films have a Co content of 100 % and the pl_$NiO_x(OH)_y$/pl_$CuO_x(OH)_y$ films have a Co content of 0 %. The admixture of Cu leads to a decrease in intensity at the VBM for the as deposited pl_$CoCuO_x(OH)_y$ samples. After Cu is dissolved, the VBM is increased due to the dominating

presence of pl_$CoO_x(OH)_y$/Ti. Sample pl_$Co_{67\%}Cu_{33\%}O_x(OH)_y$-CoCu88 for example shows a VBM of 0.9 eV after the GS test and the appearance of the characteristic Co(III) 3d feature where as the Cu 3d feature is vanished.
All in all the results indicate that the Co sites can transform to the active CoO(OH) precursor phase even in the presence of other metal oxide phases. Furthermore the detailed XPS investigations confirm the suggestion, that a mixture of separate catalyst phases are deposited by PECVD instead of one bimetallic catalyst phase. It can be concluded, that the parameter window, which is limited by the experimental setup to a certain pressure and flow regime, is not sufficient to deposit homogeneous bimetallic catalyst phases.

11. Conclusion and outlook

In this thesis a plasma enhanced chemical vapor deposition system could be successfully established to deposit sytematically thin film cobalt based oxide catalysts for the electrochemical oxygen evolution reaction (OER), for the first time.

First, the deposition of cobalt oxide was investigated in detail. It was found, that especially the operation mode (thermal versus plasma) and the choice of reactive gas (oxygen versus air) have an high impact on the resulting structure and electrochemical activity of the deposited catalysts. The thermal CVD process offered the possibility to deposit th_CoO_x as structure of rock salt (CoO) with an argon/oxygen ratio of 1 at substrate temperatures between 350-450 °C. The most active th_CoO_x required an overpotential of 0.43 V to reach a current density of 10 mA/cm^2.

With respect to the future goal to deposit the catalyst films directly onto a solar device, the plasma enhanced operation mode was investigated to realize the successful deposition at lower substrate temperatures. Operating in the plasma enhanced mode, the deposition of pl_CoO_x as structure of spinel has been found even at substrate temperatures between 180-260 °C using an argon/oxygen ratio of 1. The electrochemical performance of pl_CoO_x was optimized with respect to various preparation parameters as the substrate temperature, the layer thickness and the precursor temperature. The most active pl_CoO_x required an overpotential of 0.43 V to reach a current density of 10 mA/cm^2 and was deposited at a substrate temperature of 250 °C, a precursor temperature of 180 °C and an argon/oxygen ratio of 1.

To gain a further insight into the OER mechanisms, the catalysts surface was characterized with XPS before and after the electrochemical test. With respect to the reaction mechanism proposed in literature, the formation of different intermediates like hydroxides, oxyhydroxides and peroxohydroxides on the surface is expected. [20, 21, 55] In fact, the XPS results identify only a minor formation of hydroxide moieties on the oxide surfaces after the OER. Indeed, a slight hydroxide formation can be identified, but the surface of th_CoO_x and pl_CoO_x are predominantly present as structure of spinel after the OER with a maximum Co(III) content of 75 %. While the surface of th_CoO_x undergoes an oxidation from CoO to Co_3O_4 during OER, pl_CoO_x was already deposited as structure of spinel. Since the catalytic activity of th_CoO_x and pl_CoO_x could not be further optimized by varying the substrate temperature, precursor temperature, the argon/oxygen ratio or the deposition time, pl_$CoO_x(OH)_y$ was investigated as a starting material for the OER.

The deposition of a mixed pl_$CoO_x(OH)_y$ film was realized using air as a reactive gas. To be more precise, the detailed XPS investigation showed that the use of air lead to the deposition of a $CoO/Co(OH)_2$ mixture. The presence of hydroxide moieties in the starting material enhanced the catalytic activity drastically. The most active pl_$CoO_x(OH)_y$ required an overpotential of only 0.33 V to reach a current density of 10 mA/cm^2. By characterizing the catalysts surface after the electrochemical characterization, it could be proven, that the improved catalytic performance of pl_$CoO_x(OH)_y$ catalyst's based on the ability to transform to a CoO(OH) phase during OER. The pl_$CoO_x(OH)_y$ films, which had a Co(II) content of larger than 95 % in the initial deposited catalyst showed a Co(III) content of larger than 90 % after the galvanostatic conditioning. An

important correlation between the oxidation state and the overpotential was found by calculating the Co(III) content of differently prepared th_CoO_x, pl_CoO_x and pl_$CoO_x(OH)_y$ films: With increasing Co(III) content, the overpotential decreases. All in all, three important relationships were derived by characterizing the catalysts surface from before and after the electrochemical characterization with XPS: (i) Co(III) is identified as the active precursor oxidation state, (ii) Co(III) is stabilized best as CoO(OH) and (iii) the presence of hydroxide moieties support the potential induced formation of the CoO(OH) phase. [138]
Since there is no Co(II) observed after the galvanostatic conditioning at 10 mA/cm^2 of pl_$CoO_x(OH)_y$, the results promote the hypothesis that the active redox couple is Co(III)/Co(IV). To really identify Co(IV) an in-operando XPS technique would be necessary in future. One can assume that also the pl_CoO_x surface will slowly convert to $Co(OH)_2$, which finally is able to form a CoO(OH) phase. But the phase transformation starting from a pure oxide surface is kinetically hindered and takes therefore more time.
The same observations were made for pl_NiO_x, which was deposited using oxygen as a reactive gas and pl_$NiO_x(OH)_y$, which was deposited with air as a reactive gas. While pl_NiO_x required an overpotential of 0.45 V to achieve a current density of 10 mA/cm^2, pl_$NiO_x(OH)_y$ required only 0.37 V. The electrochemical characterization of PECVD deposited pl_$NiO_x(OH)_y$ films with different content of hydroxide moieties showed a clear correlation between the overpotential and the type of surface modification: The higher the content of hydroxide moieties, the lower is the resulting overpotential. Although the formation of NiO(OH) can be identified from a specific redox wave in the cyclic voltammetry and NiO(OH) is proposed in literature as the catalytically active and stable phase under operating conditions, the XPS results show the presence of both oxidation states, Ni(II) and Ni(III), after the electrochemical test. This observation is in contradiction to the result found for $CoO_x(OH)_y$, where only Co(III) was clearly detectable after the electrochemical characterization. As for CoO(OH), NiO(OH) is proposed in literature to operate with Ni(III)/Ni(IV) as the active redox couple for the OER. [143, 144] The predominant presence of Ni(II) in form of $Ni(OH)_2$ after the electrochemical test suggests the recovering of Ni(II) after the oxygen release by Ni(IV) under operating conditions. An analog mechanism was proposed for the well known CoPi catalyst by Surendranath. [140] They found the oxidation of Co(II) to Co(III) in the presence of phosphate by EPR and XANES as well as the further oxidation to Co(IV) during the OER . [140, 161] They also claimed that Co(II) is formed in the last reaction step when oxygen is released. [7, 140]
In addition to the deposition of single metal oxides and oxide/hydroxides an attempt was made to prepare bimetallic catalysts by PECVD. Bimetallic transition metal oxides are found in literature to be more active than the corresponding single metal compounds. [35, 36, 40, 162] However, we did not observe an electrochemical superior performance for $CoMO_x$ and $CoMO_x(OH)_y$ films (M=Ni, Fe, Cu). The bimetallic $Co_{67\%}Cu_{33\%}O_x(OH)_y$ film, which was deposited at a substrate temperature of 260 °C showed the best performance with an overpotential of 0.4 V at a current density of 10 mA/cm^2. The XPS characterization, which was performed after the electrochemical test, showed that the metals degraded independent of each other to different extends. In case of $Co_{67\%}Cu_{33\%}O_x(OH)_y$ for example, there was no more copper present within the film after the electrochemical characterization. Therefore, the activity was only related to a 1.3 nm thin

pl_$CoO_x(OH)_y$ film. Also in case of $Co_{62\ \%}Ni_{38\%}O_x$, the metal phases degraded independent from each other. While the Co content decreased by 39 %, a relative Ni loss of only 9 % was detected after OER. The results indicate that probably two separate metal catalyst phases were deposited by PECVD instead of one bimetallic catalyst phase. Only sample $Co_{37\%}Ni_{63\%}O_x(OH)_y$ did not show a significant and independent metal loss after OER in XPS. These results indicate that it is not sufficient to adopt the preparation parameters of the single metal oxide catalyst. The deposition of bimetallic oxide catalysts will have to be studied more intensively in future.
With respect to the undefined catalyst's composition and the complexity of the XPS spectra, it was difficult to study the influence of the different metals on the electronic structure in the bimetallic catalysts. Nevertheless an attempt was made to understand the interaction of Ni and Co within $Co_{37\%}Ni_{63\%}O_x(OH)_y$, since this catalyst film was stable. From the XPS spectra it could be deduced, that the $CoO_x(OH)_y$ phase within $Co_{37\%}Ni_{63\%}O_x(OH)_y$ was able to transform to CoO(OH) during OER analog to the phase transition of single metal $CoO_x(OH)_y$. The Ni $2p_{3/2}$ spectrum of $Co_{37\%}Ni_{63\%}O_x(OH)_y$ recorded after the electrochemical characterization differed from the one of single metal $NiO_x(OH)_y$. Contradictory to single metal $NiO_x(OH)_y$, in which $Ni(OH)_2$ was found as the predominant phase after the OER, a high content of NiO(OH) was detected after the OER in case of $Co_{37\%}Ni_{63\%}O_x(OH)_y$. These observations indicate that the recovering of $Ni(OH)_2$ from NiO(OH) is disturbed when oxygen is released. All in all the XPS characterization from before and after the electrochemical test show the importance of investigating the compositional changes occurring under operating conditions and that one cannot just correlate the electrochemical activity to the composition and structure of the initial as deposited catalyst. Although the electrochemical activity could not be enhanced by depositing bimetallic catalyst films, the performance of the single metal pl_$CoO_x(OH)_y$ films was remarkable and therefore of interest as catalyst for the solar water splitting device, which was established by Evonik. As a final result it should be noted, that the deposition of the most active catalyst on highly porous Ni foams as anode materials could be successfully realized. The $CoO_x(OH)_y/Ni_{foam}$ film, which was tested by the group of Prof. Schuhmann (University of Bochum), required an overpotential of only 0.31 V to reach a current density of 10 mA/cm^2. Unfortunately, the adhesion of the catalyst film on the Ni foam turned out to be not sufficient, a degradation slope of 0.318 mV/h was determined from the galvanostatic scan performed for 48 h in 1 M KOH at a current density of 10 mA/cm^2. Further investigations must focus on the improvement of the catalysts adhesion on the Ni-foam. In addition the admixture of a second metal to deposit a bimetallic catalyst phase should be further investigated. The deposition of a bimetallic oxide catalyst would allow to study the effect of a second metal on the electronic state of Co in more detail and may lead to even more active electrocatalysts for the oxygen evolution reaction.

Bibliography

[1] Bundesministerium für Wirtschaft und Energie (BMWi). *Die Energie der Zukunft- Erster Fortschrittsbericht zur Energiewende*. 2014.

[2] Hubert Landinger Evi Pschorr Schoberer Tetyana Raksha Reinhold Wurster Martin Zerta Matthias Altmann, Dr. Ulrich Bünger. *Die Rolle von Wasserstoff in der Energiewende-Entwicklungsstand und Perspektiven*. 2014.

[3] Peter Kurzweil and Otto K. Dietlmeier. *Elektrochemische Speicher*. Springer Vieweg, 2015.

[4] Mary W. Louie and Alexis T. Bell. An investigation of thin-film Ni-Fe oxide catalysts for the electrochemical evolution of oxygen. *Journal of the American Chemical Society*, 135(33):12329–12337, 2013.

[5] Lena Trotochaud, James K. Ranney, Kerisha N. Williams, and Shannon W. Boettcher. Solution-cast metal oxide thin film electrocatalysts for oxygen evolution. *Journal of the American Chemical Society*, 134(41):17253–17261, 2012.

[6] Bundesministerium für Bildung und Forschung (BMBF). *MattRessource- Materialien für eine ressourceneffiziente Industrie und Gesellschaft*. 2014.

[7] Vincent Artero, Murielle Chavarot-Kerlidou, and Marc Fontecave. Splitting water with cobalt. *Angewandte Chemie International Edition*, 50(32):7238–7266, 2011.

[8] Delahay P. Ruetschi, P. Influence of electrode material on oxygen overvoltage: A theoretical investigation. *Chem. Phys.*, 23:556, 1955.

[9] Michael E. Lyons and Michael P. Brandon. A comparative study of the oxygen evolution reaction on oxidised nickel, cobalt and iron electrodes in base. *Journal of Electroanalytical Chemistry*, 641(1–2):119–135, 2010.

[10] Lena Trotochaud, Samantha L. Young, James K. Ranney, and Shannon W. Boettcher. Nickel–iron oxyhydroxide oxygen-evolution electrocatalysts: The role of intentional and incidental iron incorporation. *Journal of the American Chemical Society*, 136(18):6744–6753, 2014.

[11] Michaela S. Burke, Lisa J. Enman, Adam S. Batchellor, Shihui Zou, and Shannon W. Boettcher. Oxygen evolution reaction electrocatalysis on transition metal oxides and (oxy)hydroxides : activity trends and design principles. *Chemistry of Materials*, 27(22):7549–7558, 2015.

[12] Juan Wang, Tian Qiu, Xu Chen, Yanluo Lu, and Wensheng Yang. Hierarchical hollow urchin-like $NiCo_2O_4$ nanomaterial as electrocatalyst for oxygen evolution reaction in alkaline medium. *Journal of Power Sources*, 268:341–348, 2014.

[13] Innocenzo G. Casella. Electrodeposition of cobalt oxide films from carbonate solutions containing Co(II)–tartrate complexes. *Journal of Electroanalytical Chemistry*, 520(1–2):119–125, 2002.

[14] C. Guyon, A. Barkallah, F. Rousseau, K. Giffard, D. Morvan, and M. Tatoulian. Deposition of cobalt oxide thin films by plasmaenhanced chemical vapour deposition (PECVD) for catalytic applications. *Surface and Coatings Technology*, 206(7):1673–1679, 2011.

[15] Young-Man Jeong, Jae-Keun Lee, Sam-Chul Ha, and Soo H. Kim. Fabrication of cobalt-organic composite thin film via plasma-enhanced chemical vapor deposition for antibacterial applications. *Thin Solid Films*, 517(9):2855–2858, 2009.

[16] Hyung-Jun Jeon, Sung-Chul Yi, and Seong-Geun Oh. Preparation and antibacterial effects of Ag–SiO_2 thin films by sol–gel method. *Biomaterials*, 24(27):4921–4928, 2003.

[17] Lynn C. Schumacher, Ingo B. Holzhueter, Ian R. Hill, and Michael J. Dignam. Semiconducting and electrocatalytic properties of sputtered cobalt oxide films. *Electrochimica Acta*, 35(6):975–984, 1990.

[18] A Dittmar, H Kosslick, J-P Müller, and M-M Pohl. Characterization of cobalt oxide supported on titania prepared by microwave plasma enhanced chemical vapor deposition. *Surface and Coatings Technology*, 182(1):35–42, 2004.

[19] Roger Kuhlman, George L. Schimek, and Joseph W. Kolis. An extended solid from the solvothermal decomposition of Co(Acac)3: Structure and characterization of $Co_5(OH)_2(O_2CCH_3)_8{\cdot}2H_2O$. *Inorganic Chemistry*, 38(1):194–196, 1999.

[20] J. K. Nørskov J. Rossmeisl, A. Logadottir. Electrolysis of water on (oxidized) metal surfaces. *Chemical Physics*, 319(1–3):178–184, 2005.

[21] J. Rossmeisl, Z. W. Qu, H. Zhu, G. J. Kroes, and J. K. Nørskov. Electrolysis of water on oxide surfaces. *Journal of Electroanalytical Chemistry*, 607(1-2):83–89, 2007.

[22] Holger Dau, Christian Limberg, Tobias Reier, Marcel Risch, Stefan Roggan, and Peter Strasser. The mechanism of water oxidation: From electrolysis via homogeneous to biological catalysis. *ChemCatChem*, 2(7):724–761, 2010.

[23] K.J. Vetter. *Electrochemical kinetics: Theoretical aspects*. Elsevier Science, 2013.

[24] C.H. Hamann and W. Vielstich. *Elektrochemie*. John Wiley and Sons Australia, Limited, 2005.

[25] W.J. Moore and D.O. Hummel. *Physikalische Chemie*. de Gruyter, 1986.

[26] R. G. Compton. *Electrode kinetics: Reactions*. Elsevier Science, 1987.

[27] Mary W. Louie and Alexis T. Bell. An investigation of thinfilm NiFe oxide catalysts for the electrochemical evolution of oxygen. *Journal of the American Chemical Society*, 135(33):12329–12337, 2013.

[28] D. A. Corrigan. The catalysis of the oxygen evolution reaction by iron impurities in thin film nickel oxide electrodes. *J. Electrochem. Soc.*, 134(2):377–384, 1987.

[29] M. Palomar-Pardavé A. B. Soto, E. M. Arce and I. González. Electrochemical nucleation of cobalt onto glassy carbon electrode from ammonium chloride solutions. *Electrochimica Acta*, 41(16):2647–2655, 1996.

[30] A. C. C. Tseung C. Q: Cui, S. P. Jiang. Reactive deposition of cobalt electrodes: Viii effect of oxygen reduction on the deposition of cobalt in Co(II) chloride dmf solution. *J. Electrochemical Soc.*, 139(6):1535–1544, 1992.

[31] M. P. Brandon M. E. G. Lyons. The oxygen evolution reaction on passive oxide covered transition metal electrodes in alkaline solution part ii - cobalt. *J. Electrochemical Sci.*, 3:1425–1462, 2008.

[32] J. Łojewska J. Tyczkowski, R. Kapica. Thin cobalt oxide films for catalysis deposited by plasma-enhanced metal–organic chemical vapor deposition. *Thin Solid Films*, 515(16):6590–6595, 2007.

[33] Arthur J. Esswein, Meredith J. McMurdo, Phillip N. Ross, Alexis T. Bell, and T. Don Tilley. Size-dependent activity of Co_3O_4 nanoparticle anodes for alkaline water electrolysis. *The Journal of Physical Chemistry C*, 113(33):15068–15072, 2009.

[34] A. T. Bell N. H. Chou, P. N. Ross and T. D. Tilley. Comparison of cobalt-based nanoparticles as electrocatalysts for water oxidation. *ChemSusChem*, 4(11):1566–1569, 2011.

[35] F. Rosalbino, S. Delsante, G. Borzone, and G. Scavino. Electrocatalytic activity of crystalline Ni–Co–M (M = Cr, Mn, Cu) alloys on the oxygen evolution reaction in an alkaline environment. *International Journal of Hydrogen Energy*, 38(25), 2013.

[36] Charles C. L. McCrory, Suho Jung, Jonas C. Peters, and Thomas F. Jaramillo. Benchmarking heterogeneous electrocatalysts for the oxygen evolution reaction. *Journal of the American Chemical Society*, 135(45):16977–16987, 2013.

[37] Alexey Serov, Nalin I. Andersen, Aaron J. Roy, Ivana Matanovic, Kateryna Artyushkova, and Plamen Atanassov. $CuCo_2O_4$ ORR/OER bi−functional catalyst: influence of synthetic approach on performance. *Journal of The Electrochemical Society*, 162(4):F449–F454, 2015.

[38] Yi Zhan, Guojun Du, Shiliu Yang, Chaohe Xu, Meihua Lu, Zhaolin Liu, and Jim Yang Lee. Development of cobalt hydroxide as a bifunctional catalyst for oxygen electrocatalysis in alkaline solution. *ACS Applied Materials and Interfaces*, 7(23):12930–12936, 2015.

[39] Yongye Liang, Yanguang Li, Hailiang Wang, Jigang Zhou, Jian Wang, Tom Regier, and Hongjie Dai. Co_3O_4 nanocrystals on graphene as a synergistic catalyst for oxygen reduction reaction. *Nat Mater*, 10(10):780–786, 2011. 10.1038/nmat3087.

[40] Tobias Grewe, Xiaohui Deng, Claudia Weidenthaler, Ferdi Schueth, and Harun Tueysuez. Design of ordered mesoporous composite materials and their electrocatalytic activities for water oxidation. *Chemistry of Materials*, 25(24):4926–4935, 2013.

[41] Yao Xiao, Ligang Feng, Chaoquan Hu, Vladimir Fateev, Changpeng Liu, and Wei Xing. $NiCo_2O_4$ 3 dimensional nanosheet as effective and robust catalyst for oxygen evolution reaction. *RSC Advances*, 5(76):61900–61905, 2015.

[42] Xiaohui Deng and Harun Tüysüz. Cobalt-oxide-based materials as water oxidation catalyst: Recent progress and challenges. *ACS Catalysis*, 4(10):3701–3714, 2014.

[43] B. E. Conway and M. Salomon. Electrochemical reaction orders: Applications to the hydrogen- and oxygen-evolution reactions. *Electrochimica Acta*, 9(12):1599–1615, 1964.

[44] A. De Battisti G. Lodi, E. Sivieri and S. Trasatti. Ruthenium dioxide-based film electrodes. *Journal of Applied Electrochemistry*, 8(2):135–143, 1978.

[45] Piero Castelli, Sergio Trasatti, Fred H. Pollak, and William E. O′Grady. Single crystals as model electrocatalysts. *Journal of Electroanalytical Chemistry and Interfacial Electrochemistry*, 210(1):189–194, 1986.

[46] S. Trasatti. Electrocatalysis: Understanding the success of dsa®. *Electrochimica Acta*, 45(15–16):2377–2385, 2000.

[47] A. B. Anderson S. P. Mehandru. *J. Electrochem. Soc.*, 136:158, 1989.

[48] Rodney D. L. Smith, Mathieu S. Prévot, Randal D. Fagan, Zhipan Zhang, Pavel A. Sedach, Man Kit Jack Siu, Simon Trudel, and Curtis P. Berlinguette. Photochemical route for accessing amorphous metal oxide materials for water oxidation catalysis. *Science*, 340(6128):60–63, 2013.

[49] Jian Wu, Yan Xue, Xin Yan, Wensheng Yan, Qingmei Cheng, and Yi Xie. Co_3O_4 nanocrystals on single-walled carbon nanotubes as a highly efficient oxygen-evolving catalyst. *Nano Research*, 5(8):521–530, 2012.

[50] Sophia R. Mellsop, Alister Gardiner, and Aaron T. Marshall. Electrocatalytic oxygen evolution on electrochemically deposited cobalt oxide films: Comparison with thermally deposited films and effect of thermal treatment. *Electrocatalysis*, 5(4):445–455, 2014.

[51] R. Parsons. The rate of electrolytic hydrogen evolution and the heat of adsorption of hydrogen. *Transactions of the Faraday Society*, 54(0):1053–1063, 1958.

[52] T. Otagawa J. O. Bockris. The electrocatalysis of oxygen evolution on perovskites. *The Journal of Electrochem. Soc.*, 131:290, 1984.

[53] S. Trasatti. Electrocatalysis in the anodic evolution of oxygen and chlorine. *Electrochimica Acta*, 29(11):1503–1512, 1984.

[54] S. Trasatti. Physical electrochemistry of ceramic oxides. *Electrochimica Acta*, 36(2):225–241, 1991.

[55] Isabela C. Man, Hai-Yan Su, Federico Calle-Vallejo, Heine A. Hansen, José I. Martínez, Nilay G. Inoglu, John Kitchin, Thomas F. Jaramillo, Jens K. Nørskov, and Jan Rossmeisl. Universality in oxygen evolution electrocatalysis on oxide surfaces. *ChemCatChem*, 3(7):1159–1165, 2011.

[56] S. Srinivasan S. Gottesfield. *J. Electroanal. Chem*, 86:89, 1978.

[57] M. Pourbaix. *Atlas of Electrochemical Equilibria in Aqueous Solutions*. Pergamon Press, 1966.

[58] Leanne G. Bloor, Pedro I. Molina, Mark D. Symes, and Leroy Cronin. Low ph electrolytic water splitting using earth-abundant metastable catalysts that self-assemble in situ. *Journal of the American Chemical Society*, 136(8):3304–3311, 2014.

[59] Michal Bajdich, Mónica García-Mota, Aleksandra Vojvodic, Jens K. Nørskov, and Alexis T. Bell. Theoretical investigation of the activity of cobalt oxides for the electrochemical oxidation of water. *Journal of the American Chemical Society*, 135(36):13521–13530, 2013.

[60] Boon Siang Yeo and Alexis T. Bell. Enhanced activity of gold-supported cobalt oxide for the electrochemical evolution of oxygen. *Journal of the American Chemical Society*, 133(14):5587–5593, 2011.

[61] Richard L. Doyle, Ian J. Godwin, Michael P. Brandon, and Michael E. G. Lyons. Redox and electrochemical water splitting catalytic properties of hydrated metal oxide modified electrodes. *Physical Chemistry Chemical Physics*, 15(33):13737–13783, 2013.

[62] M. E. Lyons L. D. Burke and O.J. Murphy. Influence of ph on the reduction of thick anodic oxide films on gold. *Journal of Electroanal. Chem.*, 132(1):247, 1982.

[63] Annette Foelske and Hans-Henning Strehblow. Structure and composition of electrochemically prepared oxide layers on Co in alkaline solutions studied by xps. *Surface and Interface Analysis*, 34(1):125–129, 2002.

[64] Michael E.G Lyons, Lisa Russell, Maria O'Brian, Richard L. Doyle, Ian Godwin, and Michael P. Brandon. Redox switching and oxygen evolution at hydrous oxyhydroxide modified nickel electrodes in aqueous alkaline solution: Effect of hydrous oxide thickness and base concentration. *Int. J. Electrochem. Sci.*, 7.

[65] James McBreen. *Nickel Hydroxides*, pages 135–151. Wiley-VCH Verlag GmbH, 2007.

[66] L. D. Burke and T. A. M. Twomey. Influence of the acid/base character of the surface on the electrocatalytic behaviour of both nickel and nickel oxide anodes, with particular reference to oxygen gas evolution. *Journal of Electroanalytical Chemistry and Interfacial Electrochemistry*, 167(1):285–290, 1984.

[67] H. Bode, K. Dehmelt, and J. Witte. Zur kenntnis der nickelhydroxidelektrode—i. Über das nickel (ii)-hydroxidhydrat. *Electrochimica Acta*, 11(8):1079–IN1, 1966.

[68] Jiajia Wu, Dun Zhang, Yi Wang, Yi Wan, and Baorong Hou. Catalytic activity of graphene–cobalt hydroxide composite for oxygen reduction reaction in alkaline media. *Journal of Power Sources*, 198:122–126, 2012.

[69] Zi Xuan Liu, Zhou Peng Li, Hai Ying Qin, and Bin Hong Liu. Oxygen reduction reaction via the 4-electron transfer pathway on transition metal hydroxides. *Journal of Power Sources*, 196(11):4972–4979, 2011.

[70] K. Chang D. Strmcnik A. P. Paulikas P. Hirunsit M. Chan J. Greeley V. Stamenkovic R. Subbaraman, D. Tripkovic and N. M. Markovic. Trends in activity for the water electrolyser reactions on 3d m(Ni, Co, Fe, Mn)hydr(oxy)oxide catalysts. *Nature Materials*, 11:550, 2012.

[71] Lucas-Alexandre Stern and Xile Hu. Enhanced oxygen evolution activity by NiO_x and $Ni(OH)_2$ nanoparticles. *Faraday Discussions*, 176(0):363–379, 2014.

[72] Minrui Gao, Wenchao Sheng, Zhongbin Zhuang, Qianrong Fang, Shuang Gu, Jun Jiang, and Yushan Yan. Efficient water oxidation using nanostructured α-nickel-hydroxide as an electrocatalyst. *Journal of the American Chemical Society*, 136(19):7077–7084, 2014.

[73] Chee Shan Lim, Chun Kiang Chua, Zdenek Sofer, Katerina Klimova, Christopher Boothroyd, and Martin Pumera. Layered transition metal oxyhydroxides as tri-functional electrocatalysts. *Journal of Materials Chemistry A*, 3(22):11920–11929, 2015.

[74] S. Srinivasan. *Chemical Vapor Deposition.* Springer Science and Buisness, 1995.

[75] Martin Peter M. Carlsson, Jan-Otto. *Handbook of Deposition Technologies for Films and Coatings (Third Edition).* Elevisier, 2010.

[76] Lichtenberg Allan J. Liebermann, Michael A. *Principles of Plasma Discharges and Materials Processing).* Wiley, 2005.

[77] Greene J.E. Walton, Scott G. *Plasmas in deposition processes.* Elevisier, 2010.

[78] K. Edvarson K. Siegbahn. X-ray spectroscopy in the precision range of 1:105. *Nuclear Physics 1*, 8:137–159, 1956.

[79] A. Einstein. Über einen die erzeugung und verwandlung des lichtes betreffenden heuristischen gesichtspunkt. *Annalen der Physik*, 322 (6):132–148, 1905.

[80] H. Hertz. Über einen einfluss des ultravioletten lichtes auf die elektrische entladung. *Ann. Physik*, 31:983, 1887.

[81] S. Hüfner. *Photoelectron Spectroscopy: Principles and Applications.* Springer Verlag, 2003.

[82] D. R. Vij. *Handbook of Applied Solid State Spectroscopy.* Springer, 2006.

[83] H. Bubert and H. Jenett. *Surface and thin film analysis: Principles, instrumentation, applications.* Wiley-VCH, Weinheim, 2002.

[84] J. Wolstenholme J. F. Watts. *An introduction to surface analysis by electron spectroscopy.* Wiley, Chichester, 2002.

[85] H. Jenett H. Bubert. *Surface and thin film analysis: Principles, instrumentation, applications.* Wiley-VCH, Weinheim, 2002.

[86] M. P. Seah and G. C. Smith. Quantitative AES and XPS: Determination of the electron spectrometer transmission function and the detector sensitivity energy dependencies for the production of true electron emission spectra in AES and XPS. *Surface and Interface Analysis*, 15(12):751–766, 1990.

[87] N. S. McIntyre and M. G. Cook. X-ray photoelectron studies on some oxides and hydroxides of cobalt, nickel, and copper. *Analytical Chemistry*, 47(13):2208–2213, 1975.

[88] C. A. McDowell D. C. Frost and I. S. Woolsey. Evidence for multiplet splitting of 2p photoelectron lines of transition metal complexes. *Chemical Physics Letters*, 17(3):320–323, 1972.

[89] T. J. Chuang, C. R. Brundle, and D. W. Rice. Interpretation of the x-ray photoemission spectra of cobalt oxides and cobalt oxide surfaces. *Surface Science*, 59(2):413–429, 1976.

[90] Sarah C. Petitto, Erin M. Marsh, Gregory A. Carson, and Marjorie A. Langell. Cobalt oxide surface chemistry: The interaction of CoO (100), Co_3O_4 (110) and Co_3O_4 (111) with oxygen and water. *Journal of Molecular Catalysis A: Chemical*, 281(1–2):49–58, 2008.

[91] Jing Yang, Hongwei Liu, Wayde N. Martens, and Ray L. Frost. Synthesis and characterization of cobalt hydroxide, cobalt oxyhydroxide, and cobalt oxide nanodiscs. *The Journal of Physical Chemistry C*, 114(1):111–119, 2009.

[92] R. de Levie. The electrolysis of water. *Electroanalytical Chemistry*, 476:92–93, 1999.

[93] Michael Wächter. *Tabellenbuch zur Chemie.* Wiley-VCH, 2012.

[94] Youngmin Lee, Jin Suntivich, Kevin J. May, Erin E. Perry, and Yang Shao-Horn. Synthesis and activities of rutile IrO_2 and RuO2 nanoparticles for oxygen evolution in acid and alkaline solutions. *The Journal of Physical Chemistry Letters*, 3(3):399–404, 2012.

[95] Jürgen Ziegler. *Photoelektrosynthese von Wasserstoff mit Silizium-Dünnschicht-Tandemsolarzellen.* PhD thesis, TU Darmstadt, 2015.

[96] L. Bergmann, T. Dorfmüller, and Schaefer C. *Gase, Nanosysteme, Fluessigkeiten.* Walter de Gruyter, 2005.

[97] Kalliopi M. Papazisi, Angeliki Siokou, Stella Balomenou, and Dimitrios Tsiplakides. Preparation and characterization of $Ir_xPt_(1-x)O_2$ anode electrocatalysts for the oxygen evolution reaction. *International Journal of Hydrogen Energy*, 37(21):16642–16648, 2012.

[98] Artjom Maljusch, Oliver Conradi, Sascha Hoch, Matthias Blug, and Wolfgang Schuhmann. Advanced evaluation of the long-term stability of oxygen evolution electrocatalysts. *Analytical Chemistry*, 88(15):7597–7602, 2016.

[99] http://www.infomine.com/investment/metal prices/1. Commodity and metal prices, 2017.

[100] Nguyen Thi Xuyen, Hae Kyung Jeong, Gunn Kim, Kang Pyo So, Kay Hyeok An, and Young Hee Lee. Hydrolysis-induced immobilization of $Pt(acac)_2$ on polyimide-based carbon nanofiber mat and formation of pt nanoparticles. *Journal of Materials Chemistry*, 19(9):1283–1288, 2009.

[101] Gabriel P. López, David G. Castner, and Buddy D. Ratner. Xps O 1s binding energies for polymers containing hydroxyl, ether, ketone and ester groups. *Surface and Interface Analysis*, 17(5):267–272, 1991.

[102] Jing Yang, Hongfei Cheng, and Ray L. Frost. Synthesis and characterisation of cobalt hydroxy carbonate $Co_2CO_3(OH)_2$ nanomaterials. *Spectrochimica Acta Part A: Molecular and Biomolecular Spectroscopy*, 78(1):420–428, 2011. (Jeanne).

[103] Jongwoo Han, Young Jin Sa, Yeonjun Shim, Min Choi, Noejung Park, Sang Hoon Joo, and Sungjin Park. Coordination chemistry of $[Co(acac)_2]$ with n-doped graphene: Implications for oxygen reduction reaction reactivity of organometallic Co-O_4-N species. *Angewandte Chemie International Edition*, 54(43):12622–12626, 2015.

[104] R. G. Charles and P. G. Haverlack. The chemical vapor deposition of cobalt metal from cobalt (ii) acetylacetonate. *Journal of Inorganic and Nuclear Chemistry*, 31(4):995–1005, 1969.

[105] M. Aslam Siddiqi, Rehan A. Siddiqui, and Burak Atakan. Thermal stability, sublimation pressures and diffusion coefficients of some metal acetylacetonates. *Surface and Coatings Technology*, 201(22–23):9055–9059, 2007.

[106] Theodor Weiss, Volkmar Zielasek, and Marcus Baeumer. Influence of water on chemical vapor deposition of ni and co thin films from ethanol solutions of acetylacetonate precursors. *Scientific Reports*, 5:18194, 2015. 26658547[pmid] Sci Rep.

[107] Joan Von Hoene, Robert G. Charles, and William M. Hickam. Thermal decomposition of metal acetylacetonates: Mass spectrometer studies. *The Journal of Physical Chemistry*, 62(9):1098–1101, 1958.

[108] Maria G. Zahl, Randi Fossheim, Knut J. BØrve, Leif J. Sæthre, and T. Darrah Thomas. Electronic properties of chlorine, methyl, and chloromethyl as substituents to the ethylene group—viewed from the core of carbon. *The Journal of Physical Chemistry A*, 119(36):9481–9493, 2015.

[109] D. Ensling, G. Cherkashinin, S. Schmid, S. Bhuvaneswari, A. Thissen, and W. Jaegermann. Nonrigid band behavior of the electronic structure of $LiCoO_2$ thin film during electrochemical li deintercalation. *Chemistry of Materials*, 26(13):3948–3956, 2014.

[110] L. Qiao, H. Y. Xiao, H. M. Meyer, J. N. Sun, C. M. Rouleau, A. A. Puretzky, D. B. Geohegan, I. N. Ivanov, M. Yoon, W. J. Weber, and M. D. Biegalski. Nature of the band gap and origin of the electro-/photo-activity of Co_3O_4. *Journal of Materials Chemistry C*, 1(31):4628–4633.

[111] Haichuan Mu, Zhiqiang Zhang, Xiaojing Zhao, Feng Liu, Keke Wang, and Haifen Xie. High sensitive formaldehyde graphene gas sensor modified by atomic layer deposition zinc oxide films. *Applied Physics Letters*, 105(3):033107, 2014.

[112] Davide Barreca, Cristian Massignan, Sergio Daolio, Monica Fabrizio, Clara Piccirillo, Lidia Armelao, and Eugenio Tondello. Composition and microstructure of cobalt oxide thin films obtained from a novel cobalt(ii) precursor by chemical vapor deposition. *Chemistry of Materials*, 13(2):588–593, 2001.

[113] Maria Magliulo, Bianca Rita Pistillo, Mohammad Yusuf Mulla, Serafina Cotrone, Nicoletta Ditaranto, Nicola Cioffi, Pietro Favia, and Luisa Torsi. Pecvd of hydrophilicCOOH functionalized coatings on electrolyte gated field-effect transistor electronic layers. *Plasma Processes and Polymers*, 10(2):102–109, 2013.

[114] Juergen Brugger, Danick Briand, R. Landgraf, M. K. Kaiser, J. Posseckardt, B. Adolphi, and W. J. Fischer. Functionalization of polymer sensor surfaces by oxygen plasma treatment. *Procedia Chemistry*, 1(1):1015–1018, 2009.

[115] Ranjit Joshi, Joerg Friedrich, and Manfred Wagner. Role of hydrogen peroxide in selective oh group functionalization of polypropylene surfaces using underwater capillary discharge. *Journal of Adhesion Science and Technology*, 25(1-3):283–305, 2011.

[116] Mikko Utriainen, Minna Kröger-Laukkanen, Leena-Sisko Johansson, and Lauri Niinistö. Studies of metallic thin film growth in an atomic layer epitaxy reactor using $M(acac)_2$ (M=Ni, Cu, Pt) precursors. *Applied Surface Science*, 157(3):151–158, 2000.

[117] H. A. Marzouk, J. S. Kim, P. J. Reucroft, R. J. Jacob, J. D. Robertson, and C. Eloi. Evaluation of copper chemical-vapor-deposition films on glass and Si(100) substrates. *Applied Physics A*, 58(6):607–613, 1994.

[118] L. Gragnaniello, S. Agnoli, G. Parteder, A. Barolo, F. Bondino, F. Allegretti, S. Surnev, G. Granozzi, and F. P. Netzer. Cobalt oxide nanolayers on Pd(100): The thickness-dependent structural evolution. *Surface Science*, 604(21–22):2002–2011, 2010.

[119] Joachim Klett, Andreas Eva, Frederick Heinz, Bernhard Kaiser, Wolfram Jaegermann, and Rolf Schäfer. Electrocatalytic performance of high-surface-area platinum catalysts synthesized by chemical vapor deposition for water splitting. *ChemCatChem*, 8(2):345–351, 2016.

[120] Xiang Liu, Huafei Zheng, Zijun Sun, Ali Han, and Pingwu Du. Earth-abundant copper-based bifunctional electrocatalyst for both catalytic hydrogen production and water oxidation. *ACS Catalysis*, pages 1530–1538, 2015.

[121] Yuqian Fan, Haibo Shao, Jianming Wang, Liang Liu, Jianqing Zhang, and Chunan Cao. Synthesis of foam-like freestanding Co_3O_4 nanosheets with enhanced electrochemical activities. *Chemical Communications*, 47(12):3469–3471, 2011.

[122] Jona Schuch. Plasma-enhanced chemical vapor deposition of nickel-, iron-, and nickel-iron-oxides for the oxygen evolution reaction, 2015.

[123] Florian Knaus. Chemische gasphasenabscheidung von ni-katalysatoren zur wasserspaltung, 2015.

[124] Andrew P. Grosvenor, Mark C. Biesinger, Roger St C. Smart, and N. Stewart McIntyre. New interpretations of xps spectra of nickel metal and oxides. *Surface Science*, 600(9):1771–1779, 2006.

[125] Mark C. Biesinger, Brad P. Payne, Leo W. M. Lau, Andrea Gerson, and Roger St C. Smart. X-ray photoelectron spectroscopic chemical state quantification of mixed nickel metal, oxide and hydroxide systems. *Surface and Interface Analysis*, 41(4):324–332, 2009.

[126] S. Oswald and W. Brückner. Xps depth profile analysis of non-stoichiometric NiO films. *Surface and Interface Analysis*, 36(1):17–22, 2004.

[127] Erin L. Ratcliff, Jens Meyer, K. Xerxes Steirer, Andres Garcia, Joseph J. Berry, David S. Ginley, Dana C. Olson, Antoine Kahn, and Neal R. Armstrong. Evidence for near-surface NiOOH species in solution-processed NiO_x selective interlayer materials: Impact on energetics and the performance of polymer bulk heterojunction photovoltaics. *Chemistry of Materials*, 23(22):4988–5000, 2011.

[128] Sol Yun, Young-Chul Lee, and Ho Seok Park. Phase-controlled iron oxide nanobox deposited on hierarchically structured graphene networks for lithium ion storage and photocatalysis. *Scientific Reports*, 6:19959, 2016.

[129] M.C.; McIntyre N.S. Payne, B.P.; Biesinger. The study of polycrystalline nickel metal oxidation by water vapour. *Journal of Electron Spectroscopy and Related Phenomena*, 175:55–65, 2009.

[130] David S. Hall, David J. Lockwood, Christina Bock, and Barry R. MacDougall. Nickel hydroxides and related materials: a review of their structures, synthesis and properties. *Proceedings. Mathematical, Physical, and Engineering Sciences / The Royal Society*, 471(2174):20140792, 2015.

[131] A. F. Carley, S. Rassias, and M. W. Roberts. The specificity of surface oxygen in the activation of adsorbed water at metal surfaces. *Surface Science*, 135(1):35–51, 1983.

[132] S. Jorgensen A.E.Gunnaes T. Valand T. Norby A. Olsen J.Tafto S. Diplas, T. Knutsen. An experimental study of the electronic struture of anodically grown films on amorphous $Ni_78Si_8B_14$ alloy. *Surf. Interface Anal.*, 40:826–829, 2008.

[133] Toru Yamashita and Peter Hayes. Analysis of XPS spectra of Fe^{2+} and Fe^{3+} ions in oxide materials. *Applied Surface Science*, 254(8):2441–2449, 2008.

[134] Shunyi Li, Jan Morasch, Andreas Klein, Christina Chirila, Lucian Pintilie, Lichao Jia, Klaus Ellmer, Michael Naderer, Klaus Reichmann, Melanie Gröting, and Karsten Albe.

Influence of orbital contributions to the valence band alignment of Bi_2O_3, Fe_2O_3, $BiFeO_3$, and $Bi_{0.5}Na_{0.5}TiO_3$. *Physical Review B*, 88(4):045428, 2013. PRB.

[135] M. Muhler, R. Schlögl, and G. Ertl. The nature of the iron oxide-based catalyst for dehydrogenation of ethylbenzene to styrene 2. surface chemistry of the active phase. *Journal of Catalysis*, 138(2):413–444, 1992.

[136] A. P. Grosvenor, B. A. Kobe, M. C. Biesinger, and N. S. McIntyre. Investigation of multiplet splitting of Fe 2p XPS spectra and bonding in iron compounds. *Surface and Interface Analysis*, 36(12):1564–1574, 2004.

[137] L. B. Backman, A. Rautiainen, M. Lindblad, O. Jylhä, and A. O. I. Krause. Characterisation of Co/SiO_2 catalysts prepared from $Co(acac)_3$ by gas phase deposition. *Applied Catalysis A: General*, 208(1–2):223–234, 2001.

[138] Natascha Weidler, Sarina Paulus, Jona Schuch, Joachim Klett, Sascha Hoch, Patrick Stenner, Artjom Maljusch, Joachim Brotz, Carolin Wittich, Bernhard Kaiser, and Wolfram Jaegermann. Coo_x thin film deposited by CVD as efficient water oxidation catalyst: change of oxidation state in XPS and its correlation to electrochemical activity. *Physical Chemistry Chemical Physics*, 18(16):10708–10718, 2016.

[139] Takafumi Akamatsu, Toshio Itoh, Noriya Izu, Woosuck Shin, and Kazuo Sato. Sensing properties of pd-loaded Co_3O_4 film for a ppb-level NO gas sensor. *Sensors (Basel, Switzerland)*, 15(4):8109–8120, 2015. 25853408[pmid] sensors-15-08109[PII] Sensors (Basel).

[140] Yogesh Surendranath, Matthew W. Kanan, and Daniel G. Nocera. Mechanistic studies of the oxygen evolution reaction by a cobalt-phosphate catalyst at neutral ph. *Journal of the American Chemical Society*, 132(46):16501–16509, 2010.

[141] J. Gregory McAlpin, Yogesh Surendranath, Mircea Dinca, Troy A. Stich, Sebastian A. Stoian, William H. Casey, Daniel G. Nocera, and R. David Britt. Epr evidence for Co(IV) species produced during water oxidation at neutral ph. *Journal of the American Chemical Society*, 132(20):6882–6883, 2010.

[142] Matthew W. Kanan and Daniel G. Nocera. In situ formation of an oxygen-evolving catalyst in neutral water containing phosphate and Co^{2+}. *Science*, 321(5892):1072–1075, 2008.

[143] Oscar Diaz-Morales, David Ferrus-Suspedra, and Marc T. M. Koper. The importance of nickel oxyhydroxide deprotonation on its activity towards electrochemical water oxidation. *Chemical Science*, 7(4):2639–2645, 2016.

[144] D. Kwabena Bediako, Yogesh Surendranath, and Daniel G. Nocera. Mechanistic studies of the oxygen evolution reaction mediated by a nickel–borate thin film electrocatalyst. *Journal of the American Chemical Society*, 135(9):3662–3674, 2013.

[145] Junqing Pan, Yanzhi Sun, Pingyu Wan, Zihao Wang, and Xiaoguang Liu. Synthesis, characterization and electrochemical performance of battery grade NiOOH. *Electrochemistry Communications*, 7(8):857–862, 2005.

[146] A. N. Mansour and C. A. Melendres. Characterization of electrochemically prepared γ-NiO(OH) by XPS. *Surface Science Spectra*, 3(3):271–278, 1994.

[147] Huigang Zhang, Xindi Yu, and Paul V. Braun. Three −dimensional bicontinuous ultrafast − charge and − discharge bulk battery electrodes. *Nat Nano*, 6(5):277–281, 2011.

[148] J. G. Kim, D. L. Pugmire, D. Battaglia, and M. A. Langell. Analysis of the $NiCo_2O_4$ spinel surface with auger and x−ray photoelectron spectroscopy. *Applied Surface Science*, 165(1):70–84, 2000.

[149] David Pyke, Kajal K. Mallick, Richard Reynolds, and Ashok K. Bhattacharya. Surface and bulk phases in substituted cobalt oxide spinels. *Journal of Materials Chemistry*, 8(4):1095–1098, 1998.

[150] Seema Verma, Amit Kumar, D. Pravarthana, Aparna Deshpande, Satishchandra B. Ogale, and S. M. Yusuf. Off−stoichiometric nickel cobaltite nanoparticles : thermal stability, magnetization, and neutron diffraction studies. *The Journal of Physical Chemistry C*, 118(29):16246–16254, 2014.

[151] A. C. Tavares, M. A. M. Cartaxo, M. I. da Silva Pereira, and F. M. Costa. Effect of the partial replacement of Ni or Co by Cu on the electrocatalytic activity of the $NiCo_2O_4$ spinel oxide. *Journal of Electroanalytical Chemistry*, 464(2):187–197, 1999.

[152] A. Zakutayev, T. R. Paudel, P. F. Ndione, J. D. Perkins, S. Lany, A. Zunger, and D. S. Ginley. Cation off−stoichiometry leads to high p−type conductivity and enhanced transparency in Co_2ZnO_4 and Co_2NiO_4 thin films. *Physical Review. B, Condensed Matter and Materials Physics*, 85(8), 2012.

[153] G.J. Exarhos, C.F. Windisch Jr., K.F. Ferris, and R.R. Owings. Cation defects and conductivity in transparent oxides. *Applied Physics A*, 89(1):9–18, 2007.

[154] John S. McCloy, Weilin Jiang, Wendy Bennett, Mark Engelhard, Jeffrey Lindemuth, Narendra Parmar, and Gregory J. Exarhos. Electrical and magnetic properties modification in heavy ion irradiated nanograin $Ni_xCo_{(3-x)}O_4$ films. *The Journal of Physical Chemistry C*, 119(39):22465–22476, 2015.

[155] M. N. Iliev, P. Silwal, B. Loukya, R. Datta, D. H. Kim, N. D. Todorov, N. Pachauri, and A. Gupta. Raman studies of cation distribution and thermal stability of epitaxial spinel $NiCo_2O_4$ films. *Journal of Applied Physics*, 114(3):033514, 2013.

[156] Changqiong Zhu, Anna Osherov, and Matthew J. Panzer. Surface chemistry of electrodeposited Cu_2O films studied by XPS. *Electrochimica Acta*, 111:771–778, 2013.

[157] T. Ghodselahi, M. A. Vesaghi, A. Shafiekhani, A. Baghizadeh, and M. Lameii. Xps study of the $Cu@Cu_2O$ core-shell nanoparticles. *Applied Surface Science*, 255(5, Part 2):2730–2734, 2008.

[158] Shude Liu, K. S. Hui, and K. N. Hui. Flower−like copper cobaltite nanosheets on graphite paper as high−performance supercapacitor electrodes and enzymeless glucose sensors. *ACS Applied Materials & Interfaces*, 8(5):3258–3267, 2016.

[159] Santosh Kumar Bikkarolla and Pagona Papakonstantinou. $CuCo_2O_4$ nanoparticles on nitrogenated graphene as highly efficient oxygen evolution catalyst. *Journal of Power Sources*, 281:243–251, 2015.

[160] J. F. Marco, J. R. Gancedo, M. Gracia, J. L. Gautier, E. Rios, and F. J. Berry. Characterization of the nickel cobaltite, $NiCo_2O_4$, prepared by several methods: an XRD, XANES, EXAFS, and XPS study. *Journal of Solid State Chemistry*, 153(1):74–81, 2000.

[161] Matthew W. Kanan and Daniel G. Nocera. In situ formation of an oxygen-evolving catalyst in neutral water containing phosphate and co^{2+}. *Science*, 321(5892):1072–1075, 2008.

[162] James B. Gerken, Sarah E. Shaner, Robert C. Masse, Nicholas J. Porubsky, and Shannon S. Stahl. A survey of diverse earth abundant oxygen evolution electrocatalysts showing enhanced activity from ni-fe oxides containing a third metal. *Energy and Environmental Science*, 7(7):2376–2382, 2014.

[163] B.A. Taleatu G.O. Egharevba A.V. Adedeji O.O. Akinwunmi B. Olofinjana C. Jeynes E.O.B. Ajayi C.U. Mordi, M.A. Eleruja. Metal organic chemical vapour deposited thin films of cobalt oxide prepared via cobalt acetylacetonate. *J. Mater. Sci. Technol.*, 25(01):85–89, 2009.

[164] N. Bahlawane, P. A. Premkumar, J. Feldmann, and K. Kohse-Höinghaus. Preparation of doped spinel cobalt oxide thin films and evaluation of their thermal stability. *Chemical Vapor Deposition*, 13(2-3):118–122, 2007.

A. Appendix

Preliminary experiments performed in a tube-oven

During the construction work of the PECVD system, a tube-oven was used to perform CVD experiments as described many times in literature. [163, 164] The substrate is placed within a quartz glass tube in the tube-oven. Figure A.1 shows a schematic illustration of the experimental setup. The advantage of using this simple CVD setup is that four substrates can be deposited at the same time. Therefore, the preliminary experiments were directed towards the deposition of CoO_x films onto various substrates like silicium, indium-tinn oxide, nickel and titanium. The disadvantage of this simple setup is that the precursor flow can not be separately controlled and the layer thickness can only be poorly adjusted.

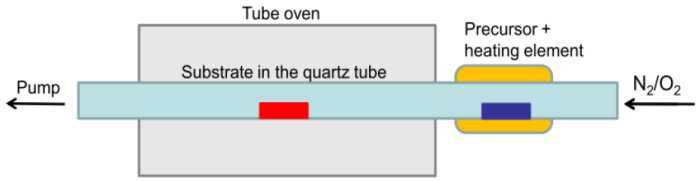

Figure A.1. Schematic illustration of the experimental CVD setup consisting of a tube oven, a quarz tube, a vacuum pump and a gas inlet.

At the beginning, crystalline CoO_x films were deposited. XPS measurements showed that CoO_x was deposited as structure of spinel. The crystallite size seems slightly decreased in case for Co_3O_4 deposited on p-Si. While the Co_3O_4 film deposited on ITO is homogeneously and smooth, the film deposited onto Ni shows a certain roughness as found for the plain Ni-foil.

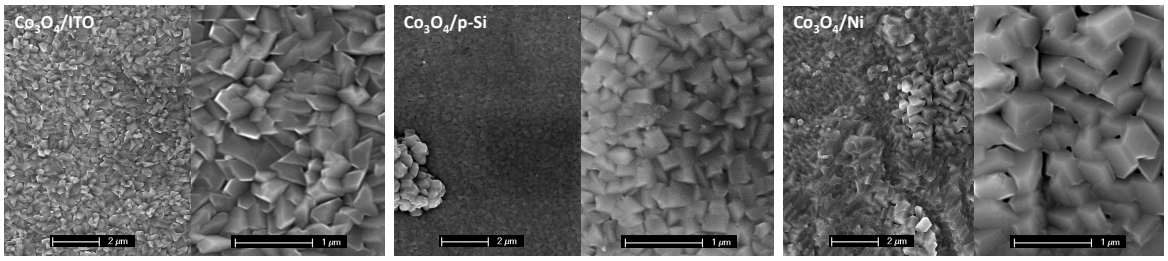

Figure A.2. SEM images of Co_3O_4 deposited onto ITO, p-Si and Ni using a substrate temperature of 550 °C, a precursor temperature of 200 °C, a deposition time of 180 min, an oxidation time of 60 min, an argon flow of 200 sccm and an oxygen flow of 300 sccm.

All films were electrochemically characterized with the specified test protocol. The electrochemical impedance spectroscopy measurements indicate a problem when ITO and Si are used as a substrate in the CVD process. The electrolyte resistance of 0.1 M KOH was found to be around 29.7 Ohm (Figure 7.2). But the impedance plots of Co_3O_4/ITO and Co_3O_4/p-Si show high resistances in the frequency range between 20 kHz-20 Hz, which are not only representing the electrolyte resistance. The additional resistances are due to a decreased conductivity of the substrates. While

the ITO layer apparently partially decomposes in the course of the deposition, the conductivity of Si decreases due to the substrates oxidation. In case of using a metal substrate like Ni, the conductivity does not drastically decrease due to the formation of a NiO passivation layer, which protects the substrate from further oxidation. Nevertheless, also in case of Ni resistances up to 76.1 Ω are obtained due to charge transfer limitations in the µm-thick crystalline films.

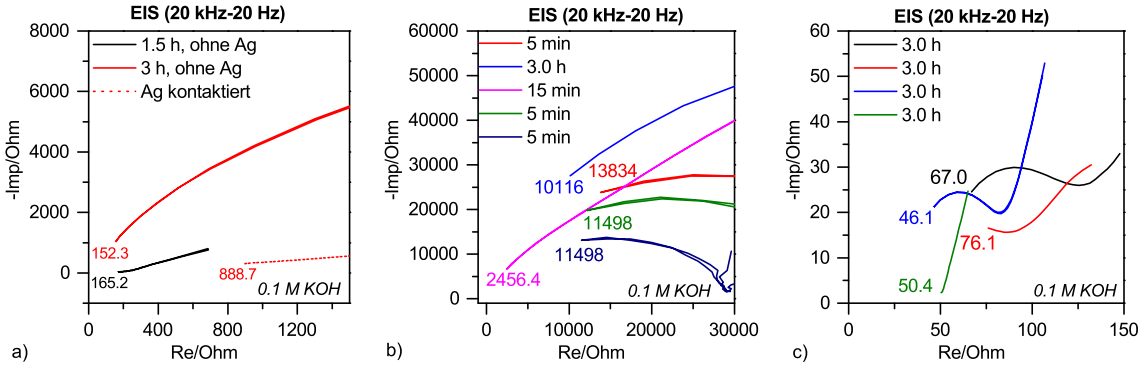

Figure A.3. Nyquist plots of Co_3O_4 deposited on a) ITO, b) Si and c) Ni recorded in the frequency range 20 kHz to 20 Hz.

The experimental setup did not offer the possibility to operate in a plasma enhanced mode. Nevertheless, the influence of plasma oxidation could be studied by carrying out a post-oxidation in the provided sputter deposition system. For this purpose, thin cobalt oxide films were deposited on Ti and Ni with a deposition time of only 10 min, a substrate temperature of 400 °C, a precursor temperature of 200 °C and an argon flow of 200 sccm. The subsequent plasma oxidation was carried out for 15 min with a sputter gas of 70 % O_2 and 30 % Ar. For comparison, the deposition of CoO_x on Ni and Ti was reproduced with the same deposition parameters and then thermally oxidized for 10 min at 400 °C in an oxygen flow of 300 sccm. The SEM images in Figure A.4 compare the plasma oxidized CoO_xfilms deposited on Ni and Ti. In contrast to the thick crystalline Co_3O_4 films shown in Figure A.2, particles are obtained on the surface of the plasma oxidized CoO_x films.

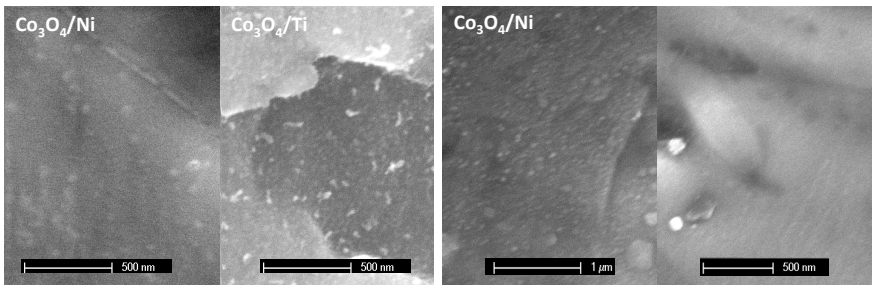

Figure A.4. SEM images of CVD prepared Co_3O_4 on Ni and Ti, which were subsequently plasma oxidized after the deposition, and of thermally oxidized Co_3O_4/Ni.

Figure A.5 a compares the cyclic voltammograms of pl_CoO_x/Ni, th_CoO_x/Ni and Ni-foil recorded in 0.1 M KOH and Figure A.5 b shows the cyclic voltammograms of pl_CoO_x/Ti, th_CoO_x/Ti and Ti-foil. In both cases, the plasma oxidized samples pl_CoO_x/Ni and pl_CoO_x/Ti show a lower onset potential and reduced overpotentials compared to the thermally oxidized films.

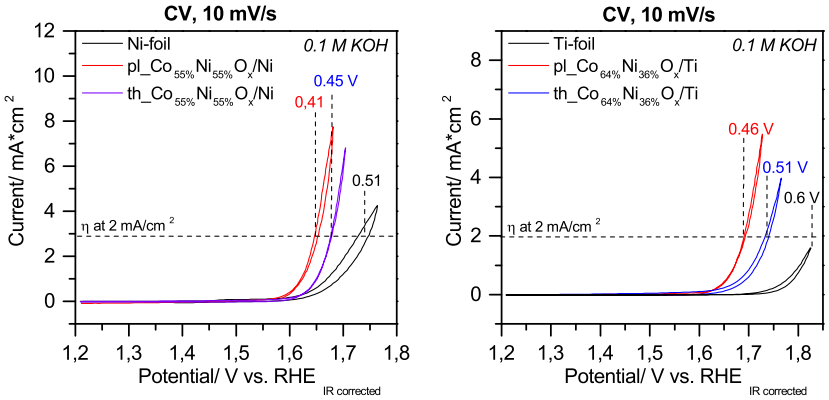

Figure A.5. Cyclic voltammograms of pl_CoO_x/Ni (red), th_CoO_x/Ni (blue) and Ni-foil (black). b Cyclic voltammograms of pl_CoO_x/Ti (red), th_CoO_x/Ti (blue) and Ti-foil (black). All cyclic voltammograms were recorded in 0.1 M KOH with a scan rate of 10 mV/s.

Although the electrochemical activity seems slightly improved for the samples deposited on Ni, Ti was used as a substrate for two reasons: First, titanium has the advantage that it is not OER active itself. Therefore, the measured activity can be related to the catalyst. Second, Ni represents a transition metal compound in the bimetallic catalysts $CoMO_xO_x$ (M= Ni, Fe, Cu). Since it is OER active, one can not relay the activity only to the catalyst. The use of Ni as a substrate would make the determination of the layer thickness by XPS impossible.

B. Acknowledgments

Ich möchte mich an dieser Stelle bei allen Personen ganz herzlich bedanken, die zum Gelingen dieser Arbeit beigetragen haben. In erster Linie gilt mein Dank natürlich Herrn Prof. Jaegermann, der immer ein offenes Ohr für meine Anliegen hatte und mich mit viel Raum zur eigenen Entfaltung trotzdem auf der richtigen Spur gehalten hat. Des weiteren gilt mein Dank auch PD Dr. Bernhard Kaiser, der jederzeit für eine Diskussion bereit war und Marga Lang die jede bürokratische Last von meinen Schultern nahm. Frau Prof. Kramm, Herrn Prof. Schäfer und Herrn Prof. Ensinger möchte ich für das Durcharbeiten und Bewerten meiner Dissertation danken.
Ein besonderer Dank gilt auch dem Werkstattteam um Jochen Rank und Michael Weber, die mich tatkräftig beim Aufbau und der Instandhaltung des Plasma-gestützten CVD Systems unterstützt haben.
Kerstin Lakus-Wollny danke ich nicht nur für die Aufnahmen etlicher SEM Bilder sondern auch für die amüsanten Frühstückspausen vor der Messzeit. In diesem Sinne auch Dankeschön an Joachim Brötz für die XRD Aufnahmen, an Christian Lohaus und Markus Motzko für Raman Messungen und Carolin Wittich für die Aufnahme von HREM Bildern.
Auch allen Projektpartnern möchte ich danken für die tolle Zeit und die inspirierende Zusammenarbeit im SuShy Konsortium. Die Projekttreffen waren stets ein Highlight. Den von mir betreuten Studenten Jona Schuch, Sarina Paulus, Florian Knaus und Jaime Ursul möchte ich für die ergebnisreiche Zusammenarbeit danken.
Abgesehen von dem sehr interessanten Thema bin ich vor allem auch wegen meiner Kollegen jeden Tag mit großer Freude zur Arbeit angetreten. Danke für die tolle Zusammenarbeit an meine Wasserspalter Joachim Klett, Jürgen Ziegler, Sven Tengeler, Florent Yang, Jona Schuch, Andreas Hajduk, Thorsten Cottre, Shasha Tao und Leslie Frotscher, die mir immer hilfsbereit zur Seite standen. Danke an die "GirlsGang"- Mercedes Carrillo, Natalia Schulz und an Markus Motzko sowie Philip Reckers für die Unterstützung, ohne euch wären die Kaffeepausen nicht das was sie waren.
Zu guter Letzt möchte ich meiner Familie aber insbesondere meinem Ehemann Heiko danken, der mir nie böse war wenn es "mal länger" wurde und mir nicht nur interessiert zugehört hat wenn es mal wieder um die Arbeit ging sondern auch immer sein bestes gab mir bei der Problemlösung zu helfen.

(Ein Teil) dieser Arbeit wurde von Evonik Industries AG und dem deutschen Bundesministerium für Bildung und Forschung innerhalb des Projekts Sustainable Hydrogen(FKZ : 03X3581A) finanziert. Zusätzlich danke ich der finanziellen Unterstützung der Darmstädter Exzellenz-Graduiertenschule für Energiewissenschaft und Energietechnik. .

C. Curriculum Vitae

Natascha Weidler, geb. Schäfer

Beruflicher Werdegang

01.12.2016 bis heute	Wissenschaftliche Mitarbeiterin bei Prof. Ulrike Kramm Fachbereich Materialwissenschaften/Chemie Fachgebiet Katalyse und Elektrokatalyse
05.2013- 06.2016	Promotion an der TU Darmstadt unter Prof. Jaegermann Fachbereich Materialwissenschaften, Fachgebiet Oberflächenforschung
04.2011- 02.2013	Hilfswissenschaftlerin an der TU Darmstadt (Prof. Buntkowsky) Fachbereich Chemie

Akademische Ausbildung

04.2011- 04.2013	Master of Science (Chemie), TU Darmstadt Thesis unter Prof. Claus, Technische Chemie, Note: 1.3
10.2007- 04.2011	Bachelor of Science (Chemie), TU Darmstadt Thesis unter Prof. Buntkowsky, Physikalische Chemie, Note: 1.0
04.2011- 02.2013	Hilfswissenschaftlerin an der TU Darmstadt (Prof. Buntkowsky) Fachbereich Chemie

Ehrenämter

05.2013- 10.2015	Gleichstellungsbeauftragte der Materialwissenschaften

Publikationen

XPS Investigation of PECVD Deposited NiO_x, $NiO_x(OH)_y$ and $CoNiO_x(OH)_y$: Influence of the Chemical Composition on the Catalytic Activity for the Oxygen Evolution Reaction

N. Weidler, J. Schuch, F. Knaus, P. Stenner, S. Hoch, A. Maljusch, R. Schäfer, B. Kaiser and W. Jaegermann

J. Phys. Chem. C, 2017, 121 (12), pp 6455–6463

CoOx Thin Film Deposited by CVD as Efficient Water Oxidation Catalyst: Change in Oxidation State in XPS and its Correlation to Electrochemical Activity

N. Weidler, S. Paulus, J. Schuch, J. Klett, S. Hoch, P. Stenner, A. Maljusch, J. Brötz, C. Wittich, B. Kaiser and W. Jaegermann

Phys. Chem. Chem. Phys., 2016, Advance Article DOI: 10.1039/C5CP05691H, Advance Article

Template-based synthesis of metallic Pd nanotubes by electroless deposition and their use as catalysts in the 4-nitrophenol model reaction

E. Felix, M. Antoni, I. Pause, S. Schaefer, U. Kunz, N. Weidler, F. Muench and W. Ensinger

Green Chem., 2015, Advance Article, DOI: 10.1039/C5GC01356A

Highly cis-selective and lead-free hydrogenation of 2-hexyne by a supported Pd catalyst with an ionic-liquid layer

F. Schwab, N. Weidler, M. Lucas and P. Claus

Chem. Commun., 2014, DOI: 10.1039/C4CC04183F

Konferenzbeiträge

03.2016	49. Jahrestreffen Deutscher Katalytiker, Weimar, *Vortrag*
09.2015	Europacat, Kazan (Russland), *Vortrag*
06.2015	CIP, St. Etienne (Frankreich), *Vortrag*
11.2014	Electrochemistry 2014, Mainz, *Poster*
05.2014	EMRS, Lille (Frankreich), *Poster*
03.2014	47. Jahrestreffen Deutscher Katalytiker, Weimar, *Poster*
03.2013	46. Jahrestreffen Deutscher Katalytiker, Weimar, *Poster*